
# EXPLORING CARBON CAPTURE AND STORAGE: BRIDGING THE GAP BETWEEN LABORATORY AND INDUSTRY

**Santiago Alexander Capelo Avilés**

UNIVERSITAT
ROVIRA i VIRGILI

# Exploring Carbon Capture and Storage: Bridging the Gap Between Laboratory and Industry.

---

SANTIAGO ALEXANDER CAPELO AVILÉS

**DOCTORAL THESIS**
**2024**

Santiago Alexander Capelo Avilés

# Exploring Carbon Capture: Bridging the Gap Between Laboratory and Industry.

## Doctoral Thesis in Chemical Technologies

Supervised by: Prof. Dr. Jose Ramón Galán Mascaros
Dr. Stefano Giancola

Institut Català d'Investigació Química (ICIQ)
Galan Mascaros Research Group

Universitat Rovira i Virgili
Institut Català d'Investigació Química

---

Tarragona, september 2024

ICIQ
Institut Català d'Investigació Química

UNIVERSITAT ROVIRA i VIRGILI

FAIG CONSTAR que aquest treball, titulat "Exploring Carbon Capture and Storage: Brindging the Gap Between Laboratory and Industry.", que presenta Santiago Alexander Capelo-Avilés per a l'obtenció del títol de Doctor, ha estat realitzat sota la meva direcció al ICIQ i al Departament d' Química d'aquesta universitat.

---

HAGO CONSTAR que el presente trabajo, titulado "Exploring Carbon Capture and Storage: Brindging the Gap Between Laboratory and Industry", que presenta Santiago Alexander Capelo-Avilés para la obtención del título de Doctor, ha sido realizado bajo mi dirección en el ICIQ y el Departamento de Química de esta universidad.

---

I STATE that the present study, entitled "Exploring Carbon Capture and Storage: Brindging the Gap Between Laboratory and Industry", presented by Santiago Alexander Capelo-Avilés for the award of the degree of Doctor, has been carried out under my supervision at the ICIQ and the Chemistry Department of this university.

---

Tarragona, 2024-06-21

El/s director/s de la tesi doctoral
El/los director/es de la tesis doctoral
Doctoral Thesis Supervisor/s

Prof. Dr. José Ramón Galán Mascarós

Dr. Stefano Giancola

# Acknowledgements

*"To become an artist, you have to be curious."*
Leonardo Da Vinci.

First and foremost, I am immensely grateful to my supervisor, José Ramón Galán Mascarós (JR). Thank you for granting me the opportunity to be part of this group and for your unwavering support and guidance throughout this journey. Your positive attitude, open-mindedness, and unwavering encouragement have been invaluable. I am incredibly fortunate to have had you as a mentor.

I would also like to extend my gratitude to my co-tutor, Stefano "Chavo." Despite the occasional language barriers haha (mixing Italian, Spanish, French and English in the same conversation), we successfully collaborated in the lab for several years. Your unwavering support in the laboratory was instrumental to this research.

My sincere thanks to Anna Casals and Paola Baldivieso for their invaluable assistance at CELSA. Your patience and understanding were crucial in navigating the complexities of balancing work between CELSA and ICIQ. Thank you for enabling me to pursue this doctoral thesis.

To my past and present labmates: thank you for your camaraderie, emotional support, and shared experiences. This journey wouldn't have been possible without your diverse perspectives and fun-loving spirit. I cherish the conversations, laughter, and anecdotes we've shared. Each of you has contributed to my growth as both a researcher and a person. Vane and Felipe, your dedication and support are the bedrock of the JR lab.

Finally, my deepest gratitude to my family and friends, the pillars of my life. Thank you to my parents, Susy and Vladi, for always supporting my pursuit of education abroad. To Rai and Sophie, you are my daily joy and the source of my resilience. To my grandparents, Romelia and Gerardo, thank you for instilling in me the appreciation

for life's simple pleasures. I am eternally grateful to everyone who has been a part of my doctoral journey.

# Contents

# List of Figures

# List of Tables

# Glossary, acronyms, and symbols.

**A** ÅAngstrom

**BT** Breakthrough

**BT**$_t$ Breakthrough time

**C** Concentration

**CC** Carbon capture

**CCS** Carbon capture and storage

**CCU** Carbon capture and utilization

$CO_2$ **wt%** $CO_2$ percentage weight loss.

$\Delta H$ Heat of adsorption

$\delta CaO$ Carbonation degree.

$\Delta_m CaCO_3$ Calcium carbonate mass difference.

**ESEM** environmental scanning electron microscopy

**EAF** Electric arc furnace.

**EDX** energy-dispersive X-ray analysis

**FTIR** Fourier Transform Infrared Spectroscopy

**IAST** Ideal adsorbed solution theory

**ICP** inductively coupled plasma

$K_a$ Adsorption mass transsfer constant.

$K_d$ Desorption mass transsfer constant.

**kW-h** Kilowatt hour.

**L/S** Liquid to solid ratio.

**MOF** Metal-organic framework

**m** mass

**min** minutes

$\mu$ micro or viscosity

**mL** milliliters

**P** Pressure

**PCC** Post-combustion carbon capture

**PSA** Pressure swing adsorption

$\phi$ void fraction

$q_s$ Adsorption capacity at saturation

$q_b$ Adsorption capacity at breakthrough point

**RW** Refractory waste.

$\rho$ density

$\rho_b$ Bulk density

$\rho_s$ Skeletal density

**SEM** scanning electron microscope

**S** Selectivity

$S_s$ Selectivity at saturation

$S_b$ Selectivity at breakthrough point

**SC** $CO_2$ secuestration capacity.

**T** Temperature

**t** time

**TGA** thermogravimetric analysis

**TAMOF-1** Triazole-acid metal-organic framework

$\theta$ angle

$v$ velocity

**V** Volumne

**VSA** Vacuum swing adsorption

**WS** White slag.

**XRD** X–ray diffraction

*Dedicated to Sophie.*

# Abstract

This doctoral thesis includes the work carried out at ICIQ and CELSA on the study of $CO_2$ capture and mineralization. In the steel industry, which notably contributes to global $CO_2$ emissions, Chapter 2 explores and evaluates current benchmark carbon capture technologies. These technologies are critically assessed for their integration potential into a secondary steel plant, namely CELSA. Process simulation and comprehensive infrastructure assessment are employed to identify technically feasible and economically viable options. Among the technologies considered, amine scrubbing and vacuum swing adsorption (VSA) with zeolite 13X emerge as the most developed and suitable solutions for carbon capture in CELSA. However, it's crucial to highlight that the results obtained during the assessment did not yield promising outcomes that would warrant immediate implementation. However, novel systems and, more importantly, promising materials and chemicals for $CO_2$ capture are emerging to undergo testing in existing industrial infrastructures. In chapters 3 and 4, the versatile metal-organic framework TAMOF-1 is characterized as a highly selective material for $CO_2$ in $CO_2/N_2$ and $CO_2/CH_4$ mixtures. It is evaluated for post-combustion $CO_2$ capture and biogas upgrading, exhibiting promising results not only experimentally but also theoretically and computationally. To achieve full utilization of CO2 in the value chain, it must not only be captured from industrial or environmental gas streams but also transformed into useful products (e.g., fuels, building materials, food feedstock) or stored in geological sources (or industrial wastes that mimic this geological behavior). Chapter 5 provides a comprehensive characterization of CELSA slags as a potential storage medium for $CO_2$ in the form of carbonates. This characterization aims to contribute insights into waste management (both solid and gaseous) and promote better practices for the circular management of these materials. By exploring the potential of CELSA slags as a $CO_2$ storage medium, this research contributes

to the development of sustainable solutions for carbon capture and utilization, aligning with broader efforts to mitigate climate change and transition to a low-carbon economy.

# Scientific contributions

1. Capelo-Avilés, S; Tomazini, R; Gallo Stampino, I; Gisperd-Guirado, F; Casals-Terre, A; Giancola, S; Galán-Mascaros, JR. A thorough assessment of mineral carbonation of steel slag and refractory waste. *J. CO2 Util.* 82, 102770 (2024).

2. Capelo-Avilés, S; Fez-Febré, M; Balestra, S; Cabezas-Giménez, J; Anton Vidal-Ferran, A; González-Cobos,J; Lillo, V; Fabelo, O; Escudero-Adán, E; Falvello, L; Parra,J; Rumori,P; Turnes-Palomino,G; Palomino-Cabello,C; Giancola, S; Calero, S; Galan-Mascaros, JR. Selective adsorption of $CO_2$ in TAMOF-1 for the separation of $CO_2/CH_4$ gas mixtures. *Adv. Funct. Mater.* 81, 102769 (2024).**Submitted**

*"If I had an hour to solve a problem I'd spend 55 minutes thinking about the problem and 5 minutes thinking about solutions."*

Albert Einstein

# 1 Introduction

# Contents

# 1.1 Background and Relevance

## 1.1.1 Growing concern about $CO_2$ emissions

The Intergovernmental Panel on Climate Change (IPCC) projects that if current trends continue, global warming is expected to reach 1.5°C between 2030 and 2050[1]. This temperature increase is primarily driven by population growth and development, which heavily relies on the use of fossil fuels. Over the past few decades, carbon dioxide ($CO_2$) emissions from fossil fuel consumption have doubled, surpassing 36.8 Gt of $CO_2$ per year[2]. Consequently, there has been an estimated increase of 0.8-1.2°C from pre-industrial levels[1,2].

The gradual rise in global temperatures has significant implications, leading to a growing range of risks to humanity, economies, and ecosystems. These risks include sea level rise, intensified extreme weather events, biodiversity loss, and threats to human health, security, food availability, and water resources[3]. Effectively addressing these challenges requires comprehensive political, economic, and technological investments on a global scale to expedite the implementation of decarbonization strategies.

The scientific and industrial communities will play a pivotal role in the endeavor to develop and enhance technologies that facilitate the effective management of $CO_2$ emissions. Notably, carbon capture and sequestration (CCS), a process involving the selective capture and permanent underground storage of $CO_2$, has been widely acknowledged as a critical component within strategies aimed at constraining global warming to levels below 2°C[3–6].

## 1.1.2 Why carbon capture??

The process of capturing $CO_2$ entails the selective separation and concentration of carbon dioxide from a gas mixture (e.g. $CO_2/N_2$, $CO_2/CH_4$). The purity level of $CO_2$ captured is crucial, depending on the specific application and intended utilization. This concept is commonly referred to as $CO_2$ capture and utilization (CCU), emphasizing the future valorization of the captured $CO_2$.

In another approach, after the $CO_2$ capture process, the focus shifts to storage the $CO_2$-rich stream in geological reservoirs. In this context, the emphasis is primarily on the secure and reliable storage of $CO_2$, with less emphasis on achieving extremely high purities. This

approach is commonly known as $CO_2$ capture and storage (CCS), recognizing the importance of effectively sequestering $CO_2$ in geological formations.

$CO_2$ capture plays a fundamental role in the integration of the energy transition mix towards a low-carbon economy and the achievement of greenhouse gas emissions neutrality goals. The following are some reasons highlighting the importance of $CO_2$ capture in this context:

**Emission reduction:** $CO_2$ capture enables the direct removal of carbon dioxide from the atmosphere, preventing its release through emission sources. By capturing and storing $CO_2$ emitted by industries, power plants, and other sectors, a significant reduction in greenhouse gas emissions is achieved.

**Complement to renewable energies:** While renewable energies are crucial for transitioning to a cleaner energy matrix, the intermittent and sometimes unpredictable generation of renewable energy can pose challenges in maintaining a constant and stable electricity supply. CO2 capture can help compensate for these variations by allowing the use of fossil fuels in combination with carbon capture and storage technologies. This facilitates a smoother transition towards an energy system based on renewable sources.

**Utilization of existing energy sources:** $CO_2$ capture enables the utilization of existing infrastructures and investments in power plants and other industrial processes that rely on fossil fuels. By implementing carbon capture and storage technologies in these facilities, the need for complete replacement can be limited, while maximizing the efficiency of the existing assets.

**Offsetting hard-to-reduce emissions:** While actions to reduce emissions at the source should be prioritized, there are sectors where complete elimination of emissions is particularly challenging, such as cement, steel, and chemical production. $CO_2$ capture offers a solution to address these "hard-to-reduce" emissions by capturing and storing the $CO_2$ released in these processes, thereby contributing to global emissions mitigation.

Bridge to negative emissions technologies: In addition to capturing $CO_2$ from emission sources, carbon capture can also play a key role in the development of negative emissions technologies. These technologies, such as direct air capture and bio-energy with carbon capture and storage (BECCS), have the potential to remove additional $CO_2$ from the atmosphere, helping to offset historical emissions

and achieve carbon neutrality goals[7,8].

Moreover, Brian et al.(2017)[9] conducted a comprehensive study utilizing historical and current IPCC data, providing compelling evidence that supports the indispensability of integrating $CO_2$ capture technologies across the energy sector to meet the 2050 net emissions commitment. Their research demonstrated that only a scenario incorporating these technologies can effectively achieve the desired outcome. Through the implementation of carbon capture technologies, the potential elimination of up to 12.6 PgC per year becomes feasible, resulting in the storage of 776-981 PgC by the year 2100.

Furthermore, their findings indicate that this particular scenario offers promising prospects for curbing the rise in atmospheric carbon concentration. By the end of the century, the projected atmospheric carbon concentration is estimated to range between 328-363 p.p.m., accompanied by a corresponding atmospheric temperature range of approximately 1.2-1.4$^{o}$C. Importantly, these figures align with the climate objective of limiting temperature rise to below 1.5$^{o}$C, representing a crucial milestone in climate mitigation efforts. Additionally, this scenario exhibits the potential for a gradual transition back to atmospheric carbon concentration levels comparable to those observed during the pre-industrial era.

In this context, the focus of this doctoral thesis on $CO_2$ capture holds significant scientific and practical importance. By investigating and enhancing the efficiency of a new $CO_2$ capture technology, this research contributes to the global efforts aimed at mitigating climate change and establishing a sustainable future.

### 1.1.3 Technological pathways for $CO_2$ capture

There are four pathways for the concentration of $CO_2$ (1.1, three of which (post-combustion, pre-combustion, and oxy-combustion) are implemented in industrial manufacturing processes. The fourth pathway involves the capture of $CO_2$ directly from the atmosphere.

**Pre-combustion:** The carbon is removed from the fuel before to enter in the combustion chamber. Syn-gas (mixture of CO and $H_2$) is produced by the fuel gasification, then the CO is oxidized to $CO_2$ and $H_2O$ reduced to $H_2$ in an shift-reactor. Then the mixture of $CO_2/H_2$ is separated, the $H_2$ for fuel and the $CO_2$ is compressed and storage.

**Oxy-combustion:** The fuel undergoes combustion in an oxygen-

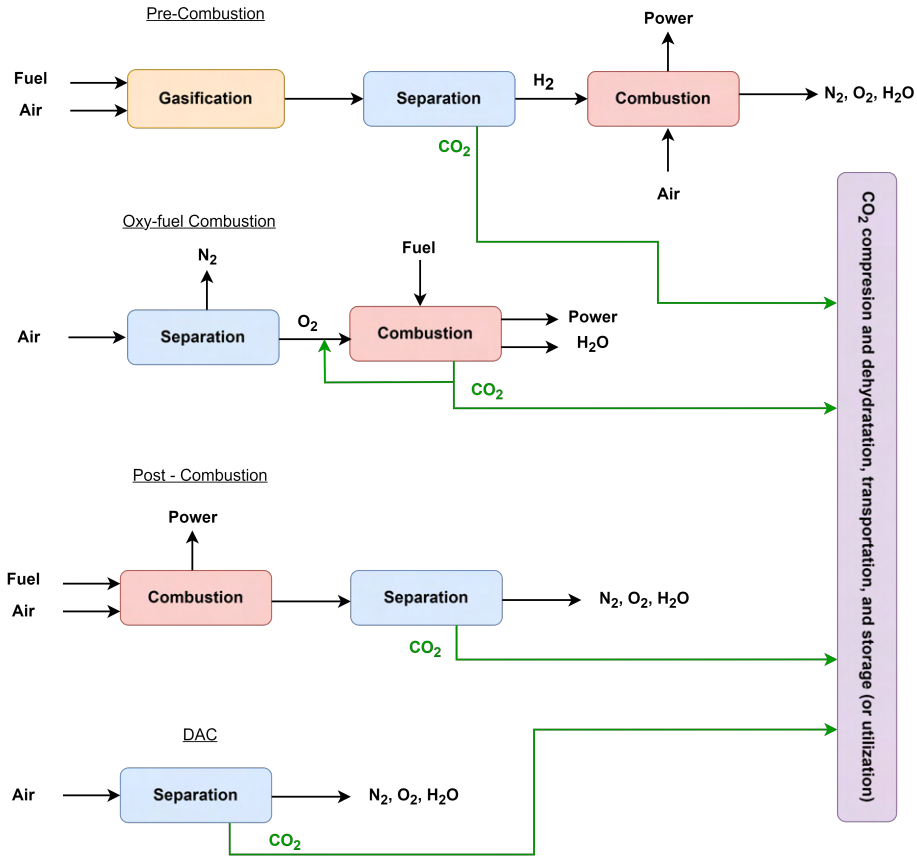


Figure 1.1: Strategies for $CO_2$ capture in power plants. Figure adapted with permission from ref.[3,10,11]

rich stream with minimal or no nitrogen content. Initially, the oxygen ($O_2$) is separated from the $O_2/N_2$ mixture found in the air (this step consumes a significant portion of the energy pathway). Subsequently, pure oxygen is employed as the oxidizing agent during the combustion of hydrocarbon fuel. This process yields flue gas, which is abundant in $CO_2$ and $H_2O$, with the latter being easily condensable.

**Post-Combustion:** Following the combustion process where the fuel reacts with oxygen, the resulting gas, known as flue gas, is composed primarily of $N_2$, $CO_2$, $O_2$, $H_2O$, and various impurities. Typically, this gas is discharged into the atmosphere as waste since it is downstream of industrial processes, requiring no modifications to existing industrial facilities for CO2 capture. The main challenge associated with this capture method lies in the energy-intensive separation of $CO_2$ from the predominantly present $N_2$ in the flue gas[12].

**Direct air capture (DAC):** This particular technological pathway focuses on the extraction of $CO_2$ from the surrounding atmosphere. As the atmospheric concentration of $CO_2$ is relatively low (approximately 400 $ppm_v$), this process demands a substantial amount of energy[13]. In recent years, it has gained prominence as a crucial strategy in mitigating the levels of atmospheric $CO_2$, alongside the three aforementioned pathways for $CO_2$ capture.

This thesis primarily centers around post-combustion $CO_2$ capture. This method holds significant importance as it allows for the installation of $CO_2$ capture infrastructure without disrupting the production process, offering a rapid solution to mitigate the $CO_2$ industrial emissions[5]. However, for it to be effective, the captured $CO_2$ must be either stored (CCS) or utilized as a carbon source to produce valuable materials like biofuels, solar fuels, plastics, and so on (CCU).

One of the primary limitations of post-combustion carbon capture is the low concentration of $CO_2$ in the flue gas, typically ranging from 4% to 20%[3,14–16]. The energy required to concentrate $CO_2$, is inversely related to its concentration in a gas mixture. The minimum energy demand is approximately 9 $kJ \cdot mol^{-1}$ of $CO_2$ captured[3]. As illustrated in Figure 1.2, depicting the minimum work required for typical $CO_2$ concentrations in gaseous streams.

Recognizing the significance of $CO_2$ capture as an additional tool, alongside renewable energies, hydrogen utilization, process optimization, and waste management, serves as the fundamental technological framework. Together with a shift in social awareness, these approaches will contribute to the achievement of the carbon neutrality goal by 2050.

## 1.2 Post-Combustion $CO_2$ Capture Technologies

Presently, the prevailing technology employed on an industrial scale for the separation of acid gases, such as $CO_2$ or $H_2S$, from combustion gases, natural gas and or other industrial processes is amine-based absorption. This technology capitalizes on the reversible nature of the reaction between an aqueous alkali solvent and an acid gas[17,18]. Nevertheless, despite its considerable advancement, this methodology confronts several critical challenges that impede the economic

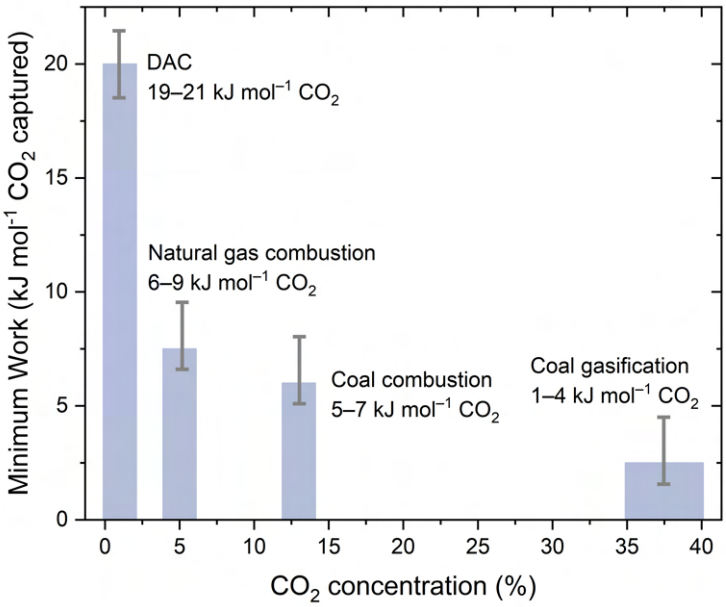


Figure 1.2: Minimum work required for $CO_2$ capture based upon initial gas concentration. Grey bars and ranges indicate the variation in minimum work anticipated for 50% $CO_2$ capture at 80% purity (lower bound) to 90% $CO_2$ capture at 99% purity (upper bound). Figure adapted with permission from ref.[3,14]

viability of $CO_2$ capture for enterprises. These challenges include the substantial energy consumption associated with amine regeneration and the production of toxic waste that poses considerable difficulties in terms of disposal and management, among other issues.

Several promising $CO_2$ capture technologies are emerging, and while some have reached advanced stages of development, further research is required to render $CO_2$ capture economically viable on a large scale. The progress of these technologies has been hindered by the fact that the cost of $CO_2$ capture has historically exceeded the cost of releasing $CO_2$ into the atmosphere. However, the changing landscape has prompted various government initiatives and industrial investments aimed at achieving technological maturity in emerging $CO_2$ capture methods[1,2,4,19]. Furthermore, the $CO_2$ concentration in flue gas typically ranges below 15%. Consequently, the thermodynamic driving force for CO2 capture from flue gas is relatively low

($CO_2$ partial pressure is typically less than 0.15 bar), posing a significant technical challenge in developing cost-effective advanced capture processes[20].

Novel $CO_2$ capture technologies possess the potential to significantly enhance the industrial-level capture process by improving energy efficiency and addressing current limitations. Among these technologies are high-temperature solid looping systems, the advancement of new solid sorbents, and the development of membranes. These advancements hold promise for reducing energy consumption and mitigating challenges associated with current capture technologies[3,19,20].

### 1.2.1 Amine-Based stripping

$CO_2$ post-combustion capture using amine aqueous solutions involves a reactive absorption-solvent regeneration process. As illustrated in Figure 1.3, a typical amine-based carbon capture system comprises two primary sections: 1) the absorption section, where $CO_2$/vapor are solubilized in a liquid amine based sorbent (capture the $CO_2$), and 2) the stripping section, where the solvent is regenerated under steam ($CO_2$ release)[21,22].

The absorber receives two inputs: flue gas enters the column from the bottom and flows upward, while the amine solvent enters from the top. The $CO_2$ content of the flue gas depends on its source. Coal-fired boilers typically emit flue gas with 10-15% $CO_2$, while natural gas-fired and biomass-fired boilers release flue gas with 4-9% $CO_2$ and 12-14% $CO_2$, respectively. Industrial process streams, such as blast furnace gas (steel industry), cement kiln off-gas, and oil refinery plant fired heater off-gas, have $CO_2$ concentrations of 22%, 19%, and 8-9%, respectively[3]. As the flue gas ascends through the absorber, it interacts with the amine solvent, enabling $CO_2$ capture. The resulting gas coming off the top of the absorber is purified and release to the atmosphere[23].

The rich solvent, laden with $CO_2$, enters the upper-middle section of the stripper and encounters steam generated in the lower section. The steam's energy effectively releases $CO_2$ from the solvent, regenerating the solvent to a lean state. This regeneration process consumes the largest portion of energy in the overall $CO_2$ capture process, typically ranging from 3.5 to 5.5 GJ ton$^{-1}$ $CO_2$, although some studies report values as low as 2.9 GJ ton$^{-1}$ $CO_2$[3,24–26]. The lean solvent,

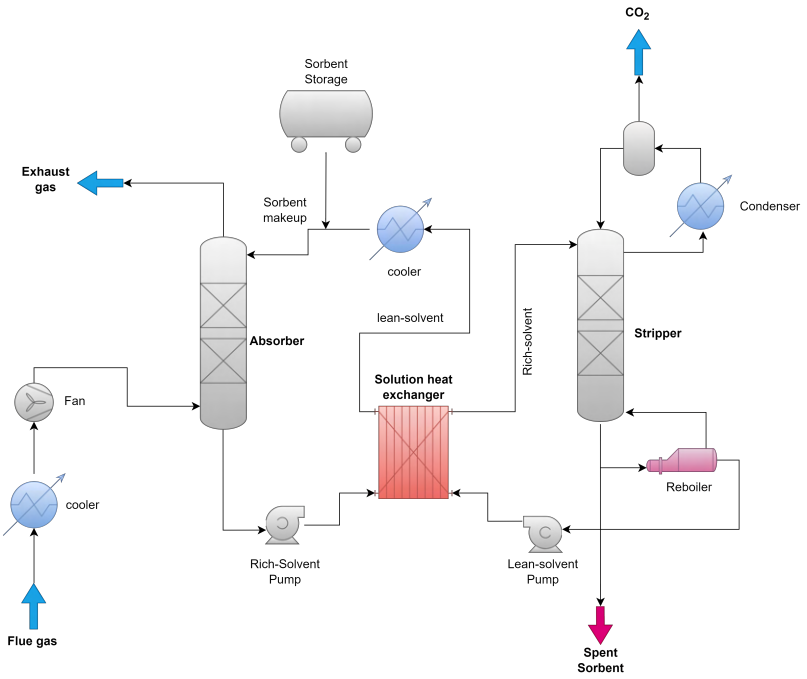


Figure 1.3: Typical and simplified process flow diagram (PFD) of amines stripping $CO_2$ capture system.

now devoid of $CO_2$, exits the stripper and returns to the absorber. However, a small fraction of the lean solvent degrades due to temperature control issues within the stripper and requires treatment before disposal.

The $CO_2$ released by the steam energy ascends to the top of the stripper and passes through a condenser to remove as much water vapor as possible, enabling its transportation to storage. The condensed water returns to the stripper for reuse.

A cross exchanger, positioned strategically between the absorber and stripper, plays a crucial role in energy optimization. It heats the rich amine entering the stripper while simultaneously cooling the lean amine exiting the stripper. The rich amine requires heating to approximately 110°C, while the lean amine is cooled to the absorber's operating temperature of around 40°C[27]. The cross exchanger utilizes the sensible heat from the hot stripper bottoms to heat the absorber bottoms, reducing the energy demand for the reboiler. In general, the lean solvent may require further cooling with cooling water to reach the desired temperature for the absorber.

### 1.2.2 Carbonation-Calcination (CaO lopping)

The concept of calcium looping (Ca-Loop) encompasses a diverse array of $CO_2$ capture process routes with varying degrees of maturity, technical complexity, and economic viability. Moreover, The Technology Readiness Level (TRL) varies depending on the type of process configuration (currently and intermediate level 5-8), all of which operate on the same thermodynamic principle. Figure 1.4 shows a simplified schematic diagram of the Ca-Loop process and its integration into a power generation plant. These process options share the common use of calcium oxide (CaO) as a regenerable sorbent for $CO_2$ capture. At high temperatures, CaO reacts with $CO_2$ to form $CaCO_3$. Subsequently, calcination of $CaCO_3$ in a $CO_2$-rich atmosphere (potentially containing steam) completes the "calcium loop." The high temperatures required for sorbent regeneration through $CaCO_3$ calcination and the high temperature of $CO_2$ absorption in the carbonation reaction distinguish calcium looping systems from other post-combustion $CO_2$ capture systems. Heat recovery can be highly efficient using advanced steam cycles, thereby reducing the overall energy penalty of the system[4,28]. The equilibrium curve of $CO_2$ on CaO establishes the relevant temperature ranges for $CO_2$ capture applications. This equilibrium indicates that it is possible to reduce the $CO_2$ concentration in a flue gas at atmospheric pressure below 1.2%vol at 650°C, while temperatures exceeding 900°C are required to produce a pure $CO_2$ stream during $CaCO_3$ calcination. The demand for high temperatures in a $CO_2$-rich calciner presents the primary challenge in determining the method for supplying the necessary heat for CaO regeneration. The calcination enthalpy of $CaCO_3$ is quite high (168 kJ/mol at 900°C), and it is inherently difficult to provide a large heat flux to a high-temperature reactor[18,29].

### 1.2.3 Pressure and Temperature swing Adsorption (PSA and TSA)

In the realm of carbon capture technologies, adsorption processes play a pivotal role in effectively sequestering $CO_2$ from industrial emissions. Diverging from absorption, where $CO_2$ dissolves in liquid solvents like amines, adsorption entails the adherence of $CO_2$ to the surface of a sorbent. This method utilizes porous dry solids, characterized by high surface areas and adsorption capacities, including

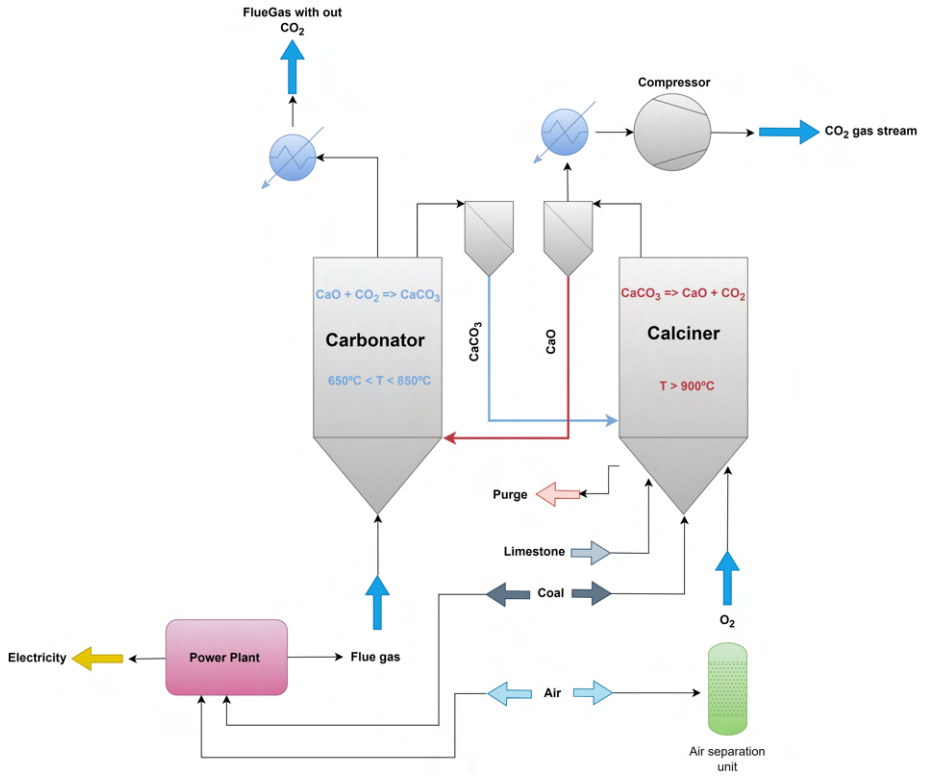


Figure 1.4: Simplified and Schematic CaO-Looping process for $CO_2$ capture in a coal-fired power plant (adapted from[18]).

silica ($SiO_2$), zeolites (aluminosilicates), activated carbon, and, more recently, Metal-Organic Frameworks (MOFs)[30].

MOFs represent a versatile class of adsorbents with remarkable tunability, enabling the synthesis of a diverse array of materials tailored for specific separations[3]. This exceptional flexibility arises from the combination of different metals with organic compounds, resulting in MOFs with customizable pore sizes, surface chemistries, and various other properties. Such adaptability positions MOFs as highly promising candidates for carbon removal applications.

The crux of this process lies primarily in the choice of adsorbent. The high selectivity of the adsorbent and its susceptibility to deterioration by pollutants commonly present in combustion gas streams (e.g., water, NOx, SOx, among others) are critical factors. Zeolite 13x stands out as the benchmark adsorbent for $CO_2$ due to its high selectivity, albeit its challenge lies in the difficulty of regeneration[31]. Nevertheless, a new material has emerged, already in production scale

and tested in industrial plants: CALF-20, a metal-organic framework[32]. This development marks a significant stride in overcoming the limitations of traditional adsorbents.

The ongoing progress in developing new materials is crucial to ensuring the sustainable implementation of $CO_2$ capture technology. The field is dynamic, with the pursuit of materials that not only enhance efficiency but also address environmental concerns and economic viability.

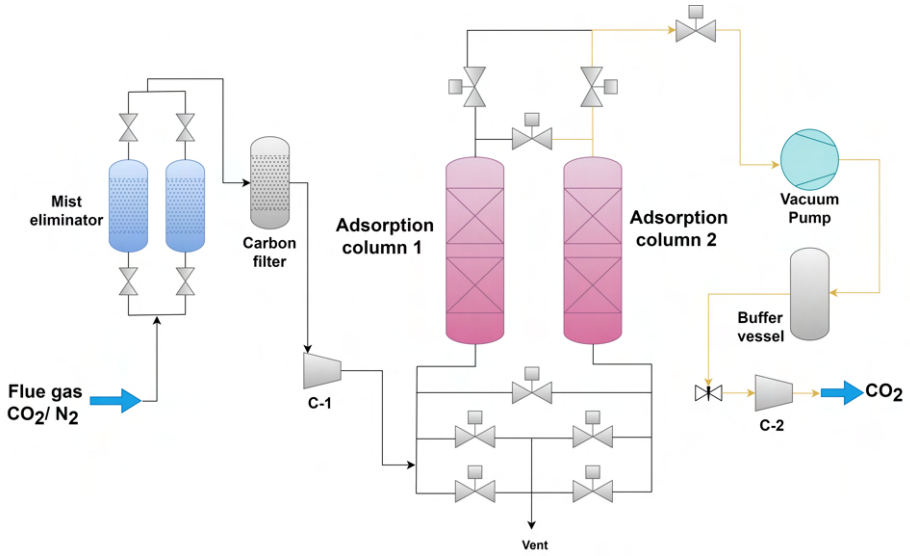


Figure 1.5: Schematic Pressure vacuum swing adsorption (PVSA) process flow diagram for post-combustion $CO_2$ capture.

The configuration of the adsorption cycle steps and the process itself are typically tailored to the type of material being used. Figure 1.5 depicts a schematic diagram of the main components of a P/VSA system. The system primarily consists of an inlet gas conditioning section, which removes impurities such as moisture, NOx, and SOx, before the gas passes through the adsorbents. This is followed by the adsorption stage in one of the columns (typically a fixed bed filled with the adsorbent) and in parallel the desorption stage in another of the adsorption columns connected with a vacuum pump (or other device that can generate a temperature or pressure differential) that can exert a pressure difference to regenerate the adsorbent and release the $CO_2$, which is then stored. Once the adsorption column is saturated, it switches roles with the column that has been regenerated, ensuring a continuous process.

The Skarstrom cycle, introduced in 1960, is the benchmark PSA cycle[33]. It employs pressurization, adsorption, blowdown, and purge steps across two synchronized beds, ensuring continuous operation without feed interruption. Optimization efforts have led to the implementation of several additional steps, typically involving the use of more columns, but each additional step introduces a significant increase in complexity, capital costs, and operating costs[16].

Critical metrics for adsorption process performance include product purity and recovery, operational pressure range, energy requirements, and scale-up considerations. Operating pressure and temperature influence $CO_2$ purity and recovery, while pressure drop in the column, affected by gas velocity and bed porosity, impacts both adsorption and desorption. Designing an effective adsorption process involves sequencing steps and determining the number of beds based on feed conditions, adsorbent properties, feed gas composition, and desired purity grades[33–35].

While adsorption processes offer simplicity, quick start-stop capabilities, and no chemical emissions, scalability remains a challenge compared to the widely used amine absorption process. The economic viability of a PSA/VSA process hinges on swing capacity, which is the difference in adsorbed gas between adsorption and desorption conditions[36–39].

### 1.2.4 Membranes-Module system

Membrane-based $CO_2$ capture systems have the potential to be a promising technology for gas separation due to their advantages of flexibility, compact size, high modularity, absence of phase transitions, simple mechanical configurations, and typically stationary operating conditions. These factors facilitate ease of scale-up[3,15,16,28,40]. However, the technological maturity of membrane-based $CO_2$ capture systems remains relatively low, primarily due to the demand for membranes with exceptional $CO_2/N_2$ selectivity, particularly for dilute CO2 streams such as flue gas. Additionally, the low pressure of post-combustion gasses necessitates large pressure gradients (to evacuate the permeate), leading to substantial energy consumption. Similar to adsorption systems, membranes exhibit thermal and chemical sensitivities to certain combustion gas components (e.g., acid gas, sulfides), necessitating pre-treatment before deployment in post-combustion applications. Due to these problems, to achieve rea-

sonable $CO_2$ recovery and purity (>90% and >95% respectively), multiple separation stages, recirculation of exhaust gas streams, and good process optimization must be implemented[16,41,42]. Figure 1.6 shows a simplified configuration of a membrane-based CO2 capture system for a coal-fired power plant.

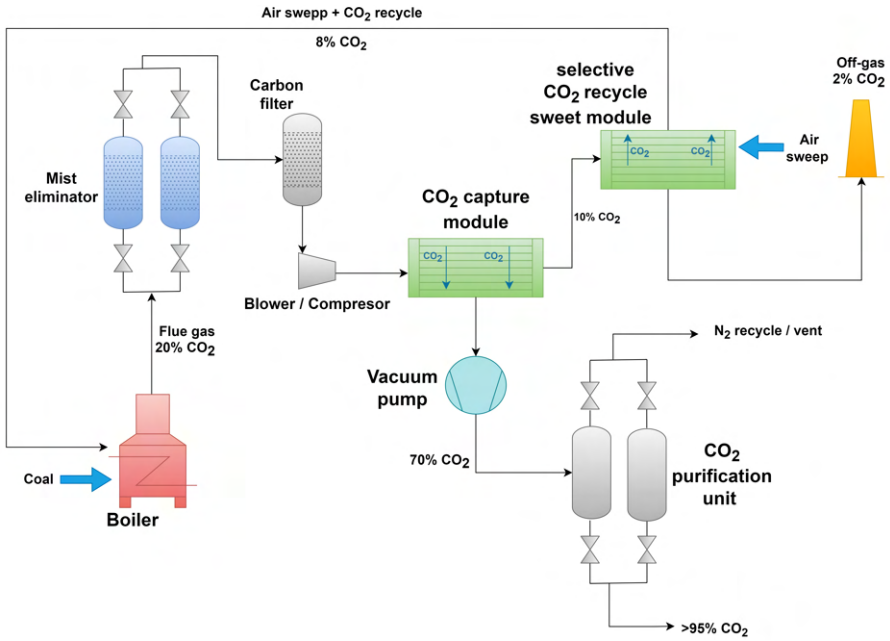


Figure 1.6: Simplified diagram of membrane $CO_2$ capture plant with selective $CO_2$ recycle at a coal-fired power plant(adapted from[41]).

The membrane separation process takes advantage of the difference in diffusion rates and sorption coefficients (properties of membrane materials) of gasses through the selective membrane. In the context of $CO_2$ capture, membranes allow preferential permeation of $CO_2$ over other compounds in a gas stream. Partial pressure differences across the membrane influence the direction and speed of the diffusion process[43].

For industrial separations, there are two common membrane geometries for gas separation: hollow fibers and spiral wound modules. These configurations maximize the surface contact area of the membrane to achieve a manageable cylindrical module (higher surface area to volume ratio reduces the vessel sizes).

In the case of hollow fibers, single- or double-layer systems can be used to form membranes. Single-layer hollow fibers have a polymer component for both the selective layer and the porous support.

Double-layer hollow fibers contain one polymer for the selective layer and a second polymer for the porous support.

A typical hollow fiber module contains on the order of 10 tightly packed hollow fibers, which are sealed at the ends with thermosetting epoxy. The feed gas can be introduced from either the shell side or the tube side of the fibers and typically flows in a countercurrent configuration with respect to the permeate stream to maximize mass transfer rates. A spiral wound membrane, on the other hand, consists of alternating layers of asymmetrical flat sheet membranes separated by porous spacers, with the permeate and feed streams flowing through alternating layers. Hollow fiber modules offer the advantage of a higher surface-area-to-volume ratio, allowing the design of smaller membrane plants for certain clearances, but require a higher pressure drop compared to spiral wound membrane modules[4,42–44]. Membrane-based CO2 capture systems have the potential to be a promising technology for gas separation, but further development is needed to improve membrane selectivity and reduce energy consumption[45].

### 1.2.5 Cryogenic $CO_2$ capture.

Cryogenic capture technology produces high-purity $CO_2$ without using chemical agents, avoiding contaminants associated with chemical absorption methods. Before the carbon capture unit, the flue gas has to be dehydrated alongside standard flue gas conditioning steps ( such as desulfurization, denitrification, and dust removal) to prevent pipeline blockages and equipment damage from freezing. At its core, cryogenic $CO_2$ capture relies on cooling the gas mixture and leveraging the distinct dew or freezing points of $CO_2$ and other gases for phase separation. This approach is categorized into two methods: liquefaction capture, which uses gas-liquid phase changes, and sublimation capture, based on gas-solid transitions. Given that $CO_2$ has a high triple point pressure (517.95 kPa), converting it to liquid under ambient pressure is unfeasible, necessitating higher pressures for liquefaction[46–48]. The prevalent techniques for achieving $CO_2$ phase transition include:

- Direct cooling and solidification, where the exhaust gas is cooled under ambient conditions to transition $CO_2$ directly from gas to solid, requiring extremely low temperatures (below -100°C).

- Multi-stage compression liquefaction compresses $CO_2$ above its critical pressure (around 73 atm) to induce liquefaction, typically followed by subsea storage. While common and straightforward, this method is energy-intensive.

- A combined compression and cooling process, initially compressing $CO_2$ to a moderate pressure before refrigeration cycles liquefy it. Subsequent pressurization allows for its storage.

- An advanced liquefaction-solidification method involves compressing $CO_2$ to a slightly lower pressure than the previous technique, cooling it to liquid form, and finally reducing its temperature and pressure to achieve solidification.

Each method showcases a unique strategy to exploit cryogenic principles for efficient $CO_2$ capture and storage.

Cryogenic distillation methods are predominantly applied to capture $CO_2$ at high concentrations. Their application for $CO_2$ recovery from flue gas is often impractical due to its elevated temperature, substantial discharge volume, and relatively low $CO_2$ concentration and partial pressure. As a result, integrated capture systems are employed, wherein an initial stage focuses on $CO_2$ pre-concentration, followed by a subsequent purification phase. Figure 1.7 illustrates a streamlined diagram of the post-combustion $CO_2$ capture process from flue gas, integrating membrane systems to enhance $CO_2$ concentration, thereby facilitating subsequent cryogenic purification step.

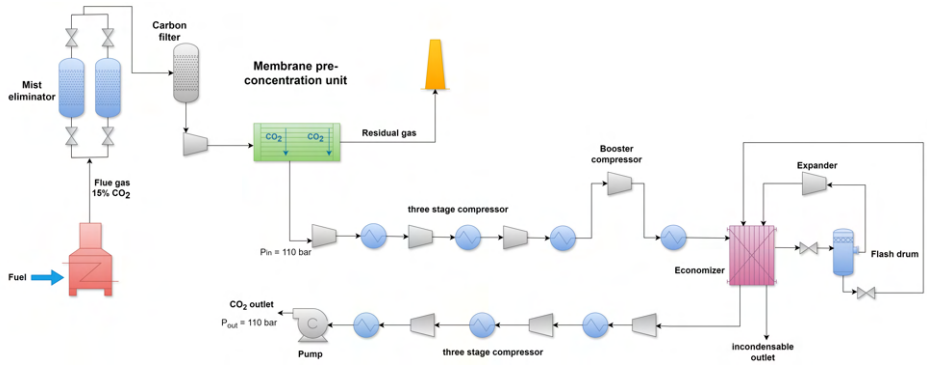


Figure 1.7: Membrane-Cryogenic condensation combined mixing flow chart[48].

## 1.3 Materials for $CO_2$ capture

Despite the industrial-scale adoption of certain carbon capture technologies, such as amine absorption, and the quasi-industrial implementation of metal oxide systems, particularly those based on calcium (Ca-loop), a significant energy gap remains to be bridged before these technologies become economically viable for companies[4,5,49].

Membrane-based technologies hold promise due to their ease of implementation, but they are still in their early stages of development and face several drawbacks, particularly in terms of material stability[50].

While less mature in the realm of $CO_2$ capture, solid adsorbents offer promising advantages over conventional capture methods, drawing inspiration from their successful applications in $O_2$ separation and air dehumidification. Advantage include:

- Substantial Energy Savings: Adsorbents have the potential to achieve a 30-40% reduction in energy consumption compared to amine-based technologies[3,30,32].
- Tunable Solid-State Capture Chemistry: Pore size and shape can be precisely controlled to optimize $CO_2$ capture[51–55].
- Adaptability to Diverse Conditions: Adsorbents and cycling configurations can be tailored to suit a wide range of thermodynamic conditions[56].
- Avoidance of Hazardous Emissions: Dry capture systems eliminate the risk of toxic or corrosive volatiles emitted by amine-based adsorption units[3,24,30,57].

This section delves into a brief overview of the main $CO_2$ absorbent classes 1.8 such as Metal-Organic Framework, Zeolites, Active Carbons, and Amines-functionalized silicas.

### 1.3.1 Activated Carbon

Porous carbons have emerged as promising adsorbents for $CO_2$ capture due to their exceptional properties, including high surface area, tunable pore structure, and excellent stability. Their affordability, easy regeneration, and resistance to harsh environments make them

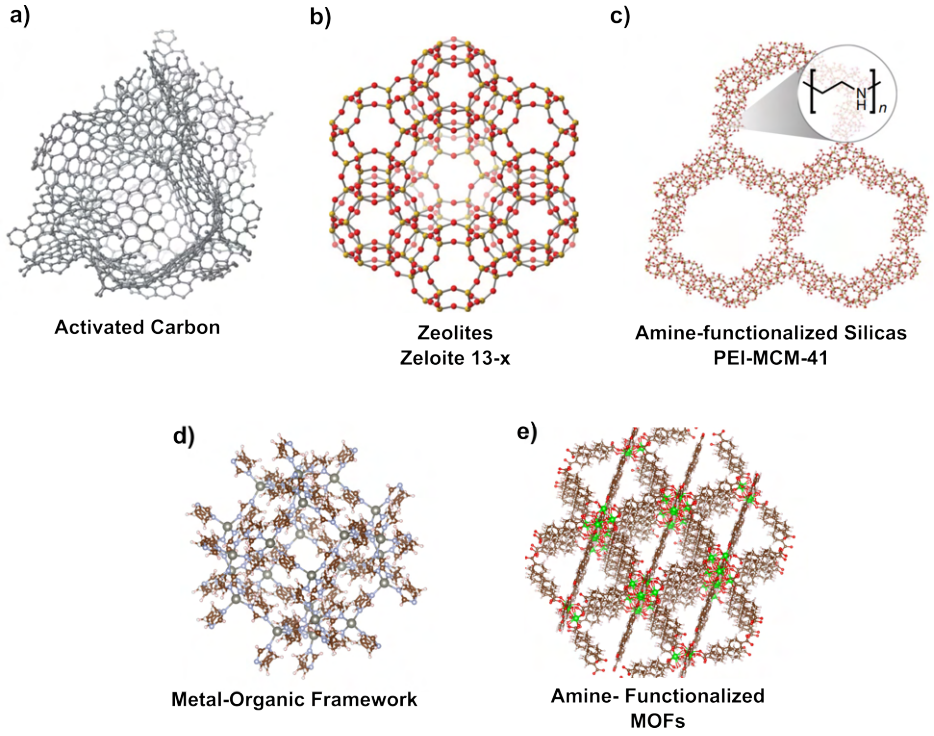


Figure 1.8: Illustrative examples of adsorbent types discussed in this section. (Adapted from[3]).

particularly attractive for industrial applications[20]. Conventional porous carbons, such as activated carbons (ACs) derived from coal, petroleum, and coconut shells, have been widely used for $CO_2$ capture. However, their surface chemistry and pore structure are often uncontrollable due to the uncertain structures of their precursors. This can lead to suboptimal $CO_2$ capture efficiency, particularly at low $CO_2$ concentrations. The development of tailored porous carbons through self-assembly, hydrothermal treatment, and pyrolysis has gained significant attention. These methods allow for precise control over the structure and properties of the carbon materials, enabling the optimization of $CO_2$ capture performance[3,30,58].

The effectiveness of $CO_2$ capture is strongly influenced by the microstructure of the adsorbents and the interactions between the adsorbent and $CO_2$ molecules. A comprehensive understanding of these factors is crucial for designing highly efficient $CO_2$ capture systems[58,59]. Precisely controlled synthesis of carbon structures offers a promising avenue for understanding the molecular-level proper-

ties of carbon materials and their $CO_2$ capture performance. This knowledge can be harnessed to guide the development of practical $CO_2$ capture applications. Porous carbons hold immense potential as adsorbents for $CO_2$ capture. Continued research efforts focused on tailoring the structure and properties of these materials are essential for optimizing their $CO_2$ capture efficiency and enabling their widespread adoption in industrial applications[3].

### 1.3.2 Zeolites

Zeolites are aluminosilicate minerals with a porous structure formed by tetrahedral units of aluminum, silicon, and oxygen. Their composition can be tailored to achieve specific properties for various applications, such as $CO_2/H_2$, $CO_2/N_2$ separation, dehumidification, among others. In gas separation processes, zeolites act as molecular sieves, allowing smaller molecules to pass through their micropores while blocking larger ones. Zeolite 13X (Na-X) is the benchmark material for $CO_2$ capture due to its ease of synthesis, low cost, and high $CO_2$ adsorption capacity. However, its performance is hindered by competition from water molecules for adsorption sites, and the high energy needed (37.2 kJ/mol) for adsorbent regeneration[4].

Zeolite 13X loses its adsorption capacity significantly in humid conditions (around 90%), due to the competitive adsorption with water vapor, which is abundant in flue gas, reducing their $CO_2$ capture efficiency over time[60]. Therefore, pre-treatment of the flue gas to remove moisture is necessary before PSA/VSA units, which increases the overall cost of $CO_2$ capture[16]. Despite these challenges, zeolites offer several advantages over other $CO_2$ capture materials. They have a uniform structure and composition, ensuring consistent performance. Moreover, they are relatively inexpensive to produce, and can withstand high temperatures and pressures, making them suitable for energy-intensive industrial applications[4,61].

Pre-drying flue gas streams, while potentially cost-prohibitive, may be essential for zeolite-based $CO_2$ capture systems to achieve optimal performance, considering that gas streams of interest for CCS are often saturated with water. Continued development of zeolites for CCS will benefit from novel design motifs, such as amine-impregnated organic/inorganic hybrids, that maintain $CO_2$ capacity and selectivity in the presence of water. However, addressing the decrease in surface area and pore volume upon amine introduction is crucial to

maximize $CO_2$ capture capacity[3,30,58].

### 1.3.3 Amine-Functionalized zeolites and silicas

Amino-functionalized silicas, like amine-based solutions, utilize the acid-base chemical selectivity of amines to effectively capture $CO_2$ in wet gas streams. By employing a solid support instead of an aqueous solvent medium, the energy costs associated with solvent heating can be eliminated, potentially leading to more efficient capture processes. Two primary methods have been developed to synthesize amine-based silica sorbents: direct impregnation and covalent tethering of aminosilanes to the supports. The selectivity of these sorbents stems from the formation of ammonium carbamate, carbamic acid, or bicarbonate species, with the product distribution influenced by amine identity, amine proximity to adjacent amine groups, and water content[3,30,59,62] .

While surface modifications of zeolites and silicas via amine immobilization generally enhance CCS performance, they also result in reduced surface area and pore volume upon amine introduction, thereby limiting CO2 capture capacity. In contrast, immobilized amines in mesoporous silicas do not suffer from surface area or pore volume reduction. However, they are susceptible to leaching problems, where the active amines desorb from the pores during regeneration, oxidation, and urea formation[30,58].

Cation exchange is a versatile and effective technique for modifying the adsorption properties of zeolites, offering two distinct advantages; 1) enhance adsorption sites: Cation exchange introduces additional interactions between $CO_2$ molecules and the cations within the zeolite structure, strengthening the adsorption sites. This modification leads to increased $CO_2$ uptake at low pressures, 2) reduced $CO_2$ Saturation Uptake: Cation exchange can also reduce the saturation uptake of $CO_2$ due to a decrease in the zeolite's free volume. This modification results in decreased $CO_2$ uptake at high pressures. These property changes induced by cation exchange present an attractive trade-off for post-combustion $CO_2/N_2$ separation. For instance, an amine-functionalized silica adsorbent like polyamide-functionalized silica PEI-MCM-41 exhibits significantly higher (approximately 40%) $CO_2$ adsorption capacity under saturated humidity conditions compared to dry conditions. However, zeolite 13x, as mentioned earlier, loses almost all of its adsorption capacity under humid

conditions[30,63].

### 1.3.4 Metal-Organic Frameworks.

Metal-organic frameworks (MOFs) are a class of crystalline porous materials composed of inorganic metal ions or clusters held together by organic linkers (Figure 1.8d). This unique architecture imparts MOFs with a remarkable tunability of their pore structures, enabling the incorporation of specific functional groups onto their internal surfaces to enhance their gas storage and separation properties. MOFs exhibit exceptionally high surface areas, reaching up to 7,000 $m^2g^{-1}$[30], allowing them to retain large quantities of guest species such as gases or liquids. By carefully selecting the building blocks, MOF structures can be tailored for a wide range of applications, including gas storage and separation, energy recovery, sensing, and catalysis[30,64–67].

Conventional MOF synthesis methods, such as hydrothermal and solvothermal processes, typically involve long reaction times (hours to days) and are limited to small laboratory scales (milligram to gram yields). These methodologies are therefore unsuitable for industrial applications due to their high energy consumption and scalability limitations. To address these challenges, researchers have developed innovative synthesis methods that reduce energy requirements, enabling the production of MOFs at room temperature. These methods often involve non-aqueous solvents such as DEF, DMF, and ETOH[68,69], but water-based synthesis is also possible, making industrial production more feasible[65]. Alternative synthesis approaches include microwave-assisted synthesis, mechanochemistry, continuous flow reactions, and spray drying[70]. The synthesis method significantly impacts the properties of MOFs, particularly their $CO_2$ capture efficiency. Therefore, optimizing MOF synthesis protocols is crucial for industrial applications.

Despite their versatility, MOFs face challenges in $CO_2$ capture applications. Their adsorption sites, often charge-dense metal cations, are susceptible to water passivation, which can significantly reduce their $CO_2$ capture capacity and selectivity. This issue is particularly relevant in carbon capture processes involving humid streams gasses. To overcome this challenge, research is focused on developing MOFs with stable and scalable structures that maintain their $CO_2$ adsorption capacity in the presence of water. Such materials hold promise

for commercialization and widespread adoption in carbon capture technologies[16,32,71].

Finally, for practical applications, MOFs require shaping into pellet, monolith, or fiber forms[56]. These structured forms enhance mechanical stability, mass transfer characteristics, and ease of handling, making them more suitable for industrial processes.

Overall, MOFs represent a promising class of materials for gas storage and separation technologies. Their tunable pore structures, functionalizable surfaces, and diverse applications make them highly versatile for a wide range of industrial needs. However, further research is necessary to overcome the challenges of scalable synthesis and gas contaminants instability, paving the way for their widespread commercialization.

### 1.3.5 Amine-functionalized MOFs.

Due to the crystalline-modular nature of MOFs, the study of the amine-functionalization of these materials is more diverse and complex than the functionalization of conventional adsorbents[72]. There are two functional-modification approaches of MOF building units with amino derivatives: 1) The first involves a *pre-synthetic modification*, wherein amino groups (1-, 2-, or 3- degree amine) alter the covalent bond before MOF synthesis[69]. However, this method presents challenges in achieving the correct MOF functionalization. The synthesis method used to create MOFs can be limiting, particularly in the case of solvothermal methods. In such methods, thermally labile ligands can cause problematic solubility or coordinate metal ions[72]. Discovering the suitable reaction conditions to synthesize a specific MOF topology with a modified ligand is often time-consuming and non-trivial. 2) The second approach is *post-synthetic modification*, based on chemical modification based on the MOF already manufactured rather than on the precursors of the molecule (monomers). The final material only requires compatibility with the newly introduced functional groups (and the necessary reaction conditions), circumventing any incompatibility with the synthetic methods required to obtain the MOF[58,72–74].

Amino group functionalization of the void spaces in Metal-Organic Frameworks (MOFs) significantly enhances their ability to adsorb and selectively uptake $CO_2$ molecules[69,74].The use of alkylamine groups ($R_1NHR_2$ or $RNH_2$) in the functionalization of MOFs has shown

promising results, as these groups are capable of interacting directly with $CO_2$ molecules, leading to the formation of a stable complex known as ammonium carbamate (C-N covalent bond formation), which significantly enhances $CO_2$ selectivity at low partial pressures ($< 100Torr$)[74–76]. Moreover, amino-functionalized MOFs have been shown to exhibit excellent resistance to the harmful effects of moisture in gas streams[74]. However, the presence of amines in the pore voids of MOFs and their high chemical affinity with $CO_2$ generates chemisorption, leading to a high energy penalty of adsorbent regeneration (Qst ($CO_2$) $\geq$60 kJ/mol, and $T > 90^oC$)[69,77,78]. Although it is relatively easy to prepare amine-functionalized MOFs at the laboratory scale, and many exhibit significantly improved $CO_2$-capturing properties in both dry and wet gas mixture conditions, several issues still need to be addressed. As mentioned earlier, chemisorption involves high regeneration energies, and their production at scale can be energy-intensive[79]. Additionally, the researchers are still determining whether modifying conventional porous adsorbents, such as silicas or zeolites, is more cost-effective than implementing post or pre-synthetic MOF modifications since the production of MOF itself is relatively costly.

## 1.4 Criteria for screening candidate $CO_2$ Capture materials

This thesis focuses on using a characteristic adsorbent for $CO_2$ capture. Therefore, this section emphasizes the criteria for selecting the best $CO_2$ adsorbent and how promising adsorbents are experimentally and theoretically evaluated.

Physical adsorbents with high selectivity to $CO_2$ are the preferred choice in the industry due to their ease of regenerability compared to chemical adsorbents. They are often used in packed bed-like columns unless composited on membranes or supported on a metal surface. When the gas enters the column, the adsorbent material selectively retains the gas for some time, allowing the other components to pass through the column[30]. The application of energy is required to recover the adsorbent and release the targeted pollutant, such as $CO_2$. The energy applied must be significantly higher than the interaction between the $CO_2$ and the active sites of the MOF. Several ways of supplying this energy boost include temperature changes (TSA), pressure changes (PSA or VSA), electrical pulses, or even impulses

from an external fluid, such as $N_2$ or He[80].

In this sense, a potential adsorbent for $CO_2$ capture must comply with the following points or at least have a balance between them, which allows its deployment at scale:

1. *High $CO_2$ adsorption capacity*: The adsorption capacity (at equilibrium) of a sorbent material is of vital importance to the capital cost of the capture system, as it dictates the amount of adsorbent required, which also sets the volume of the adsorption vessels[81]. In practice, it is preferred to use the working capacity (difference in capacity between adsorption and desorption), which must be at least greater than 2 mmol/g of adsorbent to compete with the commercial alternative of absorption with amino derivatives (1.5 - 2.0 mmol/g of sorbent solution)[19,40,80]. Remember that the $CO_2$ concentration is different for each type of industrial off-gas. Therefore, a kind of adsorbent will serve better or worse for specific applications. For example, high $CO_2$ adsorption capacity at low partial pressures (<0.15bar) of $CO_2$ is preferred for post-combustion applications (4-15% $CO_2$), but for example, for biogas upgrading applications where $CO_2$ can range from 40-70%, high capacity at higher partial pressures of this gas is preferred. The adsorption isotherm, measured through gravimetric or volumetric analysis, is a critical parameter that determines the maximum adsorption capacity of an adsorbent[82].

2. *Selectivity for $CO_2$*: A desirable feature besides having a high $CO_2$ adsorption capacity is a high $CO_2$ selectivity over other gases in the target gas mixture. The selectivity directly impacts the purity or quality of the captured CO2, as it depends on the ratio between the $CO_2$ adsorption capacity and that of another component (e.g. $N_2$, $CH_4$) in a given gas composition. Hence, it also affects the cost of transporting and storing this gas, and consequently, the economics of $CO_2$ capture in general. Flue gases (generated using fossil fuels) contain$N_2$ and $O_2$, among other compounds. Therefore, suitable absorbent materials must possess a high CO2 selectivity against these other gas components[81]. Active carbons present a noteworthy example of highly porous materials with commendable adsorption capacity. However, their selectivity towards CO2 hinders the attainment of the recommended purity (>95%)[80].

3. *Fast adsorption/desorption kinetics*: The kinetics are related to the intrinsic reaction kinetics of CO2 with the functional group of the adsorbent, as well as the mass transfer or diffusion resistance of CO2 through the porous structure of the adsorbent. If it is a supported adsorbent, the support also comes into play in the adsorption kinetics of this gas, so it should also be optimized to minimize the diffusion resistance. The kinetics can be seen in the breakthrough curves of an adsorbent (gas concentration versus time graphs). A fast kinetic is a steeper curve, so the adsorption capacity at the breakthrough point will be closer to the adsorption capacity. As most of the capture systems using adsorption columns work at the breakpoint, this property (kinetics) directly influences the amount of CO2 adsorbed, so it also impacts the design of the adsorption columns. However, its primary influence is on the adsorption/desorption cycle times, as these depend on the total adsorption capacity and kinetics. If the adsorption kinetics is fast, its analogous counterpart (desorption) will also be closed, which facilitates the removal of CO2 from the adsorbent and results in lower energy consumption in the regeneration of the adsorbent[30,73,80,81].

4. *Ease Regenerability*: Regeneration under mild conditions (low temperature, no significant pressure changes) and maintaining an efficient regeneration capacity during adsorption-desorption cycles is necessary to generate cost-effective $CO_2$ capture and compete with current amine technologies. Controversially, when there is a high adsorbent-adsorbate interaction, hence a high adsorption capacity, regeneration becomes more difficult and expensive[83,84]. Because of this, it is necessary to strike an optimal interaction balance. One of the properties associated with the degree of regeneration is the isosteric heat of adsorption. The lower the regeneration, the easier it will be (however, the adsorption will be lower) for physisorption the values are between -25 kJ/mol to -50 kJ/mol, and for chemisorption, they can range from –60kJ/mol to –90 kJ/mol[81]. This isosteric heat indicates the intensity of the interaction between the adsorbent and the molecule selective to it.

5. *Tolerance/Stability to impurities*: The industrial off-gas mixture contains various pollutants (e.g. NOx, SOx, $H_2O$, etc), which must be considered when selecting adsorbents. NOx and

SOx are always present in flue gas, and although their complete removal is difficult, a significant portion can still be captured by the adsorbent. Water is another pollutant that exists in higher concentrations than SOx and NOx. Therefore, the adsorbent's hydrophobicity is crucial for its chemical process longevity. Water removal is also possible, but it comes with a high cost, and the lower the amount of water to be removed, the greater the expense.

6. *Cost and scale-up Synthesis*: One of the main characteristics that a good adsorption material has to have, given that it has to be implemented on a large scale, is a sustainable (environmentally, socially, and economically favorable) synthesis. Since the synthesis of activated carbon and zeolites are already almost forty years old since their implementation and synthesis on a large scale, the following points are more focused on MOFs. These are the ones that suffer the most in terms of their synthesis, mainly due to the use (in some cases) of critical raw materials and especially the use of polluting solvents (in most or almost all organic syntheses, it is the most polluting raw material[85]). Therefore, in order for the most critical parameters that must be considered for the industrial scale-up of MOFs are a) the cost of raw material per kg of obtained MOF, b) the amount of MOF produced per $m^3$ of reaction mixture per day, c) conditions required for reaction agitation during synthesis, d) length of time required and amount of solvent required for sample filtration, and e) washing conditions necessary for drying (activating) prepared solids[80,81]. Recently, there has been a discussion about which materials are the most effective for capturing $CO_2$ at an industrial level. Activated carbon, zeolites, and MOFs are the most commonly discussed materials. Activated carbon and zeolites are preferred due to their ability to be synthesized at scale at a low production cost and their demonstrated mechanical and chemical stability. In contrast, the synthesis of MOFs at an industrial scale is still in its early stages and is mainly performed in laboratory and pilot scales[73].

Figure 1.9 radar bar plot qualitatively evaluates crucial metrics for material selection in carbon capture. It displays mean values for each material property, represented by bold lines, and typical variability within a material class, shown as error bars. This plot offers

a general overview of the potential of different material types for carbon sequestration. It makes it useful for those new to the field to grasp innovation opportunities in material enhancement quickly. Currently, amines are the predominant commercial option for carbon capture. However, their significant environmental and energy drawbacks highlight the unresolved challenge of sustainable $CO_2$ sequestration. In contrast, activated carbons and zeolites show limited scope for improvement. On the other hand, MOFs, silicas, and amino-functionalized MOFs, despite their current unconvincing properties, hold considerable potential for improvement due to their high customization capability. Some materials in these categories already demonstrate exceptional properties, although they are few.

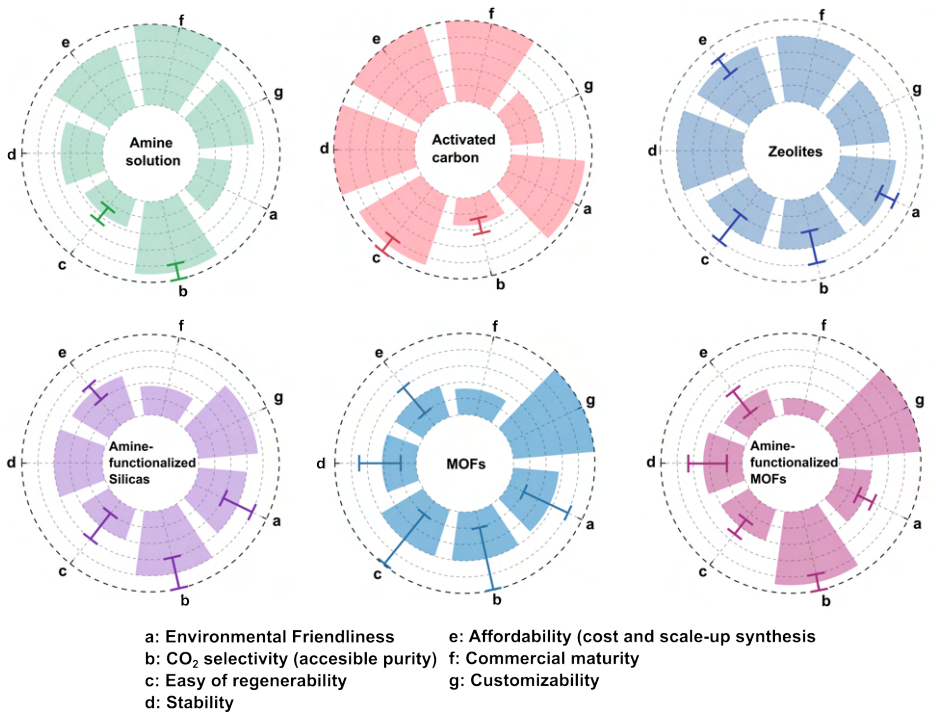


Figure 1.9: Radar bar chart for key sorbent selection criteria (adapted from[3]).

## 1.5 Standard methods for adsorbent evaluation.

A thorough understanding of thermodynamics and mass transfer (diffusion) is essential to understand adsorption processes effectively. This section presents a succinct overview of the fundamental principles for characterizing adsorbents and gaining a broad understanding of the thermodynamics and dynamics governing the adsorption process. This section exclusively addresses physical adsorption, which arises from Van der Waals and electrostatic interactions between the adsorbate and the adsorbent. Unlike chemical adsorption, which involves electron transfer and bond formation with potential dissociation, physical adsorption is more generalized and can occur in either the gas or liquid phase[58,86]. While many concepts apply to both phases, our focus here centers on gas-phase adsorption.

### 1.5.1 Common analysis for material characterization

The correct initial characterization of the material is important in order to identify the crystallographic chemical structures, morphology and to establish a correct activation and working temperature range of the adsorbent. In addition, by correctly identifying the structures and how they impact adsorption, future adsorbent materials can be better designed. The fundamental characterizations that are essential to understanding these crystalline solid materials include:

- SEM, and TEM → Morphology and particle size
- ICP, EDS → Elemental analysis
- SXRD, PXRD → Structure Determination
- TGA → Architectural stability
- FT-IR, NMR → Coordination environment

In adsorption processes, thermogravimetric analysis (TGA) is significant in determining a temperature range within which a material remains thermally stable. TGA also aids in identifying an activation temperature, which involves removing the solvent from the adsorbent

and rendering the material's porous structure accessible. Solvothermal methods or physical alterations, such as pressure changes, can accomplish this solvent removal. When combined with adsorption isotherms, the activation procedure can be optimized. However, achieving this optimization can be challenging and requires numerous trials-error tests.

### 1.5.2 Thermodynamic evaluation.

#### Adsorption isotherms.

Adsorption isotherms graphically illustrate the amount of adsorbed species within a material at different partial pressures while maintaining a constant temperature (figure 1.10). This relationship between partial pressure and adsorbed gas quantity is commonly expressed in terms of the adsorbent mass. In the low-pressure range, where isotherms are commonly assessed, fugacity, the thermodynamically rigorous phase equilibrium term, appropriately replaces partial pressure since the fugacity of an ideal gas equals its partial pressure. The equilibrium expression points to fugacity over partial pressure when dealing with higher pressures[79,82,87].Isotherms are the best descriptor of the adsorption capacity of a material.

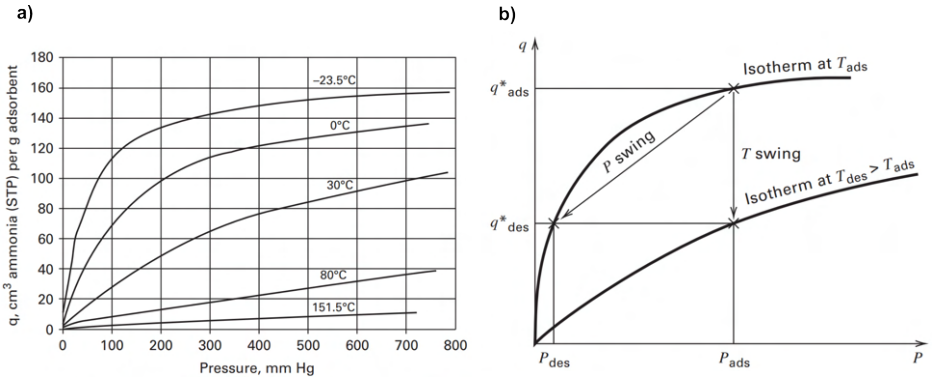


Figure 1.10: (a) Adsorption isotherms for $NH_3$ on charcoal. (b) Schematic representation of pressure and temperature swing adsorption. Reprinted from[88].

These isotherms may exhibit various shapes (Types I to VI, as depicted in Figure 1.11), with Type I, II, and V being the most frequently encountered in separation process. Type I is consistently associated with rigid microporous adsorbents. In contrast, flexible

sorbents may exhibit Type V isotherms, characterized by transitions between closed (nonporous) and open (porous) phases. While this isotherm type is uncommon, it can prove highly advantageous. The curve's steepness determines the extent to which 100% of the working capacity (amount adsorbed = amount desorbed) can be achieved in these flexible materials[69].

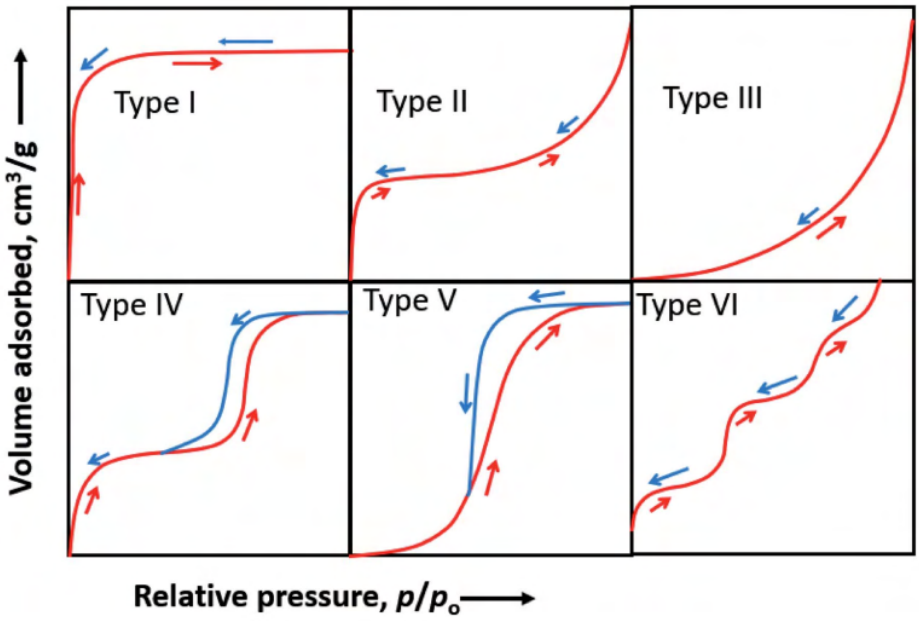


Figure 1.11: Different types of adsorption isotherms as classified by IUPAC[82]

Various procedures exist for isotherm determination. Volumetric methods typically enjoy widespread use, while gravimetric and dynamic methods offer alternative approaches. Dynamic methods entail employing a gas carrier and a gas sensor at the adsorbent's outlet to gauge the equilibrium (saturation) adsorbed gas amount.

Adsorption isotherms are essential in characterizing adsorbents and providing a deep understanding of a material's intrinsic properties regarding the interaction between the adsorbent and gas species at equilibrium. These isotherms allow us to see the maximum amount of a substance the material can hold under specific gas concentration and temperature conditions. This knowledge is essential for making decisions before delving into more detailed adsorbent characterization.

**Working Capacity.**

The work capacity ($\Delta N_{CO2}$), the difference between $CO_2$ uptake at the adsorption (loading) and desorption (release) temperature and pressure conditions of the process under consideration (1.1), is the most relevant measure of adsorption process performance.

$$\Delta N_{CO2} = N_{ads} - N_{des} \tag{1.1}$$

As previously discussed, the working capacity is also influenced by the Type of isotherm used. Figure 1.12 provides an example wherein, despite both isotherms having the same adsorption capacity at 1 bar, there is a discrepancy in their working capacities.

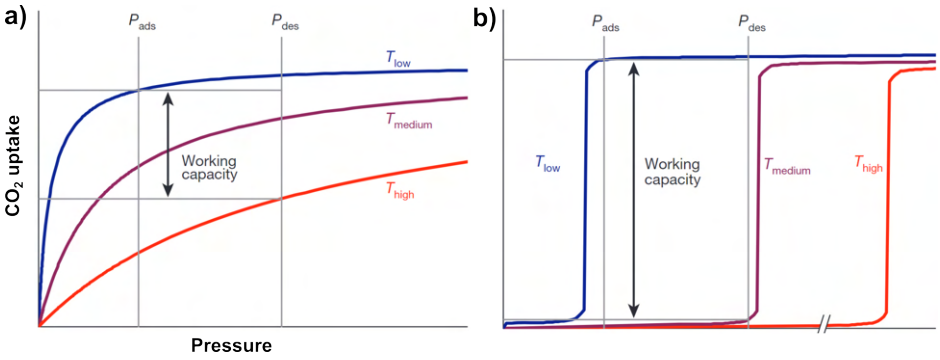


Figure 1.12: Schematic illustration of the difference in working capacity between adsorbents with the same adsorption but with two different types of isotherms. (a) type I isotherm, as found in most rigid microporous adsorbents; (b) type V isotherm (commonly called S-Type), as found in flexible adsorbents that can alternate between closed (non-porous) and open (porous) phases[79].

The working capacity is a valuable tool for preliminary vessel sizing when storing the adsorbent. A higher working capacity implies a reduced need for column volume. However, it is essential to note that working capacity does not directly measure the efficiency of an actual adsorption system (such as PSA, VSA, or TSA). This is because it does not account for the energy expended during the cycle. As a result, the working capacity cannot accurately represent the economic efficiency of the adsorption capture process[89].

### $CO_2$ Selectivity.

The $CO_2$ selectivity of a sorbent measures the ratio of $CO_2$ sorption capacity to another gas under specific conditions. Selectivity to nitrogen is crucial for carbon capture after combustion (post-combustion), while selectivity to methane plays a vital role in natural gas purification. Selectivity also impacts the purity of the adsorbed gas and the levels of the outlet gas stream (effluent). In the case of a binary mixture, adsorption selectivity (Sads) is determined by the equation 1.2.

$$S_{\text{ads}} = \frac{q_i/q_j}{p_i/p_j} \tag{1.2}$$

Here, $q_{i,j}$ and $p_{i,j}$ represent the work capacities and partial pressures for components i and j, respectively. This measurement is also referred to as ideal selectivity or molar selectivity.

In practice it is very difficult to measure multicomponent isotherms, usually the data found in the literature are referred to single-component isotherms, given their ease of measurement using commercial systems. Therefore, due to the cost and complexity of the measurements, multicomponent isotherm data as well as the selectivity between these components are often predicted using single-component adsorption isotherms. A commonly employed approach to estimate the multicomponent adsorption selectivity relies on the **Ideal Adsorbent Solution Theory (IAST)**. This method utilizes the single-component isotherms of $CO_2$ and the competing gas[70]. It operates under three assumptions, which are essential for conducting selectivity calculations:

1. The pure components form an ideal mixture (no change in area or enthalpy when mixing the pure components), a reasonable approximation for most systems.

2. The area accessible to both adsorbates is equal (i.e., the sorbent is not a molecular sieve).

3. The thermodynamic properties of the sorbent do not change relative to the thermodynamic properties of the sorbate (i.e., the sorbent is not a molecular sieve). of the sorbate (i.e., there is no phase transition induced by the sorbate).

The equations that are implicit in the IAST calculation are as follows:

$$\sum_{i=1}^{N} x_i = 1 \tag{1.3}$$

$$P y_i = P_i^0 x_i \tag{1.4}$$

$$\pi_i = \pi_{i+1} = ... = \pi_N \tag{1.5}$$

$$\pi_i = \frac{RT}{A} \int_0^{P_i^0} q_i^0(P)\, d\ln P \tag{1.6}$$

$$\frac{1}{q_{tot}} = \sum_{i=1}^{N} \frac{x_i}{q_i^0} \tag{1.7}$$

As can be seen in equation 1.3, the sum of the mole fractions of the different components of the gas mixture is equal to unity. For the equilibrium phases Rault's law (equation 1.4) can be applied. The spreading pressure $\pi$ is directly related to the chemical potential of the solid adsorbent ($\mu$s), under the adsorbing species. Since system equilibrium may only be obtained if $\mu$s is in equilibrium along the entire surface. $\pi$ is defined in equation 1.6 where A is the surface area of the adsorbent, R is the gas constant, T is the temperature,$q_0$ i is the pure component quantity adsorbed at pressure P. $P_0$ i is the vapor pressure of the pure component i in equilibrium with $q_{0i}$. Finally, since it is assumed that the adsorbed solution behaves ideally (the area covered by one adsorbed species is not affected by the other competing adsorbed species), it is expected that the $q_{tot}$ is directly related to the $X_i$ and its respective adsorbed quantity individually by the relationship in equation 1.7. By solving this system of equations, each $x_i$, $y_i$ and $q_tot$ can be calculated. Combining $x_1/y_1$ and $x_2/y_2$ into Equation 1.2 can produce the selectivity of component 1 over component 2.

The IAST is essentially the translation of Raoult's Law for vapor-liquid equilibrium to a system composed of an adsorbed phase on an adsorbent and a vapor phase. Since this is an ideal approximation, it is necessary to approximate that all vapor phase components can access all sites on the adsorbent, that the adsorbent is homogeneous, and that the intermolecular forces are equivalent between all components of the fluid. As with predictions based on Raoult's Law, significantly different interactions between different fluid species break the ideal solution approximation, and the model falls apart. IAST has

limitations in the accuracy of the predicted multicomponent isotherm data and, in general, does not capture the proper behavior of polar species or mixtures in which one of the components is strongly adsorbed[86].

**Modeling the adsorption isotherms.**

When modeling an adsorption process, extract IAST selectivity values or, adsorption heats from isothermal data, it is convenient to fit the isotherm data with adsorption models. Similar to any model applied to experimental data, a diverse range of models is available, some grounded in the fundamental principles of adsorption, while others adopt a more empirical approach.[86].

The following is a brief explanation of the most commonly used ones:

- **Henry's Law:** Physical adsorption from the gas phase is an exothermic process, so the equilibrium favors adsorption at low temperatures and desorption at higher temperatures[33,90]. Therefore at sufficiently low concentrations, the equilibrium relationship usually approximates a linear form (Henry's law):

$$q = KC \tag{1.8}$$

  The proportionality constant "$K$" is also called Henry's constant which is simply the adsorption equilibrium constant.

- **Langmuir Isotherm:** Often, the adsorption isotherm of most microporous adsorbents can be represented, at least approximately, by the ideal Langmuir model (equation 1.9).

$$\frac{q}{q_m} = \frac{K_l C}{1 + K_l C} \tag{1.9}$$

  This model was derived by considering the balance between occupied and unoccupied adsorbate sites on the adsorbent. In low concentration regions this model is reduced to Henry's law[33,90,91]. In the model $K_l$ is an equilibrium constant that is directly related to Henry's constant ($K = K_l * q_s$). This

constant can also be correlated with the adsorption area and the porosity of the adsorbent. $C$ is the adsorbate concentration at equilibrium. And $q_m$ represents the maximum adsorption capacity of the adsorbate.

- **Freundlich Isotherm:** An alternative expression to describe especially Type I isotherms is the Freundlich model (equation 1.10). This model is applicable when adsorption occurs on heterogeneous surfaces[33]. This is an empirical model, but its expression is also attributed to the fact that it defines the surface heterogeneity and the exponential distribution of active sites and their energies[90].

$$q = K_F C^{1/n} \quad ; \quad n > 1 \tag{1.10}$$

$1/n$ is the adsorption intensity, it also indicates the relative energy distribution and the hetereogeneity of the adsorbate sites.

Unlike the Langmuir model, this model cannot be reduced to Henry's expression at low concentrations. In order to obtain great entrepreneurial flexibility, the Langmuir and Freundlich models are sometimes combined (known as **Lagnmuir-Freundlich** or **Sips**). This adaptation (equation 1.11) does not have a theoretical basis, it is purely empirical which is suitable for predicting adsorption on heterogeneous surface, but avoids the limitation that the Frenlucich model had at high adsorbate concentrations[33,90]. Therefore at low concentrations this model reduces to Freundlich, but at high adsorbate concentrations, it predicts the Lagnmuir model (monolayer adsorption).

$$\frac{q}{q_m} = \frac{KC^{1/n}}{1 + KC^{1/n}} \tag{1.11}$$

- **Langmuir-Freundlich Dual-Site:** Langmuir Single-Site cannot describe a large number of real gas-solid adsorption systems well enough. For heterogeneous surfaces (as in almost all real-world materials), the adsorption energy at each site will vary, depending on the local chemistry and structure. The most favorable sites will be filled first, followed by the less favorable

ones. For heterogeneous adsorbents, the most simplified case is the following where only two different adsorption sites are available[92]. Each site can be modeled by a separate equilibrium constant, $K_1$ and $K_2$. Therefore the Langmuir-Freundlich Dual-Site model can be written as the equation 1.12.

$$q = q_A + q_B = \frac{q_1 K_1 C^{v_1}}{1 + K_1 C^{v_1}} + \frac{q_2 K_2 C^{v_2}}{1 + K_2 C^{v2}} \tag{1.12}$$

When in the equation 1.12, the coefficient $v_{1,2}$ takes the value of 1, it is known as Langmuir Dual-Site.

- **Brunauer-Emmett-Teller (BET) isotherm:** Both the Langmuir and Freundlich isotherms fall under the category of type I isotherms, which is the most frequently observed form, especially in the case of microporous adsorbents. However, certain materials, such as activated alumina and silica gel, or the adsorption of water on specific adsorbents, often exhibit type II behavior. This behavior is typically described by the BET equation 1.13.

$$\frac{q}{p/p^0} = q_s \cdot \frac{K(p/p^0)}{(1 - C(p/p^0))(1 - C(p/p^0) + K(p/p^0))} \tag{1.13}$$

Here, $P_s$ represents the saturation vapor pressure. However, it's worth noting that the physical model from which this expression was originally derived may be somewhat unrealistic, particularly when applied to microporous solids. This is because it relies on an oversimplified extension of the Langmuir mechanism to multilayer adsorption[33,93].

The BET method is still the most widely used procedure to evaluate the surface area of porous through nitrogen adsorption at cryogenic temperatures, despite the weakness of its theoretical foundations[33,94]. Nevertheless, it has also found utility in representing moisture isotherms on activated alumina, where the isotherms conform to the well-defined type II form.

**Isosteric Heat of adsorption.**

To separate two species effectively from a gas mixture, they must exhibit differing interaction energies with the adsorbent surface, ensuring one is preferentially adsorbed over the other. The quantity of adsorbate on a given mass of adsorbent hinges on the relative pressure, temperature, and the adsorbate-adsorbate interaction energy, often referred to as the "(isosteric) enthalpy of adsorption ($\Delta H_{ads}$)". This enthalpy represents the heat released during adsorption (an exothermic process). The more negative the adsorption enthalpy's magnitude, the greater the adsorption of species at a given pressure and temperature. This energy release during adsorption ($\Delta H_{ads} < 0kJ/mol$) inversely correlates with the desorption enthalpy, $\Delta H_{des}$, needed for the reverse desorption process ($\Delta H_{ads} = -\Delta H_{des}$) in physisorption (without activation barrier). In contrast, chemisorption is more complex, involving substantial interaction potentials similar to chemical bonds and higher adsorption enthalpies. It also entails activation energies, as seen in typical chemical reactions.

The $\Delta H_{ads}$ provides a guide to the energy required to regenerate the sorbent. The amount of heat required to regenerate a sorbent is a parameter that significantly influences the cost of regeneration (operating cost of a carbon capture plant).

Approaches for determining $\Delta H_a ds$ can be categorized into two primary methods: experiment-based calculations and molecular simulations. Molecular simulations often rely on isotherms derived from extensive canonical Monte Carlo simulations (GCMS) and are calculated using the ensemble fluctuation approach[95]. Experimental procedures, on the other hand, can be approached directly or indirectly. In the direct method, a calorimetric-volumetric system uses a calorimeter to measure the heat released during adsorption directly[96]. However, these systems are notably complex and costly, limiting their use in research. The most common indirect approach for determining the isosteric enthalpy of adsorption involves using adsorption isotherms as a function of the adsorbate's quantity. The reciprocal interaction energy between adsorbate molecules is typically assessed indirectly based on at least two adsorption isotherms obtained at closely spaced but different temperatures (T1, T2) with $\Delta T \approx 10 - 20K$. These isotherms serve as the foundation for either Clausius-Clapeyron or virial analysis approaches to ascertain the isosteric enthalpy of ad-

sorption[97,98]. For the Clausius-Clapeyron approach, both adsorption isotherms must be fitted using the same continuous function, such as Langmuir, dual-site Langmuir, Toth, Sips, Jovanovic, Dubinin-Radushkevic, Freundlich-Langmuir, or other suitable fits. Following this fitting process, the isotherms are analyzed for pressure (p)-load (n) data pairs with identical loads (n) at each temperature. This method is known as the "isosteric" approach and relies on the Clausius-Clapeyron equation (1.14)[98,99] , which relates the heat of adsorption to the temperature-dependent behavior of the adsorption isotherm.

$$\Delta H_{\text{ads}}(n) = -R \cdot \ln\left(\frac{p_2}{p_1} \cdot \frac{T_1 \cdot T_2}{T_2 - T_1}\right) \tag{1.14}$$

In the case of virial analysis, the isotherms are fitted according to the virial-type equation (equation 1.15), which expresses pressure (p) as a function of the gas charge (n). Virial analysis has been particularly useful for calculating adsorption enthalpies, especially for highly polarized gases like $CO_2$ and $SO_2$.

$$p = n \cdot \exp\left(\sum_{i=0}^{m} C_i n^i\right) \tag{1.15}$$

In equation 1.15, C0 represents a constant for adsorbate-adsorbent interactions, while C1, C2, and so on denote constants for double, triple, and higher-order interactions within the adsorbent field. These Ci constants are temperature-dependent, and the heat of adsorption (Qst) is determined as shown in equation 1.16.

$$Q_{\text{st}}(n) = \left(\sum_{i=0}^{m} \frac{dC_i}{dT} R T^2 n^i\right) \tag{1.16}$$

Note that $\Delta H_{ads}(n)$ or $Q_{st}(n)$ varies with loading. Most materials have different adsorption sites with different surfaces energies and thus $\Delta H_{ads}$ depends on the surface coverage of the adsorbent. Therefore, it is possible to illustrate the energetic heterogeneity (elucidate different adsorption sites of a solid surface) when $\Delta H_{ads}$ is plotted against the adsorbed amount $q$.

### 1.5.3 Adsorption column dynamics (Experimental Breakthrough):

Most (almost all) large-scale processes are carried out under dynamic conditions. Especially for processes where gas separation is performed by pressure or temperature change (PSA, VSA, or TSA) within a packed column. Properties like cyclic and long time stability, competitive adsorption and mass transfer kinetics is vital for selecting an appropriate adsorbent for a specific separation process. These properties can be obtained using dynamic methods, and all of them are essential prerequisite for the modeling, analysis and scale-up gas separation process[93,100]. Moreover, the breakthrough measurements in a fixed-bed column with a simulated gas mixture are much closer much closer to the actual practice of gas capture/separation, and multicomponent selectivity predicted using IAST. In dynamic evaluation, the gas mixture passes through the fixed bed column containing the adsorbent. At the outlet of the bed, there is a gas detector that records the gas concentration as a function of time (figure 1.13). Although it seems a simple experiment, understanding the dynamic behavior is challenging since it depends on the interplay between adsorption kinetics, adsorption equilibrium, and fluid dynamics[33,101]. However, the general pattern of dynamic behavior is usually determined by the shape of the equilibrium relationship[33,86].

The asymptotic behavior of transitions under the influence of mass transfer resistances in long and "deep" fixed-beds is important. With an unfavorable isotherm, the width of the transition becomes proportional to the depth of the bed it has crossed. For the linear isotherm, the width becomes proportional to the square root of the depth. For the favorable isotherm, the transition approaches a constant width called a constant pattern. The design of non-regenerative and many regenerative sorption systems is often based on the concept of mass transfer zone (MTZ) (figure 1.13), which closely resembles the constant pattern. The MTZ is the range of the bed where the adsroption process rapidly progresses towards equilibrium. The MTZ moves along the bed from the inlet point to the outlet point during the adsorption process.

The formal analysis of the adsorption column dynamics starts from the basic differential equation derived from a transient mass balance in a column element[102], . If the model is represented by the axially dispersed plug flow, it assumes the form of the equation 1.17.

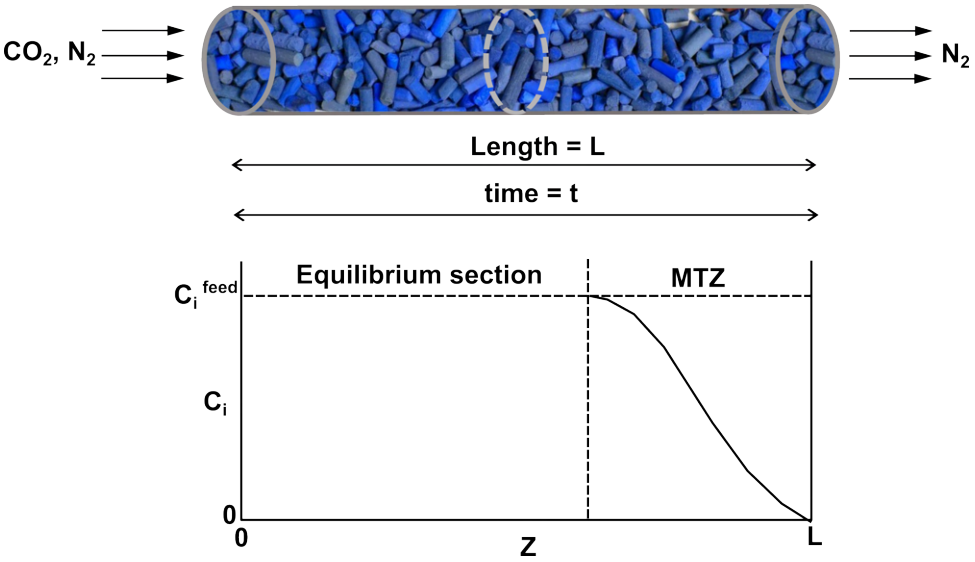


Figure 1.13: Schematic diagram of the fixed bed column for Breakthrough measurements.

By assuming plug flow, we also assume that all other variables also vary only with distance along the column.

$$\frac{\partial c}{\partial t} + \frac{\partial}{\partial z}(uc) = D_L \frac{\partial^2 c}{\partial z^2} - \left(\frac{1-\epsilon}{\epsilon}\right)\rho_p \frac{\partial \bar{q}}{\partial t} \tag{1.17}$$

$$Accumulation + Advection = Dispersion + Sink$$

$$v\frac{\partial c}{\partial z} + \frac{\partial c}{\partial t} + \left(\frac{1-\epsilon}{\epsilon}\right)\rho_p \frac{\partial \bar{q}}{\partial t} = 0 \tag{1.18}$$

In equation 1.17 $\epsilon$ is the void fraction of the bed, $v$ is the interstitial velocity of the carrier fluid, $t$ is the operating time, $z$ is the distance from the inlet of the mobile phase, $C(z,t)$ is the composition of the flowing solute and q is the concentration of solute in the stationary phase. $D_L$ is the axial dispersion coefficient, $u$ is the superficial velocity, and $\rho_p$ is the particle density. The rate of mass transfer to the particle for each component is given by Eq 1.19. If the axial dispersion and pressure drop through the column can be negligible and if the adsorbate concentration is small, the expression can be reduced to equation 1.18.

To complete the required set of equations, it is necessary to in-

clude the adsorption rate of the solute or contaminant. Several models exist to approximate the mass transfer process. These are typically based on assumptions that the velocity is proportional to the amount available for transfer and to the free sites in the solid material and lead to different forms of kinetic model[101]. However, most of the studies accept that the adsorption rate can be represented by the linear driving force model (equation 1.19 ) in terms of the overall fluid phase mass transfer coefficient[103].

$$\frac{\partial q}{\partial t} = K_L(q_e - q) \tag{1.19}$$

Where $K_L$ is a velocity constant and $q_e$ is the saturation value. $q = f(C)$ is given by the isotherm. The total concentration C in terms of partial pressures is given by eq. 1.20.

$$C = \frac{P}{R \cdot T_g} \tag{1.20}$$

P is the total pressure, $T_g$ is the gas phase temperature and R is the universal gas constant. The Ergun equation considers the terms of the pressure drop and velocity changes (eq. 1.21). where $\mu_g$ is the gas phase viscosity, $\rho_g$ is the gas phase density and dp is the particle diameter.

$$-\frac{\partial P}{\partial Z} = 150\frac{\mu_g(1-\epsilon)^2}{\epsilon^3 d_p^2}v + 1.75\frac{(1-\epsilon)}{\epsilon^3 d_p}\rho_g v^2 \tag{1.21}$$

There are boundary conditions (equations 1.22, 1.23) that are used to solve partial differential equation systems (PDE). To evaluate and model the breakthrough curve, analytical solutions of the system Equations 1.17 and 1.19 should be solved with mathematical or analytical methods.

$$C(z,0) = 0 \quad \text{and} \quad C^*(z,0) = 0,$$
$$\text{initially clean interstitial fluid for} \quad 0 \leq z \leq L. \tag{1.22}$$
$$C(0,t) = C_0,$$
$$\text{that is, constant composition at bed access.} \tag{1.23}$$

Additionally, in order to fully understand the dynamic behavior of adsorption, it is essential to perform a rigorous analysis that includes an energy balance within the column. This energy balance can be described by eq. 1.24:

$$\epsilon C_{C_g}\frac{\partial T_g}{\partial t} + C_{C_g}\frac{\partial (uT_g)}{\partial z} = \epsilon\lambda_L\frac{\partial^2 T_g}{\partial z^2} - (1-\epsilon)\rho_p C_s\frac{\partial T_s}{\partial t} + (1-\epsilon)\rho_p\sum_i(-\Delta H_i)\frac{\partial \overline{q}_i}{\partial t} - \frac{4h_w}{d_{int}}(T_g - T_w) \tag{1.24}$$

Where: $C_g$ is the molar specific heat of the gas phase, $\lambda L$ is the axial heat dispersion coefficient, $C_s$ is the solid specific heat, $(-\Delta Hi)$ is the adsorption heat for the ith component at zero coverage, $h_w$ is the internal convective heat coefficient between the gas and the wall, int d is the bed diameter, and $T_w$ is the wall temperature.

This energy balance considers various factors that contribute to the dynamic behavior of adsorption, including heat transfer between the gas and the solid, adsorption and desorption processes, and heat transfer between the column and the surroundings. By solving this energy balance, it is possible to obtain a detailed understanding of the temperature distribution within the column and its impact on the adsorption process.

**Experimental analysis of the Breakthrough cruves.**

While the theoretical underpinnings of concentration-time curve (breakthrough curve) analysis may be complex, the practical application of determining an adsorbent's capacity is relatively straightforward. By utilizing concentration data collected over time during the adsorption process, the adsorption capacity can be calculated as the area above the breakthrough curve. This approach provides a simple yet effective method for quantifying the adsorbent's capacity. Dynamic breakthrough curves[33,88] are typically plotted as the concentration of the different gas compounds in the outlet stream, in %, or the gas concentration fractions, denoted as $C/C_0$, where C and $C_0$ are the outlet and inlet concentration, respectively, as a function of time. In all cases of analysis, the time values must be corrected by subtracting

the corresponding dead time. The dead time is defined as the time required for the gas mixture to flow through the separation module and all the pipes leading to the analyzer. It depends on the dimensions of the pipes and the operating conditions (gas flow, pressure, and temperature). From the breakthrough curves, several parameters can be systematically obtained to evaluate the separation performance of the adsorbent material for a selective gas (in this study, $CO_2$) over other compounds (e.g., $CH_4$, $N_2$) under different conditions. These parameters include: the adsorption capacity of the adsorbent material for the selective gas; the selectivity of the adsorbent material for the selective gas over the other compounds; and the breakthrough time, which is the time required for the concentration of the selective gas in the effluent to reach a specified level. Moreover, the shape of the breakthrough curve, which can provide insights into the adsorption mechanism.

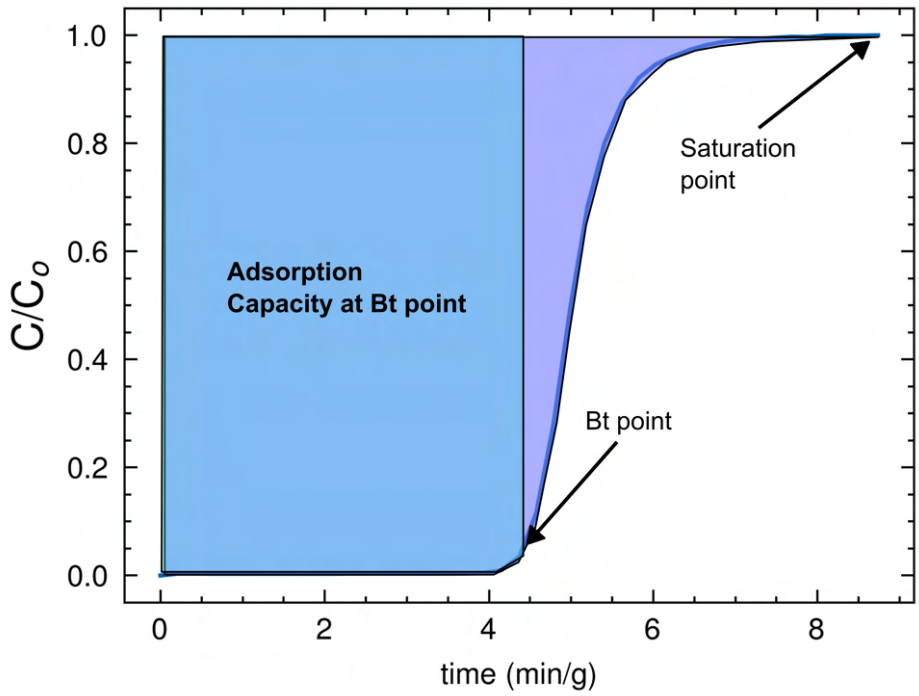


Figure 1.14: Breakthrough curve plots: adsorbate concentration in the column effluent as a function of time.

**Breakthrough time ($t_b$).** When the Mass Transfer Zone (MTZ) arrives at the end of the adsorbent bed at time $t_b$, marking the point

where the adsorbate concentration initiates an increase. This point is referred to as the breakthrough time (or breakthrough point), illustrated in figure 1.14. In binary mixtures of $CO_2$–$N_2$ and $CO_2$–$CH_4$, a $CO_2$-selective adsorbent will selectively adsorb $CO_2$, resulting in the longest breakthrough time for $CO_2$. The $CO_2$ breakthrough time represents the time required to obtain pure $CH_4$ or $N_2$ streams from the separation module with a very low $CO_2$ impurity. This parameter, measured in units of time, is directly obtained from breakthrough curves. In this study, it is defined as the time taken for the outlet stream to reach 1% of the inlet $CO_2$ concentration, indicating the breakthrough point.

**Adsorption capacity at breakthrough ($q_b$).** For process design considerations, and given the undesirability of increasing adsorbate concentration at the outlet of the column, it is crucial to determine the adsorption capacity of the adsorbent fixed-bed at the breakthrough point ($b_t$), denoted as $q_b$[103]. This parameter is the amount of a gas compound adsorbed on the MOF before it gets out of the bed, specifically when it reaches the 1% of the inlet concentration at the outlet stream. It can be directly obtained from the breakthrough time and the inlet molar flow of the gas, by subtracting the gas accumulated in the void space of the bed. The breakthrough adsorption capacity of each gas component, in units of mmol·g$^{-1}$, at given operation conditions, can be calculated through the following equation:

$$q_b = \frac{C_o F}{100} t_b - \frac{C_o}{100} \frac{V_v P}{RTM} \tag{1.25}$$

Where $C_0$ is the inlet gas concentration, in %, F is the overall inlet molar flow rate, in mmol·min$^{-1}$, $t_b$ is the breakthrough time, in min·g$^{-1}$, $V_v$ is the void volume of the bed, which has been calculated, from nitrogen adsorption isotherm at 77 K[65,104]. R is the ideal gas constant (0.082 L·atm·mol$^{-1}$·K$^{-1}$), M is the mass of the MOF (activated), P and T are the pressure and temperature in the module, respectively. Thus, the first and second terms refer to the total amount of gas retained in the bed and the amount of gas in the fluid phase, respectively, at the breakthrough point.

**Adsorption saturation capacity at saturation ($q_s$).** The adsorbate concentration in the effluent is almost negligible before reach-

ing the breakthrough point ($t_b$). As the mass transfer zone moves out of the adsorbent bed, the concentration gradually increases. Finally, the leading edge of the mass transfer front reaches the end of the bed, resulting in the effluent concentration becoming equal to the feed value (i.e., $c/c_0 = 1$) at the saturation (equilibrium) time ($t_e$).At this point, the entire bed attains equilibrium with the feed[105]. The adsorption capacity at saturation point ($q_s$) is the most commonly adsorption capacity parameter found in breakthrough studies and refers to the total amount of a gas component adsorbed on the adsorbent before this gets saturated(i.e., when the gas reaches the inlet concentration at the outlet stream). Moreover, this value closely resembles the capacity obtained from adsorption isotherms measured using volumetric or gravimetric methods. To obtain this value, first, the breakthrough curve is plotted as $C/C_o$ versus time (min). Then the total adsorption capacity of each gas, at given operation conditions, is calculated by subtracting the gas retained in the bed void space as in equation 1.25, through the following equation:

$$F \int_0^{t_{\text{sat}}} (C_0 - C)\, dt \frac{C_o F}{100M} - \frac{C_o}{100} \frac{V_v P}{RTM} \tag{1.26}$$

The length of the mass-transfer zone or , equivalently, the difference between breakthrough and equilibration times, depends on the mass-transfer rate.

**Selectivity.** The $CO_2$–$X_i$ selectivity at the breakthrough point and the saturation point is estimated at given pressure and temperature conditions, through the equations 1.27 and 1.28, respectively. Where $X_i$ refers to the gas type used, i.e, $CH_4$ or $N_2$

$$S_{b,\text{CO}_2/X_i} = \frac{q_{b,\text{CO}_2}/C_{0,\text{CO}_2}}{q_{b,X_i}/C_{0,X_i}} \tag{1.27}$$

$$S_{s,\text{CO}_2/X_i} = \frac{q_{s,\text{CO}_2}/C_{0,\text{CO}_2}}{q_{s,X_i}/C_{0,X_i}} \tag{1.28}$$

# References

1. *Global Warming of 1.5 ºC* tech. rep. Accessed: 2023-6-19 (2019).
2. *$CO_2$ Emissions in 2022* tech. rep. Accessed: 2023-6-19 (2022).
3. Siegelman, R. L., Kim, E. J. & Long, J. R. Porous materials for carbon dioxide separations. *Nat. Mater.* **20,** 1060–1072 (2021).
4. Abanades, J. C. *et al.* Emerging $CO_2$ capture systems. *Int. J. Greenhouse Gas Control* **40,** 126–166 (2015).
5. Rubin, E. S., Davison, J. E. & Herzog, H. J. The cost of $CO_2$ capture and storage. *Int. J. Greenhouse Gas Control* **40,** 378–400 (2015).
6. Ioannou, I., Galán-Martín, Á., Pérez-Ramírez, J. & Guillén-Gosálbez, G. Trade-offs between Sustainable Development Goals in carbon capture and utilisation. *Energy Environ. Sci.* (2022).
7. Keith, D. W., Holmes, G., St. Angelo, D. & Heidel, K. A Process for Capturing $CO_2$ from the Atmosphere. *Joule* **2,** 1573–1594 (2018).
8. Kumar, A. *et al.* Direct Air Capture of CO $_2$ by Physisorbent Materials. en. *Angew. Chem. Int. Ed.* **54,** 14372–14377 (2015).
9. Walsh, B. *et al.* Pathways for balancing $CO_2$ emissions and sinks. *Nat. Commun.* **8,** 14856 (2017).
10. Seoane, B. *et al.* Metal-organic framework based mixed matrix membranes: a solution for highly efficient $CO_2$ capture? en. *Chem. Soc. Rev.* **44,** 2421–2454 (2015).
11. Saenz Cavazos, P. A. *et al.* Evaluating solid sorbents for $CO_2$ capture: linking material properties and process efficiency via adsorption performance. *Front. Energy Res.* **11,** 1167043 (July 2023).
12. Balogun, H. A., Bahamon, D., AlMenhali, S., Vega, L. F. & Alhajaj, A. Are we missing something when evaluating adsorbents for CO 2 capture at the system level? *Energy Environ. Sci.* (2021).
13. Chen, H., Dong, H., Shi, Z. & SenGupta, A. K. Direct air capture (DAC) and sequestration of CO $_2$ : Dramatic effect of coordinated Cu(II) onto a chelating weak base ion exchanger. *Sci. Adv.* **9,** eadg1956 (2023).

14. Wilcox, J., Haghpanah, R., Rupp, E. C., He, J. & Lee, K. Advancing adsorption and membrane separation processes for the gigaton carbon capture challenge. *Annu. Rev. Chem. Biomol. Eng.* **5,** 479–505 (2014).

15. Nakao, S.-I., Yogo, K., Goto, K., Kai, T. & Yamada, H. *Advanced $CO_2$ capture technologies: Absorption, adsorption, and membrane separation methods* (Springer, 2019).

16. Zanco, S. E. *et al.* Postcombustion $CO_2$ Capture: A Comparative Techno-Economic Assessment of Three Technologies Using a Solvent, an Adsorbent, and a Membrane. *ACS Engineering Au* **1,** 50–72 (2021).

17. Singh, B., Strømman, A. H. & Hertwich, E. Life cycle assessment of natural gas combined cycle power plant with post-combustion carbon capture, transport and storage. *Int. J. Greenhouse Gas Control* **5,** 457–466 (2011).

18. Clarens, F., Jorge, J., Rafael, M., Rovira, M. & Vega, L. F. Life cycle assessment of CaO looping versus amine-based absorption for capturing CO 2 in a subcritical coal power plant. *Int. J. Greenhouse Gas Control* **46,** 18–27 (2016).

19. Jansen, D., Gazzani, M., Manzolini, G., Van Dijk, E. & Carbo, M. Pre-combustion $CO_2$ capture. *Int. J. Greenhouse Gas Control* **40,** 167–187 (2015).

20. Figueroa, J. D., Fout, T., Plasynski, S., McIlvried, H. & Srivastava, R. D. Advances in $CO_2$ capture technology-The U.S. Department of Energy's Carbon Sequestration Program. *Int. J. Greenhouse Gas Control* **2,** 9–20 (2008).

21. Freguia, S. *Modeling of $CO_2$ Removal from Flue Gases with Monoethanolamine* PhD thesis (The University of Texas at Austin, 2002).

22. Chabanon, E. *et al.* Chemical Engineering and Processing : Process Intensi fi cation Pushing the limits of intensi fi ed CO 2 post-combustion capture by gas – liquid absorption through a membrane contactor. *Chemical Engineering & Processing: Process Intensification* **91,** 7–22 (2015).

23. Madeddu, C., Errico, M. & Baratti, R. *$CO_2$ Capture by Reactive Absorption-Stripping* (2019).

24. Luis, P. Use of monoethanolamine (MEA) for $CO_2$ capture in a global scenario: Consequences and alternatives. *Desalination* **380,** 93–99 (2016).

25. Madeddu, C., Errico, M. & Baratti, R. Process analysis for the carbon dioxide chemical absorption–regeneration system. *Appl. Energy* **215,** 532–542 (2018).

26. Razi, N., Svendsen, H. F. & Bolland, O. Validation of mass transfer correlations for $CO_2$ absorption with MEA using pilot data. *Int. J. Greenhouse Gas Control* **19,** 478–491 (2013).

27. Nittaya, T., Douglas, P. L., Croiset, E. & Ricardez-Sandoval, L. A. Dynamic modeling and evaluation of an industrial-scale $CO_2$ capture plant using monoethanolamine absorption processes. *Ind. Eng. Chem. Res.* **53,** 11411–11426 (2014).

28. Jansen, D., Gazzani, M., Manzolini, G. & Van Dijk, E. Emerging $CO_2$ capture systems. *Int. J. Greenhouse Gas Control* **40,** 167–187 (2015).

29. Chao, C., Deng, Y., Dewil, R., Baeyens, J. & Fan, X. Post-combustion carbon capture. *Renew. Sustain. Energy Rev.* **138,** 110490 (2021).

30. Li, L., Wong-Ng, W., Huang, K. & Cook, L. P. *Materials and processes for $CO_2$ capture, conversion, and sequestration* (John Wiley & Sons, Nashville, TN, 2018).

31. Subraveti, S. G., Li, Z., Prasad, V. & Rajendran, A. Physics-Based Neural Networks for Simulation and Synthesis of Cyclic Adsorption Processes. *Ind. Eng. Chem. Res.* **61,** 4095–4113 (2022).

32. Lin, J.-B. *et al.* A scalable metal-organic framework as a durable physisorbent for carbon dioxide capture. *Science,* 1–4 (2021).

33. Douglas M. Ruthven S Farooq, K. S. K. *Pressure Swing adsorption* (John Wiley & Sons, 1996).

34. Nikolaidis, G. N., Kikkinides, E. S. & Georgiadis, M. C. A model-based approach for the evaluation of new zeolite 13X-based adsorbents for the efficient post-combustion $CO_2$ capture using P/VSA processes. *Chem. Eng. Res. Des.* **131,** 362–374 (2018).

35. Wood, K. R., Liu, Y. A. & Yu, Y. Simulation of Adsorption Processes. *Design, Simulation and Optimization of Adsorptive and Chromatographic Separations,* 1–153 (2018).

36. Dhoke, C., Zaabout, A., Cloete, S. & Amini, S. Review on reactor configurations for adsorption-based $CO_2$ capture. *Ind. Eng. Chem. Res.* **60,** 3779–3798 (2021).

37. Krishnamurthy, S. *et al.* CO $_2$ capture from dry flue gas by vacuum swing adsorption: A pilot plant study. *AIChE J.* **60,** 1830–1842 (2014).

38. Park, J., Lively, R. P. & Sholl, D. S. Establishing upper bounds on $CO_2$ swing capacity in sub-ambient pressure swing adsorption via molecular simulation of metal–organic frameworks. *J. Mater. Chem. A Mater. Energy Sustain.* **5,** 12258–12265 (June 2017).

39. Durán, I., Rubiera, F. & Pevida, C. Separation of $CO_2$ in a Solid Waste Management Incineration Facility Using Activated Carbon Derived from Pine Sawdust. *Energies* **10,** 827 (2017).

40. Anselmi, H., Mirgaux, O., Bounaceur, R. & Patisson, F. Simulation of Post-Combustion CO 2 Capture, a Comparison among Absorption, Adsorption and Membranes. *Chem. Eng. Technol.* **42,** 797–804 (2019).

41. Kniep, J. *et al.* Small pilot test results from a PolarisTM membrane 1 MWe $CO_2$ capture system (2018).

42. Drioli, E. & Babieri, G. *Membrane Engineering for the Treatment of Gases Volume 2: Gas-separation Issues Combined with Membrane Reactors* (Royal Society of Chemistry, 2018).

43. Qian, Q. *et al.* MOF-Based Membranes for Gas Separations. *Chem. Rev.* **120,** 8161–8266 (2020).

44. Chuah, C. Y. *et al.* Harnessing Filler Materials for Enhancing Biogas Separation Membranes. *Chemical Reviews* (2018).

45. Troy, S., Schreiber, A., Zapp, P. & Troy, S. Life cycle assessment of membrane-based carbon capture and storage. *Clean Technol. Environ. Policy* **18,** 1641–1654 (2016).

46. Shen, M. *et al.* Cryogenic technology progress for $CO_2$ capture under carbon neutrality goals: A review. *Separation and Purification Technology* **299,** 121734. ISSN: 1383-5866 (Oct. 2022).

47. Song, C.-F., Kitamura, Y., Li, S.-H. & Ogasawara, K. Design of a cryogenic $CO_2$ capture system based on Stirling coolers. *International Journal of Greenhouse Gas Control* **7,** 107–114. ISSN: 1750-5836 (2012).

48. Berger, A. H., Hoeger, C., Baxter, L. & Bhown, A. Evaluation of Cryogenic Systems for Post Combustion $CO_2$ Capture. en. *SSRN Electronic Journal.* ISSN: 1556-5068. `https://www.ssrn.com/abstract=3365753` (2019).

49. Subraveti, S. G., Roussanaly, S., Anantharaman, R., Riboldi, L. & Rajendran, A. Techno-economic assessment of optimised vacuum swing adsorption for post-combustion $CO_2$ capture from steam-methane reformer flue gas. *Sep. Purif. Technol.* **256,** 117832 (2021).

50. Jaschik, M., Tanczyk, M., Janusz-Cygan, A., Wojdyła, A. & Warmuzinski, K. The separation of carbon dioxide from CO 2 /N 2 /O 2 mixtures using polyimide and polysulphone membranes. *Chemical and Process Engineering - Inzynieria Chemiczna i Procesowa* **39,** 449–456 (2018).

51. Li, Z., Liu, P., Ou, C. & Dong, X. Porous Metal-Organic Frameworks for Carbon Dioxide Adsorption and Separation at Low Pressure. *ACS Sustainable Chemistry and Engineering* **8,** 15378–15404 (2020).

52. Omid T. Qazvini, R. B.
bibinitperiod S. G. T. Selective capture of carbon dioxide from hydrocarbons using a metal-organic framework. *Nat. Commun.,* 1–8 (2021).

53. Qazvini, O. T. & Telfer, S. G. MUF-16: A Robust Metal–Organic Framework for Pre- and Post-Combustion Carbon Dioxide Capture. *ACS Appl. Mater. Interfaces* **13,** 12141–12148 (2021).

54. Wang, Y. & Zhao, D. Beyond Equilibrium: Metal–Organic Frameworks for Molecular Sieving and Kinetic Gas Separation. *Cryst. Growth Des.* **17,** 2291–2308 (May 2017).

55. Bonneau, M. *et al.* Tunable acetylene sorption by flexible catenated metal-organic frameworks. *Nat. Chem.* **14,** 816–822 (2022).

56. DeWitt, S. J. *et al.* Critical Comparison of Structured Contactors for Adsorption-Based Gas Separations. en. *Annual Review of Chemical and Biomolecular Engineering* **9,** 129–152. ISSN: 1947-5438, 1947-5446 (June 2018).

57. Rubio-Martinez, M. *et al.* New synthetic routes towards MOF production at scale. *Chem. Soc. Rev.* **46,** 3453–3480 (2017).

58. Jiang, D.-e., Mahurin, S. M. & Dai, S. *Materials for Carbon Capture* ISBN: 978-1-119-09117-2 (John Wiley & Sons, 2020).

59. Oschatz, M. & Antonietti, M. A search for selectivity to enable $CO_2$ capture with porous adsorbents. *Energy Environ. Sci.* **11,** 57–70 (2018).

60. Chanut, N. *et al.* Screening the effect of water vapour on gas adsorption performance: Application to $CO_2$ capture from flue gas in metal-organic frameworks. *ChemSusChem* **10,** 1543–1553 (2017).

61. Siriwardane, R. V., Shen, M.-S., Fisher, E. P. & Losch, J. Adsorption of CO 2 on Zeolites at Moderate Temperatures. *Energy Fuels* **19,** 1153–1159 (2005).

62. Bollini, P., Choi, S., Drese, J. H. & Jones, C. W. Oxidative degradation of aminosilica adsorbents relevant to postcombustion $CO_2$ capture. *Energy Fuels* **25,** 2416–2425 (2011).

63. Bai, F. *et al.* Amine functionalized mesocellular silica foam as highly efficient sorbents for $CO_2$ capture. en. *Separation and Purification Technology* **299,** 121539. ISSN: 13835866 (Oct. 2022).

64. Hashemi, L., Masoomi, M. Y. & Garcia, H. Regeneration and reconstruction of metal-organic frameworks: Opportunities for industrial usage. en. *Coordination Chemistry Reviews* **472,** 214776. ISSN: 00108545 (Dec. 2022).

65. Corella-Ochoa, M. N. *et al.* Homochiral Metal-Organic Frameworks for Enantioselective Separations in Liquid Chromatography. *Journal of the American Chemical Society* **141,** 14306–14316. ISSN: 15205126 (Sept. 2019).

66. Núñez-Rico, J. L. *et al.* TAMOF-1 as a Versatile and Predictable Chiral Stationary Phase for the Resolution of Racemic Mixtures. *ACS Applied Materials & Interfaces* **15,** 39594–39605 (2023).

67. Sahoo, R., Mondal, S., Mukherjee, D. & Das, M. C. Metal–Organic Frameworks for CO2 Separation from Flue and Biogas Mixtures. en. *Advanced Functional Materials* **32,** 2207197. ISSN: 1616-301X, 1616-3028 (Nov. 2022).

68. Aniruddha, R., Sreedhar, I. & Reddy, B. M. MOFs in carbon capture-past, present and future. en. *Journal of CO2 Utilization* **42,** 101297. ISSN: 22129820 (Dec. 2020).

69. Baci, M. *et al. Metal-Organic Frameworks (MOFs) for Environmental Applications* (Elsevier, 2019).

70. Mukherjee, S., Kumar, A. & Zaworotko, M. J. in *Metal-Organic Frameworks (MOFs) for Environmental Applications* (ed Ghosh, S. K.) 5–61 (Elsevier, 2019).

71. Ho, M. T., Allinson, G. W. & Wiley, D. E. Reducing the cost of CO2 capture from flue gases using pressure swing adsorption. *Industrial and Engineering Chemistry Research* **47,** 4883–4890. ISSN: 08885885 (2008).

72. Cohen, S. M. Postsynthetic methods for the functionalization of metal-organic frameworks. en. *Chem. Rev.* **112,** 970–1000. ISSN: 0009-2665,1520-6890 (Feb. 2012).

73. Belmabkhout, Y., Guillerm, V. & Eddaoudi, M. Low concentration $CO_2$ capture using physical adsorbents: Are metal–organic frameworks becoming the new benchmark materials? en. *Chem. Eng. J.* **296,** 386–397 (July 2016).

74. Flaig, R. W. *et al.* The Chemistry of $CO_2$ Capture in an Amine-Functionalized Metal–Organic Framework under Dry and Humid Conditions. en. *Journal of the American Chemical Society* **139,** 12125–12128. ISSN: 0002-7863, 1520-5126 (Sept. 2017).

75. Ko, D., Siriwardane, R. & Biegler, L. T. Optimization of pressure swing adsorption and fractionated vacuum pressure swing adsorption processes for $CO_2$ capture. *Industrial and Engineering Chemistry Research* **44,** 8084–8094. ISSN: 08885885 (2005).

76. Vaidhyanathan, R., Iremonger, S. S., Dawson, K. W. & Shimizu, G. K. H. An amine-functionalized metal organic framework for preferential $CO_2$ adsorption at low pressures. en. *Chem. Commun. (Camb.),* 5230–5232. ISSN: 1359-7345,1364-548X (Sept. 2009).

77. García, H. & Navalón, S. *Metal-organic frameworks: Applications in separations and catalysis* (John Wiley & Sons, 2018).

78. Madden, D. & Curtin, T. Carbon dioxide capture with amino-functionalised zeolite-B: A temperature programmed desorption study under dry and humid conditions. en. *Microporous and Mesoporous Materials* **228,** 310–317. ISSN: 13871811 (July 2016).

79. McDonald, T. M. *et al.* Cooperative insertion of $CO_2$ in diamine-appended metal-organic frameworks. en. *Nature* **519,** 303–308 (Mar. 2015).

80. Patel, H. A., Byun, J. & Yavuz, C. T. Carbon dioxide capture adsorbents: Chemistry and methods. en. *ChemSusChem* **10,** 1303–1317 (Apr. 2017).

81. Samanta, A., Zhao, A., Shimizu, G. K. H., Sarkar, P. & Gupta, R. Post-combustion $CO_2$ capture using solid sorbents: A review. en. *Ind. Eng. Chem. Res.* **51,** 1438–1463 (Feb. 2012).

82. Thommes, M. *et al.* Physisorption of gases, with special reference to the evaluation of surface area and pore size distribution (IUPAC Technical Report). en. *Pure Appl. Chem.* **87,** 1051–1069 (Oct. 2015).

83. Sayari, A., Belmabkhout, Y. & Serna-Guerrero, R. Flue gas treatment via $CO_2$ adsorption. en. *Chem. Eng. J.* **171,** 760–774 (July 2011).

84. Mahadevaiah, R., Lalithamba, H. S., Shekarappa, S. & Hanumanaika, R. Synthesis of $\alpha$-protected formamides from amino acids using MgO nano catalyst: Study of molecular docking and antibacterial activity. *Scientia Iranica* **24,** 3002–3013 (Dec. 2017).

85. Hai, X. *et al.* Geminal-atom catalysis for cross-coupling. en. *Nature* (Sept. 2023).

86. *Gas Adsorption in Metal-Organic Frameworks* (eds Grant Glover, T. & Mu, B.) (CRC Press, Boca Raton, FL : CRC Press-Taylor & Francis Group, [2018], Sept. 2018).

87. Thomas, W. J. & Crittenden, B. in *Adsorption Technology & Design* (eds Thomas, W. J. & Crittenden, B.) 135–186 (Butterworth-Heinemann, Oxford, 1998).

88. Seader, J. D., Henley, E. J. & Roper, D. K. *Separation Process Principles, 3rd Edition* en. ISBN: 978-1-118-13962-2 (John Wiley Incorporated, Nov. 2010).

89. Seongbin, G., Jang, H. & Lee, J. H. New Performance Indicators for Evaluation of Adsorbents for $CO_2$ Capture with PSA processes. *IFAC-PapersOnLine* **49,** 651–656 (2016).

90. Ayawei, N., Ebelegi, A. N. & Wankasi, D. Modelling and Interpretation of Adsorption Isotherms. *J. Chem. Chem. Eng.* (2017).

91. Iacomi, P. & Llewellyn, P. L. pyGAPS: a Python-based framework for adsorption isotherm processing and material characterisation. en. *Adsorption* **25,** 1533–1542 (2019).

92. Tang, X., Ripepi, N., Stadie, N. P., Yu, L. & Hall, M. R. A dual-site Langmuir equation for accurate estimation of high pressure deep shale gas resources. en. *Fuel* **185,** 10–17 (Dec. 2016).

93. Sharma, S. *et al.* RUPTURA: simulation code for breakthrough, ideal adsorption solution theory computations, and fitting of isotherm models. en. *Mol. Simul.* **49,** 893–953 (June 2023).

94. Sing, K. S. W. in *Adsorption: Science and Technology* (eds Rodrigues, A. E., LeVan, M. D. & Tondeur, D.) 3–14 (Springer Netherlands, Dordrecht, 1989).

95. Sircar, S., Mohr, R., Ristic, C. & Rao, M. B. Isosteric Heat of Adsorption: Theory and Experiment. *J. Phys. Chem. B* **103,** 6539–6546 (1999).

96. Tun, H. & Chen, C.-C. Isosteric heat of adsorption from thermodynamic Langmuir isotherm. *Adsorption* **27,** 979–989 (Aug. 2021).

97. Abdulsalam, J., Mulopo, J., Bada, S. O. & Oboirien, B. Equilibria and Isosteric Heat of Adsorption of Methane on Activated Carbons Derived from South African Coal Discards. *ACS Omega* **5,** 32530–32539 (Dec. 2020).

98. Nuhnen, A. & Janiak, C. A practical guide to calculate the isosteric heat/enthalpy of adsorption: Via adsorption isotherms in metal-organic frameworks, MOFs. *Dalton Trans. J. Inorg. Chem.* **49,** 10295–10307 (Aug. 2020).

99. Pan, H., Ritter, J. A. & Balbuena, P. B. Examination of the approximations used in determining the isosteric heat of adsorption from the Clausius-Clapeyron equation. en. *Langmuir* **14,** 6323–6327 (Oct. 1998).

100. Sabouni, R., Kazemian, H. & Rohani, S. Mathematical modeling and experimental breakthrough curves of carbon dioxide adsorption on metal organic framework CPM-5. en. *Environ. Sci. Technol.* **47,** 9372–9380 (Aug. 2013).

101. Myers, T. G., Font, F. & Hennessy, M. G. Mathematical modelling of carbon capture in a packed column by adsorption. en. *Appl. Energy* **278,** 115565 (Nov. 2020).

102. Green, D. W. & Perry, R. H. *Perry's Chemical Engineers Handbook* (McGraw-Hill Book Co., London and New York, 2008).

103. Roque-Malherbe, R. M. A. *Adsorption and Diffusion in Nanoporous Materials* (CRC Press, Mar. 2007).

104. Chuah, C. Y. & Bae, T.-H. Incorporation of Cu3BTC2 nanocrystals to increase the permeability of polymeric membranes in O2/N2 separation. *BMC Chemical Engineering* **1,** 2. ISSN: 2524-4175 (Jan. 2019).

105. Gabelman, A. Adsorption can be used to treat waste streams or purify valuable components of a feed. This article describes both equilibrium and mass-transfer considerations, and reviews the fundamentals of adsorption system design. en. *Back to Basics* (2017).

*"We live in a society exquisitely dependent on science and technology, in which hardly anyone knows anything about science and technology."*

Carl Sagan

# 2

# $CO_2$ Capture at CELSA: Current Strategies, Innovations, and Future Outlook.

**Abstract** This chapter explores the viability of $CO_2$ capture in CELSA. It examines how existing carbon capture technologies can be adapted to this secondary steel industry. Two technologies were selected based on their maturity and suitability for CELSA: amine-scrubbing and VSA with zeolite 13x. These technologies were evaluated in terms of economics (total annualized cost or TAC) and energy (energy consumption per ton of $CO_2$ captured). While these technologies are relatively mature and appear to be well-suited for CELSA, the results do not indicate the immediate feasibility of their implementation. The operational expenditure (OPEX) results exceeded 30 €/$ton_{CO_2}$, and the energy consumption surpassed 600 kWh/$ton_{CO_2}$. These findings suggest that further research and development are necessary to optimize these technologies and reduce their costs and energy requirements before they can be viably implemented in CELSA.

2

## Contents

## 2.1 Introduction

Iron and steelmaking processes consume a large amount of fossil fuels, contributing to 6-7% of global $CO_2$ emissions[1]. The proposed study aims to analyze the current $CO_2$ capture (CC) technologies to comply with the European Green Deal that aims to cut $CO_2$ emissions by 2050[2]. This reduction is necessary to curtail the economic impact on companies resulting from the rise in $CO_2$ emission prices (currently valued at €90 per tonne of $CO_2$). This aligns with CELSA Group's vision, which focuses on using waste (steel scrap) and reducing or re-purposing $CO_2$ as a raw material in accordance with the circular economy principles. However, the process of capturing $CO_2$ is costly and energy-intensive, besides being the one with the highest cost in the $CO_2$ valorization cycle (capture, storage, and/or utilization)[3].

### 2.1.1 What is CELSA and what is the problem with its emissions?

COMPAÑÍA ESPAÑOLA DE LAMINACIÓN S.L. (CELSA), a company that is part of the CELSA group, one of the largest steel producers in Europe, with a production capacity of 2.5 million tons of steel per year in CELSA Barcelona. In this sense, CELSA seeks and pursues the development of new technologies that help reduce the environmental impact of its production process. The CELSA group's steel manufacturing process involves using scrap metal as its raw material. An electric arc furnace (EAF route) is used to melt the scrap metal, which provides thermal energy through the electric arc between the electrodes of the furnace. Currently, the EAF furnace, combined with secondary metallurgy, allows for the production of a significant amount of the world's steel production through the recycling of scrap metal. In Spain, the EAF route produces 9 million tonnes of steel annually, equivalent to 65% of Spanish production. In the European Union, the EAF route can produce up to 51 million tonnes of steel annually (46% of the total crude steel production)[4]. The EAF route has several advantages, such as the use of various types of raw materials (scrap metal, direct reduction iron, iron ingots, among others) and aggregates (arrivals, lime, etc.) to manufacture any steel. Depending on the limits of the raw material, the EAF route has a reduced investment and environmental impact

when compared to the blast furnace route (BF) and the use of the Basic Oxygen Furnace (BOF). The BF route combined with the BOF has an emission of 2.2 ton$CO_2$eq per tonne of crude steel produced, whereas the EAF route, in agreement with the use of reduced iron (DRI), has a value of 1.2 ton$CO_2$eq[5,6].

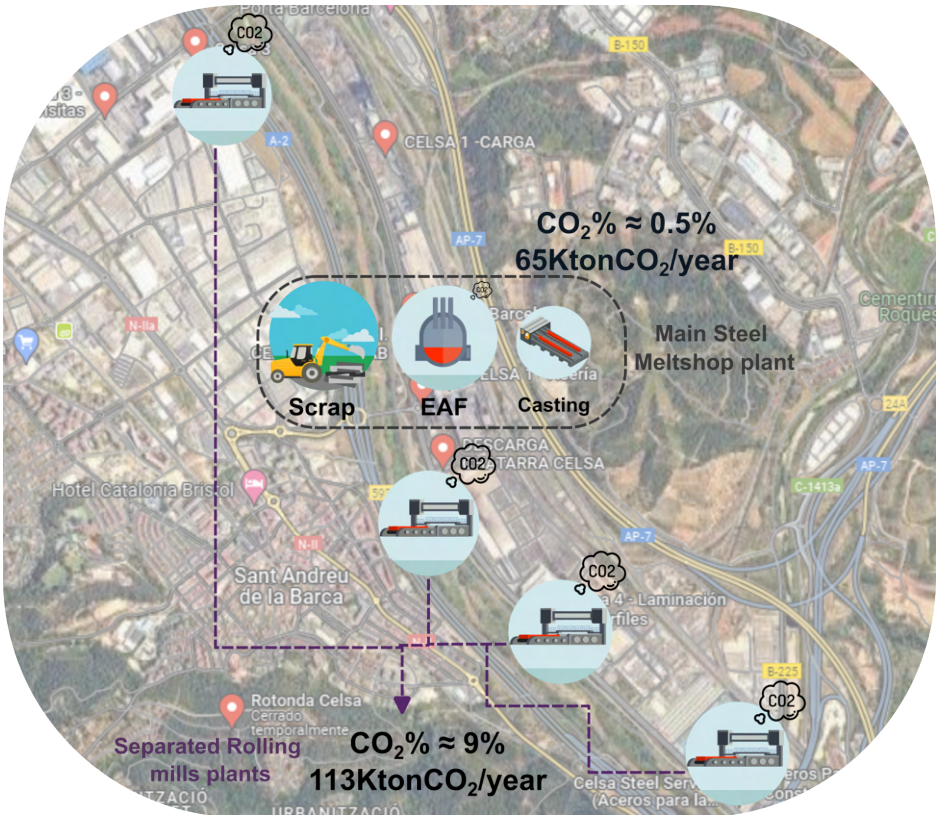


Figure 2.1: Schematic representation of the CELSA BCN company structure.

The schematic representation of how CELSA BCN's industrial plant is distributed is shown in Figure 2.1. Direct emissions in the EAF furnaces are not problematic for CELSA or similar industries. The concentration of $CO_2$ is around 0.5% mol, making it completely diluted. The small amount of $CO_2$ at the outlet is due to the use of carbon during the composition regulation of the steel casting. The amount of $CO_2$ emitted to the atmosphere as a gaseous stream in the main melting plant is approximately 15k ton$CO_2$/year. The major carbon emission focus of the Meltshop plant is the use of carbon for steel composition regulation and electrodes, which emits about

49k ton$CO_2$ annually. However, these emissions cannot be eliminated by $CO_2$ capture. The main focus of direct emissions from the EAF route is downstream of the process. Once raw steel billets are produced, they are reheated in the Rolling Mill reheating furnaces (RMF). These furnaces usually operate with natural gas ($CH_4$) as fuel to produce the energy required to mold the steel billets into the desired product (wires, barrels, etc.). The concentration of $CO_2$ in these reheating furnaces is around 9% (a characteristic of $CH_4$ combustion), and to be concentrated, it needs a minimum of 9 kJ/mol$CO_2$. However, this is just a minimum value and does not take into account any possible inefficiencies or losses that may occur in the $CO_2$ capture systems. CELSA BCN alone produces about 112,561.75 ton$CO_2$ per year due to steel rolling mills. CELSA operates across Europe with seven principal manufacturing facilities. The implementation of $CO_2$ capture technologies presents an opportunity for the company to significantly reduce its carbon footprint at the organizational level. Remarkably, this reduction can be achieved without impacting the production process. Table 2.1 displays the gas composition of one of the CELSA BCN laminations. All other rolling mills reheating furnaces off-gases demonstrate similar behavior. Alongside the dilute concentration of $CO_2$ in the exhaust stream, there are numerous impurities such as water, CO, NOx, $SO_2$, and fine particles. These impurities make it challenging to implement $CO_2$ capture technologies, which must be robust enough to endure these impurities. Usually, these impurities are eliminated before concentrating the $CO_2$. However, removing these impurities also increases the cost, with moisture removal being the most expensive[7]. Therefore, to achieve cost-effective $CO_2$ capture, the technology must be efficient in $CO_2$ capture and robust enough to withstand the impurity of water in the flue gas streams.

Table 2.1: **Gas composition of Rolling mill furnace (RMF) off-gas.**

| **Parameter** | **Value** |
|---|---|
| Pressure, bar | 1.0159 |
| Temperature, K | 509.55 |
| Moisture, %mol | 3.7 |
| $CO_2$, %mol | 8.9 |
| $O_2$, %mol | 6.4 |
| CO, mg·Nm$^{-3}$ | 0.3 |
| $NO_x$, mg·Nm$^{-3}$ | 135.2 |
| Fine particles, mg·Nm$^{-3}$ | 2.3 |
| $SO_2$, mg·Nm$^{-3}$ | 0.507 |

As can be seen in figure 2.1, CELSA has only in the BCN plant (in the other plants, it is distributed similarly) four main emission points separated by large distances, which implements this type of technology even more complicated, due to logistical and industrial integration difficulties. Contrary to sectors characterized by a singular emission source, such as power generation and cement manufacturing, where carbon dioxide capture technology can be concentrated at that specific point, the context of an industry like CELSA demands a distinct approach. For effective integration within such an industry, the technology must exhibit modularity and adaptability, enabling seamless coupling adjacent to each chimney associated with the reheating furnaces.

## 2.2 Which $CO_2$ capture technologies could be suitable for CELSA?

Figure 1.1 introduces several $CO_2$ capture strategies, among which oxy-combustion and post-combustion techniques are identified as particularly conducive to the operational environment at CELSA. Oxy-combustion, while promising in capture efficiency, demands significant capital cost and operational energy, primarily due to the requisite pure oxygen from the air. This method also necessitates comprehensive modifications to the furnace and associated systems within CELSA to mitigate increased moisture and potential condensation challenges in the effluent gases[3,8,9]. On the other hand, Post-Combustion $CO_2$ Capture (PCC) offers a technologically and economically feasible avenue to curb emissions across various industries, facilitating compliance without substantial infrastructure overhaul[8–11]. Although initially capital-intensive, PCC is projected to gain economic traction, propelled by regulatory shifts and the incremental costs tied to $CO_2$ emissions. The discourse on CCS adoption underscores fluctuating installation and operational expenses influenced by the combustion gas composition[11,12]. Advancements in $CO_2$ capture technology are crucial for enhancing cost-efficiency, particularly at lower $CO_2$ concentrations, ensuring robust capture efficacy. Accessibility to diverse technologies addressing distinct emission sources is imperative for the generalized deployment of CCS, aiming at cost reductions in emissions abatement. Recognizing that CCS applicability spans both large and small emitters accentuates the necessity for systems engineered to specific emitter profiles, optimizing efficiency and cost. The variability in plant dimensions and gas compositions negates a one-size-fits-all technological solution, advocating for a multi-technology assessment to identify the most suitable and economically advantageous CCS strategy.

### 2.2.1 Suitable Post-combustion $CO_2$ capture technologies.

Section 1.2 provides a brief overview of extensively studied PCC technologies. In addition, Figure 2.2 shows a qualitative comparison tailored to CELSA's industrial facilities, focusing on five key factors critical for effectively implementing this type of technology within

industrial production operations. The suitability of this PCC technologies may vary based on specific industrial contexts and conditions in which they are implemented. Among these, **amine scrubbing** stands out for its maturity and established benchmark for energy consumption[13]. $CO_2$ separation via absorption has undergone extensive validation at multiple scales, proving its efficacy in contrast to less tested technologies[3,11,14]. Economic analyses underscore the cost-plant size relationship, with larger installations benefiting more significantly from economies of scale. However, the inherent complexity of absorption processes often renders them suboptimal for smaller applications, which favor procedural simplicity over scale economies. For CELSA, with multiple distinct emission sources, se-

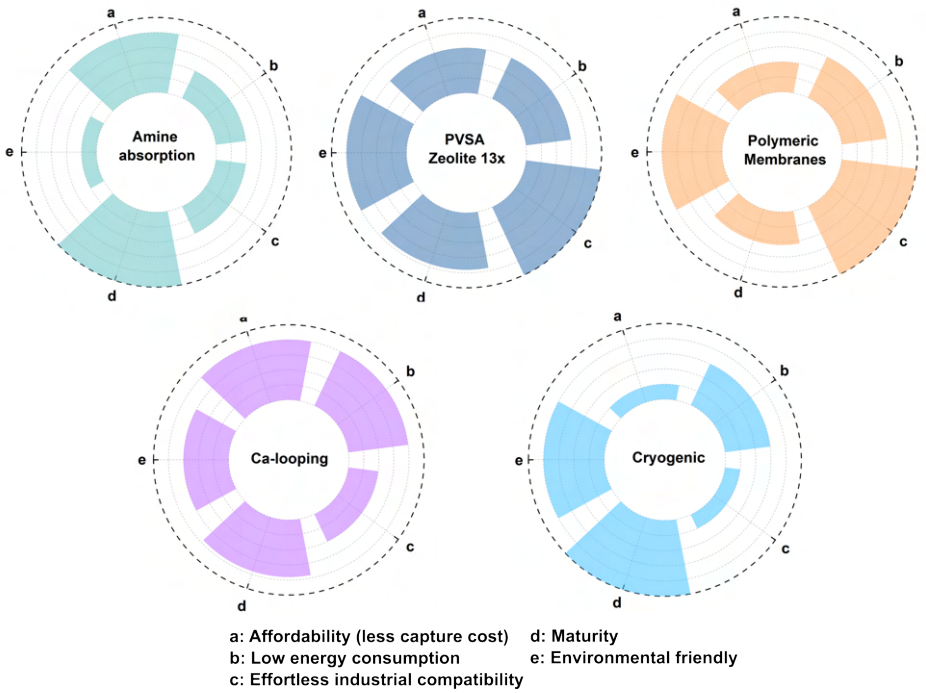


Figure 2.2: Qualitative comparison of post-combustion technologies that could be feasible for CELSA.

lecting a modular and compact PCC system is crucial to avoid the impracticality of amalgamating all exhaust streams before treatment. Expressly, amine regeneration necessitates steam, which is presumed to be an internal resource in many assessments. This assumption is valid for industries like power generation but not for CELSA, which requires an integrated steam circuit. Innovations in amine technol-

ogy and system design aim to optimize desorption and thermal efficiency, with developments in electrochemical, rotating packed beds, and membrane reactors showing promise. Conversely, **adsorption** and **membrane technologies**, noted for their straightforward design and operational simplicity, emerge as more viable at smaller scales[8,9,11]. Despite their size constraints and potential sensitivity to flue gas impurities, these methods currently present higher energy demands for low-concentration $CO_2$ streams. Generally, its integration is less complex and focuses on electrical and gas connections, with potential flue gas conditioning. For thermal adsorption-desorption processes like Temperature Swing Adsorption (TSA), additional energy integration is necessary[15]. Ongoing research in these domains primarily targets material innovations to enhance the cost-effectiveness and energy efficiency of $CO_2$ capture[11].

**CaO-looping**, a technology that has been growing lately, is a specialized subset of chemical loop technologies. It has undergone extensive investigation, with its efficacy proven not only in laboratory settings but also at the pre-industrial level[3,16]. It holds promise for significantly diminishing environmental impact and energy usage associated with amine absorption technologies, thus reducing capture costs. Currently, it stands at an advanced stage in the technology readiness spectrum (TRL 6-7)[17]. The efficacy of CaO-looping technology is highly dependent on specific industrial conditions, most notably within the power generation, cement production, and primary steel manufacturing sectors. It demonstrates peak effectiveness in facilities with a single, large-scale, direct emission source. The economic viability of PCC technology hinges on the precise thermal integration with existing industrial facilities, efficiently utilizing the inherent thermal energy produced by this technology. Essential to this integration is maintaining operational temperatures at approximately 600–700 $^{o}$C for the carbonation phase and exceeding 900$^{o}$C for the calcination phase[18,19]. For CELSA, exploring this thermal recovery option remains unknown, potentially presenting complexity given the specialized nature of their billet-reheating furnaces. The potential solution would entail substantial retrofitting to integrate the recuperated heat and elevate combustion efficiency through gas preheating. These extensive changes, however, would not be spatially impractical given the necessary large-scale infrastructure.

In power generation facilities, where steam is produced integral to turbine operation, harnessing the requisite thermal output from

CaO-looping could enhance the steam supply and overall process efficiency. Research substantiates that such synergy can significantly refine energy production and CO2 capture, potentially reducing capture costs to below €23/ton$CO_2$[3,17,20], surpassing the economic efficiency of amine absorption methods. Considering the operational distribution of cement plants and primary coal-based steelworks, implementing CaO-looping could also yield cost-effective outcomes[17,19].

In our final review of PCC technologies, we consider cryogenic $CO_2$ capture (section 1.2.5), a method akin to amine absorption capture that has reached an industrial application phase. This technology exhibits notable efficiency in $CO_2$ capture at higher partial gas pressures, with associated costs of €44/ton$CO_2$ and energy requirements between 1.9 and 2.5 MJ/ton$CO_2$[21–23]. However, its feasibility diminishes markedly with lower $CO_2$ partial pressures ($< 20\%$), resulting in increased costs around €96/ton$CO_2$ and energy consumption between 3–4 MJ/ton$CO_2$[23]. The footprint demands, and capital expenditures for installation are considerable. As with amine absorption and Ca-looping technologies, cryogenic capture necessitates precise thermal (cooling) integration within industrial facilities. It also requires the removal of water prior to entering the $CO_2$ condensation circuit to prevent the potential freezing that can obstruct pipelines and cause significant operational disruptions[22,24]. Studies applying this technology to power generation (around 15%$CO_2$) often combine it with an initial PSA/VSA or membrane-based pre-concentration stage, followed by cryogenic methods to achieve high $CO_2$ purity. This approach can lead to substantial initial capital costs, though operational expenses may be reduced[3]. Given these considerations, we surmise that cryogenic $CO_2$ capture is not an economically viable PCC technology for the CELSA reheat furnace context.

The cost-effectiveness of the five processes evaluated; $CO_2$ capture by sorption, adsorption, membrane, Ca-Loop, and cryogenic, varies according to the scale and operational parameters of the industrial facility, the specificity of separation demands, and the chosen sorbents/solvents materials in the case of absorption, adsorption and membranes PCC. While several techno-economic analyses have scrutinized these processes independently or in juxtaposition for particular applications, comprehensive comparative assessments, particularly at more minor scales with low $CO_2$ concentrations, remain limited in the literature.

## 2.3 Comparative Analysis of MEA Absorption and 13X Zeolite Adsorption as PCC.

We consider Amine absorption and Zeolite 13x adsorption the primary technologies for in-depth $CO_2$ capture analysis at CELSA's rolling mills. We base this decision on several factors: Adsorption, particularly with zeolite 13X, offers an advantageous mix of operational simplicity, cost-efficiency, and energy usage. As the technology is already well-established, developing new adsorbent materials is expected to advance in the future. Understanding the operational mechanics of adsorption is crucial, as it will inform the exploration of these emerging materials. Conversely, despite amine absorption being the most extensively researched and having the cheapest carbon capture cost, its feasibility at smaller scales and in facilities with multiple emission points remains questionable. However, as engineering firms consistently propose amine-based solutions for CELSA, it is essential to rigorously assess their profitability and practicality for $CO_2$ capture applications at CELSA.

We conducted a comparative analysis of this type of technology in terms of energy (MJ/ton$CO_2$avoided) and economics (€/ton$CO_2$ avoided). Our team performed this analysis for a pilot a pilot plant scale that CELSA planned to set up in its facilities. The results are relative to that plant scale and may vary if implemented on an industrial scale. Especially, if a comprehensive study is conducted, considering the thermal and process integration with industrial facilities. The term $CO_2$ avoided takes into account the difference of the total $CO_2$ captured minus the direct emissions due to the energy expended both in heat and electricity in the implementation of the carbon capture system.

However, it is crucial to acknowledge that certain PCC technologies may gain significance in the future–specifically, the Ca-Loop and the membrane bases PCC. The first requires precise and efficient integration with the industrial process, particularly concerning energy utilization, to ensure profitability. A comprehensive study is essential to ascertain the true potential of this capture technology. Furthermore, membrane technologies must make significant progress in achieving better durability and $CO_2$ selectivity to become cost-effective as a PCC technology.

### 2.3.1 Methodology.

The methodology comprises three primary components: 1) Simulation and evaluation of the $CO_2$ capture processes under established assumptions. 2) An overview of the economic feasibility of implementing this technology via techno-economic analysis, calculating the total annualized cost (TAC) of each $CO_2$ capture technology. 3) Economic and energetic comparison and feasibility analysis for the company CELSA.

### 2.3.2 Pilot plant study for $CO_2$ capture by amine-based absorption.

In section 1.2, we provide a concise explanation of the amine-based capture process. Based on the characteristics of CELSA's rolling mill furnace gas streams (Table 2.1), we design the process to adapt the gas conditions for the installation of amine-based $CO_2$ capture technology. All the design and simulations were performed using AVEVA PRO/II process design software. The thermodynamic property packages used are Peng-Robinson for all auxiliary units (heat exchangers, compressors, pumps, etc.) and the AMINE special package for absorber and stripper design. The process diagram flow scheme is shown in figure 2.3. The thermodynamic model as well as the simulation software was first validated by replicating several works in the literature[8,14,25–30]. A usual in the industrial $CO_2$ source for CCS, the CELSA off-gas also contain $CO_2$, $N_2$, $O_2$, $H_2O$, CO, and traces of NOx and SOx. In this work, we consider the feed as a gaseous mixture of $CO_2$, $N_2$, $O_2$, and $H_2O$. We assume that NOx and SOx have already been removed by a feed desulfurization unit. In this work, the volumetric feed compositions are chosen as follows: $CO_2$ (8.9%), $H_2O$ (3.7%), $O_2$ (6.4%), and $N_2$ (balance). All compositions remain fixed; their variation was not studied in this work. The $CO_2$ recovery percentage is set at 90%, with a concentration higher than 95%. Although, the amine absorption typically gives higher purities due to its high selectivity for $CO_2$[8]. The purity of the output stream significantly influences $CO_2$ compression[25]; a purer $CO_2$ stream reduces the cost of the compression stage if the goal is to transport and store $CO_2$, which is a significant advantage of this amine capture technology.

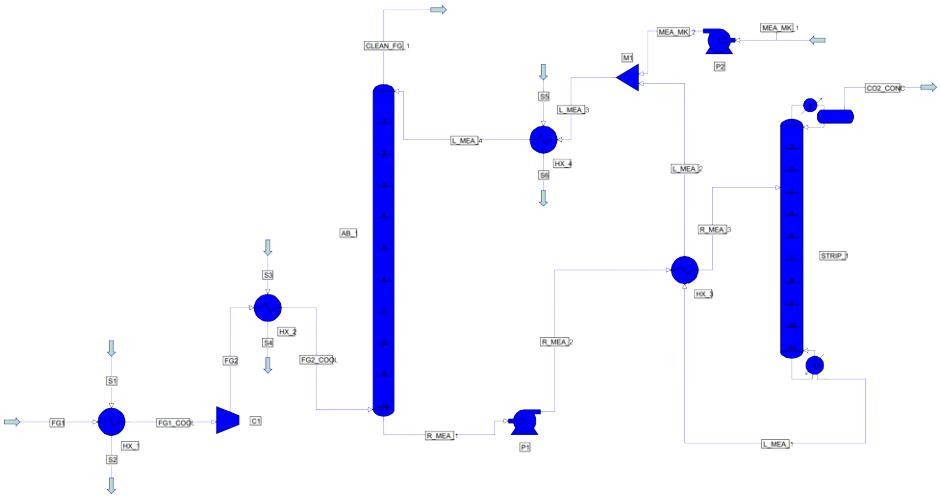


Figure 2.3: AVEVA PRO/II $CO_2$ carbon capture with MEA simulation flowsheet.

### Gas conditioning.

The combustion gases of the rolling mill furnace are first cooled from 509.5K to around 313K. The pressure is set at 1.6 bar to overcome the pressure drops in the capture system, increase the selectivity of the absorbing solution, reduce the height of the absorption column and reduce energy consumption in the stripper[31]. To achieve this, two cooling stages are proposed: one before pressurization, and another after pressurization with compressor C-1. Tube-and-shell exchangers are considered, with an overall heat transfer coefficient (U) of 1 kW/m2·K, and a compressor with an efficiency of 75%. The cooled and compressed gas is sent to the bottom of the absorption column.

### Absorption section.

In this work, we investigated the chemical absorption of carbon dioxide using a 30% by-weight aqueous solution of monoethanolamine (MEA). MEA is a commonly used solvent for $CO_2$ capture due to its high reactivity and absorption capacity[8,25,31]. As documented in various studies[14,32–37], kinetic and equilibrium reactions play a crucial role in the $CO_2$ capture process involving monoethanolamine (MEA)[26]. Specifically, a set of reactions was considered, including three ionic equilibrium reactions (Eq. 2.1 , 2.2, 2.3) and kinetic reversible reactions involving $CO_2$ (Eq. 2.4, and 2.5). These reactions represent

the complex interplay between chemical species and their transformations during $CO_2$ capture, providing a comprehensive understanding of the underlying mechanisms.

$$2H_2O \rightleftharpoons H_3O^+ + OH^- \tag{2.1}$$
$$MEA^+ + H_2O \rightleftharpoons H_3O^+ + MEA \tag{2.2}$$
$$HCO_3^- + H_2O \rightleftharpoons H_3O^+ + CO_3^{2-} \tag{2.3}$$
$$CO_2 + MEA + H_2O \rightleftharpoons MEACOO^- + H_3O^+ \tag{2.4}$$
$$CO_2 + OH^- \rightleftharpoons HCO_3^- \tag{2.5}$$

After being conditioned, the flue gas enters the bottom of a packed column and comes into countercurrent contact with the MEA lean solution. As the flue gas flows through the absorber, $CO_2$ reacts chemically with MEA and is transferred to the liquid phase. The clean gas, devoid of $CO_2$, exits the column and is vented to the atmosphere. The $CO_2$-rich MEA solution leaves the column at the bottom. A make-up process maintains a consistent MEA concentration of 30% in the lean solution fed to the absorber. The $CO_2$-lean solution, obtained from the desorber, undergoes heat exchange with the rich solution from the bottom of the absorber in HX-3 to increase its temperature before entering the make-up and cooling stage. This heat exchange maximizes process efficiency by utilizing the heat extracted from the poor solution stripper. The absorber operating pressure and temperature are crucial factors. High pressure and low temperature minimize the required number of stages and reduce the absorber's flow rate and equipment volume[38]. Running the absorber at feed gas pressure is advantageous to minimize gas compression and refrigeration costs[39]. However, to avoid an oversized absorber column, an equilibrium pressure of 1.5 bar was chosen for CELSA, which has low $CO_2$ concentrations ($\leq 10\%$). Packed columns are continuous, differential-contacting devices that are better described by mass transfer models than by equilibrium-stage concepts. However, packed-tower performance is often presented based on equivalent equilibrium stages using the packed height equivalent to a theoretical stage (HETP). The absorption column is set with 10 equilibrium stages, and the column height is calculated iteratively to maximize mass transfer efficiency between equilibrium stages, considering the minimum inflow to the absorption column and avoiding flooding and excessive pressure drop. Additionally, the column diameter must be such that it does not ex-

ceed one-eighth of the column diameter to prevent poor distribution of liquid and vapor flows. Table 2.2 provides details on the column characteristics and packing. The multistage rate-based model is employed to determine all parameters and column sizing. This model assumes mass transfer between contacting phases as the cause of separation, with equilibrium achieved exclusively at the vapor-liquid interface[14]. The Maxwell-Stefan theory is utilized to calculate mass transfer rates[26].

Table 2.2: **Absorption column characteristics.**

| **Property** | **Value** | **Units** |
|---|---|---|
| Package Heigh | 8.2 | m |
| Section ID | 0.46 | m |
| Packing type | Flexiring, metal | |
| Nominal Packing diameter | 15.875 | mm |

**Stripping section.**

The $CO_2$-rich MEA solution is pumped from the bottom of the absorber to the cross heat-exchanger (HX-3) where it is heated to 365 K due to heat exchange with the $CO_2$-lean MEA solution leaving the stripper. The heated solution is then sent to the top of the stripper. In the second stripper section, the liquid flows countercurrent to the vapor flow generated by the reboiler. From the top of the stripper, a gaseous mixture of carbon dioxide and water is sent to a partial condenser where the $CO_2$ is concentrated in the gas phase and then sent to compression, while the water is recovered in the liquid phase. The stripper usually operates at pressures higher than atmospheric because the vapor pressure of $CO_2$ increases faster compared to the vapor pressure of $H_2O$. This is because the heat of absorption of $CO_2$ in MEA is almost twice the water heat of vaporization. It is also essential that the stripper operates at a higher pressure than the absorber to reach higher temperatures and favor the transfer of $CO_2$ over water. However, this working pressure must be regulated so that the degradation temperature of the MEA (495.15K[36] ) is not reached. It is always prudent to maintain a temperature between 383-398K in order to maximize $CO_2$ desorption rates without degrading the amines over a long period[40]. Moreover, the operating temperature of the condenser on top of the stripper is important to reduce the concentration of water and achieve an adequate concentration of $CO_2$ to

be sent to compression, without affecting the operation of the compressors. Assuming plant water is available for cooling to 298.15K, the operating temperature of the condenser in this work is set to 322 K. Unlike the absorber performance, the packing height in the stripper does not have a significant influence on the mass transferred, and therefore does not have much influence on the reboiler duty[14]. This happens because, once the rich solvent is defined, the duty is used only to heat the feed and to reverse the absorption reactions, independent of the amount of contact surface available. Therefore, to determine the appropriate stripper packing height, the temperature profile is monitored to observe the internal behavior of the column. The literature suggests establishing a height that makes the temperature gradient always above 1 $Km^{-1}$[32], avoiding isothermal zones within the stripper stages. This work determined the stripper column height to be 3 meters. The characteristics of the desorption column are summarized in Table 2.3. In summary, the procedure followed in the stripper design is as follows: a.Characterization of the rich solvent and definition of the target performance regarding the amount of $CO_2$ stripped.; Column effectiveness: b. Simulation of the plant for different values of the stripper packing height; c. Evaluation of the liquid temperature gradient profiles for the corresponding values of the packing height; d. Choice of the packing height that guarantees a liquid temperature gradient higher than 1 $Km^{-1}$ at each column point; and d. Computation of the reboiler duty and the column diameter.

Table 2.3: **Stripping column characteristics.**

| **Property** | **Value** | **Units** |
|---|---|---|
| Package Heigh | 3 | m |
| Section ID | 0.308 | m |
| Packing type | Flexiring, metal | |
| Nominal Packing diameter | 15.875 | mm |

After exiting the stripper, the $CO_2$-lean MEA solution, initially at 398 K, is pumped through heat exchanger HX-3. This process reduces its temperature to 371 K. Subsequently, as previously stated, the solution goes through a make-up and cooling stage to 320 K before re-entering the absorption column.Both the solution pumps (rich/lean) and the gas compressors operate with an efficiency of 75

%. The heat exchangers have an overall mass transfer coefficient (U) of 1 $kWm^2K^{-1}$.

The table A.1 shows the list of process equipment and their conditions used for the simulation and evaluation of the $CO_2$ capture process from the off-gases of the reheating furnace.

### 2.3.3 Pilot plant study for $CO_2$ capture by 13X zeolite adsorption.

In carbon capture process processes, the adsorption using solid sorbents instead of solvents is attractive due to their stability, ease of handling, and lack of volatility and toxicity[11]. The sorbents are commercially available in large quantities and are relatively inexpensive, depending on the material and its synthesis method[41]. Certain types of materials also exhibit selectivity and capacity for $CO_2$ capture[3,11,42]. Different process configurations exist for adsorption, including temperature swing adsorption (TSA), pressure swing adsorption (PSA), and vacuum swing adsorption (VSA), as explained in section 1.2.3. The choice of configuration or combination of configurations (e.g., TSA-VSA, PSA-VSA) depends on the characteristics of the adsorbent. VSA has gained attention for its potential to achieve higher efficiencies than PSA[8,9]. However, studies have shown that applying pressure before the VSA process can enhance pressure drop and vacuum pressures, improving process efficiency[43,44]. Selecting the appropriate adsorption cycle configuration is crucial for achieving the desired separation performance, optimizing process efficiency, and minimizing equipment costs[8,45–47]. The cycle configuration employed in this study considers simplicity, a limited number of steps, and minimal auxiliary equipment parts. This approach aims to initially evaluate the influence of this technology in a pilot plant for industries such as CELSA. While increasing process complexity can improve capture efficiency regarding $CO_2$ recovery and purity, it can also increase energy consumption[9,48,49].

#### Pre-Conditoning unit.

The evaluation of $CO_2$ capture with adsorbents assumes that the CELSA off-gas exits the desulfurization unit without NOx and SOx before being sent to the capture process. The conditions of the CELSA flue gas are the same as those described for the case of amines

in Table 2.1. However, here the gas was simplified to a composition of three gases: $CO_2$, $N_2$, and $H_2O$ to facilitate the calculation and simulation of the process. This simplification is made because several articles in the literature highlight that $O_2$ does not intervene much in the interaction with $CO_2$, as $N_2$ does[50]. Additionally, in the $CO_2$ capture evaluation stage, it is assumed that the gas enters as a binary mixture of $CO_2/N_2$ for the simulation. However, the economic cost of implementing a dehydration stage down to 100 ppm of the flue gas stream is evaluated, as this has a significant impact and is one of the main criticisms of current adsorbents[11,51,52]. Nevertheless, when deciding to implement this type of technology on a large scale, it is also important to include a future rigorous calculation that describes the competitiveness of $CO_2$ with $H_2O$ in the adsorbent, if applicable, to select the best adsorbent for the adsorption capture process. However, we believe that this is not necessary for a preliminary evaluation. The process simulation of the conditioning stage (dehydration and cooling) was evaluated using AVEVA Pro/II simulation software. The simulation diagram flow of the conditioning unit process is shown in Figure 2.4. In this pre-conditioning stage, the blower (B1) undertakes the system's pressure drop up to 1.2 bar. The gas is then cooled with a direct contact cooler (DDC1) up to 59°C, followed by a pre-condensation stage to remove water. The gas is then dehydrated in a TSA process with Silica Gel. The dehydrated flue gas is compressed to the adsorption pressure of 2.69 bar. The water vapor leaving the silica gel column regeneration is recycled and mixed with the flue gas.

**Vacuum swimg adsorption (VSA) section.**

We employed the Machine-Assisted Adsorption Process Learning and Emulation (MAPLE) framework, a data-driven surrogate model that accurately emulates the operation of cyclic steady-state adsorption processes[45,53–55]. This framework is based on a robust mathematical model that describes the key physical phenomena within the adsorption column. The physical model equations are described in the equations 2.6, 2.7, 2.8, 2.9. Moreover, this study makes several assumptions: 1) the gas phase behaves like non-interacting particles, obeying the ideal gas law, 2) the flow in the column is described by an axially dispersed plug flow model, combining plug flow and axial dispersion, 3) the fluid and solid phases are in thermal equilibrium,

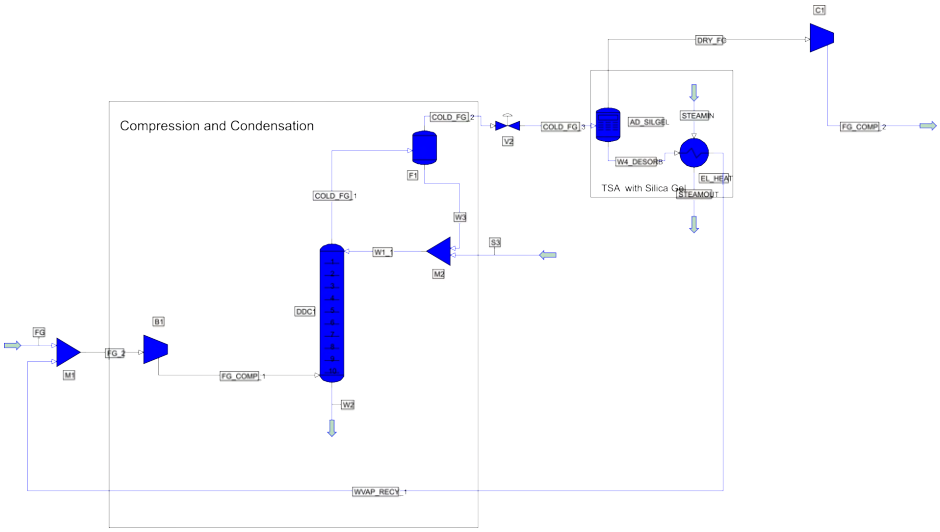


Figure 2.4: AVEVA PRO/II pre-conditioning stage simulation process flow diagram.

with no temperature gradient, 4) the column is adiabatic, with no heat transfer to the surroundings, and 5) the mass transfer between the gas and solid phases follows a linear driving force (LDF) model, where the mass transfer rate is proportional to the concentration difference between the phases.

Since our objective was not to design a new process but to evaluate an existing technology, MAPLE provide a suitable tool. Additionally, MAPLE considers the case of post-combustion $CO_2$ capture from dry flue gas, through a two configuration of a four-step vacuum swing adsorption (VSA) process; one with Feed pressurization (FP) and one with light product pressurization (LPP) shown in figure 2.5. Specifically, we use the LPP (Figure 2.5 b) configuration because it enhances the overall efficiency of the process. This has been demonstrated both at laboratory[54] and pilot scale[56].

Overall mass balance:

$$\frac{1}{P}\frac{\partial P}{\partial t} - \frac{1}{T}\frac{\partial T}{\partial t} = -\frac{T}{P}\frac{\partial}{\partial z}\left(\frac{P}{T}v\right) - \frac{1-\epsilon}{\epsilon}\frac{RT}{P}\sum_{i=1}^{n_{comp}}\frac{\partial q_i}{\partial t} \tag{2.6}$$

Component mass balance:

$$\frac{\partial y_i}{\partial t} + \frac{y_i \partial P}{P \partial t} - \frac{y_i \partial T}{T \partial t} = \frac{T}{P} D_L \frac{\partial}{\partial z}\left(\frac{P}{T}\frac{\partial y_i}{\partial z}\right) - \frac{T}{P}\frac{\partial}{\partial z}\left(\frac{y_i P}{T} v\right) - \frac{RT}{P}\frac{1-\epsilon}{\epsilon}\frac{\partial q_i}{\partial t} \tag{2.7}$$

Mass transfer rate:

$$\frac{\partial q_i}{\partial t} = k_i(q_i^* - q_i); \quad k_i = \frac{C_i}{q_i^*}\frac{15\epsilon D_p}{r_p^2}; \quad D_P = \frac{D_M}{\tau} \tag{2.8}$$

Pressure Drop:

$$-\frac{\partial P}{\partial z} = \frac{150}{4}\frac{1}{r_p^2}\left(\frac{1-\epsilon}{\epsilon}\right)^2 \mu v \tag{2.9}$$

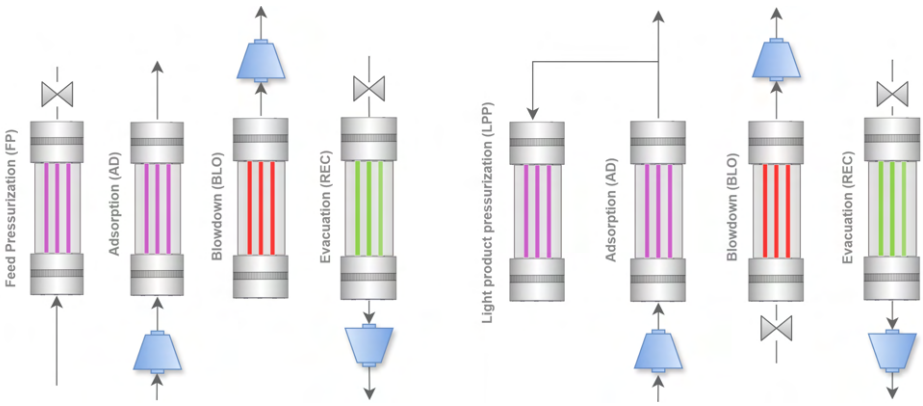


Figure 2.5: VSA process configurations: a) Feed pressurization (FP) and b) Light product pressurization (LPP). Adapted from[53,55]

The LPP cycle comprises the following steps: 1) Feed: $CO_2/N_2$ feed mixture ($CO_2$ mole fraction yF) enters the column bottom at interstitial velocity vF and pressure PH (2.6 bar) for time tADS. $N_2$-enriched product exits the column top; 2) Purge: vacuum is applied from the top of the column, reducing column pressure to PINT to

maximize $N_2$ removal while minimizing $CO_2$ loss; 3) Evacuation: vacuum is applied from the bottom of the column, reducing pressure to PL for $CO_2$ product recollection; and, 4) Light Product Pressurization (LPP): Feed step product pressurizes the column back to PH, enhancing $CO_2$ recovery. The simulation runs each cycle step sequentially using a finite volume scheme to discretize mass and energy balance PDEs. MATLAB's ode23s solver is used for the resulting ODEs. The key performance indicators (KPIs) calculated by the model are a) $CO_2$ Purity (%), as the ratio of $CO_2$ moles to total moles ($CO_2$ + $N_2$) in the product; b) $CO_2$ Recovery (%), as the ratio of product stream $CO_2$ to feed stream $CO_2$; c) the Energy consumption, that is the sum of feed pressurization, purge, and evacuation energies (main engine isentropic efficiency = 75%); and d) the Productivity, as the moles of product $CO_2$ per unit adsorbent volume per cycle time (sum of all stage durations). All the KPIs equations are described in Eq.2.10, 2.11, 2.12, and 2.13.Simulations model a single bed cycling through stages until reaching a cyclic steady state (CSS).

$$PurityCO_2 = \frac{n_{CO_2}^{EVAC}}{n_{CO_2}^{EVAC} + n_{N_2}^{EVAC}} \times 100 \tag{2.10}$$

$$RecoveryCO_2 = \frac{n_{CO_2}^{EVAC}}{n_{CO_2}^{FEED}} \times 100 \tag{2.11}$$

$$Productivity = \frac{n_{CO_2}^{EVAC}}{V_{ads} \times t_{cycle}} \tag{2.12}$$

$$Energy = \frac{E_{ADS} + E_{BLOW} + E_{EVAC} + E_{PRESS}}{CO_2 \text{mass in product}} \tag{2.13}$$

Our study focused on Zeolite 13X, a widely recognized adsorbent for $CO_2$ capture[8]. Validating the model is crucial in the simulation process of carbon capture, as it relies on established data. We employed a simplified single-site Langmuir (SSL) model, to describe the competitive adsorption equilibrium of $CO_2$ and $N_2$ within the isotherm data on zeolite 13X. The SSL model is a generic isotherm that can capture the behavior of many practical systems with a small set of parameters[8,49]. The SSL model is described by equation 2.14, where $q_i*$ is the equilibrium solid-phase loading, $b_i$ is the equilibrium constant for component i, and $q_{sat}$ is the saturation capacity.

Table 2.4: **Parameters used in the simulation of the $CO_2$ capture process by adsorption with 13X zeolite.**

| Parameter | Value | units |
|---|---|---|
| **SSL isotherm parameters for Zeolite 13x[57]** | | |
| $Q_{sat}$ | 4,960.70 | mol m-3 |
| b0,$CO_2$ | 2.50E-06 | m3 mol-1 |
| b0,$N_2$ | 2.70E-06 | m3 mol-1 |
| bi($CO_2$) | 7.29E-01 | m3 mol-1 |
| bi($N_2$) | 2.00E-03 | m3 mol-1 |
| $-\Delta UCO_2$ | 31.19 | kJ mol-1 |
| $-\Delta UN_2$ | 16.38 | kJ mol-1 |
| **Adsorbent properties** | | |
| Bulk Density | 1000 | kg m-3 |
| Specific heat capacity | 1070 | J·kg-1·K-1 |
| **Process Properties** | | |
| yfeed $CO_2$ | 0.09 | |
| Temperature feed | 298.15 | K |
| PH high pressure | 2.69 | bar |
| PI intermediate pressure | 0.137 | bar |
| PL low pressure | 0.02 | bar |
| Feed velocity | 1 | m·s-1 |
| t ads | 66.8 | s |

The equilibrium constant's temperature dependence is described by equation 2.15, where $\Delta H_i$ is the enthalpy of adsorption, R is the ideal gas constant, and T is the temperature. While a dual-site Langmuir (DSL) model would provide a more accurate representation of the adsorption behavior, the SSL isotherm was chosen because it is simple to use and can reasonably approximate the experimental data. The relevant parameters used in the simulations, including the thermodynamic conditions, are summarized in Table 2.4.

$$q_i^* = \frac{q_{sat} b_i C_i}{1 + b_{CO_2} C_{CO_2} + b_{N_2} C_{N_2}} \tag{2.14}$$

$$b_i = b_{i,0} * \exp(-\Delta H_i / R * T) \tag{2.15}$$

As MAPLE is based on the simulation of a generic $CO_2$ VSA capture process[55], it assumes that the gas entering the process is

dehydrated and at a low temperature (25°C). The data obtained from the conditioning-stage process simulation in AVEVA/PROII software (excluding the water content in the output composition) was then interfaced with MAPLE (which runs within MATLAB environment), to assess the overall impact of implementing this $CO_2$ capture process. Figure 2.6 shows the simplified diagram flow of the overall process. Vacuum pumps have been thought to deliver consistent volumetric flow rates across various vacuums. In reality, vacuum pump flow rates comply with certain performance curves. However, the hypothesis of a consistent volumetric flow rate is employed for a more generic design framework than the one used here. The Table A.2 shows the list of process equipment and their conditions used for the simulation of the conditioning and VSA process with zeolite 13x for post-combustion $CO_2$ capture.

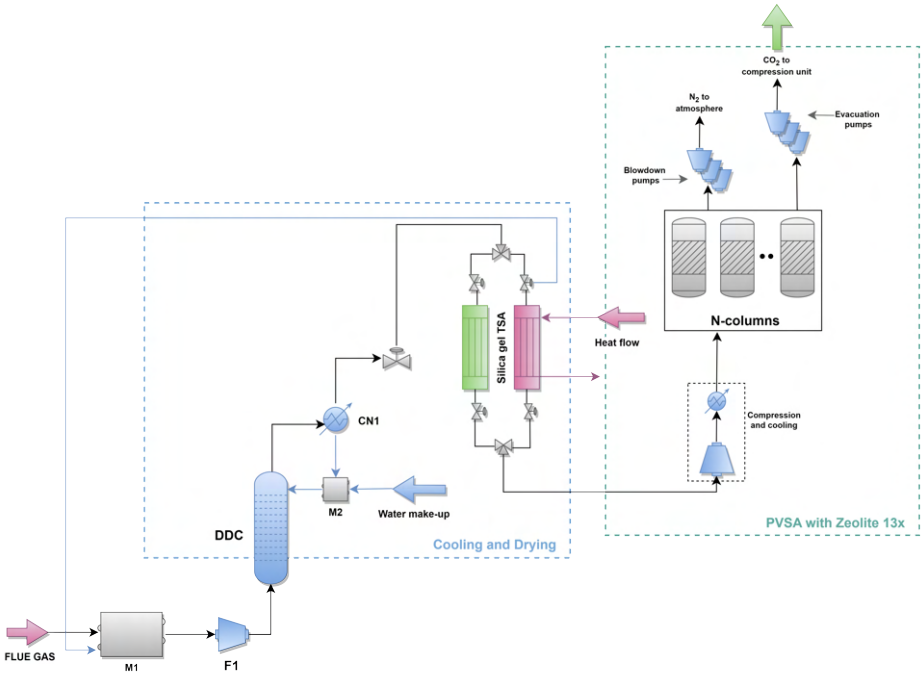


Figure 2.6: $CO_2$ capture by 13X zeolite adsorption process flow diagram.

### Columns shceduling.

The VSA system's transient nature requires programming the cycle with the minimum number of columns for continuous operation.

Key considerations include a continuous feed with constant throughput, separate purge and evacuation vacuum pumps, simultaneously coupled stages, and a dedicated vacuum pump for each column. Subraveti's[9,45,58] procedure was used to determine the column scheduling, with each train comprising the minimum number of columns and vacuum pumps required for continuous operation. The minimum number of columns per train was calculated using Eq. 2.16. Where $t_i$ represents the duration of step i in the cycle.

$$N = Ceiling\left(\frac{\sum_{i=steps} t_i}{t_{ADS}}\right) \tag{2.16}$$

### 2.3.4 Economic evaluation

In this study, we employ the Total Annualized Cost (TAC) per unit mass of captured $CO_2$ as the basis for the cost analysis. This approach is consistent with several prior works[8,25,38,59]. The TAC comprises two components: annualized investment cost (AIC) and annual operating cost (AOC), as shown in Equation 2.17.

$$TAC = AIC + AOC \tag{2.17}$$

$$AIC = \phi \times TPC + AMC \tag{2.18}$$

$$\phi = \frac{i(1+i)^n}{(1+i)^n - 1} \tag{2.19}$$

The AOC encompasses all expenses incurred for utilities necessary for the process's operation, primarily energy and cooling supplies. On the other hand, the AIC constitutes the sum of the initial plant purchase cost (which includes capital investments subject to annualization[38,39,48]) and the ongoing maintenance costs, as detailed in equation 2.18. Here, TPC and AMC represent the total plant and annual maintenance cost, respectively, while $\phi$ is the capital recovery factor. It relates to the discount rate $i$ and the annuities received $n$, which equals the life of the time plant. Equation 2.19 provides its definition. All costs are given in $e_{2023}$ per $t_{CO2}$ captured.

Table 2.5: **Total plant cost (TPC) components.**

| Total installed equipment cost (TIC) | Indirect cost (IDC) | Balance of plant (BOPC) |
|---|---|---|
| equipment purchased cost | engineering and supervision | auxiliary buildings |
| installation costs | construction expenses | service facilites |
| intrumentation and control costs | contractor fees | site development |
| painting, insulation, electrical, piping costs | contingencies | |
| building, service facilities costs | start-up expenses | |
| spare parts | | |
| taxes, insurance, freight charges | | |

$$TPC = TIC + IDC + BOPC = TIC(1 + 0.32 + 0.2) \tag{2.20}$$

(2.21)

The AMC can be quantified as a percentage ($5\%$[8,25,39]) of the total plant cost (TPC), with a capital recovery factor of 0.154. The TPC is calculated as the sum of three components: the total equipment installed cost (TIC), indirect costs (IDC), and the balance of plant costs (BOPC). These components are all expressed proportionally to the TIC, as shown in equation 2.20. Table 2.5 provides a detailed list of the components that make up the terms of equation 2.20.

The total investment costs (TIC) comprise both equipment purchase costs (EPC) and equipment installation costs (EIC), as shown in equation 2.22. Furthermore, the EIC can be expressed as proportions of EPC for each principal piece of equipment[8,38,45,59], as detailed in Table 2.6.

$$TIC = EPC + EIC \tag{2.22}$$

The annual operating hours were set as a fixed value of 8000 hours, and this value was utilized to calculate the operating costs (AOC). To calculate the equipment purchase cost (EPC), the equations of Seider et al.[38] have been used. Table 2.7 provides a detailed breakdown of the costs associated with utilities(cooling, electricity, and heating.) used in the economic calculation. The detailed equations for each equipment are shown below.

### Liquid Pumps.

In the absorption process, the cost of solution pumps is expressed according to Equation 2.23, where $S = QH^{0.5}$. The flow rate $Q$ in

Table 2.6: **Equipment installation costs (EIC) as a percentage of equipment purchase costs (EPC).**

| Equipment | % of EPC equivalence |
|---|---|
| blowers | 42%EPC |
| fans | 61%EPC |
| compressor | 49%EPC |
| vacuum pumps | 12%EPC |
| liquid pumps | 30%EPC |
| heat exchangers | 61%EPC |
| refrigerating units | 46%EPC |
| towers, adsorption columns, membrane modules, coolers | 62%EPC |

Table 2.7: **Cost of utilities used in the $CO_2$ capture process.**

| Utility | Unit | Value | Ref. |
|---|---|---|---|
| Electricity | €/kWh | 0.0625 | [8] |
| Steam | €/tonSteam | 13.905 | [60,61] |
| Cooling water | €/kWh | 0.0463 | [8] |

gal/min, and the pump head is $H$ in ft.

$$EPC_{pump} = \exp 9.7171 - 0.6019[ln(S)] + 0.0519[ln(S)]^2 \qquad (2.23)$$

**Vacuum pumps.**

Assuming no air leakage, $S$ is approximated as the flow rate of the gas mixture entering the equipment. The acquisition cost is determined by the type of pump selected and calculated using equations 2.24-2.27.

$$\text{liquid-ring} \quad S: 50-350 ft^3/min \rightarrow EPC = 8.250 S^{0.35} \tag{2.24}$$

$$\text{three-stage lobe} \quad S: 60-240 ft^3/min \rightarrow EPC = 7.120 S^{0.41} \tag{2.25}$$

$$\text{three-stage claw} \quad S: 60-270 ft^3/min \rightarrow EPC = 8.630 S^{0.36} \tag{2.26}$$

$$\text{screw compressors} \quad S: 50-350 ft^3/min \rightarrow EPC = 9.590 S^{0.38} \tag{2.27}$$

**Blowers.**

The purchase cost of the blower is calculated using equation 2.28. $F_M$ if a material factor, for carbon steel is 1. $C_B$ is defined with equation 2.29.

$$EPC_{blower} = F_M C_B \tag{2.28}$$

$$C_B = \exp\left[6.8929 + 0.7900 ln(P_c)\right] \tag{2.29}$$

The consumed power (PC) is derived by dividing the brake power by the efficiency of the motor ($\eta M$). In the case of an electric motor, $\eta M$ is typically 90%[8]. When considering blowers, the representative size factor is the brake power ($PB$) by equation 2.30. This can be calculated from the inlet volumetric flow rate ($Q_I$), inlet and outlet pressures ($p_I, p_O$), and the isoentropic efficiency ($\eta B$), which assume ideal gas conditions and a constant specific heat ratio ($\gamma$).

$$PB = \frac{Q_I p_I}{\eta_B} \frac{\gamma}{\gamma - 1} \left[ \left( \frac{p_O}{p_I} \right)^{\frac{\gamma-1}{\gamma}} - 1 \right] \tag{2.30}$$

**Compressors.**

The compressor purchased cost is evaluated as the equation 2.31. Factor FD is considering 1 for electric drives, FM is 1 same as blower and CB is calculated by equation 2.32

$$EPC_{compressor} = F_D F_M C_B \tag{2.31}$$

$$C_B = \exp\left[7.5800 + 0.8ln(P_c)\right] \tag{2.32}$$

**Heat exchangers.**

The purchase cost of each heat transfer equipment, which includes heat exchangers, coolers, reboilers, condensers and inter-stage coolers, are calculated based on equation 2.36. The cost of each piece of equipment is obtained from the heat transfer area ($A_{h,c}$) used to exchange heat from a hot fluid to a cold one. The heat transfer area is calculated by equation 2.33, where Q, U and $\Delta T_{ml}$ being the heat duty, the global heat transfer coefficient and the log-mean temperature difference, respectively. We use a $C_B$ expression for shell and tube "fixed-head" heat exchangers. The pressure factor $F_P$ is calculated as equation 2.35.

$$A_{h,c} = \frac{Q}{U\Delta T_{lm}} \tag{2.33}$$

$$C_B = \exp\left[a + b(ln(A)) + c(ln(A))^2\right] \tag{2.34}$$

$$F_P = 0.9803 + 0.018\left(\frac{P}{100}\right) + c\left(\frac{P}{100}\right)^2 \tag{2.35}$$

$$EPC_{HX} = F_P \cdot F_M \cdot F_L \cdot C_B \tag{2.36}$$

The heat transfer are is either determined through design calculations (in the case of TSA columns for the silica-gel dehydration system) or obtained by performing an energy balance considering fluid temperatures, heating or cooling duties, and the heat transfer coefficient. Carbon steel (FM = 1) is used as the construction material for all heat exchangers, with the exception of the solution heat exchanger (HX-3) in the absorption system. This deviation is attributed to the corrosive nature of amines at high temperatures[8,14,30,36,40,45,59]. For HX-3, stainless steel is chosen as the shell/tube material, and its FM value is calculated using equation 2.37.

Table 2.8: **Cost of packing materials for absorption and adsorption columns.**

| **Material** | **Unit** | Value | Ref. |
|---|---|---|---|
| Flexi ring, metal, 15.8 mm | 1703.4 | €/m3 | [8] |
| Pelletized Zeolite 13x | 6 | €/kg | [62] |
| Pelletized Silica-gel | 2 | €/kg | [63] |

$$F_M = 2.70 + \left(\frac{A}{1000}\right)^{0.07} \tag{2.37}$$

**Pressure and contactor vessels.**

Equation 2.38 calculates the acquisition cost for absorption and adsorption columns. Fm is the construction material factor, and Cv,n (2.39) is the free-on-board (FOB) purchase cost of an empty vessel with weight Wn. Cpl,n (2.41) represents the added cost for platforms and ladders, while Vp,n is the de adsorber packaging volume.

The cost of packing depends on the specific technology, according to the data reported in table 2.8. It encompasses the cost of metallic packing for absorption columns and the cost of adsorbent inventory for adsorption columns. Finally, CDR,n is a column's installed cost of flow distributors (and redistributors for absorption). For an initial cost estimate, in the absence of a vendor quote, the installed cost of a liquid distributor in an absorption column can be approximated as 125 $\$/ft_2$ of the column's cross-sectional area. As a general rule, distributors should be installed at each feed point, and for conservative estimates, redistributors should be placed approximately every 20 feet[38].

Vessel weight is determined using Equation 2.40, where $L_n$ and $D_n$ are the length and diameter, respectively, $t_S$ is the shell thickness, and $\rho$ is the material density. The shell thickness is calculated based on the column diameter, module of elasticity, and maximum allowable stress, which are influenced by operating temperature and pressure levels. The overall thickness is then rounded up to the nearest fabrication value.

$$EPC, n_{vessel} = FM \cdot C_{v,n} + C_{pl,n} + V_{p,n} \cdot C_{PK} + C_{DR,n} \quad (2.38)$$

$$C_{v,n} = \exp 7.27 + 0.182[ln(W_n)] + 0.0229[ln(W_n)]^2 \quad (2.39)$$

$$W_n = (\pi(D_n + t_s)(0.8D_n + L_n)t_s\rho) \quad (2.40)$$

$$C_{pl,n} = 7.27(D_n)^{0.182}(L_n)^c \quad (2.41)$$

Differences exist in their geometrical proportions, specifically for adsorption columns. For VSA columns, a height-to-diameter (H/D) ratio between 3–4[9,25,38] has to be considered. However, for the TSA silica-gel dehydration system, a type of shell exchanger adaptation, a H/D ratio between $2-3$ is preferable[48,64]. For TSA columns, the cost of a vessel with the same total adsorption bed cross section is added to the cost of a "flat head" type shell and tube heat exchanger with a single-pass tube bundle. The cost of TSA columns includes the cost of a vessel with the same total adsorption bed cross-section added to the cost of a "flat head" type shell and tube heat exchanger with a single pass tube bundle. Each column also has associated switching valve costs. The number of switching valves per column is estimated based on the adsorption cycle configuration, and the estimated purchase cost of each valve is 500–1000 euros, which varies depending on its size and configuration (2–way or 3–way).

## 2.4 Results and Discussion.

In Section 2.1.1 , we discussed $CO_2$ capture technologies suitable for CELSA's reheating furnaces. Two mature technologies were selected for the presented analysis: absorption (With MEA-solution solvents) and adsorption (with Zeolite 13x). The development and innovation of these technologies primarily involve new solvents (for absorption) and materials (for adsorption), as the process design is well-established[8,15,65,66]. The economic and technical studies of implementation of new technologies in a company are influenced by most of the available knowledge not only of the new technologies, but of the knowledge itself, of the production process of each industry[39,48]. Most studies focus on low concentration ($< 10\%$) $CO_2$ capture post-combustion, in a general way, or for power generation plants. However, each industry has its unique production configuration, which

can significantly impact the feasibility of different technologies. The analysis conducted for CELSA is based on my knowledge gained during my previous tenure at the company. It combines relevant studies from literature[8,9,25,45,53,55,59–61], adapted specifically to CELSA's secondary steel industry and its reheating furnaces, where the highest percentage of post-combustion $CO_2$ emissions is concentrated, as illustrated in Figure 2.1.

### 2.4.1 Capital Expenditure (CAPEX)

Capital expenditure (CAPEX) encompasses a company's investments in acquiring or upgrading fixed assets. These investments significantly influence strategic decision-making. Our analysis assessed the total plant cost (TPC) of $CO_2$ capture technologies, considering both equipment-installed cost (TIC) and associated infrastructure(IDC and BOPC). Figure 2.7a shows the TIC divided for each section of the two types of $CO_2$ capture technologies analyzed for CELSA, amine-stripping and VSA with zeolite 13x. The amine-absorption plant demonstrated a lower TIC at €466/ton$_{CO2}$ compared to the adsorption plant utilizing Zeolite 13X (€539/ton$_{CO2}$), representing a 15.6% difference. This cost differential was reflected in the TPC. We observe that the Amine-absorption $CO_2$ capture (CC) technology, without conditioning, has a marginally higher cost of approximately 5% compared to the VSA process using Zeolite 13x. However, the determining factor that penalizes the adsorption technology in this particular case is its flue gas conditioning, which incurs a significantly higher cost, estimated to be 61% more than the amine-absorption process. The Total equipment Installation Cost (TIC) associated with gas conditioning encompasses several key processes. These include the cooling of the CELSA gases achieved through direct contact with the gas, the pre-drying system utilizing a temperature swing process (TSA) with Silica-gel, and the impulsion of the gas to overcome the pressure losses inherent to the system. In the case of VSA, an additional compression step of the dry gas is included to ensure efficient working capacity, ultimately contributing to a higher efficiency in $CO_2$ separation. For an amine-absorption system, post-drying with triethylene glycol (TEG) was required to remove water before the $CO_2$ utilization or storage. In the case of VSA, the final compression step and the type of gas-drying system used significantly increase the cost of the CC equipment. Among

the drying methods, TSA silica-gel (used to achieve a humidity level below 100 ppm) is more expensive than the post-drying system with triethylene glycol (TEG) for amine absorption. The cost of TSA silica-gel pre-drying is €237.57/ton$_{CO2}$, while the cost of TEG post-drying is €146.7/ton$_{CO2}$. Therefore, the cost of adsorption-based CC technology implementation increases significantly due to the requirement of conditioning factors. The cost of auxiliary equipment in the case of amine adsorption is significantly higher than in the adsorption system (53 with respect to €20/ton$_{CO2}$), primarily due to the increased complexity of the integration and amine systems compared to the adsorption systems. The total investment cost (TIC) of auxiliary equipment includes the cost of switching valves in the adsorption system and the cost of liquid pumps and secondary heat exchangers in the case of amine absorption. This cost difference is one of the reasons why adsorption systems are often considered more attractive for industrial implementation[11]. The primary cost driver in the $CO_2$ capture installation was the separation columns. The zeolite adsorption columns were considerably more expensive (18%) than the scrubber and stripper of the amine-absorption technology. This difference is primarily attributed to the longer regeneration time of the 13X zeolite compared to its adsorption time (74 respecto to 380 seconds). Consequently, more columns are required to process the flue gas and achieve the desired target (90% recovery and 95% purity). In contrast, the amine absorber is heavily influenced by the partial pressure of $CO_2$, leading to an increase in its height to attain a high $CO_2$ recovery rate. However, this increase in height does not result in a proportional increase in cost, unlike the adsorption columns, where the cost of each column is multiplied by the total number of columns. Therefore, it is essential to consider adsorbents that exhibit not only high selectivity for $CO_2$ but also facile desorption properties to minimize the number of adsorption columns required and optimize the overall cost of the $CO_2$ capture process.

### 2.4.2 Operational Expenditure (OPEX)

In this study, we evaluate the operational expenditure (OPEX) of the $CO_2$ capture plant, focusing primarily on the annual operating cost (AOC). The AOC is dominated by the process's energy requirements and utility consumption, including cooling process water and solvent replenishment (MEA and TEG for amine absorption). Fig-

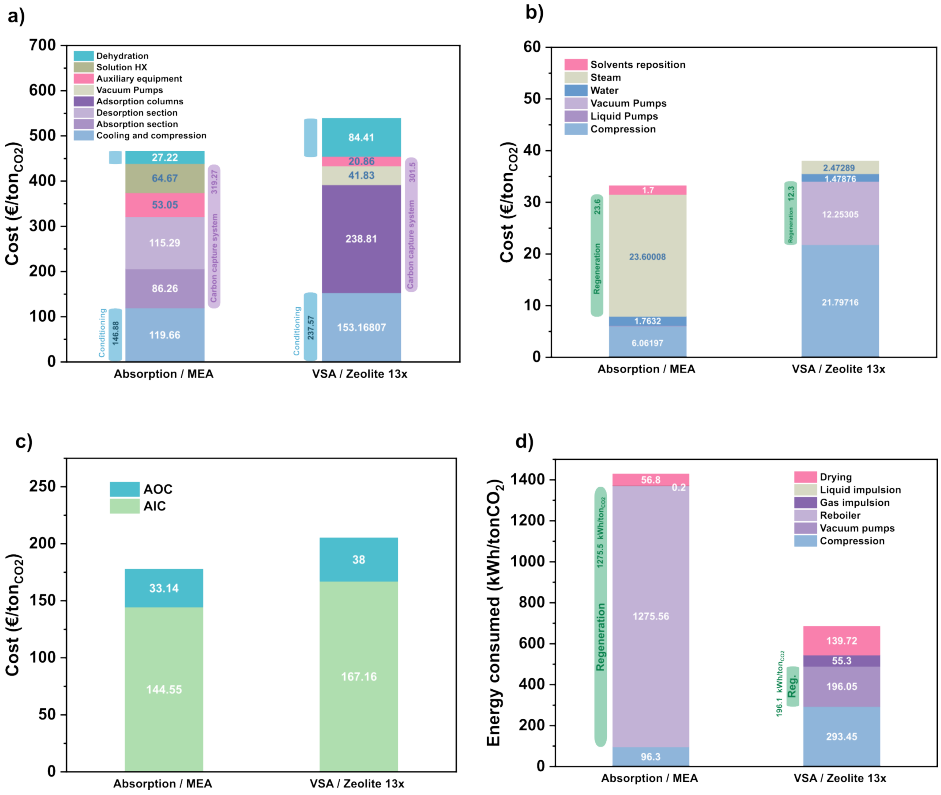


Figure 2.7: Comparison of economic and energetic performance of MEA and VSA CC technologies.a) Total plant cost (TPC) breakdown. b) Annual operating cost (AOC) breakdown. c) Total annualized cost (TAC) breakdown. d) Energy consumption breakdown.

ure 2.7b illustrates the economic breakdown of these factors for each capture technology. Amine absorption incurs the highest regeneration operating cost (€23.6/ton$_{CO2}$) due to steam usage for regenerating the desorption column. In contrast, the VSA process utilizes electrical energy for vacuum pump operation, resulting in a lower regeneration cost of €12.15/ton$_{CO2}$. However, the VSA process requires gas impulsion at a higher pressure (2.6 bar) during the initial adsorption stage to enhance working capacity. This incurs a higher cost (€21.8/ton$_{CO2}$) than amine absorption (€6/ton$_{CO2}$), where compression is only needed to overcome system pressure drops in the absorption and desorption columns. Amine absorption also involves additional costs like liquid pumping (€0.1/ton$_{CO2}$) and solvent replacement (MEA solution for $CO_2$ capture and TEG for dehydration, at a combined cost of €1.7/ton$_{CO2}$). The VSA process incurs an extra cost of €2.47/ton$_{CO2}$ for steam used in regenerating the pre-dehydration with silica gel. Cooling water consumption costs are comparable between the two processes, with a slight advantage (19%) for amine absorption. Although the energy consumption for regeneration is higher in amine absorption than in vacuum swing adsorption (Figure 2.7d), the cost of steam is lower than the cost of electricity, making the operating costs of the amine absorption process competitive with those of the vacuum swing adsorption process.

### 2.4.3 Total Annualized Cost (TAC)

Figure 2.7c depicts the decomposition of the Total Annual Cost (TAC) into the Annual Investment Cost (AIC) and Annual Operating Cost (AOC) with a $CO_2$ recovery of 90% and a purity exceeding 95%. Under these conditions and for the specified plant size, the overall TAC for the Vacuum Swing Adsorption (VSA) process is €205/ton$_{CO2}$, representing a 15% increase compared to the amine absorption process. Notably, the ratio of AIC to AOC remains similar for both processes, ranging between 22-23%. However, the AOC for VSA is higher than that of amine absorption, with values of 38 and 33.1 €/ton$_{CO2}$, respectively.

The AOC for absorption technology involves maintaining an inflow of aqueous MEA solution to the AB-1 column with a mole fraction of 0.3. This is achieved through a replenishment flow rate of 3 kmol/h of the aqueous MEA solution, containing 90% mol of MEA. Este make-up de solucion de MEA representa un 5% del AOC. More-

over, the AOC breakdown reveals that steam constitutes a significant portion, accounting for 71% of the total AOC. It is essential to note that while improving the productivity of an amine-absorption system requires optimizing the $CO_2$ desorption process, this comes at the cost of increased energy consumption[14,30,36]. The steam consumption rate in the reboiler rises, leading to higher temperatures in the desorber head, which can affect the overall efficiency of the system[67].

In the VSA process, compression is responsible for 57% of the AOC, while vacuum pumps consume 32%. These two factors account for more than 80% of the VSA process's operating costs. This is largely influenced by the process design, which depends on the adsorbent type. The design of the columns (length and diameter) to process a certain volume of gas is determined by the adsorbent's characteristics, and the number of columns required is influenced by the ease of gas regeneration (which is correlated to the number of vacuum pumps needed)[9,45]. The compression required in the gas drive and conditioning phase (9% of the total AOC) can be marginally reduced, as the gas needs to be cooled and driven to the adsorption columns. However, the power consumption per compression in the adsorption and desorption steps could be significantly decreased by developing new types of adsorbent materials. It is important to consider that the AIC of the VSA process could potentially increase if the very low-cost 13x zeolite is replaced with a new generation adsorbent, which is likely to be more expensive[8,61]. Additionally, the vapor cost in the AOC (6% of the total) could be eliminated by using a moisture-resistant adsorbent. Zeolite 13x has limited resistance to moisture, and $H_2O$ competes with $CO_2$ for adsorption sites. Thus, finding an adsorbent with enhanced moisture resistance could significantly reduce operating costs[15,68,69].

The AIC for amine-absorption and VSA-based carbon capture processes account for 81% of the total technology-associated investment cost (TAC). The gas separation columns contribute the most to the AIC in both absorption and VSA processes. Moreover, the cost of AIC and AOC of flue gas conditioning (cooling and compression) in both technologies are unavoidable expenses.

In the case of the absorption process, the AIC does not decrease significantly with the change of solvents[26,32–34,70]. This is because the infrastructure, particularly for this type of process, depends heavily on the $CO_2$ concentration in the flue gas, the absorber dimensions, and the desorption rate for the stripper dimensions. Unlike

the absorption process, the VSA process offers opportunities for cost reduction. Compression, the number of columns, and dehydration account for a total of 71% of the total AIC in the VSA process. Pre-dehydration and compression before adsorption contribute to 33% of the total AIC. Therefore, innovation and development in adsorption technologies for CC are primarily focused on discovering new materials that can lower the systems costs. This is crucial for making adsorption CC technology economically viable and displacing established amine-based technologies[11,45,71,72].

### 2.4.4 Energy consumption.

Figure 2.7d illustrates the contribution of various energy consumption components in amine-absorption and VSA CC technologies. The amine-absorption process consumes nearly double the energy compared to the VSA process, registering 1371.9 versus 684.5 kWh/$ton_{CO2}$.

Regarding flue gas drive and compression, the VSA system exhibits an approximately three-fold higher energy consumption. This is attributed to the necessity of operating at elevated pressure in the VSA process to enhance the adsorption capacity. However, excluding the high-pressure adsorption step (i.e., considering only gas drive), the VSA and absorption systems exhibit more comparable values at 55.3 and 96.3 kWh/$ton_{CO2}$, respectively. These latter values possess limited variability, while the dry gas compression in the VSA system (293.4 kWh/$ton_{CO2}$) presents potential for reduction through optimized system design and the development of novel adsorbent materials[8,25,45].

Comparing the regeneration processes in both technologies, the energy consumption associated with amine regeneration in the stripper is approximately 6.5 times higher than the work performed by vacuum pumps to desorb $CO_2$ from adsorption columns. Despite this significant difference, the amine-absorption system still boasts a lower annual operating cost (AOC) due to the more economical nature of steam compared to electricity. Notably, in the amine-absorption system, steam consumption in the stripper reboiler accounts for a substantial 92% of the total energy consumption, while this figure stands at only 28% for the VSA process.

With respect to gas dehydration processes, pre-dehydration using silica gel before flue gas entry into the VSA system exhibits higher energy consumption (139 kWh/$ton_{CO2}$) compared to post-dehydration

with triethylene glycol (TEG) in the amine-absorption system (56.8 kWh/$ton_{CO2}$). Although TEG systems are applicable to both VSA and amine-absorption processes, they are typically preferred when moisture concentrations are less dilute, as is the case at the end of the absorption process. TEG dehydration systems effectively remove water to prevent freezing in pipes before liquefying $CO_2$ for transportation and storage purposes[59,73].

### 2.4.5 Outlook.

CO2 utilization presents a double win for industries: reducing direct emissions and creating new markets within the circular economy, specifically the carbon economy. However, for $CO_2$ to be utilized or stored, it must be concentrated[3,74–77] to make downstream processes economically viable. The major hurdle lies in the high energy and economic cost of $CO_2$ capture, often exceeding other stages in the CO2 valorization chain (capture-utilization or capture-storage)[78,79]. Our present small-scale study examined the economic and energy impact of a $CO_2$ capture pilot plant for CELSA. While the findings may apply to larger scales, it represents a preliminary assessment. Thermodynamic data was estimated, potentially deviating from real-world scenarios. Pilot plant testing and a future industrial-scale study are crucial next steps. These studies should consider the plant's energy and process interconnections, such as waste heat recovery and gas recirculation. In CELSA's case, integrating waste streams could make CaO-looping CC technology a contender. It deserves evaluation alongside existing amine absorption and VSA-Zeolita 13X technologies. While both amine absorption and CaO-looping require significant infrastructure, their applicability might be limited by CELSA's dispersed emission points. Conversely, adsorption and membrane technologies offer advantages due to their modularity, especially for industrial deployment. Beyond capture studies, future research should investigate the fate of captured $CO_2$. This includes exploring diverse scenarios and models for circular economic integration with complementary industries or $CO_2$ storage options. By quantifying costs, energy inputs, and potential savings, such analyses will provide a clearer picture of $CO_2$ capture and utilization's economic viability and sustainability. Furthermore, all studies considering different CO2 capture options and utilization or storage technologies must include a life cycle assessment (LCA)[13,79,80]. This is critical to comprehensively evaluate

the technology's environmental impact – both directly and indirectly – leading to more informed decision-making. Future research can significantly contribute to advancing $CO_2$ capture and utilization by addressing these critical aspects, ultimately integrating them into a broader sustainable industrial ecosystem.

## 2.5 Conclusions.

In this study, we investigate alternative routes for post-combustion $CO_2$ capture of CELSA stream flue gas. The flue gas contains 8.9% $CO_2$ mol and 3.7% $H_2O$ mol at the rolling-mill reheating furnace stack exit temperature and pressure of 236°C and 1.01 bar, respectively. The objective is to recover 90% $CO_2$ and deliver it at 95% purity. We qualitatively evaluated different established $CO_2$ capture (CC) processes based on literature data and their suitability for implementation in an industry like CELSA. Two technologically mature CC processes were selected for rapid implementation and testing at the industrial level. These processes are intended to be representative of the separation technology on which they are based: 1) adsorption using an aqueous solution of MEA and 2) adsorption, specifically by pressure and vacuum changes (VSA) using zeolite 13x in conventional fixed beds. In the case of adsorption, the gaseous flue was dried before introduction into the $CO_2$ capture unit. However, for the adsorption with the amine solution, the dehydration process is done after $CO_2$ capture. Both technologies are well characterized in the literature, providing reliable data for detailed modeling, simulation, and validation of the process, as well as for realistic cost estimation. We expect that any of the capture processes considered can be feasibly implemented and operated in an industrial plant today. However, for the time being, we considered simple process configurations. In a future industrial implementation, these configurations will need further study and optimization, especially in the thermal integration with the existing CELSA steel industrial plant. While there may be better liquid sorbents, solid adsorbent materials, or process configurations, or materials that do not require feed pre-drying, we chose to focus on well-known and widely researched technologies and materials to provide useful information on $CO_2$ capture after combustion.

As a preliminary step, robust and established simulation tools were employed to simulate the processes for all the technologies un-

der consideration. For the simulation, a pilot CO2 capture plant of the various technologies utilized was considered, with a capture rate of 800 tonCO2/year and the previously stated objectives. While productivity is a parameter that would need to be defined for each CC technology type, it was not used as a comparison variable. However, energy demand and economic evaluation are defined consistently across technologies and can be directly compared. The energy demand of each equipment was determined through thermodynamic equations, and the economic evaluation was performed by calculating the total annual cost (TAC) of the studied DC technologies.

Based on the techno-economic comparison within the investigated plant size and capture rate range, the straightforward adsorption-based process employing an aqueous MEA solution exhibits superior cost performance compared to the adsorption-based separation process utilizing Zeolite 13x. Notably, the VSA process was approximately 15% more expensive than the adsorption process. While there is no significant economic distinction between the two technologies currently, the VSA process possesses substantial potential for cost reduction, particularly in the gas dehydration process (contributing 13% of the total annualized cost) and the compression operation (accounting for 18% of the total annualized cost), as well as in terms of infrastructure requirements (such as the number of columns, vacuum pumps, etc.). In the VSA process, the adsorption columns alone constitute approximately 47% of the TAC This advantage stems from developing novel adsorbent materials, particularly those with enhanced moisture resistance and sorption capabilities. In contrast, the absorption process is inherently limited by the physicochemical properties of the flue gas.

The comparative energy analysis revealed that the amine absorption process exhibited significantly higher energy consumption (1372 kWh / $ton_{CO2}$) compared to the VSA (Vacuum Swing Adsorption) process (685 kWh / $ton_{CO2}$). Despite this difference in energy consumption, the annual operating cost (AOC) exhibited a marginally lower cost for the amine-absorption process, with a difference of only 14%. This apparent anomaly can be attributed to the differing energy sources utilized by the two processes. The amine-absorption process employs steam for regeneration, while the VSA process relies on electrical energy. In the context of the analysis, the cost of steam was lower than that of electrical energy, leading to a lower AOC for the amine-absorption process.

In the amine-absorption process, the steam consumption for regeneration accounts for approximately 92% of the total energy consumption, making it a crucial aspect to consider. This process is particularly suitable for industries that have access to steam within their own facilities. However, CELSA lacks its own steam generation capabilities. In the present study, the cost of steam used was taken from the available literature[8,59,61], and this cost is an estimate as an accesible hot utility. It is important to note that the optimal approach would be to design and install a small steam generator, taking into account the consumption of natural gas and the associated installation costs. Industries such as power generation are more inclined to adopt systems that require steam, as they typically have the necessary infrastructure and steam availability. By implementing such systems, industries can take advantage of the high steam consumption efficiency of the amine-absorption process. This optimization can lead to significant cost savings and improved overall process efficiency. Therefore, in industries like CELSA, where steam is unavailable, the amine-absorption process's AOC can be significantly increased.

The VSA process, which employs adsorbents, faces challenges in competing with amine-absorption. The primary limitation lies in the maximum velocities attainable in these systems. This necessitates the use of numerous columns and potentially multiple parallel trains. While using multiple modules offers a degree of robustness, it presents two significant hurdles. Firstly, complexity arises from integrating the numerous modules and managing the associated piping and control systems. Secondly, cost is a major factor, as each column adds to the overall expense, accounting for a substantial percentage of the total plant. It is challenging to anticipate cost savings from economies of scale. Consequently, the scale of the capture plant emerges as a critical consideration. Despite the challenges, VSA technology may still be more appealing for small and medium-scale point sources, such as CELSA rolling mill furnaces, due to its reduced complexity and cost competitiveness compared to other available technologies.

# References

1. Zhao, Q. *et al.* Co-treatment of Waste From Steelmaking Processes: Steel Slag-Based Carbon Capture and Storage by Mineralization. *Frontiers in Chemistry* **8,** 1–7 (2020).
2. Europea, U. *Communication from the commission to the European parliament, the European council, the European economic and social committee and the committe of the regions* research rep. (EUROPEAN COMMISSION, 2023).
3. Abanades, J. C. *et al.* Emerging $CO_2$ capture systems. *Int. J. Greenhouse Gas Control* **40,** 126–166 (2015).
4. ESTEP. *Green steel by EAF route: a sustainable value chain in the EU Circular Economy scenario* research rep. (ESTEP, 2019). `https://www.estep.eu/assets/Uploads/20191129-WorkshopReport-ESTEP-EAFGreenSteel-FinalDraft.pdf`.
5. $CO_2$ *Emissions in 2022* tech. rep. Accessed: 2023-6-19 (2022).
6. Williams, M. *et al. how clean is the us steel industry nv* 2019. `https://www.belfercenter.org/sites/default/files/files/publication/how-clean-is-the-us-steel-industry-nv.pdf`.
7. Goyal, P., Purdue, M. J. & Farooq, S. Adsorption and diffusion of moisture and wet flue gas on silica gel. en. *Chem. Eng. Sci.* **227,** 115890. `http://dx.doi.org/10.1016/j.ces.2020.115890` (115890 2020).
8. Zanco, S. E. *et al.* Postcombustion $CO_2$ Capture: A Comparative Techno-Economic Assessment of Three Technologies Using a Solvent, an Adsorbent, and a Membrane. *ACS Engineering Au* **1,** 50–72 (2021).
9. Subraveti, S. G., Roussanaly, S., Anantharaman, R., Riboldi, L. & Rajendran, A. Techno-economic assessment of optimised vacuum swing adsorption for post-combustion $CO_2$ capture from steam-methane reformer flue gas. *Sep. Purif. Technol.* **256,** 117832 (2021).
10. Rubin, E. S., Davison, J. E. & Herzog, H. J. The cost of $CO_2$ capture and storage. *Int. J. Greenhouse Gas Control* **40,** 378–400 (2015).

11. Siegelman, R. L., Kim, E. J. & Long, J. R. Porous materials for carbon dioxide separations. *Nat. Mater.* **20,** 1060–1072 (2021).

12. Hassan, S. M. N. *Techno-Economic Study of $CO_2$ Capture Process for Cement Plants* PhD thesis (University of Waterloo, Waterloo, Canada, 2005).

13. Ioannou, I., Galán-Martín, Á., Pérez-Ramírez, J. & Guillén-Gosálbez, G. Trade-offs between Sustainable Development Goals in carbon capture and utilisation. *Energy Environ. Sci.* (2022).

14. Madeddu, C., Errico, M. & Baratti, R. *$CO_2$ Capture by Reactive Absorption-Stripping* (2019).

15. Balogun, H. A., Bahamon, D., AlMenhali, S., Vega, L. F. & Alhajaj, A. Are we missing something when evaluating adsorbents for CO 2 capture at the system level? *Energy Environ. Sci.* (2021).

16. Fan, L.-S., Zeng, L., Wang, W. & Luo, S. Chemical looping processes for $CO_2$ capture and carbonaceous fuel conversion – prospect and opportunity. en. *Energy & Environmental Science* **5,** 7254. ISSN: 1754-5692, 1754-5706 (2012).

17. Carlos Abanades, J., Criado, Y. A. & García, R. Countercurrent moving bed carbonator for $CO_2$ capture in decoupled calcium looping systems. en. *Chemical Engineering Journal* **461,** 141956. ISSN: 13858947 (Apr. 2023).

18. Grasa, G. S. & Abanades, J. C. $CO_2$ Capture Capacity of CaO in Long Series of Carbonation/Calcination Cycles. en. *Industrial & Engineering Chemistry Research* **45,** 8846–8851. ISSN: 0888-5885, 1520-5045 (Dec. 2006).

19. Fu, C., Roussanaly, S., Jordal, K. & Anantharaman, R. Techno-Economic Analyses of the $CaO/CaCO_3$ Post-Combustion $CO_2$ Capture From NGCC Power Plants. en. *Frontiers in Chemical Engineering* **2,** 596417. ISSN: 2673-2718 (Jan. 2021).

20. Perejón, A. *et al.* The Calcium-Looping technology for $CO_2$ capture: On the important roles of energy integration and sorbent behavior. en. *Applied Energy* **162,** 787–807. ISSN: 03062619 (Jan. 2016).

21. Wang, X. & Song, C. Carbon Capture From Flue Gas and the Atmosphere: A Perspective. *Front. Energy Res.* (2020).

22. Berger, A. H., Hoeger, C., Baxter, L. & Bhown, A. Evaluation of Cryogenic Systems for Post Combustion $CO_2$ Capture. en. *SSRN Electronic Journal.* ISSN: 1556-5068. https://www.ssrn.com/abstract=3365753 (2019).

23. Shen, M. *et al.* Cryogenic technology progress for $CO_2$ capture under carbon neutrality goals: A review. *Separation and Purification Technology* **299,** 121734. ISSN: 1383-5866 (Oct. 2022).

24. Tuinier, M., Hamers, H. & Van Sint Annaland, M. Techno-economic evaluation of cryogenic $CO_2$ capture—A comparison with absorption and membrane technology. en. *International Journal of Greenhouse Gas Control* **5,** 1559–1565. ISSN: 17505836 (Nov. 2011).

25. Hasan, M. M. F., Baliban, R. C., Elia, J. A. & Floudas, C. A. Modeling, Simulation, and Optimization of Postcombustion CO 2 Capture for Variable Feed Concentration and Flow Rate. 2. Pressure Swing Adsorption and Vacuum Swing Adsorption Processes. en. *Industrial & Engineering Chemistry Research* **51,** 15665–15682. ISSN: 0888-5885, 1520-5045 (Dec. 2012).

26. Zhang, Y. *et al.* Rate-based process modeling study of $CO_2$ Capture with aqueous monoethanolamine solution. *Industrial and Engineering Chemistry Research* **48,** 9233–9246. ISSN: 08885885 (2009).

27. Plaza, J. M., Wagener, D. V. & Rochelle, G. T. Modeling $CO_2$ capture with aqueous monoethanolamine. *Energy Procedia* **1,** 1171–1178. ISSN: 18766102 (2009).

28. Tobiesen, F. A., Juliussen, O. & Svendsen, H. F. Experimental validation of a rigorous desorber model for $CO_2$ post-combustion capture. *Chemical Engineering Science* **63,** 2641–2656. ISSN: 00092509 (2008).

29. Hara, N., Taniguchi, S., Yamaki, T., Nguyen, T. T. & Kataoka, S. Bi-objective optimization of post-combustion $CO_2$ capture using methyldiethanolamine. en. *International Journal of Greenhouse Gas Control* **122,** 103815. ISSN: 17505836 (Jan. 2023).

30. Rackley, S. A. in *Carbon Capture and Storage (Second Edition)* (ed Rackley, S. A.) 115–149 (Butterworth-Heinemann, Boston, 2017). ISBN: 978-0-12-812041-5. http://www.sciencedirect.com/science/article/pii/B9780128120415000064.

31. Seader, J. D., Henley, E. J. & Roper, D. K. *Separation Process Principles, 3rd Edition* en. ISBN: 978-1-118-13962-2 (John Wiley Incorporated, Nov. 2010).

32. Madeddu, C., Errico, M. & Baratti, R. Process analysis for the carbon dioxide chemical absorption–regeneration system. *Appl. Energy* **215,** 532–542 (2018).

33. Luis, P. Use of monoethanolamine (MEA) for $CO_2$ capture in a global scenario: Consequences and alternatives. *Desalination* **380,** 93–99 (2016).

34. Hwang, G. S., Stowe, H. M., Paek, E. & Manogaran, D. Reaction mechanisms of aqueous monoethanolamine with carbon dioxide: A combined quantum chemical and molecular dynamics study. *Physical Chemistry Chemical Physics* **17,** 831–839. ISSN: 14639076 (2015).

35. Nittaya, T., Douglas, P. L., Croiset, E. & Ricardez-Sandoval, L. A. Dynamic modeling and evaluation of an industrial-scale $CO_2$ capture plant using monoethanolamine absorption processes. *Ind. Eng. Chem. Res.* **53,** 11411–11426 (2014).

36. Alie, C. F. *$CO_2$ Capture With MEA: Integrating the Absorption Process and Steam Cycle of an Existing Coal-Fired Power Plant* PhD thesis (2004).

37. Yeh, J. T. & Pennline, H. W. Aqua ammonia process for simultaneous removal of $CO_2$, SO2 and NOx. **4,** 89–104 (2004).

38. Seider, W. D. *et al. Product and Process Design Principles: Synthesis, Analysis, and Evaluation* en. ISBN: 978-1-119-63698-4 (Wiley, May 2020).

39. Peters, M. S., Timmerhaus, K. D. & E.West, R. *Plant Design and Economics for Chemical Engineers* ISBN: 0-07-239266-5 (McGraw Hill, New York, 2003).

40. Davis, J. & Rochelle, G. Thermal degradation of monoethanolamine at stripper conditions. *Energy Procedia* **1,** 327–333. ISSN: 18766102 (2009).

41. Brickett, L. *Carbon Dioxide Capture Handbook* (US Department of Energy (DOE)/NETL, 2015, Aug. 2015).

42. Sayari, A., Belmabkhout, Y. & Serna-Guerrero, R. Flue gas treatment via $CO_2$ adsorption. en. *Chem. Eng. J.* **171,** 760–774 (July 2011).

43. Riboldi, L. & Bolland, O. Overview on Pressure Swing Adsorption (PSA) as $CO_2$ Capture Technology: State-of-the-Art, Limits and Potentials. *Energy Procedia* **114.** ISSN: 18766102 (2017).

44. Capocelli, M. *et al.* Post-combustion $CO_2$ capture by RVPSA in a large-scale steam reforming plant. *Journal of $CO_2$ Utilization* **32,** 53–65. ISSN: 22129820 (2019).

45. Subraveti, S. G., Li, Z., Prasad, V. & Rajendran, A. Physics-Based Neural Networks for Simulation and Synthesis of Cyclic Adsorption Processes. *Ind. Eng. Chem. Res.* **61,** 4095–4113 (2022).

46. Samanta, A., Zhao, A., Shimizu, G. K. H., Sarkar, P. & Gupta, R. Post-combustion $CO_2$ capture using solid sorbents: A review. en. *Ind. Eng. Chem. Res.* **51,** 1438–1463 (Feb. 2012).

47. Nikolaidis, G. N., Kikkinides, E. S. & Georgiadis, M. C. A model-based approach for the evaluation of new zeolite 13X-based adsorbents for the efficient post-combustion $CO_2$ capture using P/VSA processes. *Chem. Eng. Res. Des.* **131,** 362–374 (2018).

48. Green, D. W. & Perry, R. H. *Perry's Chemical Engineers Handbook* (McGraw-Hill Book Co., London and New York, 2008).

49. Douglas M. Ruthven S Farooq, K. S. K. *Pressure Swing adsorption* (John Wiley & Sons, 1996).

50. Chao, C., Deng, Y., Dewil, R., Baeyens, J. & Fan, X. Post-combustion carbon capture. *Renew. Sustain. Energy Rev.* **138,** 110490 (2021).

51. Lin, J.-B. *et al.* A scalable metal-organic framework as a durable physisorbent for carbon dioxide capture. *Science,* 1–4 (2021).

52. Boyd, P. G. *et al.* Data-driven design of metal-organic frameworks for wet flue gas $CO_2$ capture. en. *Nature* **576,** 253–256. ISSN: 1476-4687 (Dec. 2019).

53. Pai, K. N., Prasad, V. & Rajendran, A. Generalized, Adsorbent-Agnostic, Artificial Neural Network Framework for Rapid Simulation, Optimization, and Adsorbent Screening of Adsorption Processes. en. *Industrial & Engineering Chemistry Research* **59,** 16730–16740. ISSN: 0888-5885, 1520-5045 (Sept. 2020).

54. Estupiñan Perez, L., Sarkar, P. & Rajendran, A. Experimental validation of multi-objective optimization techniques for design of vacuum swing adsorption processes. en. *Separation and Purification Technology* **224,** 553–563. ISSN: 13835866 (Oct. 2019).

55. Pai, K. N., Prasad, V. & Rajendran, A. Experimentally validated machine learning frameworks for accelerated prediction of cyclic steady state and optimization of pressure swing adsorption processes. en. *Separation and Purification Technology* **241,** 116651. ISSN: 13835866 (June 2020).

56. Krishnamurthy, S. *et al.* CO $_2$ capture from dry flue gas by vacuum swing adsorption: A pilot plant study. *AIChE J.* **60,** 1830–1842 (2014).

57. Khurana, M. & Farooq, S. Adsorbent Screening for Postcombustion CO 2 Capture: A Method Relating Equilibrium Isotherm Characteristics to an Optimum Vacuum Swing Adsorption Process Performance. en. *Industrial & Engineering Chemistry Research* **55,** 2447–2460. ISSN: 0888-5885, 1520-5045 (Mar. 2016).

58. Khurana, M. & Farooq, S. Integrated Adsorbent Process Optimization for Minimum Cost of Electricity Including Carbon Capture by a VSA Process. *AIChE Journal* **65,** 184–195. ISSN: 15475905 (2019).

59. Hasan, M. M. F., Baliban, R. C., Elia, J. A. & Floudas, C. A. Modeling, Simulation, and Optimization of Postcombustion CO 2 Capture for Variable Feed Concentration and Flow Rate. 1. Chemical Absorption and Membrane Processes. en. *Industrial & Engineering Chemistry Research* **51,** 15642–15664. ISSN: 0888-5885, 1520-5045 (Dec. 2012).

60. Danaci, D., Bui, M., Mac Dowell, N. & Petit, C. Exploring the limits of adsorption-based $CO_2$ capture using MOFs with PVSA – from molecular design to process economics. en. *Molecular Systems Design & Engineering* **5,** 212–231. ISSN: 2058-9689 (2020).

61. Danaci, D., Webley, P. A. & Petit, C. Guidelines for Techno-Economic Analysis of Adsorption Processes. *Frontiers in Chemical Engineering* **2,** 602430. ISSN: 2673-2718 (Jan. 2021).

62. Su, F. & Lu, C. $CO_2$ capture from gas stream by zeolite 13X using a dual-column temperature/vacuum swing adsorption. en. *Energy & Environmental Science* **5,** 9021. ISSN: 1754-5692, 1754-5706 (2012).

63. Grande, C. A., Morence, D. G. B., Bouzga, A. M. & Andreassen, K. A. Silica gel as a selective adsorbent for biogas drying and upgrading. en. *Ind. Eng. Chem. Res.* **59,** 10142–10149. ISSN: 0888-5885,1520-5045 (May 2020).

64. Towler, G. & Sinnott, R. *Chemical engineering design: principles, practice, and economics of plant and process design* Second edition. en. ISBN: 978-0-08-096659-5 (Elsevier, Butterworth-Heinemann, Amsterdam Heidelberg, 2013).

65. Clarens, F., Jorge, J., Rafael, M., Rovira, M. & Vega, L. F. Life cycle assessment of CaO looping versus amine-based absorption for capturing CO 2 in a subcritical coal power plant. *Int. J. Greenhouse Gas Control* **46,** 18–27 (2016).

66. Li, L., Wong-Ng, W., Huang, K. & Cook, L. P. *Materials and processes for $CO_2$ capture, conversion, and sequestration* (John Wiley & Sons, Nashville, TN, 2018).

67. Anselmi, H., Mirgaux, O., Bounaceur, R. & Patisson, F. Simulation of Post-Combustion CO 2 Capture, a Comparison among Absorption, Adsorption and Membranes. *Chem. Eng. Technol.* **42,** 797–804 (2019).

68. Qasem, N. A. & Ben-Mansour, R. Adsorption breakthrough and cycling stability of carbon dioxide separation from $CO_2$/N2/H2O mixture under ambient conditions using 13X and Mg-MOF-74. *Applied Energy* **230,** 1093–1107. ISSN: 03062619 (2018).

69. Santos, M. P., Grande, C. A. & Rodrigues, A. E. Dynamic study of the pressure swing adsorption process for biogas upgrading and its responses to feed disturbances. *Industrial and Engineering Chemistry Research* **52,** 5445–5454. ISSN: 08885885 (2013).

70. Nakao, S.-I., Yogo, K., Goto, K., Kai, T. & Yamada, H. *Advanced $CO_2$ capture technologies: Absorption, adsorption, and membrane separation methods* (Springer, 2019).

71. Chen, H., Dong, H., Shi, Z. & SenGupta, A. K. Direct air capture (DAC) and sequestration of CO $_2$ : Dramatic effect of coordinated Cu(II) onto a chelating weak base ion exchanger. *Sci. Adv.* **9,** eadg1956 (2023).

72. Yang, H., Fan, S., Lang, X., Wang, Y. & Nie, J. Economic comparison of three gas separation technologies for $CO_2$ capture from power plant flue gas. *Chinese Journal of Chemical Engineering* **19,** 615–620. ISSN: 10049541 (2011).

73. Chebbi, R., Qasim, M. & Abdel Jabbar, N. Optimization of triethylene glycol dehydration of natural gas. en. *Energy Reports* **5,** 723–732. ISSN: 23524847 (Nov. 2019).

74. Fang, S. *et al.* Photocatalytic $CO_2$ reduction. en. *Nature Reviews Methods Primers* **3,** 1–21. ISSN: 2662-8449 (Aug. 2023).

75. Zondervan, J. R. *et al.* Rock organic carbon oxidation $CO_2$ release offsets silicate weathering sink. en. *Nature* **623,** 329–333. ISSN: 1476-4687 (Nov. 2023).

76. Melo Bravo, P. & Debecker, D. P. Combining $CO_2$ capture and catalytic conversion to methane. *Waste Disposal & Sustainable Energy* **1,** 53–65. ISSN: 2524-7980 (2019).

77. Jakobsen, J., Roussanaly, S. & Anantharaman, R. A techno-economic case study of $CO_2$ capture, transport and storage chain from a cement plant in Norway. *J. Clean. Prod.* **144,** 523–539. ISSN: 0959-6526,1879-1786 (Feb. 2017).

78. Chiavazzo, E. Looking for massive carbon capture. en. *Nature Sustainability* **6,** 483–484. ISSN: 2398-9629 (May 2023).

79. Frei, M. S. *et al.* Atomic-scale engineering of indium oxide promotion by palladium for methanol production via $CO_2$ hydrogenation. en. *Nature Communications* **10,** 3377. ISSN: 2041-1723 (July 2019).

80. C.D'Angelo, S. *et al.* Environmental and economic potential of decentralised electrocatalytic ammonia synthesis powered by solar energy. en. *Energy & Environmental Science* **16,** 3314–3330 (2023).

*"It doesn't matter how beautiful your theory is, it doesn't matter how smart you are. If it doesn't agree with experiment, it's wrong."*

Richard Feynman



# 3

# TAMOF-1 as an Adsorbent for Carbon Capture: Preliminary Assessment for Post-Combustion $CO_2$ Removal

**Abstract** In this chapter, we provide a thorough analysis of the performance of TAMOF-1 in a continuous, steady-state adsorption process for $CO_2/N_2$ separation. TAMOF-1 demonstrates an exceptional ability to selectively capture $CO_2$ from a mixture of $CO_2$ and $N_2$, exhibiting high selectivity and remarkable adsorption uptake (up to 3.7 mmol $g^{-1}$ $CO_2$ at room T and P) across a wide range of concentrations. To assess the feasibility of the adsorption system in a continuous process, we have designed and analyzed an experimental vacuum swing adsorption (VSA) process. This performance evaluation aims to establish TAMOF-1 as a highly promising material for $CO_2$ capture, bridging the gap between effective adsorption and practical regeneration in real-world applications.

## Contents

# 3.1 Introduction.

Beyond pollution remediation and global warming mitigation, carbon dioxide capture (CC) holds vital significance in numerous fields[1,2]. The burning of fossil fuels for electricity generation, industrial processes, and transportation is the primary source of this excess $CO_2$ in the atmosphere[1,3]. As we explained before the Post-combustion carbon capture (PCC) is a pathway for technologies designed to capture carbon dioxide from the flue gas of power plants and/or industrial facilities. The goal of PCC is to reduce the amount of $CO_2$ released into the atmosphere and mitigate the effects of global warming.

Current technologies for $CO_2$ capture (CC) suffer from important limitations such as high energy consumption and/or poor $CO_2$ capture performance especially at low pressure[4–7]. The current technologies for CC at industrial level are:i) scrubbing (chemical and physical) ; ii) physisorption processes; iii) cryogenic separation; iv) partial distillation; and v) membrane separation. Chemical scrubbing (such as amine scrubbing), is considered by many the best and most mature technology for $CO_2$ removal[1,8–10]. This process involves selective chemical absorption of carbon dioxide. However, this technology has three major drawbacks i) high energy consumption for solvent regeneration due to the chemical nature of the interactions involved[11,12], ii) waste generation (solid salts and gaseous compounds due to chemical degradation of amines)[13], and iii) the large footprint which is techno-economically unviable, specially for small industrial facilites[14]. Another well-established industrial technology for gas separation is physisorption such as pressure swing adsorption (PSA), vacuum swing adsorption (VSA) or thermal swing adsorption (TSA)[15]. These processes involve at least two consecutive steps. In the first one, CO2 is selectively adsorbed by the active component at high/ambient pressure (PSA/VSA) and/or low temperature (TSA)[16]. In the following step, the adsorbent is regenerated by $CO_2$ desorption by pressure swing/vacuum (PSA/VSA) or/and at high temperature (TSA). Physisorption has advantages over chemical absorption because it typically demands lower energy consumption during the second (regeneration) step[17]. The combustion gas (flue gas) is produced at low pressure (close to the ambient pressure) and temperatures (180 – 255 $^{o}$C). The swing pressure process offers thus the most economically affordable option for upgrading avoiding the need of expensive components (such ad heat exchanger in the the of amines scribbing[15,18])

and depending of the adsorbent material reducing the operating expenditures (OPEX) and avoiding high operating pressure to achieve good process performance[5,19].

However, $CO_2$ capacity of physisorption technologies is limited. High adsorption pressures (> 4 bar) are needed to reach competitive performance when compared with chemical scrubbing[20]. Moreover, a complete and fast adsorbent regeneration usually requires heating[21]. Currently, the benchmark material for PSA-based CC is the molecular sieve 13X[22]. This commercially available zeolite has acceptable $CO_2$ adsorption capacity and selectivity. However, its regeneration requires high energy consumption, very similar to that needed for amine scrubbing[15,23]. Indeed, an efficient cyclic, continuous 13X-based process with good cost-effective capacity for reliable $CO_2$ gas removal requires high adsorption pressures (high $\Delta P$) and/or high desorption temperatures[24]. Even in these conditions, recovering high purity gases, as $CO_2$ (> 99%), with this technology remains a challenge, since $CO_2$ selectivity decreases at higher pressures. Carbon-based materials are another class of adsorbents offering the advantage of low cost and easy regeneration although they are limited by a low adsorption capacity and selectivity, especially at low pressures[5]. New materials combining competitive performance in selective $CO_2$ uptake, and release, are needed to realize widespread CC technologies. Demonstration at the industrial scale, and versatility to different gas stream features are additional key challenges towards CC market penetration[5,6,22,25].

Metal-organic frameworks (MOFs) have been proposed for $CO_2$ capture[19,26–28]. The most successful examples are based on selective chemisorption: excellent $CO_2$ capture performance, but with highly endothermic regeneration process, and uncertain chemical stability. MOF materials offering physisorption processes combining high $CO_2$ uptake and low energy consumption upon $CO_2$ release are just emerging[5,21]. Some of the most remarkable candidates include CALF-20[6], a Zn-based oxalate-bridged framework with high performance in $CO_2$ capture from flue gas, and an extraordinary robustness under humid conditions; or USTA-16[29], that is a MOF with K+ counterions as active sites ($K_2Co_3(cit)_2$, this material shows both high volumetric (160 $cm^3$ $cm^{-3}$) and gravimetric $CO_2$ capacities (4.2 mol $kg^{-1}$ at 1 bar and 298 K; 0.9 mol $kg^{-1}$ at 0.15 bar and 333 K). Along this line, our group has discovered a new material, TAMOF-1[30,31] (Figure 3.1), obtained from cheap and non critical raw materials by

reaction of a copper salt and a derivative of the natural amino acid L-histidine under soft-chemistry conditions, with good synthetic scalability. TAMOF-1 (triazole acid metal–organic framework) is a chiral MOF with high stability upon water and organic solvents and permanent porosity. It is formed by the coordination of copper(II) (as a metallic center) and (S)-3-(1H-imidazol-5-yl)2-(4H-1,2,4-triazol-4-yl)-propanoic acid (as an organic linker). Due to the presence of stereogenic centers in their linkers, TAMOF-1 can be used for the separation of certain chiral molecules[30]. Moreover, this material has a 3D network, made from 10 Å wide (Figure 3.1b), helicoidal, intercommunicated channels, decorated with multiple dangling functional groups carboxylate, triazole and imidazole (Figure 3.1a) exhibiting a BET specific surface area of 980±50 $m^2$ $g^{-1}$ , micropore volume of 0.38 $cm^3$ $g^{-1}$, ando also, permanent porosity towards humidity, acids and/or bases (Figure 3.1d). Table 3.1 shows a summary of crystal and physical properties of TAMOF-1. In a previous studies, was also reported the performance of TAMOF-1 as stationary phase for the chromatographic separation of racemic mixtures of organic substances thanks to its porosity and homochirality[30]. Moreover, the characteristic shape and size of its channels and pores, as well as the Cu metal center, make TAMOF-1 a good candidate for separating also a wide variety of volatile organic compounds such as benzene–cyclohexane system (cyclic compound reconnection), hexane isomers (degree of branching reconnection), and xylene isomers (positional isomers reconnection). Remarkably, separation of these molecules has been proved in both liquid and gas phase[31,32].

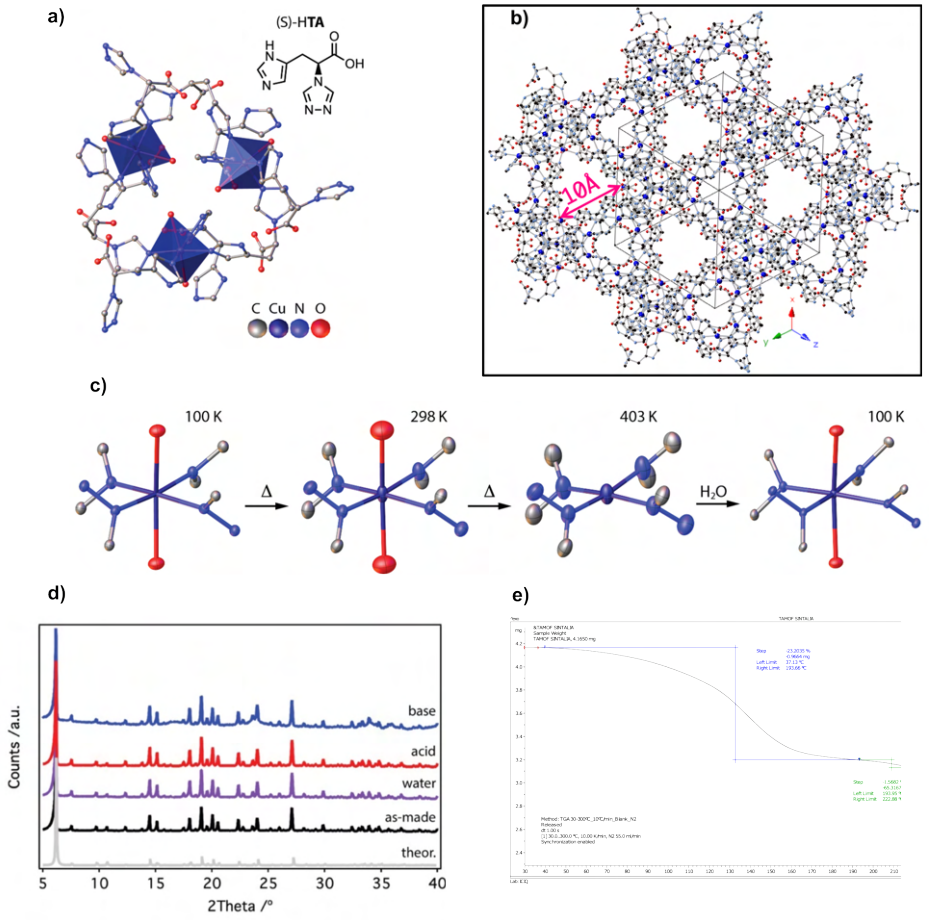


Figure 3.1: a) Structure of the linker L-2-deaza-2-(4H-1,2,4-triazol-4-yl)histidine (S-HTA) and projection of the crystal structure of TAMOF-1 on the [111] plane. b) Representation of crystal structure of TAMOF-1, showing the network of open 10 Å-wide channels. c) Thermal cycle for the coordination geometry of $Cu^{II}$ centers. Thermal ellipsoid plots at 3 Å from the metal crystallographic position at 100, 298, and 403 K (dehydrated state), and again at 100 K after rehydration by controlled addition of water. d) PXRDs of TAMOF-1 confirming structural integrity after incubation in water during 96 hours at neutral (purple), acid (red) and basic (blue) conditions. e) Thermogravimetric analysis in air for a TAMOF-1 powder sample. Figure was taken and adapted from Corella-Ochoa et al.[30].

The multi-kilogram scale production of TAMOF-1 has been demonstrated in powder form (particle size $< 10\mu m$); from common reagents and avoiding safety-related issues. Additionally, TAMOF-1 was also

Table 3.1: Summary of TAMOF-1 Crystal and physical properties.

| Formula | $[Cu(H_2O)_2(C_8H_8N_5O_2)_2]\cdot 6H_2O$ |
|---|---|
| molecular weight [g $mol^{-1}$] | 583.93 |
| crystal system | cubic |
| space group | $P4_3/32$ |
| susrface area BET [$m^2$ $g^{-1}$] | 980.5 |
| pore volume [cm3 $g^{-1}$] | 0.38 |
| framework density [g m-3] | 1.14 |
| particle size [$\mu m$] | 0.2-10 |
| crystal size [$mm^3$] | 0.05x0.05x0.03 |

pelletized using widely available, safe, and affordable materials (e.g., bentonite, and water). The resultant pellets (Figure 3.2) exhibited remarkable porosity, with a surface area of approximately 850 $m^2$ $g^{-1}$ and a micropore volume of 0.34 $cm^3$ $g^{-1}$, comparable to the powder form. Moreover, this pellets exibhist a mechanically stable and stress resistant (>10bar) bodies of spherical shape ($\approx$ 2.5–3.5 mm diameter).

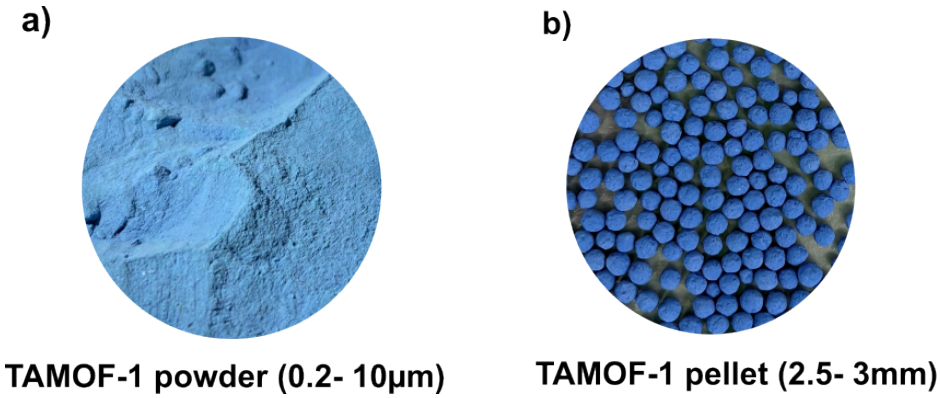


Figure 3.2: (a) Powder and (b) pelletized TAMOF-1.

In this study, we thoroughly characterized TAMOF-1 (in powder and pellet forms) as a selective $CO_2$ adsorbent for post-combustion capture from $CO_2/N_2$ gas mixtures. Adsorption isotherms reveal exceptional CO2 capacity and selectivity over a broad range of concentrations, temperatures, and pressures. Fixed-bed breakthrough experiments demonstrate TAMOF-1's ability to efficiently capture $CO_2$ from $N_2$ streams at dynamic conditions, even at low $CO_2$ con-

centrations. The weak interactions between $CO_2$ and TAMOF-1 result in rapid diffusion and efficient desorption, as evidenced by the nearly vertical breakthrough curves. This translates to a simple and energy-efficient regeneration process. Furthermore, TAMOF-1 exhibits durable dynamic adsorption/desorption performance, achieving high $CO_2$ purity and recovery in a VSA process. Benchmarking against other adsorbent demonstrates TAMOF-1's promising performance, particularly in terms of $CO_2$ capture recovery and productivity, which directly impact operational costs. Notably, the TAMOF-1 pellet outperforms the powder form in terms of regeneration efficiency. This study highlights TAMOF-1's potential to bridge the gap between effective adsorption and affordable regeneration. Its scalable synthesis (>10kg), robust material properties in and pellet form, and exceptional performance with combustion gas-type conditions make it a strong candidate for large-scale $CO_2$ capture applications.

## 3.2 Experimental section.

### 3.2.1 Chemical and Materials.

TAMOF-1, with molecular formula $[Cu(H_2O)_2(C_8H_8N_5O_2)_2]\cdot 6H_2O$, has been synthesized following the procedure described in a previous publication[30]. A complete crystal structure characterization can also be found therein, and is also described in table B.1. All reagents employed in the synthesis were of commercial grade and used without further purification. The bentonite ($Al_2O_3 \cdot 4SiO_3 \cdot H_2O$) used as a binder for MOF pellet formation was supplied by Sigma Aldrich. Molecular Sieve 13x and its pelletized form, with a chemical formula $Na_{86}[(AlO_2)_{86}(SiO_2)_{106}]\cdot xH_2O$, was also supplied by Sigma Aldrich.

### 3.2.2 Particle and bulk density.

The skeletal density of the TAMOF-1 particle (density of the particle without porosity) was determined by helium pycnometer measurements carried out on a Quantachrome micro Ultrapyc 1200e. Bulk density was measured as a function of adsorbent bed height, internal pipe diameter, and post-column packing.

### 3.2.3 Thermogravimetric analysis.

TAMOF-1 thermal stability up to 423–433 K has been confirmed by thermogravimetric analysis (TGA) performed using a TGA/SDTA851 Mettler.

### 3.2.4 Pellet synthesis.

The TAMOF-1 pellets were synthetized in a Caleva Multi Lab (CML) equipment. The synthesis of pellets involves several steps: weighing, mixing, homogenization, extrusion, spheronization, and drying. First, 0.19 g of TAMOF-1 and 2 g of Bentonite are weighed. These weighed materials are added to a mixer for 3 minutes at 60 rpm. Water is quickly added for approximately 20 seconds to ensure proper mixing with the bentonite and TAMOF-1 mixture. The wet mixture is then homogenized and is gradually added to the extruder at 80 rpm. The extruded material is transferred to a spheronizer and rotated at 1230 rpm for 3 minutes. Finally, the obtained pellets are dried at room temperature for 72 hours.

### 3.2.5 Adsorption isotherms.

Adsorption isotherms for $CO_2$ and $N_2$ were measured using an Autosorb iQ (Quantachrome) at 303 K and pressures up to 10 bar. Additionally, $CO_2$ adsorption isotherms were collected at various temperatures ranging from 303–333 K up to 1 bar. Before starting the analysis set, the sample is activated at 150$^{o}$C for 15h under vacuum ($10E^{-06}$ torr). As the sample is hygroscopic, a degassing is performed at 120$^{o}$C for 2 hours between each measurement step to eliminate traces of moisture by contact with air.

### 3.2.6 Dynamic fixed-bed column adsorption experiments.

**Gas separation module.**

In our breakthrough experiments, we maintained a ratio of bed height to column inner diameter (Hb/Di) between 3–4[12]. We used a 1-inch tube (1.95 cm inner diameter) as the separation module, with a bed height ranging from 5.3 to 5.8 cm. For larger-scale applications, the

diameter will depend on the gas velocity, and the height will be chosen to achieve a reasonable breakthrough time, pressure drop, and cost[33]. The TAMOF powder and its pelletized form were packed in the middle of the module to create a compact bed, while the remaining volume was filled with glass wool. The aim was to maintain a consistent bed length of 5.9 cm for both the TAMOF-1 powder and pellet samples. This was achieved by adjusting the packing of the materials. The amount of TAMOF-1 powder packed was 10.2 g (7.88 g dehydrated), while the amount of TAMOF-1 pellet packed was 10.8 g (8.8 g dehydrated). The column configuration packing are shown in Figure 3.3.

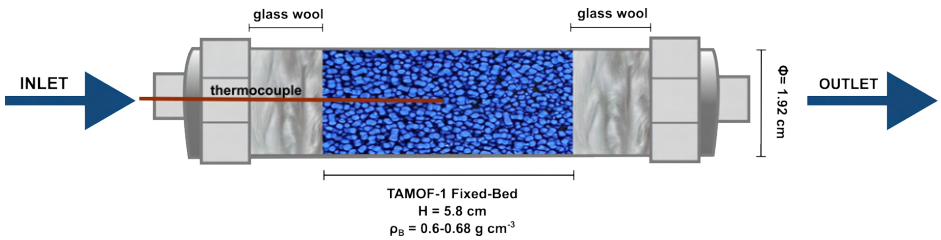


Figure 3.3: Column packing configuration for TAMOF-1 powder and pellet samples.

**Activation Procedure.**

Prior to each measurement, TAMOF-1 was activated in-situ at 393 K (1 K $min^{-1}$) to remove water. Two activation methods were tested. i) This method utilized a nitrogen ($N_2$) flow of 200–300 ml/min through the column, monitoring the water content in the outlet stream. ii) The second method placed the column under vacuum for 15 hours, monitoring the vacuum pressure, which reached a minimum of $10^{-2}$ mbar. These activation methods ensured the adequate dehydration of the TAMOF-1 material before each measurement, minimizing the influence of water on the experimental results. To assess the effectiveness of the activation, we tested the column with pure $CO_2$ gas after each activation procedure. The adsorption performance was evaluated using thermodynamic $CO_2$ adsorption values obtained from adsorption isotherms.

### 3.2.7 Set-up and Experimental conditions.

Breakthrough measures were performed by using the experimental set-up shown in Figure 3.4a. Gas cylinders of $N_2$ (Praxair, 99.999%), and $CO_2$ (Air Liquide, 99.998%) were used. The flows/compositions of the inlet gas stream were controlled upstream the separation module by a set of calibrated mass flow controllers (Bronkhorst EL-FLOW). A manometer and a backpressure controller (Bronkhorst, EL-PRESS) were placed downstream the separation module. A manometer was also used upstream the bed to monitor the actual pressure at the bed inlet under no pressure control conditions. Unless otherwise stated, all pressure values are reported in units of absolute bar (bar). Small inlet pressures were measured under no pressure control conditions (overall inlet flow between 30–250 NmL/min). In particular inlet pressures of 1.05–1.8 bar were measured depending on the CO2 saturation degree of the bed and the flow rate used. The separation module was heated by a linear power silicone heating wire (Ø 3mm FOR-FLEX NORMAL, Electricfor) rolled around the column, the temperature was measured with a K-type thermocouple (Thermocoax) inserted in the middle of the bed, and it was controlled with a temperature controller EZ-Zone (Watlow). The outlet stream of the column was on-line analyzed by micro gas chromatograph (MGC, Agilent MicroGC 490) equipped with Molsieve MS5A, using Ar as carrier gas (99.999 % purity), and Poraplot U column, using He as carrier gas (99.999 % purity), along with thermal conductivity detectors (TCD). In the experiments conducted, a partial flow of N2 in the inlet gas mixture was maintained below 25 NmL/min. Additionally, during column activation with pure $CO_2$, a nitrogen flow of 30 NmL/min was blended with the gas exiting the separation module to meet the flow requirements of the gas chromatograph (GC). A non-return valve with minimal pressure drop was employed to prevent reverse flow. The transit time or death time of the gas in the set-up was also evaluated and subtracted at each operation condition.

All experiments were conducted at 1 bar and 25$^{o}$C under initial gas conditions. However, the operating pressure is based on the system pressure drop. The gas outlet concentration was registered, and the equilibrium was reached, indicated by a concentration comparable to the initial set concentration (adsorbent saturation).

**Breakthrough experiments (BT) linked with regeneration.**

Prior to regeneration analysis, initial breakthrough (BT) experiments were conducted using $CO_2$ concentrations of 6%, 15%, and 30% (balance $N_2$) at a total flow rate of 30 ml/min. Each BT experiment utilized a fully regenerated column, achieved by purging with $N_2$ at 250 ml/min for 15 hours at 120°C (initial activation procedure).

**Breakthrough experiments (BT) for the Oxygen effect.**

To investigate the effect of oxygen on CO2 recovery and purity, the initial breakthrough (BT) experiment was conducted using an inlet gas mixture containing 6% $CO_2$, 84% $N_2$, and 10% $O_2$.

**Breakthrough experiments with different gas velocities.**

These experiments utilized a column activated by the second method. Prior to each BT experiment, the column was purged with $N_2$ at 100 ml/min for 2 hours at 80°C to ensure removal of residual gases. Subsequently, 30 ml /min of He was flowed through, and the gas concentration was recorded to verify complete column cleanliness (no $CO_2$ detection and $N_2$ concentration consistent with baseline). The column was then isolated. In this experimental study, three distinct total gas flow rates were employed: 86 ± 1 ml/min, 177 ± 2 ml/min, and 269 ± 1 ml/min. These flow rates corresponded to gas velocities of 0.005, 0.010, and 0.015 m/s, respectively. The primary objective of these experiments was to attain a target concentration of 6% $CO_2$(He balance). Additionally, each experiment was conducted at varying temperatures (25–80 °C) and pressures (1–5 bar) for different gas velocities.

### 3.2.8 Regeneration.

The regeneration of TAMOF-1 powder after saturation was investigated under varying vacuum hold times. We aimed to maintain identical temperature conditions as those used in the breakthrough experiments (isothermal). However, a decrease in temperature was observed due to the vacuum application. This regeneration study was conducted for the three inlet gas compositions used in the BT experiments 3.2.7: 6%, 15%, and 30% $CO_2$ ($N_2$ balance). Additionally, regeneration was evaluated for activation type 2 using only 6%

$CO_2$, and the same experiment was repeated with TAMOF-1 pellets.

**Determining the equal Breakthrough and cleaning time.**

Following saturation (Step 1), TAMOF-1 was regenerated by applying a vacuum (Step 2) from the column bottom for a duration equal to the previously measured breakthrough time, the steps are shown in Figure 1b and 1c, respectively. This regeneration-saturation cycle (Steps 1–2) was repeated until the breakthrough time in Step 1 became equivalent to the vacuum regeneration time in Step 2 in the last three measures. The $CO_2$ and $N_2$ concentrations in Step 1 were continuously monitored with the GC.



**Determining the amount of $CO_2$ desorbed at different vacuum times.**

The regeneration process involved a two-step cycle repeated until a steady state was achieved. In Step 1 (saturation), the module was saturated by flowing the inlet gas mixture through the TAMOF-1 separation column. Step 2 involved applying a vacuum for a predetermined duration. This cycle (Steps 1-2) was repeated until the amount of $CO_2$ desorbed during the last three measurements showed minimal change in the $CO_2$ desorbed amount, indicating a steady state. The vacuum hold time used was 0.08, 0.5, 2, 10, and 30 minutes. In some cases, the latter times change depending on the previously measured breakthrough times (BT) to match them. Additionally, a regeneration cycle with a vacuum hold time equal to the final BT was performed. The amount of $CO_2$ desorbed by the vacuum is determined by integrating the concentration-time curve obtained during Step 1 using equation 1.26. Integration is performed until the saturation point is reached.

**Determining the N2 remaining inside the column.**

To quantify the final $CO_2$ purity achievable during TAMOF-1 column regeneration, the amount of residual nitrogen ($N_2$) inside the column was measured. This procedure was performed after the final regeneration cycle (Steps 1–2) using an insulated module. The measure analysis began with cleaning the inlet gas line; pure $CO_2$ flowed through the line at a 130ml/min flow rate until the entire line, including the bypass, reached a pressure slightly above atmospheric

(e.g., 1.1 bar). The gas supply was then closed, followed by a vacuum applied to the line for 3 minutes. This cleaning step with $CO_2$ purge was repeated three times to ensure the thorough removal of any gas line contaminants. Next, the gas collection cylinder was attached to the top of the column and evacuated for 2 minutes to remove air. $CO_2$ gas then flowed through the column at a 30 ml/min flow rate with the cylinder inlet valve open to collect the desorbed gas (Figure 1d). Once the cylinder pressure reached a 1.2 bar, the inlet gas flow was stopped, and the cylinder was isolated from the column. The cylinder was then connected to the micro-GC gas inlet line (Figure 1e). The gas inlet line was then evacuated for 3 minutes with the cylinder closed. Gas sample analysis starts immediately after closing the GC vacuum and opening the cylinder valve. This measurement cycle (involving collection and micro-GC analysis) was repeated until the $N_2$ concentration in the collected gas matched the baseline level established earlier.

### 3.2.9 Baseline of the $N_2$ concentration.

To assess the purity of the regenerated $CO_2$, the inherent $N_2$ concentration in the gas chromatograph (GC) baseline, resulting from air intake in the GC line, was used. The TAMOF-1 column was initially saturated with 30 Nml/min $CO_2$ flow rate and then isolated. A gas collection cylinder was attached to the column top and evacuated for 3 minutes. Subsequently, $CO_2$ gas was flowed through the column into the cylinder until reaching 1.2 bar gauge pressure, at which point the gas lines were closed. The GC inlet line was then evacuated for 3 minutes with the cylinder closed. Gas concentration analysis commenced immediately upon closing the GC vacuum line and opening the cylinder valve. This process was iterated until the last three baseline concentration values exhibited less than 5% deviation.

#### Experimental cyclic design and Key performance indicators (KPI) determination.

The $CO_2$ adsorption evaluation cycle, based on the experimental steps detailed in sections 3.2.8, 3.2.8, and 3.2.8, and also schematized in the Figure 3.4, was designed to assess both $CO_2$ purity and recovery. This four-step cycle mirrors the classic Pressure Swing Adsorption (PSA)/Vacuum Swing Adsorption (VSA) process[34,35]. The cy-

cle comprises the following steps: (a) Pressurization: The column is pressurized with feed gas to 1.15 bar (determined by column pressure drop). (b) Adsorption: As described in section 3.2.8 (Figure 3.4b), $CO_2$ is preferentially adsorbed by TAMOF-1. The $CO_2$ adsorption capacity ($Qad_{CO2}$) is determined by integrating the breakthrough curve (up to 0.01 C/Co). The breakthrough time should be the same as regeneration time. (c) Blow-down: Column pressure is reduced to vent non-selective components ($N_2$). Optimizing this step can increase $CO_2$ purity at the expense of $CO_2$ recovery. Experimental data from sections 3.2.8, and 3.2.8 allows for quantification of $CO_2$ and $N_2$ loss during blow-down step, which is crucial for calculating recovery and purity. (d) Recovery: Vacuum is applied to the column (Figure 3.4c) to desorb captured $CO_2$ and residual $N_2$ inside the column. Desorbed $CO_2$ is quantified by integrating the breakthrough curve up to saturation (eq. 1.26). This data, combined with adsorption data, enables evaluation of $CO_2$ recovery efficiency and final product purity. $CO_2$ recovery and purity can be calculated using equations 3.1 and 3.2, respectively, considering $CO_2$ desorbed per vacuum regeneration time and residual $N_2$ in the column. This cycle design facilitates a comprehensive assessment of $CO_2$ capture performance, informing the optimization of both recovery and purity.

$$CO_2 recovery = \frac{Qad_{CO2} - Qde_{CO2}(blow_i)}{Qad_{CO2}} \times 100 \tag{3.1}$$

$$CO_2 purity = \frac{Qad_{CO2} - Qdes_{CO2}(blow_i)}{Qad_{CO2} - Qdes_{CO2}(blow_i) + Qdes_{N2}(blow_i)} \times 100 \tag{3.2}$$

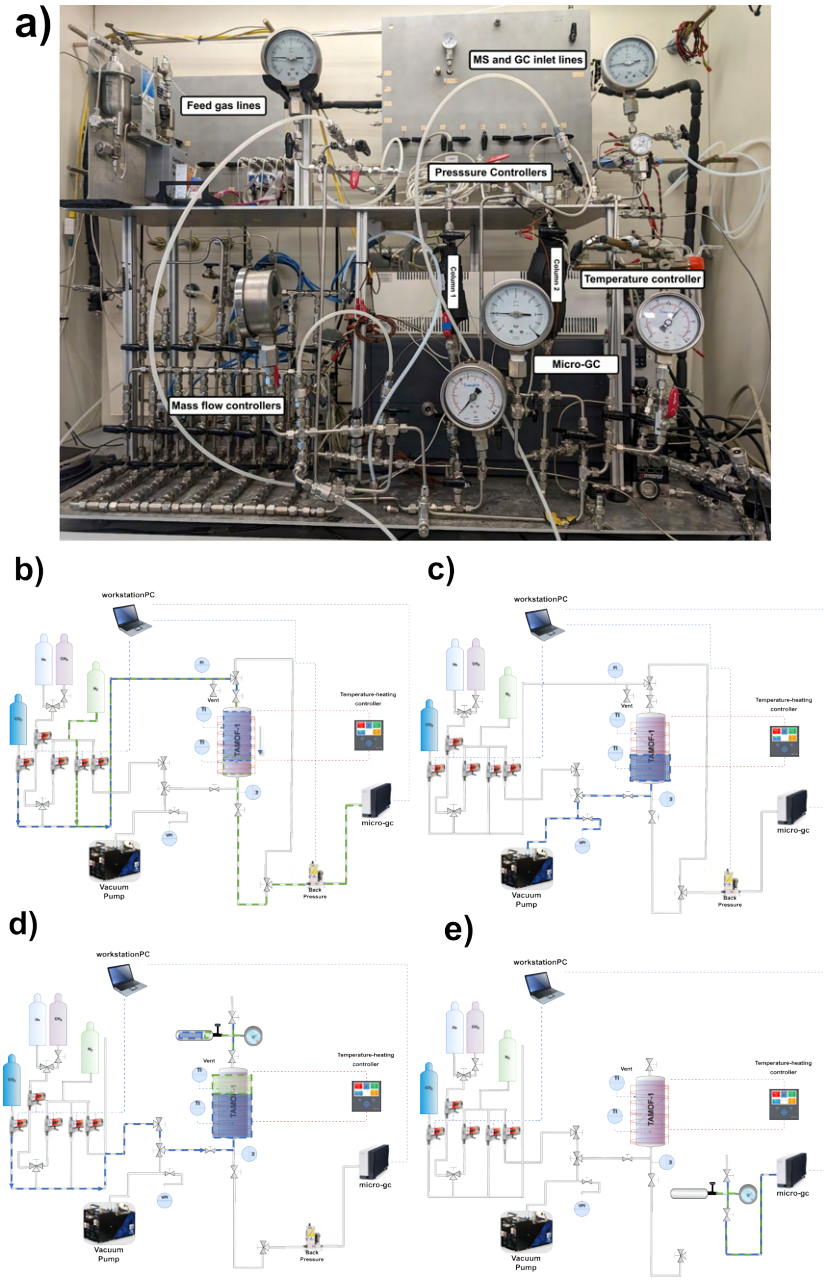


Figure 3.4: Experimental set-up for breakthrough experiments. (a) Photograph of the entire experimental set-up. (b-e) Schematic illustrations of the process: (b) Adsorption, (c) Regeneration of the adsorbent, (d) Recollection the $N_2$ remaining in the adsorbent, and (e) measurement of the $N_2$ concentration inside the gas sample cylinder.

## 3.3 Modeling.

This section focuses on fitting isotherms and breakthrough curves to understand the interaction of the adsorbent with $CO_2$ and $N_2$. Isotherm fitting elucidates the equilibrium behavior of the adsorbent with both gases, while breakthrough curve fitting estimates the kinetics of the selective gas ($CO_2$) with TAMOF-1. All model parameters were optimized to best match the experimental data obtained in the laboratory.

### 3.3.1 Adsorption isotherm modeling.

The adsorption isotherms of $CO_2$ and $N_2$ at 25$^{o}$C up to 1 bar were fitted with four models: Langmuir (single-site), Freundlich, Sips, and Langmuir-Freundlich (Dual-Site). The corresponding equations (1.9, 1.10, 1.11, and 1.12, respectively) are described in section 1.5.2. This fitting aimed to identify the best-fitted model and estimate the isosteric enthalpy of adsorption ($\Delta Hads$), as described in section 1.5.2.

The Freundlich isotherm is an empirical relationship derived from experimental isotherm data. Acknowledging the unphysical behavior of the Freundlich isotherm near saturation, Sips[36,37] proposed a more generalized form (eq. 1.11). Moreover, the Langmuir-Freundlich (Sips) model is a simple model that effectively reproduces the equilibrium adsorption behavior of TAMOF-1. We used this model to fit the experimental isotherm data at low $CO_2$ partial pressures (0–1 bar) and high pressures (1–10 bar).

### 3.3.2 Breakthrough curve modeling.

To formulate a breakthrough curve for this system, a mathematical model was applied based on the following assumptions: (1) The flow pattern is described by the axially dispersed plug flow model. (2) The system operates under isothermal conditions. (3) The frictional pressure drop through the column is negligible. (4)The adsorption equilibrium isotherm is described by the Sips isotherm. (5) The adsorbent particles are spherical, homogeneous in size, and have a uniform density. (6) The velocity of the gas is constant. (7) The driving force is the concentration gradient of the adsorbed phase. (8) The diffusion coefficient is constant. Additionally, the experimental data used for the fitting of the breakthrough curves are shown in Table

B.4. Under these assumptions, a set of governing scaled equations was derived, as described in section 1.5.3.

The energy balance equation (Eq. 1.24) is not applied in the modeling of the fixed-bed system with TAMOF-1, assuming isothermal conditions. The Sips isotherm model (Eq. 1.11) is utilized to correct the un-physical behavior of the Freundlich isotherm and fit the experimental data. The commonly used $C^{1/n}$ term corresponds to an adsorption term proportional to $C^m(qm-q)$ (Eq. 1.19), which can be expressed in the form $C^m(qm-q)^n$, where C is the concentration, and, m and n represent the partial order of the chemical reaction. However, it is the ratio m/n that determines the isotherm shape. Therefore, we keep the single parameter model[36,38]. In the limit $KC^m << 1$, the Freundlich relation is retrieved, while for m = 1, the Sips model reproduces the Langmuir isotherm. Due to the difficulty of analysis nonlinear equations it is common to study a linear approximation of Eq. 3.3. A linear adsorption equation is obtained by placing the Langmuir isotherm into a linear kinetic relation (Eq. 1.19). Consequently, the equations used to reproduce the sink term and isotherm (Eqs.1.19 and 1.11) were modified to Eqs. 3.3 and 3.4, respectively. Trying to keep the simplicity in the model with a single term, and adding a robust one that can reproduce the TAMOF-1 adsorption rate.

$$\frac{\partial q}{\partial t} = K_a C^m (q_m - q) - K_d q^n \tag{3.3}$$

$$q_e = \frac{q_m K^{1/n} C^{m/n}}{1 + K^{1/n} C^{m/n}} \tag{3.4}$$

Where $q_e$ refers to the equilibrium adsorbed amount at a given concentration, $q_m$ is the maximum adsorbed amount, $K$ is the equilibrium constant, $K_a$ and $K_d$ are the adsorption and desorption rate constants, respectively, and $m$ and $n$ are the Sips isotherm parameters.

The mass balance described by the equation 1.18 in conjunction with the equation described above was solved numerically using the ordinary finite difference equations (ODE) method using MATLAB solver. The model parameters were optimized to best fit the experimental breakthrough data obtained in the laboratory.

# 3.4 Results and discussion.

## 3.4.1 Adsorption isotherms.

**TAMOF-1 powder.** Single gas ($CO_2$, and $N_2$) adsorption isotherms of TAMOF-1 powder up to 10 bars were measured in the 293–353 K temperature range (Figure 3.5a). As a function of temperature, all isotherms maintain their characteristic shapes, with gas uptake increasing as the temperature decreases. Type I isotherms are obtained for $CO_2$, without reaching a plateau (saturation) in the investigated pressure range. In example at 293K, $CO_2$ adsorption capacity of 4.2 mmol $g^{-1}$ and 6.7 mmol $g^{-1}$ are obtained at 1 and 10 bars, respectively. Linear isotherms are obtained for $N_2$, indicating selective preferential uptake of carbon dioxide with respect to nitrogen. The BET surface area calculated from the $N_2$ isotherm at 77 K was 980 m2 $g^{-1}$. From the different adsorption models available (See section 1.5.2), the dual-site Langmuir-Freundlich model shows the best fitting for the $CO_2$ adsorption isotherms (Figures B.1).

See, for instance, the comparison with Langmuir-Freundlich (Sips) model at different range concentrations (Figure B.2). This indicates that at least two different adsorption sites are responsible for dominant $CO_2$ uptake. Tables B.2 and B.3 show the isotherm parameters and regression coefficients. In figure 3.5c shows the CO2/N2 selectivity calculated by the ideal adsorption solution theory (IAST). This calculated selectivity at 1 bar and 298K was 205, 160, and 135 for a 6:94, 15:85, and 30:70 $CO_2/N_2$ mixture, respectively. Moreover, the IAST plot reveals a decreasing trend in selectivity with increasing partial gas pressure (concentration). This behavior suggests that TAMOF-1 is more capable of resolving the separation of $CO_2/N_2$ at lower partial gas pressures. This is in contrast to common materials where obtaining good selectivity at low $CO_2$ concentrations is often challenging. The change in the curve's shape, characterized by increasing slightly selectivity at high concentrations, indicates that $CO_2$ molecules at high concentrations can access more active sites within the TAMOF-1 framework compared to lower concentrations. This observation provides brief insights into the material's adsorption behavior and its potential for efficient $CO_2/N_2$ separation under varying gas partial pressure conditions (concentrations). Another important remark is the complete adsorption/desorption reversibility obtained for all the gases (figure 3.5a) with no hysteresis observed. This behav-

ior aligns with the physical nature of the gas adsorption phenomena within TAMOF-1 network and underscore the structural rigidity of this material. The isosteric enthalpy of adsorption, $\Delta H_{ads}$ was estimated via an indirect approach from the $CO_2$ adsorption isotherms at the different temperatures using the Clausius-Clapeyron equation (eq. 1.14). The zero- loading heat of adsorption for $CO_2$ was –39 kJ $mol^1$. Figure 3.5b shows the evolution of $-\Delta H_{ads}$ with $CO_2$ uptake. A high $-\Delta H_{ads}$ is found at low pressure (zero coverage, $-\Delta H_{0ads=0}$), and then it rapidly decreases as $CO_2$ uptake increases, approaching the bulk-phase sublimation heat of $CO_2$, 25–27 kJ $mol^{-1}$, at adsorption capacity higher than 2 mmol $g^{-1}$. This energy range points to a physical gas adsorption process, and denotes a heterogeneous adsorption process occurring at multiple adsorption sites with different surface energies. This typical physisorption behavior prove the capability of these MOF to resolve $CO_2/N_2$ mixtures in a wide pressure and temperature range, with low energy need to regenerate the material from $CO_2$ in the initial adsorption sites.

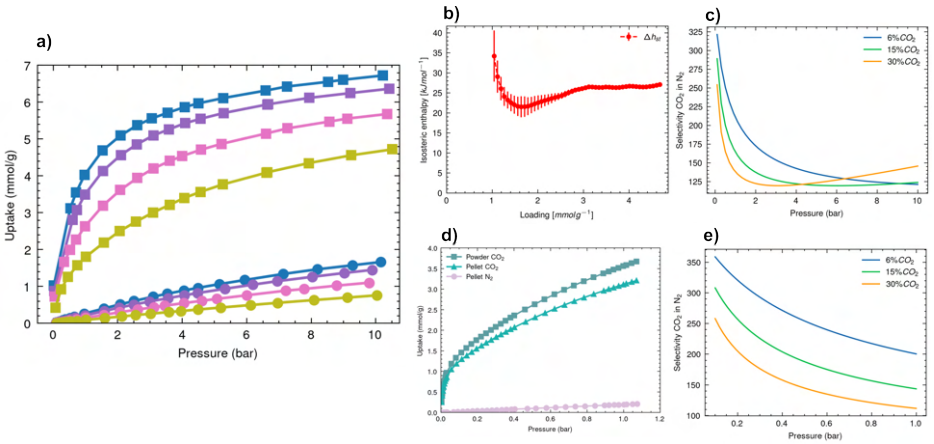


Figure 3.5: Isotherms of TAMOF-1 for $CO_2$ and $N_2$. TAMOF-1 powder: (a)Singles gas $CO_2$ (squares) and $N_2$ (points) adsorption isotherms at temperature range 293K–353K up to 10 bar. (b) Heat of adsorption ($\Delta H_a ds$) calculated as a function of $CO_2$ uptake. (c) IAST selectivity of $CO_2/N_2$ mixtures at 303 K up to 10 bar. TAMOF-1 pellet: (d) Single gas $CO_2$ adsorption isotherms of TAMOF-1 pellets and powder at 303K and 1 bar. (e) IAST selectivity of $CO_2/N_2$ mixtures at 303K up to 1 bar.

**TAMOF-1 pellet.** TAMOF-1 pelletized readily with 12% bentonite retained an expected high BET surface are up to 850 $m^3 g^{-1}$. As shown in Figure 3.5d, TAMOF-1 pellets also exhibited a high

equilibrium $CO_2$ adsorption capacity of 3.2 mmol $g^{-1}$ at 303 K and 1 bar, representing an 11% reduction compared to TAMOF-1 powder (3.6 mmol g-1) at same conditions. Moreover, Figure 3.5e reveals an IAST selectivity trend similar between powder and pellet TAMOF-1. With a selectivity values calculated at 1 bar and 298 K: 200, 143, and 111 for a 6:94, 15:85, and 30:70 $CO_2/N_2$ mixture, respectively.

**Sips fitting aproximation of the adsorption isotherms.**

The Sips equation (Langmuir-Freundlich approximation), detailed in equations 3.3 and 3.4, effectively describes adsorption equilibrium in both isotherms and breakthrough curves[36,38,39]. While the dual-site Langmuir-Freundlich model offers a thermodynamically sound fit with acceptable physical parameters, its complexity hinders incorporation into breakthrough curve modeling. Conversely, the single-site Langmuir model, favored for its simplicity, fails to accurately represent TAMOF-1 equilibrium behavior, particularly at low partial pressures (<10%) relevant to the performed breakthrough curves (Figure B.2). To address this, the Sips model emerges as a suitable alternative, correcting the non-physical behavior of the Freundlich equation while maintaining a simpler form[36,39]. Adaptation of this model, specifically in the reaction degrees (m and n) of $CO_2$ with TAMOF-1 active sites, is necessary. Figure B.2 illustrates how varying m and n influence the model's fit to experimental data. At low $CO_2$ partial pressures, n=2 and m=1 provide the best fit, suggesting different active site accessibility compared to high $CO_2$ partial pressures where n=3 and m=2 are optimal. Selecting n=2 and m=1 for low concentrations yields a qm value of approximately 9, representing the theoretical maximum adsorption capacity of TAMOF-1 under ideal conditions. This finding underscores the need for a nuanced model that captures the complex adsorption behavior of TAMOF-1 across varying $CO_2$ concentrations. Additionally, also supporting on the isosteric heat curve (Figure 3.5b), it is evident that TAMOF-1 possesses at least two distinct active sites for $CO_2$ adsorption. At high $CO_2$ concentrations, the evolved heat is less than 30 kJ/mol, indicating that this fraction of $CO_2$ is weakly bound and easily released. In contrast, the more strongly bound $CO_2$, which is challenging to remove, is likely anchored to the Cu(II) ions within the framework. According to the Sips isotherm modeling, we propose that each $CO_2$ molecule interacts with two Cu(II) centers, and each Cu(II) can bind

up to two $CO_2$ molecules. Thus, the approximate relationship at higher $CO_2$ partial pressures, the strongly bound $CO_2$ species can be represented as $(CO_2)_2Cu_3$ ($2CO_2$ molecules bind with 3 Coppers).



### 3.4.2 TAMOF-1 Adsorption/Desorption (Regeneration) Measurements: First Activation

To gain insights into the performance of TAMOF-1 powder as an adsorbent capable of not only adsorbing but also regenerating (cleaning from $CO_2$) easily under various operating conditions, a comprehensive regeneration study was conducted. As previously mentioned, these studies were carried out with activation type 1 (cleaning with $N_2$). Vacuum regeneration was selected to simulate a pressure swing physisorption process (VSA/PSA), which is widely employed in industry. This approach aimed to assess the suitability of TAMOF-1 for such processes.

**Breakthrough measures.**

In figure 3.6a we report nitrogen/carbon dioxide breakthrough curves through a TAMOF-1 powder bed after activation at 1 bar and 298 K at different $CO_2/N_2$ ratios. Gas separation parameters obtained from the breakthrough curves are reported in Table S19 (See SI for details). Pure $N_2$ ($\geq$ 99.9%) elutes first and speedily from the bed. Regular S-shaped curves were instead observed for $CO_2$. Effective $CO_2/N_2$ separation is achieved in all cases as $CO_2$ is sensibly delayed. This confirms slower $CO_2$ diffusion through the TAMOF-1 bed. By reducing $CO_2$ molar flow, the related curves shift towards higher breakthrough times (BTt). Bt($CO_2$) increases from 1.84 to 6.5 min $g^{-1}$ when $CO_2/N_2$ ratio is reduced from 30:70 to 6:94. In contrast, BT($N_2$) point is almost constant, independent of the $CO_2$ fraction. This can be attributed to the extremely fast $N_2$ elution which makes differentiation and measuring experimentally difficult. The adsorption capacities at saturation ($q_s$) and breakthrough point ($q_b$) of carbon dioxide and nitrogen were evaluated. The qb($CO_2$) were 0.57, 0.62, and 0.67 for $CO_2/N_2$ ratios of 6:94, 15:85, and 30:70, respectively. At the saturation point, the capacity increased approximately 1.38 times the breakthrough capacity, with $q_s(CO_2)$ values of 0.79, 0.86, and 0.92 for each $CO_2$ concentration increment. Moreover, the breakthrough time followed the expected trend[40], with the longest

BTt($CO_2$) of 7.3 min $g^{-1}$ observed for the 6% CO2 concentration. As the gas concentration increased, the BT time decreased, reaching a value of 1.84 min $g^{-1}$ for 30% $CO_2$. Nitrogen showed non or minimal interaction in all three concentration cases, and the BT($N_2$) point could not be detected precisely with the micro-GC (not even with the mass spectrometer). Therefore, the selectivity ($S_b(CO_2/N_2)$), particularly at the BT point, could not be determined. However, the selectivity at saturation ($S_S$), though not entirely realistic, was estimated to be 123.7, 48.7, and 25.9 for 6:94, 15:85, and 30:70 $CO_2/N_2$ rations, respectively. The selectivity increased as the $CO_2/N_2$ ratio in the feed gas mixture decreased, exhibiting similar behavior to the ideal selectivity evaluated from the single-gas adsorption isotherms (Figure 3.5c,e). TAMOF-1 demonstrated an enhanced ability to separate $CO_2/N_2$ mixtures more easily and selectively at $CO_2$-dilute concentrations.

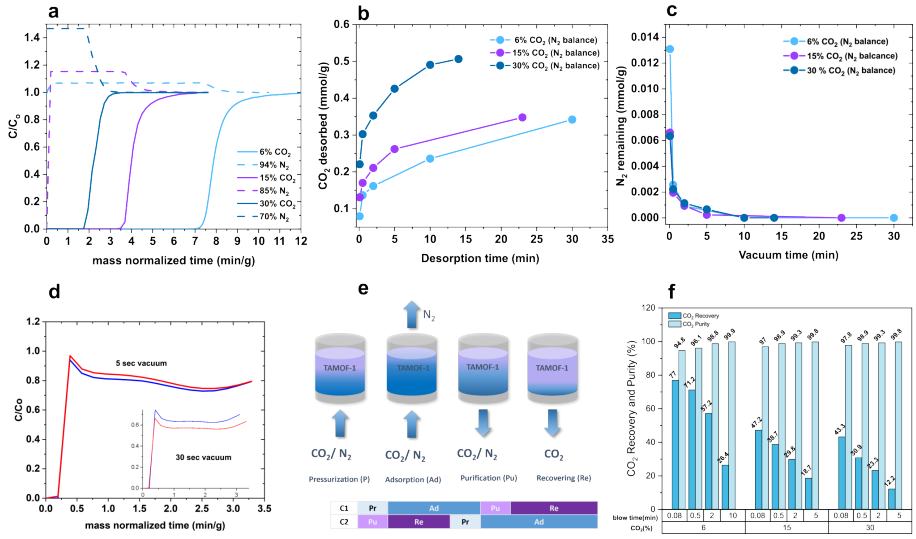


Figure 3.6: Regeneration study in TAMOF-1: (a) BT measures at different $CO_2$ gas concentrations (6,15, and 30%) at 25ºC and 1bar. (b) $CO_2$ desorbed in function of vacuum cleaning time. (c) $N_2$ remaining inside the column in the function of the vacuum cleaning time. (d) Influence of $O_2$ in $CO_2$ desorption and $N_2$ remaining inside the column. (e) Column configuration for cycle analysis. (f) Key performance indicators ($CO_2$ recovery and purity) at different gas mixtures ratios and blow-down times.

**Adsorption/desorption measures.**



The regeneration study aimed to evaluate the amount of $CO_2$ desorbed at different vacuum times and determine the remaining trapped $N_2$ in the column after vacuum cleaning. As shown in Figures 3.6b and c, the $CO_2$ concentration increase corresponds to a higher $CO_2$ adsorption on TAMOF-1. At higher partial pressures, more $CO_2$ is desorbed within the same vacuum time interval. Notably, 30 seconds of vacuum cleaning desorbed 0.08 mmol $g^{-1}$ of $CO_2$ at a ratio of $6CO_2$:$94N_2$, while decreasing this ratio to $30CO_2$:$70N_2$ led to a higher $CO_2$ desorption of 0.22 mmol $g^{-1}$. The desorption kinetics of CO2 exhibit an inverse exponential pattern, characterized by a steeper slope at higher $CO_2$ concentrations. This observation suggests that $CO_2$ desorbs more rapidly as the concentration of $CO_2$ increases, indicating a concentration-dependent desorption process. This phenomenon can be attributed to the competition between $CO_2$ molecules for available desorption sites, leading to faster desorption at higher $CO_2$ concentrations. However, considering high-purity $CO_2$ co-filtration at high CO2 partial pressures, the amount of recovered CO2 may be reduced, potentially affecting the efficiency of the $CO_2$ capture process. The maximum vacuum cleaning time was determined based on achieving an equivalence between adsorption time (at the breakthrough point) and regeneration time (vacuum cleaning). Figure 3.6b illustrates also, that lower $CO_2$ concentrations result in longer equivalence times between adsorption and desorption. The corresponding times for 6:94, 15:85, and 30:70 $CO_2/N_2$ ratios were 30, 23, and 14 minutes, respectively. The residual $N_2$ in the column (Figure 3.6c) appears to be released rapidly, irrespective of the gas fraction used in the adsorption step. The curves depicting the amount of $N_2$ remaining in the column as a function of applied vacuum time exhibit similar behavior and magnitude. Approximately 0.002 mmol $g^{-1}$ of $N_2$ remains in the column after only 30 seconds, and it is almost entirely eliminated after 5 minutes of vacuum cleaning. This suggests that the extremely weak interaction between $N_2$ and the framework allows for its straightforward removal from TAMOF-1, which does not pose a challenge. In contrast, $CO_2$ could present difficulties in terms of recovery (as previously mentioned) if it is not recirculated, given its facile elimination within a certain range.

**Effect of the Oxigen in the $CO_2$ recovery and purity.**

In combustion gas streams, excess $O_2$ added to ensure proper combustion, exits as an eluent in the stack off-gasses[41–43]. To evaluate its influence on both $CO_2$ desorption and $N_2$ retention in the column, the same procedure performed for the binary mixture of 6CO2:94N2 was repeated for $6CO_2$:$10O_2$:$84N_2$. The mixture with the lowest $CO_2$ concentration was chosen, as we hypothesized that $N_2$ would be the most competitive gas, especially in hindering $CO_2$ elimination. Figure 1d shows the adsorption step (step 1) after 5 and 30 seconds of vacuum cleaning (step 2). The desorbed $CO_2$ appears unaffected by the added $O_2$ concentration, with a slight increase of 7% at 30 seconds. However, the amount of $N_2$ remaining in the column is lower in the presence of $O_2$, with differences of 0.0035 and 0.00054 mmol $g^{-1}$ at 5 and 30 seconds, respectively. This suggests that $N_2$ exits quickly in both cases, indicating that the presence of $O_2$ does not affect the extremely low interaction of $N_2$ in TAMOF-1. Therefore, the analyses were performed with binary mixtures, consistent with the theoretical literature, where most studies focus on binary $CO_2/N_2$ mixtures due to their greater difficulty of separation, especially at low $CO_2$ concentrations[8,22,44,45].

**VSA Cycle key performance inficators anaylisis.**

The vacuum swing adsorption (VSA) cycle, utilizing a single laboratory column and extrapolated to a two-column continuous process, is illustrated in Figure 3.6e (detailed in section 3.2.9). Figure 3.6f demonstrates the relationship between $CO_2$ recovery, purity, blow-down time, and inlet gas partial pressure. Experimental data reveal that shorter blow-down times are required for high $CO_2$ purity as $CO_2/N_2$ ratio in gas inlet mixture increases. Specifically, achieving >99.9% $CO_2$ purity necessitates at least 10 minutes for a $6CO_2$:$94N_2$ inlet ratio, whereas 5 minutes suffice for both 15:85 and 30:70 ratios. To meet carbon capture and storage (CCS) requirements (minimum 95% $CO_2$ purity, 110 bar, 30°C), a 5-second blow-down appears optimal across all tested inlet gas ratios. This shorter duration, however, leads to lower $CO_2$ recovery rates: 77%, 47%, and 43% for 6:94, 15:85, and 30:70 $CO_2/N_2$ ratios respectively. While a 99.9% $CO_2$ purity could enhance $CO_2$ valorization in specific markets (e.g., food), it significantly compromises recovery rates (27%, 19%, and 13% for the respective ratios). This trade-off highlights the importance of balanc-

ing purity and recovery objectives. The ease with which TAMOF-1 releases $CO_2$ contributes to lower $CO_2$ recovery at longer blow-down times. To improve overall capture efficiency, recirculation of a portion of the $CO_2$ removed during blow-down is recommended. These findings underscore the need for further optimization to enhance $CO_2$ recovery while maintaining acceptable purity levels, especially at lower $CO_2$ concentrations in the inlet gas.



### 3.4.3 Activation of TAMOF-1.

To obtain the highest adsorption capacity of $CO_2$ for TAMOF-1, the activation process is a critical step that needs to be carried out before its use. Before each adsorption isotherm measurement, a dehydration step is performed at 150°C and 10-6 torr to prevent exceeding the degradation temperature of TAMOF-1, which is above 200°C. This procedure is a standard protocol successfully employed with this material, as reported in the literature[30,31]. In contrast, we followed the first activation method (section 3.2.6) for the dynamic experiments in the packed bed column. i) With this activation method at 393 K (1 $K \cdot min^{-1}$) using 200 $NmL \cdot min^{-1}$ of $N_2$ flowrate for 15 hours in 10g of TAMOF-1 (hydrated) bed column. Notably, after only 3 hours, no water could be detected in the micro-GC connected online to measure the water concentration. This observation provided initial evidence suggesting that the activation was successful, prompting us to experiment using this activation method. However, following the completion of the TAMOF-1 regeneration study described in section 3.2.8, 3.2.7, 3.2.7, (performed with the first activation method), we observed an increase in the adsorption capacity after cleaning the column under vacuum for 15 hours at 80 °C before subsequent analyses. The initial breakthrough experiment with pure $CO_2$ gas conducted after vacuum cleaning revealed a significant enhancement in the $CO_2$ adsorption capacity, reaching up to 2.98 $mmol \cdot g^{-1}$. Notably, in previous experiments with the activation method with N2 flow, the $CO_2$ adsorption capacity remained at 2.1 $mmol \cdot g^{-1}$. At this point, we decided to initiate a preliminary study of the activation procedure in a fixed-bed column before proceeding with the planned experiments (Breakthrough experiments at different gas velocities). As is standard practice, first, we performed experimental $CO_2$ adsorption isotherms with a degassing procedure involving $N_2$ flow and vacuum up to 10-6 Torr. Notably, the vacuum procedure resulted in a 25%

increase in $CO_2$ adsorption by weight. Additionally, the color of the activated material differed; $N_2$ activation resulted in a gray color, while vacuum activation resulted in a light violet color, as shown in Figure 3.7.

We conducted further experiments to optimize the activation procedure of the TAMOF-1 fixed-bed column. Based on our initial observations, we tested the same procedure in a fixed-bed column, using vacuum and heating the column up to 120°C (second activation method). We initially used a glass column to monitor the color change during activation inside the column visually. We also experimented with different methods of applying vacuum within the column. The most effective approach was to apply a vacuum simultaneously from both the bottom and top of the column, which facilitated faster removal of water from the pores of TAMOF-1. Applying a vacuum from only one side of the column leads to uneven complete activation on one side of the TAMOF-1 bed. This occurs because the powder packs on the side where the vacuum is not applied, reducing the pressure (vacuum) on that side. As a result, water is not effectively removed from that side, leading to inefficient activation.

One of the reasons suggesting that flowing $N_2$ through the column is not as effective as vacuum, even when water concentration in the outlet gas is no longer visible, is that the hydration water is removed with low energy. However, the coordination water in the 3D structures of TAMOF-1 units, where octahedral Cu(II) is connected to four deprotonated ligands (two imidazolate and two triazolate ligands) and two $H_2O$ molecules, requires higher energy to be removed and reach complete activation. This process involves the loss of the two coordination positions occupied by $H_2O$ after activation and a color change (Figure 3.7d). A weight loss of 22.7% is observed in the powder material when complete hydration is achieved. Using this activation type in a small column (1g of TAMOF-1), an increase in the $CO_2$ adsorption capacity up to 4.2 $mmol \cdot g^{-1}$ with pure $CO_2$ is observed (Figure 3.7c), similar to the value obtained in the adsorption isotherms under similar conditions. Consequently, this activation procedure was selected for the subsequent experiments, including breakthrough curves with various gas velocities and a repeated regeneration study, although only at one condition (6% $CO_2$, 25°C, and 1 bar). We employ the same type 2 activation before the analysis for pellets. All subsequent experiments were conducted using this activation without encountering any issues. We hypothesize also

that applying a vacuum from only one side of the column could be sufficient for the pellet column. Pelletization of the TAMOF-1 powder increases macroporosity while preventing the overpacking of the material. Moreover, it would ensure a consistent vacuum pressure throughout the column, which could benefit even in VSA processes.



In this small secction, we aimed to emphasize the critical role of the activation in your adsorbent material, particularly for TAMOF-1. While TAMOF-1 is a robust material, its performance is highly dependent on the correct execution of the activation process. If an activation is performed incorrectly, it cannot be rectified by subsequent activations. Specifically, performing a type 2 activation after an initial type 1 activation does not result in the desired activation state, leading to diminished adsorption performance compared to a single, correctly performed type 2 activation. After proper activation, TAMOF-1 can be conveniently regenerated (or reactivated) if it loses some adsorption capacity during operation, effectively restoring its full adsorption potential. This has been extensively demonstrated through multiple analyses employing the same material. Notably, the regeneration process does not significantly alter the structural integrity or adsorption properties of TAMOF-1, making it a durable and reusable material. The facile regeneration capability is particularly advantageous for practical applications, as it reduces the need for frequent material replacement and minimizes waste production[5].

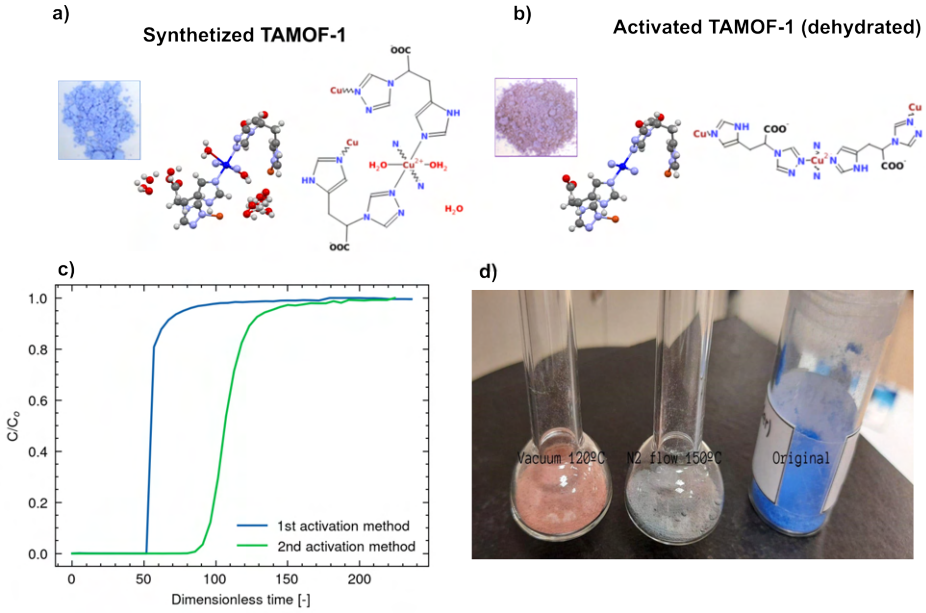


Figure 3.7: 3D structure of (a) as-synthetized and (b) activated TAMOF-1 powder. Colour code for spheres: hydrogen (white), carbon (grey), nitrogen (violet), oxygen (red) and copper (blue). (c) $CO_2$ breakthrough curves of TAMOF-1 powder after activation with $N_2$ flow and vacuum. (d) Pictures of the TAMOF-1 powder colors after activation with $N_2$ flow (middle) and vacuum (left).

### 3.4.4 TAMOF-1 Adsorption/Desorption (Regeneration) Measurements: Second Activation

The physisorption performance of TAMOF-1 for $CO_2$ was observed to improve after the second activation (section 3.4.3). In light of previous regeneration study results (after the first activation), TAMOF-1 tends to perform better at lower $CO_2$ concentrations. Industrial applications, where current post-combustion $CO_2$ capture technologies encounter the most challenges, necessitate a focus on the inlet gas ratio to the $6CO_2$:$94N_2$ capture system while maintaining the operating conditions of temperature (298 K) and pressure (1 bar). Although future optimization for higher $CO_2$ concentrations is not ruled out, this regeneration study addressed this aspect.

Figure 3.8a presents the breakthrough curve of the post-activation column (blue), along with the sequential curves measured after each vacuum regeneration. TAMOF-1 $CO_2$ uptake capacity at saturation, $q_s(CO_2)$, was 1.03 mmol $g^{-1}$, exhibiting a 28% increase compared

to its breakthrough point capacity, $q_b(CO_2)$, with a Breakthrough time of 9.45 min $g^{-1}$ (7.88 g de TAMOF-1 powder activated). The BT($CO_2$) point, similar to the cleaning vacuum time, occurred at 41 minutes. This observation suggests that vacuum regeneration does not entirely remove $CO_2$ from TAMOF-1, as remnant $CO_2$ remains within the material's pores. The cyclic stability of the material was assessed by repeating the cleaning process and measuring the BT 10 times, resulting in consistent BT and cleaning times of 41 minutes.

Figures 3.8b and 3.8c illustrate the $CO_2$ desorbed and residual $N_2$ quantities at varying vacuum times. Even after 120 minutes of vacuum, the desorbed $CO_2$ (0.87 mmol $g^{-1}$) remains lower than the total $CO_2$ adsorbed by TAMOF-1. Notably, at 41 minutes of desorption time (equivalent to the adsorption time), 0.65 mmol $g^{-1}$ of $CO_2$ is desorbed, while minimal vacuum times of 5 and 30 seconds yield 0.12 and 0.125 mmol $g^{-1}$ respectively. The residual $N_2$ at 30 seconds is $5.11x10^{-4}$ mmol $g^{-1}$, compared to 0.1 mmol $g^{-1}$ without vacuum. Using the VSA configuration (section 3.2.9), the recovered $CO_2$ amount and purity were calculated (Figure 3.8d). Without blow-down time, 86% pure $CO_2$ is recovered. A 30-second blow-down increases purity to 99.9%, but recovery drops to 80%. The $CO_2$ physisorption benchmark zeolite 13x (powder) under identical conditions ($6CO_2$:94 $N_2$, 298K, 1 bar) reveals a high $CO_2$ adsorption capacity at saturation (qs=3 mmol $g^{-1}$) with a breakthrough time of 38 min $g^{-1}$ (8.1 g of activated 13x zeolite). However, zeolite 13x exhibits significant $CO_2$ retention, requiring 90 minutes for desorption and yielding 0.88 mol $g^{-1}$ of desorbed $CO_2$. The $CO_2$ concentration step is also slow, taking nearly 2 minutes to reach 99.8% purity with a substantial $CO_2$ loss of 0.238 mmol $g^{-1}$. In contrast, TAMOF-1, under the same VSA cycle, achieves 99.8% $CO_2$ purity with an 81% recovery rate, compared to 65.7% for zeolite 13x (Figure 3.8e). This translates to respective $CO_2$ mass flow recoveries of 0.015 and 0.01 m3 $h^{-1}$ $kg^{-1}$.

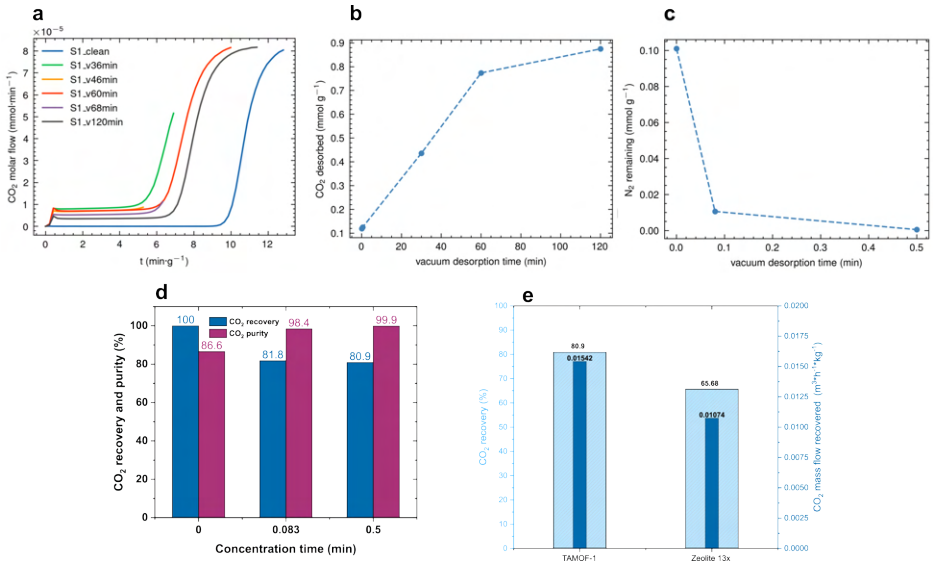


Figure 3.8: Experimental results of the regeneration measurements: (a) $CO_2$ Breakthrough curves at different regeneration time under vacuum; (b) amount of $CO_2$ desorbed at different regeneration time under vacuum; and (c) $N_2$ remaining inside the column after regeneration with vacuum.

### 3.4.5 TAMOF-1 Pellet Adsorption/Desorption (Regeneration) measures.

For industrial applications, transitioning from powder to structured forms (e.g., metal-supported, pellets, membranes) is crucial[5,22,46,47]. Preliminary isotherm analyses (Figure 3.5d) of previously synthesized TAMOF-1 pellets with 12% bentonite binder show promising results. These pellets withstand up to 10 bar pressure without significant particle loss ($< 1\%$). Additionally, these pellets also exhibit a remarkable specific surface area, approximately 848 $m^2\ g^{-1}$. Consequently, testing their performance under dynamic conditions (breakthrough measurements) in the same VSA system configuration used for TAMOF-1 powder is warranted. Figure 3.9a compares the breakthrough curves of the pellet and powder using pure $CO_2$ to assess total adsorption and activation. Notably, the pellet exhibits only a 6% reduction in $CO_2$ adsorption capacity at saturation ($q_s = 3.52$ mmol $g^{-1}$) compared to the powder. The similar S-curve shapes suggest comparable mass transfer mechanisms, potentially attributed to the low gas velocity used due to the pure $CO_2$ environment (gas velocity approaching zero until breakthrough).

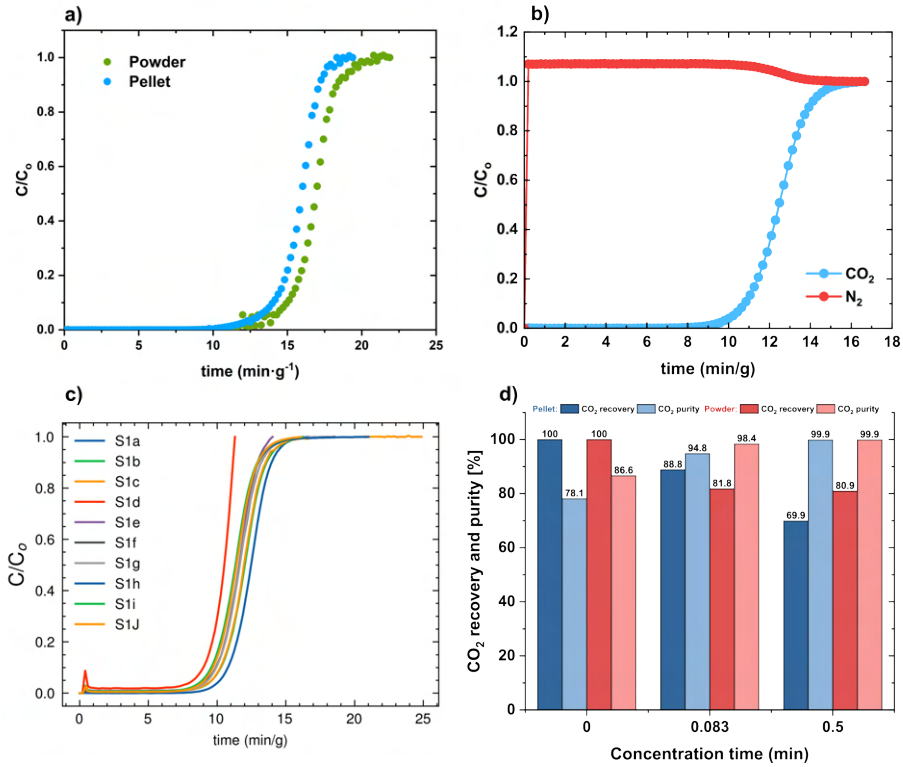


Figure 3.9: (a) TAMOF-1 powder and pellet Breakthrough curves with pure $CO_2$ at 298K and 1bar.(b) $CO_2$ and $N_2$ breakthrough curves on TAMOF-1 pellet for $6CO_2$:$94N_2$ ratio at 298K and 1 bar. (c) TAMOF-1 pellet breakthrough curves of $CO_2$, with a feeding $CO_2/N_2$ gas mixture with a 6:94 concentration at a total flow of 30 NmL min$^{-1}$, 298 K and 1.05 bar. The data include a batch of TAMOF-1 that was preliminarily activated (S1a), and measurements were taken after steady state with an 80 min vacuum regeneration time (S1b–S1J). (d) $CO_2$ recovery and purity as a function of the blow-down time for TAMOF-1 pellets and powder at 30 NmL min$^{-1}$, 298 K, and 1.05 bar.

The performance of the TAMOF-1 pellet was evaluated under inlet gas conditions of $6CO_2$:$94N_2$ at 298K and 1 bar. Figure 3.9b displays the $CO_2$ and $N_2$ breakthrough curves. Similar to the TAMOF-1 powder, the pellet exhibits minimal interaction with $N_2$, with an estimated $CO_2$ selectivity of 163. The $CO_2$ adsorption capacity at saturation ($q_s$) is 1.04 mmol g$^{-1}$, and at breakthrough ($q_b$) is 0.85 mmol g$^{-1}$, with a breakthrough time of 9.40 min g$^{-1}$. An 80-minute vacuum cleaning time was determined to be equivalent to the breakthrough time during adsorption. Remarkably, there is only a 6% decrease

in qs($CO_2$) for the TAMOF-1 pellet (0.98 mmol $g^{-1}$) under steady-state adsorption/desorption cycles with an 80-minute vacuum time (Figure 3.9c). The steady-state qb($CO_2$) is 0.747 mmol $g^{-1}$. Cyclic stability tests over 10 adsorption/desorption cycles revealed no loss in adsorption performance. Using the experimental data of desorbed $CO_2$ at different vacuum times (5 sec, 30 sec, 80 min) and residual $N_2$ inside the column, along with the procedure established for the TAMOF-1 powder, the $CO_2$ recovery capacity and purity in the VSA cycle were calculated. Figure 3.9d compares the pellet and powder data, showing similar $CO_2$ purity values at 5 seconds (95% and 98%, respectively) and 30 seconds (99.9%) of vacuum concentration time (blow-down). However, the pellet's recovery is compromised compared to the powder, with 88.8% recovery at 5 seconds (vs. 81.8% for powder) and 69.9% at 30 seconds (vs. 80.9%). Without blow-down time, assuming full recovery at steady state, the $CO_2$ purity is 78.1% for the pellet and 86.6% for the powder. These results suggest that the pellet exhibits faster desorption kinetics. This is further supported by the minimal reduction ($\approx$ 6%) in adsorption capacity from the first adsorption after activation to steady state, compared to the powder ($\approx$ 38%). This faster desorption necessitates shorter vacuum times for $CO_2$ concentration to avoid significant $CO_2$ loss without recirculation.

### 3.4.6 Breakthrough curves data at different gas velocities.

When scaling up gas separation technologies for industrial applications, it is crucial to characterize both equilibrium (via adsorption isotherms) and kinetics (via breakthrough curves) under various operating conditions (temperature, pressure, gas velocity). This enables the effective transfer of these parameters from laboratory to larger scales[12,48].

Figure 3.10 shows the breakthrough curves for TAMOF-1 powder exposed to a mixture of 6% $CO_2$ (He balance). The curves illustrate the effects of manipulating three variables: pressure (1–5 bar), temperature (25–80°C), and gas velocity (0.005–0.015 m $s^{-1}$); i) Pressure: As expected, the adsorption capacity ($q_s$) tends to increase proportionally with the partial pressure of $CO_2$. At 298K and 1 bar, qs($CO_2$) is 0.9 mmol $g^{-1}$, increasing to 1.74 mmol $g^{-1}$ at 5 bar (Figure 3.10a). This is consistent with the increased $CO_2$ partial

pressure driving adsorption. ii) Temperature: Adsorption capacity is inversely proportional to temperature. At 1 bar and 0.005 m s-1, qs($CO_2$) values are 0.9, 0.59, and 0.28 mmol $g^{-1}$ at 25, 50, and 80ºC respectively (Figure 3.10b). This reflects the exothermic nature of adsorption, where higher temperatures hinder $CO_2$ uptake. iii) Gas Velocity: Adsorption capacity appears independent of gas velocity within the measured range. At 298K and 1 bar, qs($CO_2$) remains constant at 0.90 mmol $g^{-1}$ across all three velocities (Figure 3.10c). This suggests that mass transfer limitations are not significant within this range. Furthermore, for the measurements at 1 bar, a reduced pressure drop of ¡ 0.15 bar was noted at the highest velocity of 0.015 m $s^{-1}$. For detailed experimental data at each operating condition, refer to Figure B.3. This comprehensive overview provides valuable insights into the interplay between temperature, pressure, and gas velocity, in the TAMOF-1 powder adsorption performance.

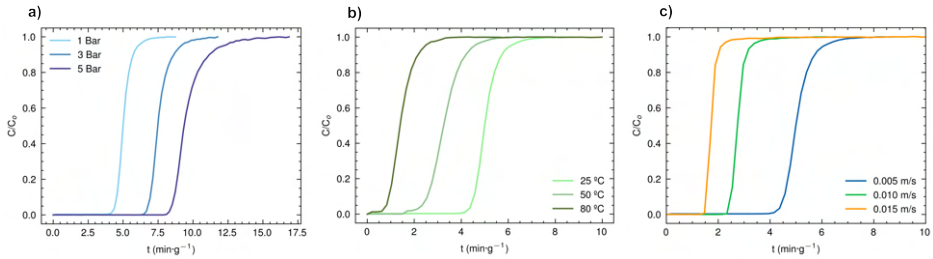


Figure 3.10: Breakthrough curves for 6:94 $CO_2$/He gas mixture: (a) Different pressure at 25ºC and v=0.005 m $s^{-1}$ , (b) Different temperature at 1bar and v=0.005 m $s^{-1}$ and (c) Different gas velocity at 25ºC and 1 bar.

Characterizing TAMOF-1 under dynamic adsorption conditions allows for a more accurate estimation of its mass transfer by calculating the mass transfer coefficient (MTC). Since the linear adsorption equation cannot fully capture key physical aspects[38], we employed the Sips model (order n=2, m=1) and validated it against breakthrough experimental data at varying velocities (0.005 – 0.015 m $s^{-1}$) under 298 K and 1 bar. Using equations 1.17 (section 1.5.3), 3.3, and 3.4, we estimated the transfer coefficients Kad and Ked. Figure B.4 shows the experimental data and the fitted curve for TAMOF-1 powder. Kad values were 0.003, 0.006, and 0.008 $m^3 kg s^{-1}$ for gas velocities of 0.005 m $s^{-1}$, 0.010 m $s^{-1}$, and 0.015 m $s^{-1}$, respectively. Interestingly, the Kde parameter (describing desorption) exhibited higher values than Kad (0.42, 0.84, and 1.27 $s^{-1}$), suggesting that TAMOF-1 des-

orbs easily at lower concentrations (low adsorption rates). This aligns with findings in section 3, demonstrating rapid adsorption/desorption rates and the need for short blow-down times, albeit with potential for significant $CO_2$ loss at longer blow-down durations. While adsorption and desorption coefficients may vary with temperature and flow rate, they should remain constant with respect to concentration and q based on the proportionality assumption. To verify this, we conducted breakthrough measurements at a constant velocity (0.005 m $s^{-1}$) but varying concentrations (1, 2.5, and 6% $CO_2$). The Kad coefficient exhibited a slight variation as a function of concentration ($0.003 \pm 0.0005\ m^3 kg s^{-1}$), suggesting that the nonlinear sink model accurately captures the physics without violating model assumptions. Detailed results of all experiments can be found in Table S1.

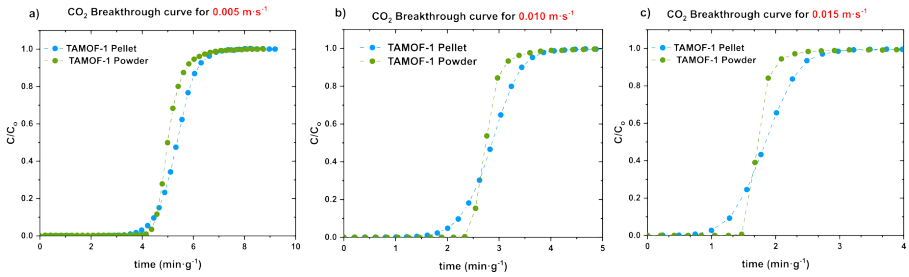


Figure 3.11: Breakthrough curves for TAMOF-1 powder and pellet at different gas velocities: (a) 0.005, (b)0.010, and (c)0.015 m $s^{-1}$, under 298 K and 1.05 bar.

TAMOF-1 pellets were evaluated under the same velocity range (0.005–0.015 m $s^{-1}$), pressure, and temperature conditions (298K, 1 bar) as the powder form. Figure 3.11 displays the breakthrough curves for powder and pellet TAMOF-1 shape at varying gas velocities. Both forms (pellet and powder) exhibit similar saturation adsorption capacities ($0.93 \pm 0.03$ mmol $g^{-1}$) across the tested velocities. However, due to differences in mass transfer (evident in the distinct S-curve shapes), the breakthrough adsorption capacities differ. The breakthrough times for the pellet are 3.64, 1.61, and 0.87 min $g^{-1}$ at 0.005, 0.010, and 0.015 m $s^{-1}$, respectively. As the figure illustrates, the curve slope becomes steeper with increasing velocity, resulting in higher breakthrough adsorption capacities ($q_b$) at lower velocities. Specifically, $q_b(CO_2)$ values for the pellet are 0.66, 0.55, and 0.45 mmol $g^{-1}$ at 0.005, 0.010, and 0.015 m $s^{-1}$, respectively. In addition to these analyses, the mass transfer coefficient $K_{ad}$

in TAMOF-1 decreases as expected, due to the increase in macroporosity, which facilitates faster desorption but slower mass transfer (steeper curves and lower $K_{ad}$ values). Figure B.5 presents the experimental breakthrough curve data for the TAMOF-1 pellet at different evaluated rates, along with the curves fitted to the experimental values. The $K_{ad}$ values for the TAMOF-1 pellet were $1.7\times10^{-5}$, $2.3\times10^{-5}$, and $2.8\times10^{-5}$ $m^3kg^{-1}s^{-1}$, corresponding to each gas velocity increment, respectively.

## 3.5 Outlook.

An ideal adsorbent for post-combustion $CO_2$ capture should possess several key attributes: i) high $CO_2$ adsorption capacity, ii) rapid adsorption/desorption kinetics, iii) high selectivity for $CO_2$ over $N_2$ and $O_2$, functionality in humid conditions, iv) mild regeneration conditions, v) structural formability (e.g., beads, laminates, monoliths), vi) chemical, mechanical, and thermal stability, and vii) low-cost, scalable production[49]. TAMOF-1 demonstrates potential in meeting most of these criteria, offering a promising pathway towards cost-effective and reliable industrial-scale $CO_2$ capture. However, while theoretical hypotheses suggest competition between water and $CO_2$ adsorption in TAMOF-1, practical evaluation under cyclic conditions is necessary to confirm its performance. If unsatisfactory, a dehumidification system may be required, potentially increasing capture costs. Investigating hydrophobic filler incorporation into TAMOF-1 pellets for improved performance in humid environments is a potential avenue for future research. Other MOFs may exhibit superior properties in one or more of the aforementioned criteria, but not all. Notably, many reported MOFs, despite high $CO_2$ capacity or selectivity, cannot tolerate even ambient moisture. CALF-20 stands out as a MOF with promising results[6] across all criteria, warranting future comparative evaluation against TAMOF-1. Zeolite 13x, despite high $CO_2$ adsorption capacity, underperforms under cyclic conditions due to high energy consumption for desorption and sensitivity to water[50]. In gas separations, simple metrics like selectivity and working capacity often correlate poorly with process performance, as evidenced by our study. Zeolite 13x exhibits high adsorption capacity at low $CO_2$ partial pressures but underperforms under cyclic conditions compared to TAMOF-1. A recent studies screening high-

lights the importance of detailed process modeling and optimization in sorbent selection[5,18,22,51,52]. Cost and scalability of synthesis are crucial factors. Many MOFs require expensive, non-commercial aprotic solvents or linkers. TAMOF-1 utilizes readily available, low-cost components (water, methanol, and ethanol as solvents) and scalable synthesis methods[30,32]. While materials may exhibit exceptional individual features, their integration with optimal process engineering conditions, such as capture conditions and available waste energy for regeneration, is key. TAMOF-1's moderate uptake at lower partial pressures and high uptake at higher pressures make it suitable for pressure swing processes at lower temperatures. We are currently developing a mobile pilot plant (Figure 3.12) for scaling up the $CO_2$ capture process via VSA (vacuum swing adsorption) to evaluate TAMOF-1's real-world performance under real gas conditions. This will provide critical data for scaling up to industrial levels. TAMOF-1's high selectivity and fast kinetics enable faster cycling, enhancing process productivity, with results expected to clarify points iii) and iv). Given its scalability and durability, TAMOF-1 may pave the way for widespread MOF use in large-scale industrial gas separation, particularly for post-combustion $CO_2$ capture. Efficient capture is a crucial step in reducing greenhouse gases, and integrating advanced materials with advanced processes will facilitate larger demonstration projects to validate MOFs in real-world $CO_2$ capture scenarios. This study provides valuable initial observations and trends regarding TAMOF-1's potential for post-combustion $CO_2$ capture. However, further analysis is needed to assess its feasibility for industrial implementation, including energy consumption, water competitiveness, real gas testing, and techno-economic evaluation.

Figure 3.12: Post-combustion $CO_2$ capture pilot plant using VSA with TAMOF-1.

## 3.6 Conclusions.

TAMOF-1, a stable and robust homochiral metal-organic framework (BET specific surface area = 980 ± 50 $m^2 g^{-1}$), demonstrates selective $CO_2$ adsorption from gas streams, reaching up to 3.7 mmol $g^{-1}$ at 1 bar and 298K. Adsorption isotherms confirm preferential $CO_2$ uptake over $N_2$ across a wide pressure range (0–10 bar), yielding favorable separation parameters for $CO_2/N_2$ mixtures. High IAST selectivity (up to 205) is achieved across various $CO_2/N_2$ concentrations (6–30%), pressures (1–10 bar), and temperatures (293–353 K). Importantly, the weak interactions between $CO_2$ and TAMOF-1 enable easy, low-energy regeneration. A modified Langmuir-Freundlich (Sips) isotherm model accurately fits the $CO_2$ equilibrium isotherms, while the Langmuir model describes the $N_2$ isotherms.

Dynamic column breakthrough experiments with binary $CO_2/N_2$ mixtures (6:94, 15:85, 30:70) at 298K and 1.05 bar reveal a concentration-dependent desorption process, with faster $CO_2$ desorption at higher concentrations. The longest breakthrough time (7.3 min $g^{-1}$) occurs at the lowest $CO_2$ concentration (6%). $N_2$ interaction with TAMOF-1 is minimal, allowing for high $CO_2$ purities (>99.9%) after 5 minutes of vacuum regeneration. An experimental 4-step vacuum swing adsorption (VSA) configuration demonstrates ∼95% $CO_2$ purity and ∼77% recovery with only 5 seconds of vacuum at 6:94 $CO_2/N_2$.

Vacuum activation of TAMOF-1 nearly doubles its adsorption capacity compared to $N_2$ purging, underscoring the importance of activation methods. Cyclic performance tests (VSA) under flue gas conditions (6:94 $CO_2/N_2$, 298K, 1.05 bar), using the second activation method (vacuum), reveal that TAMOF-1 outperforms benchmark zeolite 13x, achieving 25% higher $CO_2$ recovery at ∼ 99.8% purity. Pellet and powder forms of TAMOF-1 exhibit comparable adsorption capacities (∼ 1 mmol $g^{-1}$) under dynamic conditions (298K, 1 bar, 6:94 $CO_2/N_2$). However, the pellet desorbs more easily, leading to higher purities at shorter concentration times but lower recovery at longer times.

Single-component $CO_2$ breakthrough experiments with 6:94 $CO_2$/He at various velocities (0.005, 0.010, 0.015 m $s^{-1}$) further validate the modified Sips model. Both pellet and powder exhibit fast kinetics, with adsorption mass transfer coefficients ($K_{ad}$) of 3 – 8 $\times 10^{-3}$ $m^3 kg^{-1} s^{-1}$ (powder) and 1.7– 2.8 $\times 10^{-5}$ $m^3 kg^{-1} s^{-1}$ (pellet).

Given these performance metrics, TAMOF-1 pellets show promise for post-combustion carbon capture using pressure/vacuum swing adsorption technologies. Its tunable regeneration protocol allows for flexible adaptation to time and energy constraints. Ongoing efforts focus on scaling up and optimizing the VSA process, evaluating real-world industrial stability, and ultimately assessing the techno-economic feasibility of TAMOF-1 for large-scale $CO_2$ capture.

# References

1. Brickett, L. *Carbon Dioxide Capture Handbook* (US Department of Energy (DOE)/NETL, 2015, Aug. 2015).
2. *$CO_2$ Emissions in 2022* tech. rep. Accessed: 2023-6-19 (2022).
3. Xie, J., Xia, Z., Tian, X. & Liu, Y. Nexus and synergy between the low-carbon economy and circular economy: A systematic and critical review. en. *Environ. Impact Assess. Rev.* **100,** 107077. ISSN: 0195-9255,1873-6432 (May 2023).
4. Hasan, M. M. F., Baliban, R. C., Elia, J. A. & Floudas, C. A. Modeling, Simulation, and Optimization of Postcombustion CO 2 Capture for Variable Feed Concentration and Flow Rate. 1. Chemical Absorption and Membrane Processes. en. *Industrial & Engineering Chemistry Research* **51,** 15642–15664. ISSN: 0888-5885, 1520-5045 (Dec. 2012).
5. Siegelman, R. L., Kim, E. J. & Long, J. R. Porous materials for carbon dioxide separations. *Nat. Mater.* **20,** 1060–1072 (2021).
6. Lin, J.-B. *et al.* A scalable metal-organic framework as a durable physisorbent for carbon dioxide capture. *Science,* 1–4 (2021).
7. Keith, D. W., Holmes, G., St. Angelo, D. & Heidel, K. A Process for Capturing $CO_2$ from the Atmosphere. *Joule* **2,** 1573–1594 (2018).
8. Nakao, S.-I., Yogo, K., Goto, K., Kai, T. & Yamada, H. *Advanced $CO_2$ capture technologies: Absorption, adsorption, and membrane separation methods* (Springer, 2019).
9. Figueroa, J. D., Fout, T., Plasynski, S., McIlvried, H. & Srivastava, R. D. Advances in $CO_2$ capture technology-The U.S. Department of Energy's Carbon Sequestration Program. *Int. J. Greenhouse Gas Control* **2,** 9–20 (2008).
10. Wilcox, J., Haghpanah, R., Rupp, E. C., He, J. & Lee, K. Advancing adsorption and membrane separation processes for the gigaton carbon capture challenge. *Annu. Rev. Chem. Biomol. Eng.* **5,** 479–505 (2014).
11. Rackley, S. A. in *Carbon Capture and Storage (Second Edition)* (ed Rackley, S. A.) 115–149 (Butterworth-Heinemann, Boston, 2017). ISBN: 978-0-12-812041-5. `http://www.sciencedirect.com/science/article/pii/B9780128120415000064`.

12. Green, D. W. & Perry, R. H. *Perry's Chemical Engineers Handbook* (McGraw-Hill Book Co., London and New York, 2008).

13. Liu, H., Idem, R. & Tontiwachwuthikul, P. *Post-combustion $CO_2$ Capture Technology: By Using the Amine Based Solvents* ISBN: 978-3-030-00921-2. `http://link.springer.com/10.1007/978-3-030-00922-9` (Springer International Publishing, Cham, 2019).

14. Luis, P. Use of monoethanolamine (MEA) for $CO_2$ capture in a global scenario: Consequences and alternatives. *Desalination* **380,** 93–99 (2016).

15. Zanco, S. E. *et al.* Postcombustion $CO_2$ Capture: A Comparative Techno-Economic Assessment of Three Technologies Using a Solvent, an Adsorbent, and a Membrane. *ACS Engineering Au* **1,** 50–72 (2021).

16. Seider, W. D. *et al. Product and Process Design Principles: Synthesis, Analysis, and Evaluation* en. ISBN: 978-1-119-63698-4 (Wiley, May 2020).

17. Riboldi, L. & Bolland, O. Overview on Pressure Swing Adsorption (PSA) as $CO_2$ Capture Technology: State-of-the-Art, Limits and Potentials. *Energy Procedia* **114.** ISSN: 18766102 (2017).

18. Subraveti, S. G., Roussanaly, S., Anantharaman, R., Riboldi, L. & Rajendran, A. How much can novel solid sorbents reduce the cost of post-combustion $CO_2$ capture? A techno-economic investigation on the cost limits of pressure–vacuum swing adsorption. *Applied Energy* **306,** 117955. ISSN: 03062619 (Jan. 2022).

19. *Gas Adsorption in Metal-Organic Frameworks* (eds Grant Glover, T. & Mu, B.) (CRC Press, Boca Raton, FL : CRC Press-Taylor & Francis Group, [2018], Sept. 2018).

20. Danaci, D., Bui, M., Mac Dowell, N. & Petit, C. Exploring the limits of adsorption-based $CO_2$ capture using MOFs with PVSA – from molecular design to process economics. en. *Molecular Systems Design & Engineering* **5,** 212–231. ISSN: 2058-9689 (2020).

21. Hu, Z., Wang, Y., Shah, B. B. & Zhao, D. $CO_2$ Capture in Metal-Organic Framework Adsorbents: An Engineering Perspective. *Advanced Sustainable Systems* **3,** 1800080. ISSN: 2366-7486 (2019).

22. Balogun, H. A., Bahamon, D., AlMenhali, S., Vega, L. F. & Alhajaj, A. Are we missing something when evaluating adsorbents for CO 2 capture at the system level? *Energy Environ. Sci.* (2021).

23. Hasan, M. M. F., Baliban, R. C., Elia, J. A. & Floudas, C. A. Modeling, Simulation, and Optimization of Postcombustion CO 2 Capture for Variable Feed Concentration and Flow Rate. 2. Pressure Swing Adsorption and Vacuum Swing Adsorption Processes. en. *Industrial & Engineering Chemistry Research* **51,** 15665–15682. ISSN: 0888-5885, 1520-5045 (Dec. 2012).

24. Riboldi, L. & Bolland, O. Evaluating Pressure Swing Adsorption as a $CO_2$ separation technique in coal-fired power plants. *International Journal of Greenhouse Gas Control* **39,** 1–16. ISSN: 17505836 (2015).

25. Abanades, J. C. *et al.* Emerging $CO_2$ capture systems. *Int. J. Greenhouse Gas Control* **40,** 126–166 (2015).

26. Mukherjee, S., Kumar, A. & Zaworotko, M. J. in *Metal-Organic Frameworks (MOFs) for Environmental Applications* (ed Ghosh, S. K.) 5–61 (Elsevier, 2019).

27. Jiang, D.-e., Mahurin, S. M. & Dai, S. *Materials for Carbon Capture* ISBN: 978-1-119-09117-2 (John Wiley & Sons, 2020).

28. Baci, M. *et al. Metal-Organic Frameworks (MOFs) for Environmental Applications* (Elsevier, 2019).

29. Masala, A. *et al.* $CO_2$ Capture in Dry and Wet Conditions in UTSA-16 Metal–Organic Framework. en. *ACS Applied Materials & Interfaces* **9,** 455–463. ISSN: 1944-8244, 1944-8252 (Jan. 2017).

30. Corella-Ochoa, M. N. *et al.* Homochiral Metal-Organic Frameworks for Enantioselective Separations in Liquid Chromatography. *Journal of the American Chemical Society* **141,** 14306–14316. ISSN: 15205126 (Sept. 2019).

31. González-Galán, C. *et al.* Separation of Volatile Organic Compounds in TAMOF-1. *ACS Applied Materials & Interfaces* **14,** 30772–30785. ISSN: 1944-8244 (July 2022).

32. Núñez-Rico, J. L. *et al.* TAMOF-1 as a Versatile and Predictable Chiral Stationary Phase for the Resolution of Racemic Mixtures. *ACS Applied Materials & Interfaces* **15,** 39594–39605 (2023).

33. Gabelman, A. Adsorption can be used to treat waste streams or purify valuable components of a feed. This article describes both equilibrium and mass-transfer considerations, and reviews the fundamentals of adsorption system design. en. *Back to Basics* (2017).

34. Douglas M. Ruthven S Farooq, K. S. K. *Pressure Swing adsorption* (John Wiley & Sons, 1996).

35. Durán, I., Rubiera, F. & Pevida, C. Separation of $CO_2$ in a Solid Waste Management Incineration Facility Using Activated Carbon Derived from Pine Sawdust. *Energies* **10,** 827 (2017).

36. Myers, T. G., Font, F. & Hennessy, M. G. Mathematical modelling of carbon capture in a packed column by adsorption. en. *Appl. Energy* **278,** 115565 (Nov. 2020).

37. Ayawei, N., Ebelegi, A. N. & Wankasi, D. Modelling and Interpretation of Adsorption Isotherms. *J. Chem. Chem. Eng.* (2017).

38. Myers, T. G., Cabrera-Codony, A. & Valverde, A. On the development of a consistent mathematical model for adsorption in a packed column (and why standard models fail). en. *Int. J. Heat Mass Transf.* **202,** 123660. ISSN: 0017-9310,1879-2189 (Mar. 2023).

39. Myers, T. G. & Font, F. Mass transfer from a fluid flowing through a porous media. en. *Int. J. Heat Mass Transf.* **163,** 120374. ISSN: 0017-9310,1879-2189 (Dec. 2020).

40. Seader, J. D., Henley, E. J. & Roper, D. K. *Separation Process Principles, 3rd Edition* en. ISBN: 978-1-118-13962-2 (John Wiley Incorporated, Nov. 2010).

41. Sayari, A., Belmabkhout, Y. & Serna-Guerrero, R. Flue gas treatment via $CO_2$ adsorption. en. *Chem. Eng. J.* **171,** 760–774 (July 2011).

42. Rubin, E. S., Davison, J. E. & Herzog, H. J. The cost of $CO_2$ capture and storage. *Int. J. Greenhouse Gas Control* **40,** 378–400 (2015).

43. Van De Haar, A. *et al.* Dynamics of Postcombustion $CO_2$ Capture Plants: Modeling, Validation, and Case Study. *Industrial and Engineering Chemistry Research* **56,** 1810–1822. ISSN: 15205045 (2017).

44. Madeddu, C., Errico, M. & Baratti, R. *$CO_2$ Capture by Reactive Absorption-Stripping* (2019).

45. Jansen, D., Gazzani, M., Manzolini, G. & Van Dijk, E. Emerging $CO_2$ capture systems. *Int. J. Greenhouse Gas Control* **40,** 167–187 (2015).

46. Ioannou, I., Galán-Martín, Á., Pérez-Ramírez, J. & Guillén-Gosálbez, G. Trade-offs between Sustainable Development Goals in carbon capture and utilisation. *Energy Environ. Sci.* (2022).

47. Nagireddi, S., Agarwal, J. R. & Vedapuri, D. Carbon Dioxide Capture, Utilization, and Sequestration: Current Status, Challenges, and Future Prospects for Global Decarbonization. *ACS Engineering Au* (2023).

48. Pai, K. N., Prasad, V. & Rajendran, A. Practically Achievable Process Performance Limits for Pressure-Vacuum Swing Adsorption-Based Postcombustion $CO_2$ Capture. en. *ACS Sustainable Chem. Eng.* **9,** 3838–3849. ISSN: 2168-0485,2168-0485 (Mar. 2021).

49. Samanta, A., Zhao, A., Shimizu, G. K. H., Sarkar, P. & Gupta, R. Post-combustion $CO_2$ capture using solid sorbents: A review. en. *Ind. Eng. Chem. Res.* **51,** 1438–1463 (Feb. 2012).

50. Qasem, N. A. & Ben-Mansour, R. Adsorption breakthrough and cycling stability of carbon dioxide separation from $CO_2$/N2/H2O mixture under ambient conditions using 13X and Mg-MOF-74. *Applied Energy* **230,** 1093–1107. ISSN: 03062619 (2018).

51. Nguyen, T. T., Lin, J.-B., Shimizu, G. K. & Rajendran, A. Separation of $CO_2$ and $N_2$ on a hydrophobic metal organic framework CALF-20. en. *Chemical Engineering Journal* **442,** 136263. ISSN: 13858947 (Aug. 2022).

52. Subraveti, S. G., Roussanaly, S., Anantharaman, R., Riboldi, L. & Rajendran, A. Techno-economic assessment of optimised vacuum swing adsorption for post-combustion $CO_2$ capture from steam-methane reformer flue gas. *Sep. Purif. Technol.* **256,** 117832 (2021).

*"An expert is one who has made all the mistakes that can be made in a very small field."*

Niels Bohr



# 4

# Selective adsorption of $CO_2$ in TAMOF-1 for the separation of $CO_2/CH_4$ gas mixtures.

**Abstract** In this chapter, we introduce TAMOF-1, an eco-friendly metal-organic framework (MOF) designed to efficiently separate carbon dioxide from methane and nitrogen in biogas type mixtures. TAMOF-1 demonstrates exceptional $CO_2$ adsorption capacity, remarkable cyclic stability, and efficient regeneration properties. Computational analysis corroborates its superior sorption and transport characteristics. These attributes position TAMOF-1 as a promising candidate for industrial $CO_2$ capture and biogas purification utilizing pressure/vacuum swing adsorption technology. Ongoing research endeavors focus on evaluating TAMOF-1's performance under realistic conditions and optimizing operating parameters to maximize its potential for practical applications.

# Contents

# 4.1 Introduction.

The presence of $CO_2$ in gas streams is detrimental to the environment as greenhouse gas emissions and an undesirable impurity in industrial feedstocks. It is particularly problematic in methane-based gas mixtures like biogas and natural gas, where it can significantly reduce the fuel's quality and heating value[1,2]. Biogas, obtained from the anaerobic fermentation of biological residues, is a promising green alternative to natural gas[3,4]. It offers a sustainable solution for converting biowaste into renewable energy while reducing greenhouse gas emissions[5]. However, the separation and capture of $CO_2$ from biogas pose significant challenges. The main challenges in $CO_2$ separation from biogas include: i) Similar kinetic diameters of $CH_4$ and $CO_2$ molecules, making physical separation methods based on size exclusion ineffective. ii) Preference for low-pressure operations (close to 1 bar) to minimize energy consumption from compression work, resulting in a low driving force for separation. iii) The requirement for very high $CO_2$ removal efficiency ($\geq 98\%$) to meet pipeline-grade specifications and ensure effective utilization as a fuel.[6,7] Overcoming these challenges requires advanced technologies and materials that can selectively and efficiently separate $CO_2$ from $CH_4$ under mild operating conditions. Research efforts are focused on developing novel separation processes, such as membrane separation, adsorption, and chemical absorption, to achieve high $CO_2$ removal efficiency while minimizing energy consumption and meeting the stringent requirements for biogas upgrading. At a large scale, capturing $CO_2$ for methane purification is primarily achieved through water scrubbing and chemical (amine) scrubbing[8,9], which are well-established technologies[10,11]. However, these methods have significant drawbacks: *i*) High energy requirement for solvent regeneration: Both water scrubbing and amine scrubbing require substantial energy input to regenerate the solvents used in the $CO_2$ capture process. This energy requirement can be a major operational cost, especially for large-scale applications. *ii*)Large footprint: Both scrubbing systems typically require extensive infrastructure and equipment, resulting in a large physical footprint. This can be a limiting factor for small-scale industries or facilities with limited space. In the case of amine scrubbing, an additional drawback is *iii*) Waste management: Amine scrubbing generates solid salts and traces of gaseous compounds due to amine degradation. These waste products require proper han-

dling, treatment, and disposal, which can pose environmental and regulatory challenges. This necessitates the development of alternative solutions based on novel and cutting-edge materials. The separation of $CO_2/CH_4$ mixtures directly in the gas phase would be highly desirable. In this context, a promising process for gas separation is physisorption[12,13]. Due to the physical nature of the interactions involved, this process typically requires lower energy consumption during the regeneration step compared to processes governed by strong chemical interactions such as chemisorption in solid or liquid adsorbents. Different technologies based on physisorption are available, such as pressure swing adsorption (PSA)[14,15], vacuum swing adsorption (VSA)[16], and thermal swing adsorption (TSA)[17]. These technologies involve at least two consecutive steps, to operate in continuous. *Step*1) First, $CO_2$ is selectively adsorbed by the active component at high pressure and/or low temperature, and *Step*2) then, the adsorbent is regenerated by $CO_2$ desorption at lower pressure/vacuum (PSA/VSA) or/and at higher temperature (TSA). The search for efficient physisorbents for $CO_2$ removal has led to the investigation of various porous materials[18]. Benchmark zeolites exhibit competitive separation performance at high pressures (4–7 bar), with acceptable adsorption capacity and selectivity. However, their high regeneration energy requirement is a drawback[19,20]. Carbon-based materials provide advantages in terms of low cost and easy regeneration but are limited by lower adsorption capacity and selectivity. The limitations of these adsorbents currently restrict the commercial use of carbon capture (CC) technologies to niche applications. To open up new opportunities for CC, suitable materials are needed that combine high adsorption capacity at low/moderate working pressures, high selectivity for $CO_2$ over molecules of similar dimensions (e.g. $CH_4$ and $N_2$), low-energy regeneration, and fast adsorption/desorption kinetics. Such materials would enable the implementation of CC not only for biogas upgrading but also in many other fields, especially if CC becomes economically competitive with current $CO_2$ emission rights.

Metal-organic frameworks (MOFs) are a class of crystalline and porous materials[21,22] synthesized by the self-assembly of metal ions or clusters with organic ligands or linkers[23,24]. These materials exhibit exceptional properties[25], including high accessible surface areas (up to 6200 $m^2g^{-1}$)[26], exceptionally high porosities (up to 90%)[27], tunability in pore dimensions and morphology[28], versatile function-

ality[29], and thermal and chemical stability[30]. Due to these properties, MOFs are considered promising materials for selective gas separations, potentially able to overcome the intrinsic limitations of traditional adsorbents[31–33]. Although over 70,000 MOFs have been discovered to date, only a few have shown promising features for adsorption/desorption protocols or as membrane components for $CO_2$ capture[21,34]. Some notable examples include CALF-20, a Zn-based oxalate-bridged framework with high performance in $CO_2$ capture from flue gas and remarkable robustness under humid conditions[35], and $Mg_2(dobpdc)$, a Mg-based tetramine-functionalized framework[36] with exceptional cyclability and stability during $CO_2$ capture from flue gas. In the case of $CO_2/CH_4$ separations for biogas upgrading, MUF-16 ($Co(Haip)_2$, Haip = 5-aminoisophthalic acid) is a noteworthy MOF[37]. It can capture carbon dioxide from hydrocarbons with exceptional selectivity, although with moderate $CO_2$ adsorption capacity. Another interesting MOF is $Qc-5-Cu-sql$, a Cu-quinoline-5-carboxylic acid supramolecular network that exhibits excellent $CO_2/CH_4$ selectivity via a molecular sieving mechanism. However, in this case, too, moderate $CO_2$ adsorption capacity is reported[38]. In many instances, critical elements affecting the industrial feasibility of MOFs as selective $CO_2$ adsorbents, including the scalability and sustainability of the synthesis process and the shaping of the materials into desired forms such as beads, pellets, or monoliths, have not received sufficient attention[39].

TAMOF-1 is the first in a series of novel homochiral MOFs based on natural amino acid derivatives, by transformation of the $\alpha-$amino unit into a triazole group[40,41]. TAMOF-1 ($[Cu(S-TA)_2].xH_2O$, $S-HTA = (S)-3-(1H-imidazol-5-yl)-2-(4H-1,2,4-triazol-4-yl)-propanoic\ acid$) is easily synthesized at large scale from low-cost raw materials just by reaction of a copper(II) salt with L-histidine derivative ($imidazole-5-ylmethyl$)-($1,2,4-triazol-4-yl$)$acetate(L1)$ in water. This material has a 3D network, made from 10 Å wide, helicoidal, intercommunicated channels, decorated with multiple dangling functional groups carboxylate, triazole and imidazole exhibiting a BET specific surface area of 980±50 $m^2g^{-1}$ and a micropore volume of 0.38 $cm^3g^{-1}$[42]. Moreover, water can be initially removed and the material can be activated for gas separation just after mild heating up to 353–393 K in presence of vacuum. These conditions are milder than those generally required for common MOFs or zeolites[43,44].

In our previous reports, we demonstrated the remarkable performance of TAMOF-1 as a stationary phase for enantioselective chromatographic separations of racemic mixtures, owing to its intrinsic porosity and homochirality[41]. This unique combination of properties enables efficient chiral recognition and separation of enantiomers. Furthermore, TAMOF-1 has been successfully employed for the kinetic resolution of chiral substrates via catalytic coupling reactions, showcasing its potential in asymmetric synthesis[42]. Beyond its enantioselectivity, TAMOF-1 also exhibits exceptional capability for the separation of volatile organic compounds (VOCs), including the challenging benzene-cyclohexane system and xylene isomers[45]. The characteristic shape and size of its channels and pores, along with the presence of the Cu metal center, contribute to its high efficiency in VOC separations. Notably, TAMOF-1 demonstrates versatility by achieving effective separations in both liquid and gas phases. Moreover, in Chapter 3 we demonstrate that TAMOF-1 possesses an extraordinary capacity for $CO_2$ adsorption, making it a promising material for industrial applications. It exhibits impressive selectivity for $CO_2$ over $N_2$, rendering it suitable for $CO_2$ capture and separation processes. Crucially, TAMOF-1 displays excellent cyclic stability, maintaining high performance in terms of $CO_2$ recovery and purity over multiple adsorption-desorption cycles. This stability is of paramount importance for practical applications, as it ensures the long-term viability and efficiency of the material.

Here we report how TAMOF-1 is a highly selective physisorbent to resolve $CO_2/CH_4$ mixtures and in a broader context, aiming upgrading the biogas. Breakthrough experiments with a bed of TAMOF-1 powder show its capability to selective separate $CO_2$ from methane and nitrogen in ternary $CO_2/CH_4/N_2$ gas mixtures, with efficient performance in a wide concentration. Indeed, $CO_2$ adsorption properties depend just on the $CO_2$ relative molar flow, with negligible effects from the presence of other gases ($CH_4$ and/or $N_2$). TAMOF-1 exhibits a high selectivity for $CO_2$ over $CH_4$ across a broad concentration range. By combining experimental adsorption data with theoretical tools such as Monte Carlo simulations and molecular dynamics, it was observed that $CH_4$ undergoes rapid mass transfer within TAMOF-1, facilitating its efficient removal with high purity. Additionally, TAMOF-1 demonstrated remarkable cyclic stability in adsorption/desorption experiments when employed as a pellet. These findings highlight the promising potential of TAMOF-1 as an adsor-

bent for $CO_2/CH_4$ mixtures, particularly in the biogas gas context. This material offers a promising solution to bridge the gap between effective adsorption and affordable regeneration, making it a viable candidate for practical applications.

## 4.2 Materials and methods.

### 4.2.1 Materials.

TAMOF-1, with molecular formula $[Cu(H_2O)_2(C_8H_8N_5O_2)_2].6H_2O$, was synthesized following the procedure described in a previous publication[41]. The structure and purity of the samples was confirmed by powder X-ray diffraction (Fig. C.1). Following the procedure outlined in Chapter 3, a TAMOF-1 pellet was also synthesized.



### 4.2.2 Adsorption isotherms.

Adsorption isotherms of carbon dioxide,methane and nitrogen, (up to 10 bar) at 298K were carried out with an Autosorb iQ (Quantachrome). Adsorption isotherms of $CO_2$ were also performed at several temperatures, between 293–333 K. Prior to analysis, the sample was degassed and dehydrated (activated) for 24 hours at 423 K and $10^{-6}$ Torr.

### 4.2.3 Dynamic fixed-bed column adsorption experiments.

#### Gas separation module.

For the breakthrough experiments, different tubes loaded with different TAMOF-1 amounts were used as separation modules . Noteworthy, the experiments gave consistent per mass results. Two different columns were used: *Column 1*: 1 g TAMOF-1 powder (0.77 g dehydrated), bed length and inner diameter: 1.45 cm and 1.27 cm; *Column 2*: 10.1 g TAMOF-1 powder (7.84 g dehydrated), and 10.86 g TAMOF-1 pellet (8.38 g dehydrated), bed length and inner diameter: 5.9 cm and 1.95 cm. Scaling the system does not affect TAMOF-1 performance. In both, TAMOF-1 was packed within the module with glass wool support at the top and the bottom of the column.

**MOF activation procedure.**

Prior to measurements, TAMOF-1 was activated in situ for water removal. The activation was performed at 393 K for 15 hours by applying a vacuum ($10^{-1}$ mbar) at both the top and the bottom of the module. This procedure removes any residual water molecules that may interfere with the adsorption of $CO_2$. After activation, the performance of the adsorption was evaluated by flowing pure $CO_2$ (5 ml $min^{-1}$) through the TAMOF-1 and measuring the adsorption capacity. The measured adsorption capacity should be consistent with the value measured by the adsorption isotherm.



### 4.2.4 Set-up and Experimental conditions.

Breakthrough measures were performed by using the experimental set-up shown in Figure C.2. Gas cylinders of, CH4 (Linde, 99.998%), $CO_2$ (Air Liquide, 99.998%), $CO_2/CH_4$ mixture with composition of 50.3/49.7% (Messer) and $N_2$ (Praxair, 99.999%) were used. The flows/compositions of the inlet gas stream were controlled upstream the separation module by a set of calibrated mass flow controllers (Bronkhorst EL-FLOW). A manometer and a backpressure controller (Bronkhorst, EL-PRESS) were placed downstream the separation module. A manometer was also used upstream the bed to monitor the actual pressure at the bed inlet under no pressure control conditions. Unless otherwise stated, all pressure values are reported in units of absolute bar (bar). The separation module was heated by a linear power silicone heating wire ($\theta$ 3mm FOR-FLEX NORMAL, Electricfor) rolled around the column, the temperature was measured with a K-type thermocouple (Thermocoax) placed in between the module and the silicon heating wire, and in contact with both. It was controlled with a temperature controller EZ-Zone (Watlow). The outlet stream of the column was on-line analyzed by micro gas chromatograph (MGC, Agilent MicroGC 490) equipped with Molsieve MS5A, using Ar as carrier gas (99.999 % purity), and Poraplot U column, using He as carrier gas (99.999 % purity), along with thermal conductivity detectors (TCD). In the experiments performed with a pure $CO_2/CH_4$ mixture flow below 30 ml $min^{-1}$, a nitrogen flow of 30 NmL $min^{-1}$ was mixed with the gas coming out from the separation module in order to meet the flow requirements of the GC. In this case, a non-return valve with negligible pressure drop was used to avoid reverse flow. Prior to each measurement, following

a thorough cleaning of the column, it is filled with Helium gas. The transit time or death time of the gas in the set-up was also evaluated and subtracted at each operation condition.

**Breakthrough measures TAMOF-1 powder.**

Breakthrough curve measurements for TAMOF-1 powder were conducted under varying conditions in two columns. In the *Column 1 (1g)*, measurements were taken with varying $CO_2/CH_4$ ratios of 25:75, 50:50, and 75:25, as well as with a constant 50% $CO_2$ concentration and varying $CH_4/N_2$ ratios of 50:50:0, 50:25:25, and 50:0:50. All measurements in the small column were conducted at 25ºC and 1.05 bar. In the *Column 2 (10g)*, measurements were performed with a constant 5% $CO_2/CH_4$ mixture (He balance), but with varying $CO_2/CH_4$ ratios of 50:50, 30:70, and 70:30. These measurements were conducted with a total inlet gas velocity of 0.015 m $s^{-1}$ at 25ºC and 1.05 bar.



**Adsorption–desorption cycles test.**

Adsorption/desorption cycling was performed on a packed bed of activated TAMOF-1 pellets using *column 2*. A 50:50 $CO_2/CH_4$ mixture was introduced at a total flow rate of 30 ml $min^{-1}$, under conditions of 25ºC and 1.05 bar. Desorption was achieved through vacuum regeneration, with each cycle's duration determined by the breakthrough point observed during adsorption. A total of 10 cycles were evaluated.

**Computational methods.**

Monte Carlo (MC) and Molecular Dynamics (MD) simulations were performed by Salvador R.G. Balestra and Sofia Calero from the Eindhoven University to investigate the sorption and transport properties of carbon dioxide, methane, and nitrogen molecules both individually and as mixtures within the TAMOF-1 material. The theoretical analysis focused on discerning the mechanisms that explain the separation process of mixtures of interest from a molecular perspective. In addition to sorption and transport properties we also calculated the breakthrough curves. To conduct these, the simulations were performed at various temperatures, from $263.15 - 333.15K$. They used a cubic supercell with dimensions of 2 x 2 x 2 for TAMOF-1. The initial

relaxation of the atomic coordinates was achieved using an extended semi-empirical tight-binding model known as GFN2-xTB,[46] which was performed using DFTB+ code (v. 22.2)[47]. The $CO_2$ model comprises three Lennard-Jones sites with charges centered on each atom. The carbon–oxygen bonds remain fixed, while the Lennard-Jones parameters and the molecular structure of $CO_2$ were derived from research conducted by García-Sánchez et al[48]. For the $N_2$ molecule, they adopted the model proposed by Potoff and Siepmann[49], which incorporates three charged sites and two Lennard-Jones sites centered on each N atom. Regarding the $CH_4$ molecule, they used an uncharged united atom model[50], considering the $CH_4$ group as a single interaction center with its own effective potentials. TAMOF-1 framework was assumed to be rigid during both the MC and MD simulations. To accurately capture the interactions between the adsorbates and framework, a van der Waals interactions were employed. Furthermore, Coulombic interactions were considered for the $CO_2$ and $N_2$ molecules. The Ewald method was used in these cases. The Lennard-Jones parameters were derived from the well-established DREIDING potential[51], except for the Cu atoms, for which we adopted parameters from the UFF potential[52]. The mixed Lennard-Jones parameters were calculated using Lorentz-Berthelot mixing rules. To perform the MC and MD simulations, the reliable RASPA code[53] was used, and followed the established protocols. This protocol has been used successfully for other Cu-paddlewheel MOF (Cu-BTC)[54].The adsorption isotherms were determined through MC simulations using a Grand Canonical ensemble ($\mu$ VT). The pressure values were converted to fugacity using the Peng-Robinson equation of state. The simulation conducted minimum of $10^6$ MC cycles. Within each MC cycle, the following trial MC moves were randomly selected for a given molecule: translation, rotation, reinsertion at random positions, and swapping (insertion or deletion). Binary isotherms and selectivities were calculated using IAST using the RUPTURA code[55]. The time step used in the MD simulations was 0.5 fs to carry out 108 cycles of simulation. During the MD simulation, the radial distribution functions and atomic mean squared displacements were calculated. To study the transport properties of $CO_2$ and $CH_4$, we equilibrated the systems using a canonical ensemble (NVT). Subsequently, using the microcanonical ensemble (NVE), the self-diffusion coefficients for $CO_2$ and $CH_4$ from the measured mean-squared displacement at several concentrations and temperatures was calculated.

# 4.3 Results and discussion.

## 4.3.1 Adsorption isotherms measures.

Single-gas ($CO_2$, $CH_4$, and $N_2$) adsorption isotherms of TAMOF-1 powder were measured up to 10 bars in the 293-353 K temperature range (Figure 4.1). All isotherms retain their characteristic shapes with increasing gas uptake as the temperature decreases. Type I isotherms are observed for $CO_2$, indicating microporous behavior without reaching a plateau (saturation) within the studied pressure range. For instance, at 298 K, $CO_2$ adsorption capacities of 3.8 and 6.5 mmol $g^{-1}$ are achieved at 1 and 10 bars, respectively. In contrast, both $CH_4$ and $N_2$ exhibit near-linear isotherms, suggesting negligible adsorption. This behavior demonstrates the selective preferential adsorption of carbon dioxide over $CH_4$ and $N_2$, with the adsorption capacity following the order $CO_2 << CH_4 < N_2$.

The $CO_2$ adsorption isotherm was successfully fitted using the Langmuir-Freundlich model, revealing a maximum theoretical adsorption capacity ($q_m$) of 10.6 mmol $g^{-1}$. Conversely, $CH_4$ and $N_2$ adsorption isotherms were accurately described by the Langmuir model. Comparison with the single-site Langmuir-Freundlich model in a log(q) vs. log(P) plot (Figure C.4) suggests that at least two distinct adsorption sites contribute to the dominant $CO_2$ uptake. Isotherm parameters and regression coefficients are detailed in Table C.1. Table C.2 presents the $CO_2/CH_4$ selectivity values calculated using Ideal Adsorbed Solution Theory (IAST). At 298 K and 1 bar, selectivity values of 35.6, 32.8, and 31.8 were obtained for 30:70, 50:50, and 70:30 $CO_2/CH_4$ gas mixtures, respectively. Importantly, complete adsorption/desorption reversibility was observed for all gases (Figure 4.1c) without hysteresis, confirming the physical nature of gas adsorption within the TAMOF-1 network and emphasizing the material's structural rigidity. The behavior of the $CO_2$ isosteric heat of adsorption ($-\Delta H_{ads}$) was described before in chapter 3. With a high $-\Delta H_{ads}$ is found at low pressure (zero coverage), and then it rapidly decreases as CO2 uptake increases, approaching the bulk-phase sublimation heat of $CO_2$, 26-27 kJ $mol^{-1}$, at an adsorption capacity higher than 2 mmol $g^{-1}$.

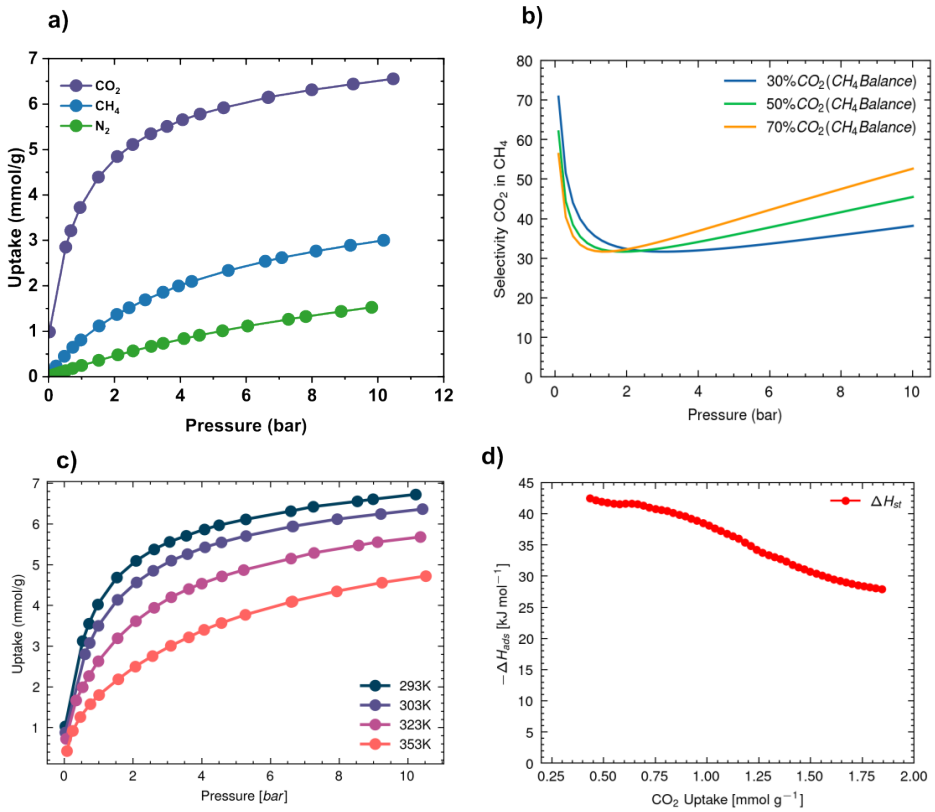


Figure 4.1: a) Adsorption/desorption isotherms of $CO_2$, $CH_4$ and $N_2$ in a TAMOF-1 powder sample at 25ºC up to 10 bar. b) IAST selectivity of different $CO_2/CH_4$ gas mixtures with varying ratios at 25ºC up to 10 bar. c) Adsorption/desorption isotherms of $CO_2$ with a temperature range 293K–353K up to 10 bar. d) $CO_2$ isosteric heat of adsorption as a function of $CO_2$ uptake.

### 4.3.2 Breakthrough measures.

In Figure 4.2a, the methane/carbon dioxide breakthrough curve through a TAMOF-1 powder bed at 1 bar and 298 K is presented, with a 50:50 ratio of mixture gas. The rivalry between $CO_2$ and $CH_4$ becomes evident in the ascending pattern (rolling–up effect) exhibited by the methane curve as it emerges from the TAMOF-1 bed, reflecting their competitive dynamics. Methane exhibits a lower affinity compared to $CO_2$, resulting in a breakthrough time ($BT_t$) of 8 min $g^{-1}$ for CH4 and 16.4 min $g^{-1}$ for $CO_2$. At the breakthrough point, the $CO_2$ capacity $q_b(CO_2)$ is 1.65 mmol $g^{-1}$, which is 34% lower than the total adsorption capacity $q_s(CO_2)$ of 2.5 mmol $g^{-1}$. Methane exhibits an approximate $q_s(CH_4)$ capacity of 1 mmol $g^{-1}$. Under these conditions, a high selectivity of $CO_2$ with respect to methane is observed, with a selectivity value $S_s(50CO_2 : 50CH_4)$ of 2.5. Figure 4.2b presents the breakthrough curves for diverse $CO_2/CH_4$ ratios (25:75, 50:50, and 75:25). Pure methane ($\geq$ 99.9%) elutes first and rapidly from the bed. Typical S-shaped curves were observed for $CO_2$ adsorption, with a slight steepening of the curve as the $CO_2$ concentration increased. Effective $CO_2/CH_4$ separation is achieved in all cases due to significantly delayed CO2 elution. This confirms slower $CO_2$ diffusion through the TAMOF-1 bed. Reducing the $CO_2$ molar flow shifts the related curves towards longer breakthrough times. $BT_t(CO_2)$ increases from 16.4 to 18.7 min $g^{-1}$ when the $CO_2/CH_4$ ratio is reduced from 50:50 to 25:75. Conversely, $BT_t(CH_4)$ also decreases with $CH_4$ concentration but is less noticeable, with a reduction of $BT_t(CH_4)$ from 9.9 to 6.7 min $g^{-1}$ for concentrations ranging from 25% to 75%. The extremely rapid elution of $CH_4$ makes experimental differentiation challenging. Carbon dioxide and methane adsorption capacities were also evaluated. Additionally, the selectivities ($S_s$) exhibit a decreasing trend as the $CO_2/CH_4$ ratio decreases, with $S_s(25 : 75) > S_s(50 : 50) > S_s(75 : 25)$. Gas separation parameters obtained from the breakthrough curves are reported in Table C.3 (See SI for details).

Nitrogen is a commonly encountered gas in various gas streams, often in combination with carbon dioxide $CO_2$ and $CH_4$. To evaluate the separation performance of TAMOF-1 for $CO_2/CH_4/N_2$ mixtures, fixed-bed column experiments were conducted by varying the $CH_4/N_2$ ratio while maintaining a constant $CO_2$ concentration of 50% (Figure 4.2c). The breakthrough curves for $CO_2$ exhibit perfect

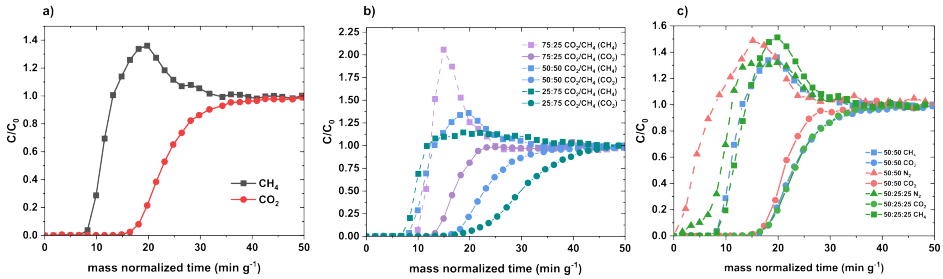


Figure 4.2: a) Breakthrough curves of $CO_2$ and $CH_4$ for 50:50 gas composition. b) Breakthrough curves of $CO_2$ (solid line) and $CH_4$ (dashed line) for binary mixtures with different composition: $CO_2/CH_4$: 25/75 (green), 50/50 (blue), 75/25 (purple). c) $CO_2$ and $CH_4$ breakthrough curves in different inlet gas mixtures: $CO_2/CH_4$=50/50 (blue), $CO_2/N_2$=50/50 (red), $CO_2/CH_4/N_2$=50/25/25 (green). All measurements were performed with 0.77 g of activated TAMOF-1 at 298 K, minimum pressure ($\Delta$ P=0.1bar) and overall flow rate of 5 NmL $min^{-1}$.



overlap, regardless of the $CH_4/N_2$ ratio. This observation suggests that the diffusion of $CO_2$ through TAMOF-1 is unaffected by the presence or type of other gas components ($CH_4$ or $N_2$) in the inlet gas mixture. Consequently, the $CO_2$ adsorption capacities remain relatively constant ($q_s = 2.5 \pm 0.03$ mmol $g^{-1}$, $q_b = 1.67 \pm 0.02$ mmol $g^{-1}$) across different $CH_4/N_2$ ratios, as shown in Table C.3 . It is evident that the selectivity for $CO_2/CH_4$ separation depends solely on the relative concentration of $CO_2$ and $CH_4$ in the inlet gas mixture. Notably, similar $CO_2/CH_4$ selectivities were observed for both binary ($CO_2/CH_4$) and ternary ($CO_2/CH_4/N_2$) gas mixtures with the same $CO_2$ concentration of 50%, yielding selectivity values of $S_s = 2.5$ and $S_s = 2.1$, respectively.

As expected, the values follow the same trend regardless of the $CH_4/N_2$ ratio present in the inlet mixture. These gases do not affect the adsorption capacity, which depends directly on the $CO_2$ concentration, in agreement with isotherms measures (Figure 4.1). It is important to mention that $N_2$, when present, exits as first and almost immediately from the column with elution time almost coincident with the dead time. This finding highlights the exceptional $CO_2/N_2$ separation performance, as discussed in detail in Chapter 3.

Understanding mass transfer under dynamic conditions is crucial, as laboratory setups often require a carrier gas (e.g., He) to replicate higher gas velocities unachievable with pure gas mixtures. Figure 4.3

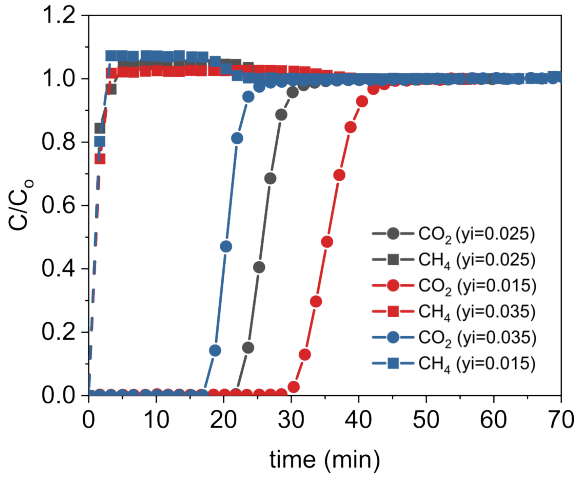


Figure 4.3: Breakthrough curves of $CO_2$ (dots) and $CH_4$ (squares) in a He carrier gas (95% concentration) at different $CO_2/CH_4$ gas-mixture ratios (30:70, 50:50, and 70:30) and a total gas velocity of 0.015 m $s^{-1}$. All measurements were performed with 7.84 g of activated TAMOF-1 at 298 K, pressure of 1.05 ($\Delta$ P=0.3bar) and overall flow rate of 269 NmL $min^{-1}$.



illustrates breakthrough curves at 0.015 m $s^{-1}$ total gas velocity with varying $CO_2/CH_4$ ratios. Consistent S-shaped $CO_2$ curves indicate similar mass transfer rates, while the absence of $CH_4$ breakthrough suggests minimal interaction with the TAMOF-1 pore structure. This behavior contrasts with Figure 4b, where higher CH4 adsorption was observed. Under dynamic conditions under the presence of a carrier gas (e.g, He), both selectivity values, Ss and Sb, increase compared to those evaluated with pure gas mixtures at lower velocities (Table S18). This suggests that $CH_4$ has a very weak interaction with TAMOF-1, as the inner He carrier gas readily displaces it, preventing accurate measurement of its breakthrough point. Conversely, $CO_2$ exhibits stronger interaction, resulting in longer $BTt(CO_2)$ of 17.8, 22, and 30.4 minutes for decreasing $CO_2/CH_4$ ratios (30:70, 50:50, and 70:30). $CH_4$ adsorption capacity at saturation is negligible (0.02 $\pm$ 0.01 mmol $g^{-1}$) across all ratios, while $CO_2$ adsorption capacity increases with concentration ($q_s = 0.59 \rightarrow 0.78 mmol g^{-1}$), as expected. These experimental results align with the theoretical computational modeling discussed in Section 4.3.4.

### 4.3.3 Adsorption/desorption cycles test.



Cyclic desorption studies are crucial for evaluating the robustness and practical applicability of TAMOF-1 pellets in industrial settings, such as biogas upgrading for $CH_4$ purification. The regeneration of a saturated TAMOF-1 bed appears straightforward, requiring only vacuum application at constant temperature, eliminating the need for thermal heating. In Figure 4.4 the concentration profiles of both $CH_4$ and $CO_2$ perfectly coincide in all cases from step1b–1j, suggesting no degradation of TAMOF-1 after consecutive adsorption/desorption cycles. The material fully recovers its performance, achieving a working capacity greater than 99% under steady-state conditions within the studied operation parameters. Ten adsorption/desorption cycles (a–j) were conducted. The initial adsorption step (1a) after activation reveals $CO_2$ and $CH_4$ adsorption capacities of 1.74 mmol $g^{-1}$ and 0.4 mmol $g^{-1}$, respectively, resulting in a $CO_2/CH_4$ selectivity ($S_s$) of 4.4. This exceeds the selectivity observed with TAMOF-1 powder under identical conditions, highlighting one of the advantages of the pellet form. Moreover, the $CO_2$ breakthrough capacity ($q_b(CO_2)$) experiences a minor reduction to 1.4 mmol g, representing only a 19% loss of total capacity. Subsequent cycles (b-j) maintain consistent breakthrough points for both $CO_2$ (20 min) and $CH_4$ ($< 1$ min), indicating stable steady–state capacities of 1.5 mmol $g^{-1}$ and 0.4 mmol $g^{-1}$ for $CO_2$ and $CH_4$, respectively. At steady state, $q_b(CO_2)$ is 1.14 mmol $g^{-1}$. This highlights the rapid and nearly complete regeneration achievable with approximately 22 minutes of vacuum (Step 2), matching the $CO_2$ breakthrough time in Step 1.

TAMOF-1 pellets exhibit fast desorption and cyclic stability (up to 10 cycles), maintaining their steady–state $CO_2$ adsorption capacity. However, for practical industrial implementation, system design optimization is essential, focusing on maximizing $CH_4$ purity rather than $CO_2$ recovery. Regeneration time can be further reduced by increasing nitrogen flow rate, lowering pressure, or elevating temperature. While these results are promising, and highlight the potential of TAMOF-1 as an adsorbent for pressure/vacuum/thermal swing adsorption processes. Further optimization is necessary to fully realize the potential of TAMOF-1 pellets for biogas upgrading.

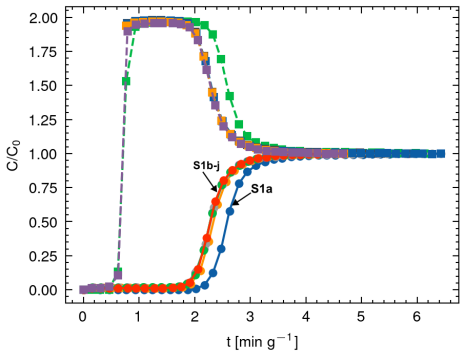


Figure 4.4: $CO_2$ and $CH_4$ breakthrough curves after vacuum regeneration time (matching the $CO_2$ breakthrough time). Measures were performed with 8.38 g of activated TAMOF-1 pellet at 298 K, pressure of 1.05 bar and overall flow rate of 30 NmL $min^{-1}$.



### 4.3.4 Computational analysis and adsorption mechanisms.

The single-component adsorption isotherms for $CO_2$, $CH_4$, and $N_2$ molecules on TAMOF-1 were calculated in the temperature range of 263–333 K and the pressure range of $1 - 10^7$ Pa. The simulation results demonstrated excellent agreement with experimental data, validating the models (Figure 7). The protocol of Myers and Monson[56] was employed to calculate excess adsorption, allowing for direct comparison with experimental data. Furthermore, the determination of several energy parameters associated with carbon capture from single-component isotherms of $CO_2$ and $N_2$ revealed that TAMOF-1 exhibits a low parasitic energy, a volumetric working capacity of 23.463 kg $m^{-3}$, and a final $CO_2$ molar purity of the mixture of 0.904. These characteristics are highly desirable for carbon capture applications.

The calculated adsorption isotherms were fitted to a dual site (for $CO_2$) and single site (for $CH_4$ and $N_2$) Langmuir-Freundlich model using the RUPTURA software[55] (solid lines in Figure 4.5). Subsequently, we proceeded to compute the binary isotherms and determine the adsorption selectivities for $CO_2$:$CH_4$ and 14 $CO_2$: 84 $N_2$ mixtures (representing the composition of dry post-combustion flue gas). The resulting adsorption selectivities are depicted in Figure 4.5 (bottom-right). Notably, in all cases, the adsorption of $CO_2$ surpasses that of $CH_4$ or $N_2$, primarily due to the stronger interactions between

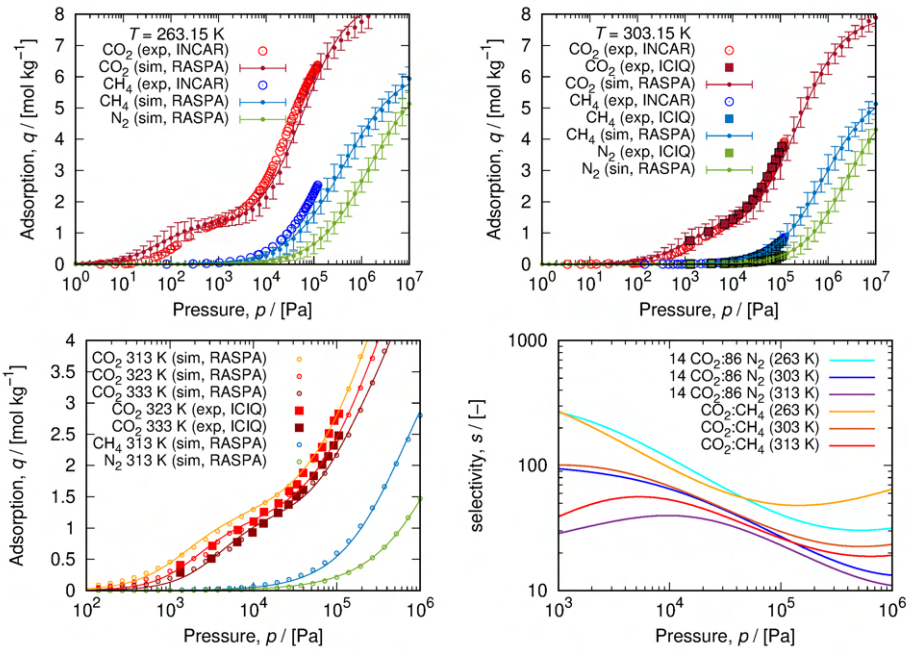


Figure 4.5: Top and bottom-left panel: Calculated excess adsorption isotherm (empty circles) and experimental isotherms (solid points, see legend for more details) at 263.15 K, 303.15 K, 313 K, 323 K, and 333 K. Errors are estimated from the standard deviation in the adsorption processes. Bottom-right panel: Selectivity $s_j^i = q^i/q^j$, where $i$ is $CO_2$, and $j$ is $CH_4$ or $N_2$. Figure provided by Salvador R.G. Balestra and Sofia Calero (results are yet to be published.)

$CO_2$ molecules and the adsorption surfaces.

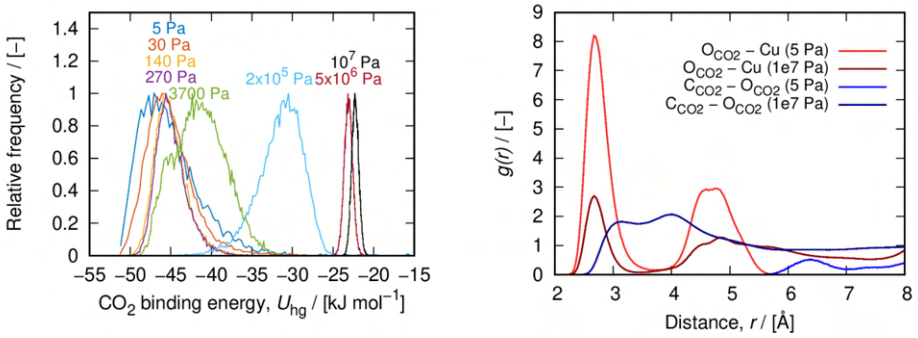


Figure 4.6: (left) Histogram for the $CO_2$-TAMOF-1 interaction energy, $U_hg$, at several values of pressure. (right) Radial distribution function $g(r)$ for $O_{CO_2} - C_{CO_2}$(intermolecular) pairs, and $O_{CO_2} - Cu$ atoms. Figure provided by Salvador R.G. Balestra and Sofia Calero (results are yet to be published).

At low pressure values (1–500 Pa), carbon dioxide molecules are primarily located within the narrow channels created by the triad of Cu atoms, as revealed by simulation. A dominant interaction occurs between $CO_2$ and two Cu atoms, resulting in high values for the heat of adsorption $Q_{st}^{CO_2}$ ($\sim$ 50 kJ mol$^{-1}$). This finding aligns with experimental observations, confirming the accuracy of the simulation($Q_{\text{st}} \sim -\langle U_{hg} \rangle + RT$, where $\langle U_{hg} \rangle$ is the mean interaction energy between the $CO_2$ and the TAMOF-1 at very low pressure). However, as the $CO_2$ pressure increases, the $CO_2 - CO_2$ interactions become sufficiently strong to displace some of the adsorbed $CO_2$ molecules from the energetically favorable binding sites. This is evident from the radial distribution functions between $CO_2 - CO_2$ and $CO_2 - Cu$ atoms depicted in Figure 4.6. Figure 4.6 (left panel) reveals that the interaction energy between the CO2 molecule and the adsorption surface remains stable at approximately $-45 kJ mol^{-1}$ up to 3 kPa and gradually decreases with pressure to $-23 kJ mol^{-1}$. The isosteric heat of adsorption, as shown in Figure 4.1d, supports these findings. It decreases as the $CO_2$ uptake increases. This observation suggests that the interactions between the adsorbent and $CO_2$ molecules weaken as more $CO_2$ is adsorbed. This weakening of interactions can be attributed to several factors, such as the saturation of adsorption sites, steric hindrance between adsorbed $CO_2$ molecules, or changes in the electronic structure of the adsorbent. Although

this trend is qualitatively similar for $CH_4$ and $N_2$, the range of energies and pressures varies, and its effect on adsorption is negligible. For instance, in the case of $CH_4$, the interaction energy ranges from $-25 kJmol^{-1}$ (low pressure) to $-12 kJmol^{-1}$ (high pressure). The adsorption selectivity of $CO_2$ over $CH_4$ or $N_2$, as depicted in Figure 4.5 (bottom right), can be primarily attributed to two factors at intermediate pressures. Firstly, the electrostatic interactions between $CO_2$ molecules and the copper paddlewheel contribute to the selectivity. Secondly, the confinement of $CO_2$ molecules within the pocket-cages of the TAMOF-1 structure also plays a role. However, at high pressures, the narrow pores formed by the triad of copper atoms can limit the selectivity.

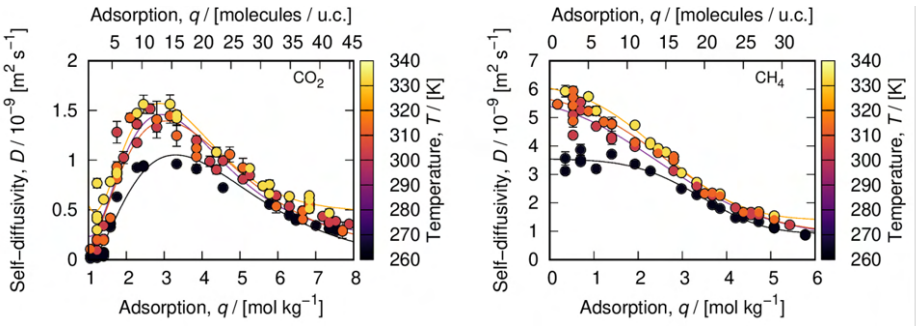


Figure 4.7: Self-diffusivity coefficient (D) for $CO_2$ (left) and $CH_4$ (right) at various temperatures and adsorption loadings. Solid lines are fitted to the data as guiding references to assist the reader. Figure provided by Salvador R.G. Balestra and Sofia Calero (results are yet to be published.)

The self-diffusion coefficients (D) of $CO_2$ and $CH_4$ were calculated using MD simulations at varying temperatures and adsorption loadings (Figure 4.7). $CO_2$ consistently exhibits lower diffusivity than $CH_4$. At low loading (1 to 4 $CO_2$ molecules per unit cell), $CO_2$ molecules are confined in adsorption pockets formed by the triad Cu atoms, resulting in extremely low diffusivity (i.e., $D_s^{CO_2} \sim 10^{-10}$ m $s^{-1}$). As pressure increases, $CO_2$ molecules diffuse from the pocket adsorption site to the main channel, leading to a maximum diffusivity at $\sim 3$ mol $kg^{-1}$ of adsorption loading for all temperatures (e.g., at 333 K, the self-diffusivity is approximately $D_s^{CO_2} \sim 1.6 \times 10^{-9}$ m $s^{-1}$). Beyond this loading (three molecules per Cu triad), $CO_2$ molecules are primarily adsorbed in the (chiral) channel, hindering transport and causing a progressively decreasing diffusivity. In contrast to $CO_2$, $CH_4$ molecules reach their peak self-diffusivity at infinite dilution for

all temperatures (see Figure 4.7-right). $CH_4$ diffusion decreases with increasing adsorption. For instance, at 333 K and for 1 molecule per unit cell, the self-diffusivity coefficient is $D_s^{CH_4} \sim 6 \times 10^{-9}$ m s$^{-1}$.

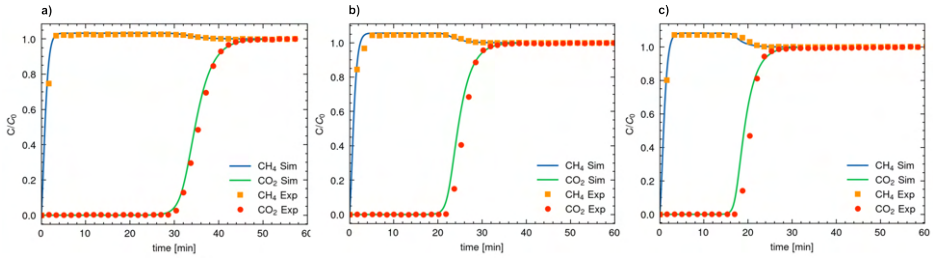


Figure 4.8: Calculated breakthrough curves (lines) and experimental values (dots) for $CO_2$ and $CH_4$ at 1.05 bar ($\Delta P = 0.25$ bar) and 298.15 K for three compositions: a) 95He: 15$CO_2$:35$CH_4$, b) 95He:25$CO_2$:25$CH_4$, and c) 95He:35$CO_2$:15$CH_4$.

Breakthrough curves for $CO_2$ and $CH_4$ were computationally predicted for a column bed length of 5.8 cm and a gas pressure of $1.05 - -1.3$ bar at 298 K (Figure 4.8). Helium was used as the carrier gas, mimicking the experimental system depicted in Figure 4.3. Three gas compositions were investigated: 0.95 He: 0.05(0.35 $CO_2$: 0.15 $CH_4$), 0.95 He: 0.05(0.25 $CO_2$: 0.25 $CH_4$), and 0.95 He: 0.05(0.15 $CO_2$: 0.35 $CH_4$). The fitted Langmuir-Freundlich parameters obtained from Figure 4.8 were utilized in these calculations. Initially, the bed column was entirely filled with helium. The void fraction of the adsorbing bed was set to 0.3. The general behavior observed in Figure 4.8 qualitatively aligns with the experimental curves presented in Figure 4.3. Notably, the eluting behavior remains qualitatively unaffected by the composition of the gas mixture.

## 4.4 Outlook.

TAMOF-1 demonstrates exceptional selectivity in separating $CO_2$ from $CH_4$ and $N_2$, a rare feat among existing materials. Importantly, it exhibits high adsorption capacity and cyclic stability in both powder and pellet forms, essential for industrial–scale $CO_2$ capture applications. The material maintains a steady-state cycling capacity ($q_s(CO_2)$) of approximately 1.5 mmol g$^{-1}$ without degradation after the second cycle. Additionally, its high IAST selectivity and equilib-

rium capacity at 1 bar and 298K ($> 3$ mmol $g^{-1}$) make it competitive with other materials reported in the literature (Figure 4.9).

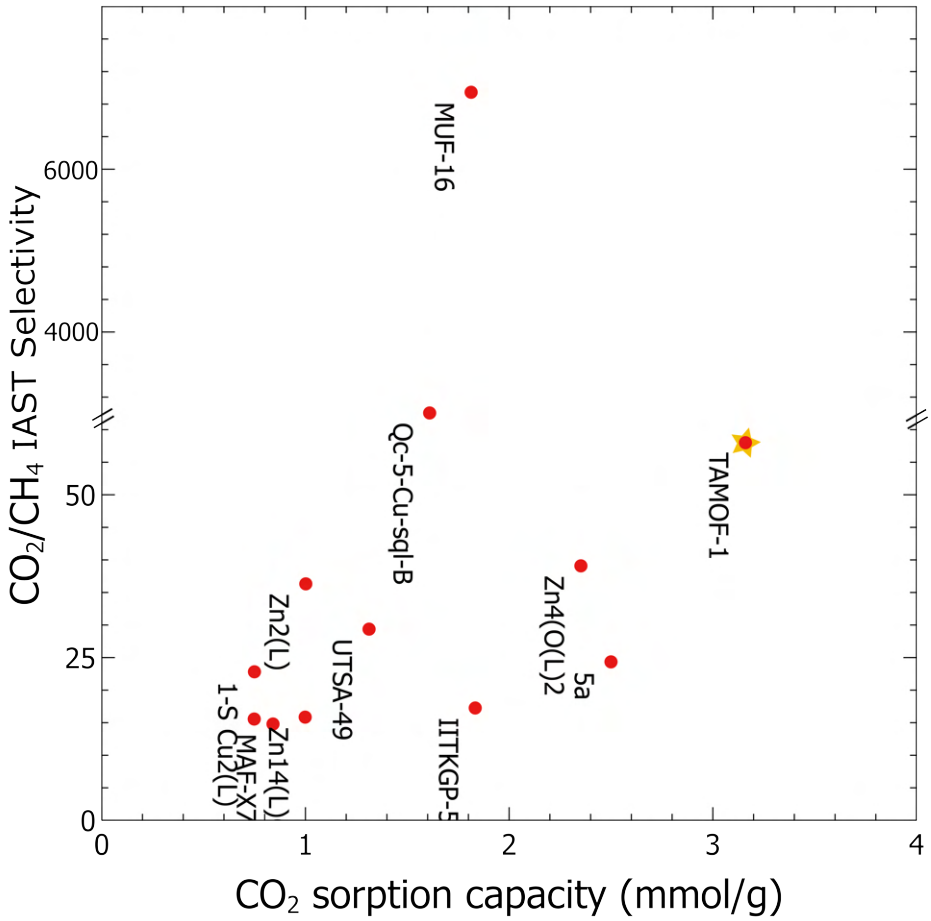


Figure 4.9: Sorption capacity versus separation selectivity plots for biogas (IAST selectivity values higher than 20 for biogas at ambient temperature, i.e., above 293 K are considered). Adapted from Sahoo et al. 2023[39].

While these preliminary results are promising for TAMOF-1's potential in biogas purification, further studies are needed to validate its effectiveness and robustness under real-world industrial conditions. For a $CO_2$ capture material to be truly sustainable, it must operate optimally in the presence of gas impurities(e.g, water, hydrogen sulfide, siloxanes.), as even trace amounts can remain after pre-purification steps. Adding such steps increases the cost of $CO_2$ capture technology, potentially rendering it unviable. Therefore, the next critical step for TAMOF-1 is to assess its performance and ro-

bustness against impurities under real operating conditions. Additionally, optimizing the operational cycle for biogas upgrading is essential.

## 4.5 Conclusions.

TAMOF-1, a stable, robust, homochiral metal organic framework (BET specific surface area = 980±50 $m^2$ $g^{-1}$) has shown selective adsorption of $CO_2$ from gas streams. Adsorption isotherms confirm the $CO_2$ preferential uptake with respect to $CH_4$ in a large pressure range, resulting in good separation parameters for CO2/CH4 gas mixtures. $CO_2/CH_4$ mixtures can be effectively separated with high selectivity (>30) in a wide $CO_2/CH_4$ concentration (30:70–70:30), at room temperature (298K) and pressure (1.05bar). Elution behavior of $CO_2$ through the TAMOF-1 bed depends just on the $CO_2$ molar flow and it is not affected by the presence of the other gasses investigated ($CH_4$ and/or $N_2$). Furthermore, under high gas velocity conditions with a carrier gas (e.g, He), $CH_4$ interaction with TAMOF-1 is negligible or absent, leading to increased $CO_2/CH_4$ selectivity. The $CO_2$ breakthrough curve retains its nearly vertical S-shape, indicating faster mass transfer under the evaluated conditions (0.015 m $s^{-1}$, 298 K, and 1.05 bar).

Computational evaluations using Monte Carlo and molecular dynamics simulations are in excellent agreement with experimental data, showcasing the exceptional sorption and transport properties of $CO_2$, $CH_4$, and $N_2$ in TAMOF-1. These findings provide valuable insights into the molecular-level interactions and behaviors of these gases within the TAMOF-1 framework.

The interactions between $CO_2$ and TAMOF-1 enable efficient and rapid regeneration of the TAMOF-1 bed. Applying a vacuum at room temperature and atmospheric pressure effectively evacuates the adsorbed $CO_2$, restoring the TAMOF-1 matrix to its original state and preparing it for the next separation cycle. This regeneration process exhibits minimal loss of adsorption capacity during continuous adsorption/desorption cycles. Notably, the regeneration process can be further accelerated by increasing the sweep gas flow, or elevating the temperature. These modifications enhance the rate of $CO_2$ desorption, allowing for faster regeneration of the TAMOF-1 bed.

Given these performance metrics, TAMOF-1 shows promise for

integration into pressure/vacuum swing adsorption (PVSA) technologies. Its convenient regeneration protocol, adaptable to specific time and energy constraints through operational parameter tuning, further enhances its practicality. Ongoing efforts are focused on designing and optimizing a $CO_2$ capture and purification process utilizing TAMOF-1, and an evaluation of the behavior of the TAMOF-1 in the presence of the characteristic impurities found in biogas-type exhaust gasses.

# References

1. Nocito, F. & Dibenedetto, A. Atmospheric $CO_2$ mitigation technologies: carbon capture utilization and storage. *Current Opinion in Green and Sustainable Chemistry* **21,** 34–43 (2020).
2. Chouikhi, N., Brandani, F., Pullumbi, P., Perre, P. & Puel, F. Biomethane production by adsorption technology: New cycle development, adsorbent selection and process optimization. *Adsorption* **26,** 1275–1289 (2020).
3. Chuah, C. Y. *et al.* Harnessing filler materials for enhancing biogas separation membranes. *Chemical reviews* **118,** 8655–8769 (2018).
4. Cavenati, S., Grande, C. A. & Rodrigues, A. E. Removal of carbon dioxide from natural gas by vacuum pressure swing adsorption. *Energy & fuels* **20,** 2648–2659 (2006).
5. D'Alessandro, D. M., Smit, B. & Long, J. R. Carbon dioxide capture: prospects for new materials. *Angewandte Chemie International Edition* **49,** 6058–6082 (2010).
6. Li, Z., Liu, P., Ou, C. & Dong, X. Porous Metal-Organic Frameworks for Carbon Dioxide Adsorption and Separation at Low Pressure. *ACS Sustainable Chemistry and Engineering* **8,** 15378–15404 (2020).
7. Gao, W. *et al.* Industrial carbon dioxide capture and utilization: state of the art and future challenges. *Chemical Society Reviews* **49,** 8584–8686 (2020).
8. Elfving, J. *et al.* Experimental comparison of regeneration methods for $CO_2$ concentration from air using amine-based adsorbent. *Chemical Engineering Journal* **404,** 126337 (2021).
9. Angelidaki, I. *et al.* Biogas upgrading and utilization: Current status and perspectives. *Biotechnology advances* **36,** 452–466 (2018).
10. Chaffee, A. L. *et al.* $CO_2$ capture by adsorption: materials and process development. *International journal of greenhouse gas control* **1,** 11–18 (2007).

11. Peters, L., Hussain, A., Follmann, M., Melin, T. & Hägg, M.-B. $CO_2$ removal from natural gas by employing amine absorption and membrane technology—A technical and economical analysis. *Chemical Engineering Journal* **172,** 952–960 (2011).

12. Liu, R.-S. *et al.* Advances in post-combustion $CO_2$ capture by physical adsorption: from materials innovation to separation practice. *ChemSusChem* **14,** 1428–1471 (2021).

13. Liu, Y. *et al.* Multifunctional covalent organic framework (COF)-Based mixed matrix membranes for enhanced $CO_2$ separation. *Journal of Membrane Science* **618,** 118693 (2021).

14. Majchrzak-Kuceba, I., Wawrzyńczak, D. & Ściubidło, A. Application of metal-organic frameworks in VPSA technology for $CO_2$ capture. *Fuel* **255,** 115773 (2019).

15. Danaci, D., Bui, M., Mac Dowell, N. & Petit, C. Exploring the limits of adsorption-based $CO_2$ capture using MOFs with PVSA – from molecular design to process economics. en. *Molecular Systems Design & Engineering* **5,** 212–231. ISSN: 2058-9689 (2020).

16. Raganati, F., Miccio, F. & Ammendola, P. Adsorption of carbon dioxide for post-combustion capture: a review. *energy & fuels* **35,** 12845–12868 (2021).

17. Singh, G. *et al.* Emerging trends in porous materials for $CO_2$ capture and conversion. *Chemical Society Reviews* **49,** 4360–4404 (2020).

18. Pardakhti, M. *et al.* Trends in solid adsorbent materials development for $CO_2$ capture. *ACS applied materials & interfaces* **11,** 34533–34559 (2019).

19. Siriwardane, R. V., Shen, M.-S., Fisher, E. P. & Losch, J. Adsorption of CO 2 on Zeolites at Moderate Temperatures. *Energy Fuels* **19,** 1153–1159 (2005).

20. Li, J.-R., Sculley, J. & Zhou, H.-C. Metal–organic frameworks for separations. *Chemical reviews* **112,** 869–932 (2012).

21. Younas, M. *et al.* Recent progress and remaining challenges in post-combustion $CO_2$ capture using metal-organic frameworks (MOFs). *Progress in Energy and Combustion Science* **80,** 100849 (2020).

22. Férey, G. Hybrid porous solids: past, present, future. *Chemical Society Reviews* **37,** 191–214 (2008).

23. Ge, X. & Ma, S. $CO_2$ capture and separation of metal–organic frameworks. *Materials for carbon capture,* 5–27 (2020).

24. Bozbiyik, B. *et al.* Adsorption and separation of n-hexane and cyclohexane on the UiO-66 metal–organic framework. *Microporous and mesoporous materials* **183,** 143–149 (2014).

25. Bazer-Bachi, D., Assié, L., Lecocq, V., Harbuzaru, B. & Falk, V. Towards industrial use of metal-organic framework: Impact of shaping on the MOF properties. *Powder technology* **255,** 52–59 (2014).

26. Furukawa, H., Cordova, K. E., O'Keeffe, M. & Yaghi, O. M. The chemistry and applications of metal-organic frameworks. *Science* **341,** 1230444 (2013).

27. Deng, H. *et al.* Large-pore apertures in a series of metal-organic frameworks. *science* **336,** 1018–1023 (2012).

28. Xue, D.-X. *et al.* Tunable rare earth fcu-MOF platform: access to adsorption kinetics driven gas/vapor separations via pore size contraction. *Journal of the American Chemical Society* **137,** 5034–5040 (2015).

29. Czaja, A. U., Trukhan, N. & Müller, U. Industrial applications of metal–organic frameworks. *Chemical Society Reviews* **38,** 1284–1293 (2009).

30. Hanikel, N. *et al.* Rapid cycling and exceptional yield in a metal-organic framework water harvester. *ACS central science* **5,** 1699–1706 (2019).

31. Li, B., Wang, H. & Chen, B. Microporous metal–organic frameworks for gas separation. *Chemistry–An Asian Journal* **9,** 1474–1498 (2014).

32. Abdelhameed, R. M., Emam, H. E., Rocha, J. & Silva, A. M. Cu-BTC metal-organic framework natural fabric composites for fuel purification. *Fuel Processing Technology* **159,** 306–312 (2017).

33. Kumar, S., Srivastava, R. & Koh, J. Utilization of zeolites as $CO_2$ capturing agents: Advances and future perspectives. *Journal of CO2 Utilization* **41,** 101251 (2020).

34. Demir, H., Aksu, G. O., Gulbalkan, H. C. & Keskin, S. MOF membranes for $CO_2$ capture: past, present and future. *Carbon Capture Science & Technology* **2,** 100026 (2022).

35. Lin, J.-B. *et al.* A scalable metal-organic framework as a durable physisorbent for carbon dioxide capture. *Science,* 1–4 (2021).

36. Kim, E. J. *et al.* Cooperative carbon capture and steam regeneration with tetraamine-appended metal–organic frameworks. *Science* **369,** 392–396 (2020).

37. Qazvini, O. T. & Telfer, S. G. MUF-16: A Robust Metal–Organic Framework for Pre- and Post-Combustion Carbon Dioxide Capture. *ACS Appl. Mater. Interfaces* **13,** 12141–12148 (2021).

38. Chen, K.-J. *et al.* Tuning Pore Size in Square-Lattice Coordination Networks for Size-Selective Sieving of $CO_2$. en. *Angewandte Chemie International Edition* **55,** 10268–10272. ISSN: 1433-7851, 1521-3773 (Aug. 2016).

39. Sahoo, R., Mondal, S., Mukherjee, D. & Das, M. C. Metal–Organic Frameworks for CO2 Separation from Flue and Biogas Mixtures. en. *Advanced Functional Materials* **32,** 2207197. ISSN: 1616-301X, 1616-3028 (Nov. 2022).

40. OCHOA, M. d. l. N. C., GARCíA, V. L. & MASCAROS, J. R. G. *A crystalline metal organic framework* en. Aug. 2019. `https://patents.google.com/patent/US20190256528A1/en`.

41. Corella-Ochoa, M. N. *et al.* Homochiral Metal-Organic Frameworks for Enantioselective Separations in Liquid Chromatography. *Journal of the American Chemical Society* **141,** 14306–14316. ISSN: 15205126 (Sept. 2019).

42. Núñez-Rico, J. L. *et al.* TAMOF-1 as a Versatile and Predictable Chiral Stationary Phase for the Resolution of Racemic Mixtures. *ACS Applied Materials & Interfaces* **15,** 39594–39605 (2023).

43. Hamon, L., Jolimaître, E. & Pirngruber, G. D. $CO_2$ and $CH_4$ separation by adsorption using Cu-BTC metal- organic framework. *Industrial & Engineering Chemistry Research* **49,** 7497–7503 (2010).

44. Asadi, T., Ehsani, M. R., Ribeiro, A. M., Loureiro, J. M. & Rodrigues, A. E. $CO_2/CH_4$ Separation by Adsorption using Nanoporous Metal organic Framework Copper-Benzene-1, 3, 5-tricarboxylate Tablet. *Chemical Engineering & Technology* **36,** 1231–1239 (2013).

45. González-Galán, C. *et al.* Separation of Volatile Organic Compounds in TAMOF-1. *ACS Applied Materials & Interfaces* **14,** 30772–30785. ISSN: 1944-8244 (July 2022).

46. Bannwarth, C., Ehlert, S. & Grimme, S. GFN2-xTB—An accurate and broadly parametrized self-consistent tight-binding quantum chemical method with multipole electrostatics and density-dependent dispersion contributions. *Journal of chemical theory and computation* **15,** 1652–1671 (2019).

47. Hourahine, B. *et al.* DFTB+, a software package for efficient approximate density functional theory based atomistic simulations. *The Journal of chemical physics* **152** (2020).

48. Garcia-Sanchez, A. *et al.* Transferable force field for carbon dioxide adsorption in zeolites. *The Journal of Physical Chemistry C* **113,** 8814–8820 (2009).

49. Potoff, J. J. & Siepmann, J. I. Vapor–liquid equilibria of mixtures containing alkanes, carbon dioxide, and nitrogen. *AIChE journal* **47,** 1676–1682 (2001).

50. Martin, M. G. & Siepmann, J. I. Transferable potentials for phase equilibria. 1. United-atom description of n-alkanes. *The Journal of Physical Chemistry B* **102,** 2569–2577 (1998).

51. Mayo, S. L., Olafson, B. D. & Goddard, W. A. DREIDING: a generic force field for molecular simulations. *Journal of Physical chemistry* **94,** 8897–8909 (1990).

52. Coupry, D. E., Addicoat, M. A. & Heine, T. Extension of the universal force field for metal–organic frameworks. *Journal of Chemical Theory and Computation* **12,** 5215–5225 (2016).

53. Dubbeldam, D., Calero, S., Ellis, D. E. & Snurr, R. Q. RASPA: molecular simulation software for adsorption and diffusion in flexible nanoporous materials. *Molecular Simulation* **42,** 81–101 (2016).

54. Gutiérrez-Sevillano, J. J., Caro-Pérez, A., Dubbeldam, D. & Calero, S. Molecular simulation investigation into the performance of Cu–BTC metal–organic frameworks for carbon dioxide–methane separations. *Physical Chemistry Chemical Physics* **13,** 20453–20460 (2011).

55. Sharma, S. *et al.* RUPTURA: simulation code for breakthrough, ideal adsorption solution theory computations, and fitting of isotherm models. en. *Mol. Simul.* **49,** 893–953 (June 2023).

56. Myers, A. & Monson, P. Adsorption in porous materials at high pressure: theory and experiment. *Langmuir* **18,** 10261–10273 (2002).

*"Creativity is thinking up new things. Innovation is doing new things."*

Theodore Levitt.

# 5

# A thorough assessment of mineral carbonation of steel slag and refractory waste



**Abstract** This study explores the potential of mineral-carbonation of steelmaking slags, particularly White Slag (WS) and various Refractory Wastes (RWs), to mitigate CO2 emissions and valorize industrial wastes. Experiments were performed with waste materials from the production lines at CELSA. We delved into direct aqueous carbonation, evaluating the performance and characteristics of these wastes under different experimental conditions. Our findings reveal that all slags can effectively sequester $CO_2$. This process is effective not only for pure $CO_2$ but also for diluted flue gases under mild conditions ($\leq$ 100 ºC, $\leq$ 6 bar). WS exhibited peak $CO_2$ sequestration capacities (SC) of 359.79 $gCO_2/kg_{slag}$ (pure $CO_2$) and 276.65 $gCO_2/kg_{slag}$ (diluted flue gas). The RWs presented different kinetic behavior, reaching a maximum SC of 311 $gCO_2/kg_{slag}$ after prolonged times. Chemical and morphological evaluations confirmed the transformation of CaO to $CaCO_3$, with MgO remaining largely inert. Additionally, the process indicate the encapsulation of toxic metals, particularly Pb.

## Contents

# 5.1 Introduction.

The annual global $CO_2$ emissions from fossil fuel combustion and industrial activities exceed 36.5 gigatons[1]. To enhance industrial sustainability and mitigate this environmental burden, transitioning to a circular carbon economy is essential. This approach focuses on converting waste into valuable resources, thereby reducing carbon footprints[2]. $CO_2$ mineralization emerges as a practical solution within the circular economy framework. By capturing, storing, and utilizing CO2, this process not only reduces atmospheric carbon but also establishes a waste-to-resource supply chain[3]. A particularly promising avenue is the use of industrial solid wastes as $CO_2$ capture media[4,5]. Various industrial wastes can react with $CO_2$ to produce diverse carbonates[6], adding value to sectors such as steel[7], metallurgy[8], cement[9,10], and mining[11]. Alkaline solid wastes hold significant potential in $CO_2$ mineralization, transforming industrial byproducts into valuable construction materials while mitigating atmospheric $CO_2$[12–14]. Life cycle assessments (LCAs) demonstrate the sustainability of these processes[15–18], paving the way towards a circular, climate-optimal economy with net emission reductions[19–21]. Global implementation of this technology could potentially reduce $CO_2$ emissions by 4.02 gigatons annually, equivalent to 12.5% of anthropogenic emissions[22]. Furthermore, direct air capture of $CO_2$ has proven feasible, expanding the possibilities for carbon capture and utilization[23].

The steel industry, contributing to 8% of global emissions with 2.9 $GtCO_2$ annually[24,25], is actively seeking to reduce its carbon footprint through process optimization. However, these efforts fall short of the ambitious decarbonization targets[1,24,26,27]. Notably, estimates suggest that 43.5% of potential direct $CO_2$ reduction could be achieved through mineralization of iron and steel slags alone[22]. Integrating carbon capture and storage protocols into the circular economy framework is therefore crucial for meeting environmental goals[22,28]. Approximately 35.1% of total steel production consists of byproducts (slag, dust, process gas, etc.), with 2.7% classified as non-recoverable waste[29,30]. Historically, steel slag was considered waste and disposed of in landfills[30]. However, modern approaches are repurposing some types of slag as green cementitious materials and quarry fillers, diverting them from landfills[25,31,32]. Beyond their use in construction, steel slag holds potential in diverse applications, including

$CO_2$ mineralization[33–35], nutrient recovery[36], wastewater treatment[37], and soil enhancement[38]. Effective utilization and management of slag has become a central concern for the steel industry. Studies demonstrate that carbonation of steel slag improves its properties, enhancing hardness and chemical reactivity[39,40]. These advancements show promise for future applications in pavement, cement, and concrete products[31,41,42].

Slag–carbonation has garnered significant attention in waste management and environmental sustainability due to its promising potential. However, widespread industrial implementation requires addressing several challenges. A thorough assessment of the carbonation potential of diverse industrial residues and the identification of optimal operating conditions to minimize energy consumption are crucial for large–scale adoption[22,43]. While numerous studies have investigated slag carbonation processes[39,41,44–51], there remains a knowledge gap regarding the detailed analysis of these wastes, their origins, and intrinsic properties. Research specifically focused on slag from the secondary steel industry, utilizing low-concentration flue gas (<15% $CO_2$), is limited. Most mineralization studies have concentrated on slag from the primary steel industry, which involves high carbon dioxide concentrations in off-gas streams. Additionally, refractory waste, a potential candidate for $CO_2$ mineralization, has received little attention. Electric Arc Furnace (EAF) and Basic Oxygen Furnace (BOF) route slags are often discussed collectively, with their properties attributed to the total slag output of a steelmaking process[52,53]. However, it is crucial to recognize that each slag originates from a distinct sub-process stream. The source of the slag significantly influences its unique properties, impacting its potential for valorization. White slag (ladle furnace slag) is frequently analyzed for mineralization reactions, but refractory waste (residue adhering to furnace refractories) also shows promise due to its elevated basicity from metal oxides (e.g., CaO, MgO).

The lack of comprehensive knowledge regarding the origin and independent valuation of steel slags, from both practical industrial and academic viewpoints, necessitates further targeted research. Combining these perspectives is crucial for a holistic understanding of waste valorization, particularly for materials with unique properties that pose challenges to their valuation. This study examines four waste streams from the secondary steel industry, primarily derived from scrap and recycling processes (Figure 5.1a). White slag (WS)

incurs the lowest management costs among these wastes, with some non-carbonated portions utilized in cement plants and quarry backfills. However, a substantial amount still ends up in landfills. The remaining three wastes originate from the demolition of refractories associated with the EAF, ladle furnace, and pouring tundish. These refractory waste (RW) streams exhibit distinct characteristics and chemical compositions due to the interaction between the cast steel and the specific refractory surface area in each furnace. Consequently, RW management costs vary, with tundish RW being the most expensive and complex to manage, mainly due to its high lead (Pb) content. To optimize waste management costs and mitigate heavy metal leaching (e.g., Cr, Pb), secondary steel companies often combine these three RW streams into a single category called "refractory waste." This approach dilutes heavy metal concentrations, a critical consideration as most of this waste is landfilled. Figure 5.1b illustrates the $CO_2$ equivalent emission factors associated with primary raw materials used in steel production, highlighting methane as the largest contributor within the secondary steel industry, primarily due to its use in reheating furnaces. Figure 5.1c presents an overview of the annual management costs of major steel industry wastes, emphasizing the high costs associated with white slag and refractory waste (€307k and €486k, respectively). This context underscores the potential of $CO_2$ mineralization as a dual-purpose strategy for addressing waste management challenges and curbing $CO_2$ emissions in real-world industrial settings.

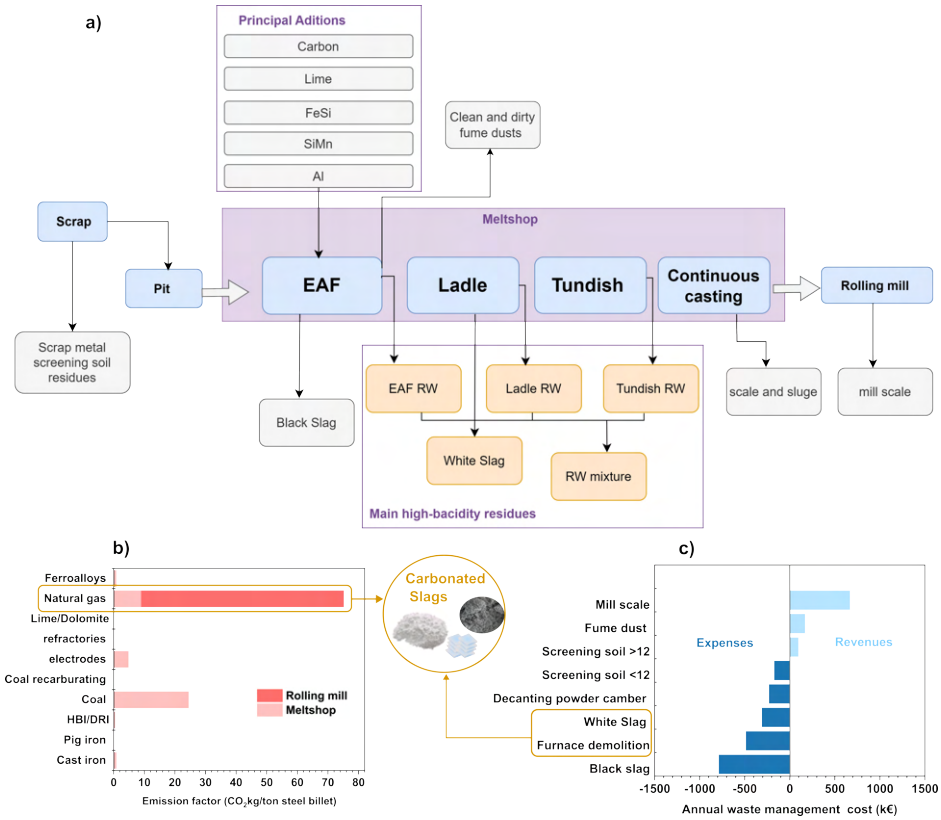


Figure 5.1: (a) Flow diagram of steel industry waste origins, (b) $CO_2$ equivalent emission factor for raw materials in billet production, and (c) Annual waste management cost in the steel industry (Negative values indicate losses, positives values indicate income from waste management). reprinted with permission from[54].

The composition of steel slag varies depending on the specific production process, but typically contains significant amounts of calcium (Ca) and magnesium (Mg) in various forms (oxides, hydroxides, silicates, aluminosilicates)[34,39,55,56], along with residual elements from steelmaking (Fe, Mn, Cr, Ti, S, V, etc.). Two primary slag carbonation methods exist in the steel industry: direct and indirect. The indirect route involves extracting $Ca^+$ and $Mg^+$ ions under acidic conditions, followed by their reaction with $CO_2$ to produce high-purity carbonates[25,39,53,57–60]. This method is generally more costly[25,34]. Conversely, the direct method involves mineralization reactions within the slag, eliminating the need for metal extraction. This route comprises two variants: solid-gas contact (moisture con-

tent <0.2) and solid-liquid-gas interaction (aqueous mineral carbonation). Direct carbonation offers a competitive advantage over the indirect route, as it does not require a continuous acid supply for metal extraction and can be performed at the waste source. However, the resulting carbonates often lack the high purity necessary for specific applications like food and pharmaceuticals[52]. Nonetheless, they find valuable use in construction and as soil additives[39,40,52]. This study focuses on direct aqueous carbonation due to its cost-effectiveness and ability to achieve high carbonation degrees rapidly. The presence of water in this process promotes ion dissolution, facilitating carbonate ion formation and thus accelerating carbonation rates and increasing carbonation degrees[39,44,45,56,61].

$$(Ca,Mg)_xSi_yO_{x+2y+z}H_{2z(s)} + xCO_{2(g)} \rightarrow x(Ca,Mg)CO_{3(s)} + ySiO_{2(s)} + 2H_2O_{(l)} \quad (5.1)$$

In the aqueous phase, the primary mineralization reaction (Eq. 5.1) involves the hydration of free calcium and magnesium oxides ($f-CaO/MgO$) to form $Ca(OH)_2$ and $Mg(OH)_2$, respectively, followed by their carbonation to $CaCO_3$ and $MgCO_3$[25,40]. Despite $MgCO_3$ having a lower enthalpy of formation ($-118 kJmol^{-1}$) than $CaCO_3$ ($-179 kJmol^{-1}$), the higher charge density of $Mg^{2+}$ due to its smaller ionic size and higher lattice energy hinders reaction kinetics. The conversion of MgO to $MgCO_3$ requires a lattice change, a process not easily achieved under standard conditions. MgO remains largely unreacted even when exposed to 1 atm $CO_2$ across a temperature range from ambient to 500°C. Attempts to enhance the reaction rate by increasing MgO surface area have yielded limited success. While elevated pressure may accelerate the reaction, it might not be practical for real-world applications[60,61]. Consequently, under mild conditions, mineralization predominantly involves the conversion of CaO to $CaCO_3$, as discussed herein. This process generates several important intermediate products, as documented in previous studies[25,39,62]. Notably, the material composition and crystalline structure significantly influence the mineralization of $CO_2$ in steel industry slagzhang$_{2023}$carbon.

This study aims to accelerate the implementation of $CO_2$ mineralization of basic wastes, offering insights into sustainable secondary steel industry waste management and $CO_2$ emission reduction. By focusing on environmentally responsible and economically viable waste

valorization, we investigate the $CO_2$ sequestration capabilities of four steelmaking byproducts: white slag (WS), tundish refractory waste (TRW), ladle refractory waste (LRW), and electric arc furnace refractory waste (ERW). We conduct a detailed analysis of the influence of various process parameters on mineralization, employing diverse analytical techniques to assess the composition and structure of both carbonate and non-carbonate phases in the slags and residual water. Our research prioritizes mild operational conditions to emphasize the techno-economic feasibility of valorizing these materials through $CO_2$ mineralization. Uniquely, we evaluate the reactivity of each waste individually and in combination (specifically for RWs), recognizing their distinct origins and properties. In contrast to the broad generalizations in existing literature, our analysis elucidates the specific $CO_2$ sequestration potential inherent to each waste type, facilitating more targeted and effective utilization strategies.



## 5.2 Materials and methods.

### 5.2.1 Materials.

The solid by-products White Slag (WS) and refractories wastes (RWs) were procured from Compañia Española de Laminación S.L (CELSA), located in Barcelona, Spain. The RW encompasses three distinct types of refractories sourced from various stages in the steel production process: Tundish furnace refractories waste (TRW), Electric arc furnace refractories waste (ERW), and Ladle furnace refractories waste (LRW). For clarity in subsequent references, the abbreviation RWs signifies the composite of these three refractories wastes. To ensure sample homogenization, both WS and RWs samples underwent ball mill grinding at a rate of $15 s^{-1}$ during 30 min, followed by sieving with a $200 \mu m$ mesh size. Post-screening particle size distribution analysis shows that the average particle size for non-carbonated WS and RW is 167 $\mu m$ and 35–37 $\mu m$, respectively. The processed samples were then securely stored within capped containers, ensuring their consistency throughout the course of the study.

### 5.2.2 Experimental procedure.

**Slurry formation.** Deionized water was employed to create the WS and RW slurries. Each sample (WS and RWs) was thoroughly mixed

with deionized water at a designated liquid-to-solid (L/S) ratio. The pH of the suspension was measured before introducing it into the mineralization reactor. The experiments were carried out using ratios of 5, 10, 20, 30, and 35 mL $g^{-1}$. **Mineralization Reactor.** We conducted $CO_2$ mineralization in a cylindrical semi-batch reactor with an inner diameter of 60 mm and length of 40 mm. A bed-type stirrer attached to a magnet at the base of the shaft equipped this reactor. A closed section in the agitator accommodates the sludge sample for carbonation. The gas is introduced through the agitator shaft and distributed inside the chamber containing the solid material, which favors the interaction between the gas, solid, and liquid phases. At the top of the reactor are three connections: two for gas inlet and outlet, and a third for pressure control. For a visual representation of the precise geometrical attributes of the reactor, see Figure D.16.

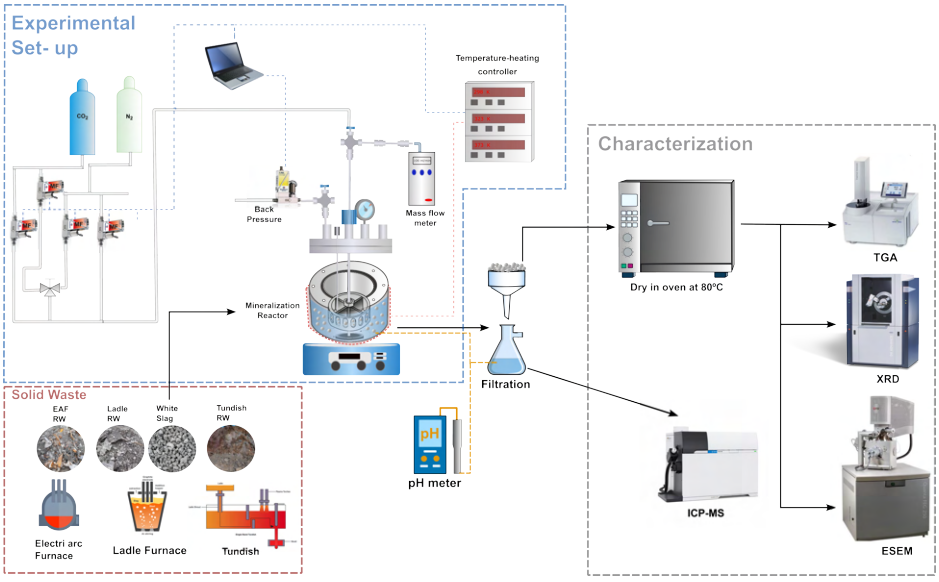


Figure 5.2: **Experimental Set-up** for CO2 mineralization with steel wastes and samples characterization techniques. reprinted with permission from[54].

**Mineralization experiment.** We conducted mineralization measurements using the experimental setup depicted in Figure 5.2. We used gas cylinders containing $N_2$ (Praxair, 99.999%) and $CO_2$ (Air Liquide, 99.998%). A set of calibrated mass flow Precise control over the composition and flow of the inlet gas stream was achieved using a set of calibrated mass flow controllers (Bronkhorst EL-FLOW) lo-

cated upstream of the separation module achieved precise control of the composition and flow rate of the inlet gas stream. We monitored the actual pressure by using the pressure gauge upstream of the reactor and managed pressure adjustments through a needle valve in the outlet gas line. All pressure values are given in absolute bar unless otherwise stated. A linear power silicone heating cable ($\phi$ 3mm FOR-FLEX NORMAL, Electricfor) was wrapped around the reactor to ensure efficient heating of the mineralization reactor. Temperature measurement was facilitated by a K-type thermocouple (Thermocoax) in contact with the outer wall of the reactor, under the control of an EZ-Zone temperature controller (Watlow). We initiated the reaction mixture using a magnetic stirring plate below the mineralization reactor.

For the white slag (WS), the experimental assessment encompassed two gas compositions: pure $CO_2$ and a $CO_2$ (10%)/$N_2$ (90%) mixture, designed to replicate the off-gas stream from the CELSA rolling mill furnace. We maintained a consistent total inlet gas flow rate of 100 NmL/min throughout the experiments. Initially, we conducted the experiments by varying pressures (2, 4, and 6 bar), T ($25^{o}$C, $50^{o}$C, and $100^{o}$C), stirring rate (100–600 rpm), and liquid-to-solid ratio (5-35 ml $g^{-1}$). Additionally, we determined the maximum carbonation capacity of the WS material through an extended 12-hour experiment using pure $CO_2$ at $25^{o}$C, 3 bar pressure, and 500 rpm stirring rate. After completing the initial measurement set, we also identified optimal operating conditions. Considering the company's waste blending practice to meet environmental standards, we later investigated mineral carbonation for the refractory waste mixture (RWs) by mixing the individual refractory waste (RW) in equal proportions (33 wt% each). The RWs mixture underwent testing at different reaction times (15–390 min) and total gas pressure (2–6 bar). Furthermore, the carbonatation reaction performance of each RW was compared (conditions: 60 min and 4 bar). All experiments utilized a 20 L/S ratio and 500 rpm. From the mineralization reaction, the reacted slurry samples of WS and RWs were promptly withdrawn and subjected to filtration through quantitative filter paper (Filter-Lab, 0.16 mm thickness, 2–4 $\mu m$ pore size, 55 mm diameter). The resulting filtered carbonated material was then dried at $105^{o}$C in an oven for 8 hours and stored in a sealed container.

To homogenize the dry carbonated samples for RWs, we incorporated an additional ball milling ($15s^{-1}$ for 30 min). Contrarily, this

step remained superfluous in the case of WS samples due to their inherent homogeneity. To ensure the reliability of our results, we conducted each measurement three times. Considering these replicates, we calculated the experimental error based on the standard deviation of the measurements, which is represented by error bars in Figure 5.3 and 5.4.

### 5.2.3 Physicochemical characterization.

The thermal characteristics of both white slag and refractory wastes were analyzed before and after the carbonation process using a thermogravimetric analyzer (TGA/SDTA 851 Mettler). For each analysis, approximately 20 $\pm$ 3 mg of powdered waste was placed within alumina capsules (100 $\mu L$ capacity). The analysis involved a controlled heating program, with a ramp rate of 10ºC per minute, spanning from 30–1000ºC, all conducted under a $N_2$ flow environment. To perform the semi-quantitative mineral composition tests, X-ray diffraction measurements (XRD) were made using a Bruker-AXS D8-Advance diffractometer with vertical theta-theta goniometer, incident- and diffracted-beam Soller slits of 2.5º, a fixed 0.5º receiving slit and an automatic Air scattering knife on the sample surface. The angular $2\theta$ range was between 5–80º. The data was collected with an angular step of 0.02º at a step/time of 0.5s. Cuk$\alpha$ radiation was obtained from a copper X-ray tube operated at 40 kV and 40 mA. Diffracted X-rays were detected with a LynxEye-XE-T PSD detector with an opening angle of 2.94º. Quantitative phase analysis was derived from XRD powder patterns using the Rietveld refinement[63], with TOPAS v6 software. The background was modelized with a 2nd order Chebyshev polynomial. The instrumental contribution to the diffraction profile was calculated with the Fundamental Parameters Approach[64]. The relative quantitative phase analysis was obtained by refining the Rietveld scale factor for each phase and applying the corresponding well-known equations[65]. The peak width of each phase was contribution of the crystallite size effect and discarding any contribution of the microstrain to the peak width. The averaged integral breadth was obtained from the resulting fitted Voigt function to the whole diffractogram. The Scherrer equation[66] was then applied to obtain the apparent crystallite size (refer to Section D of the supplementary information for detailed of the Rietveld method employed). X-ray fluorescence (XRF) analysis of the four types of waste was

provided by CELSA. Fourier Transform Infrared Spectroscopy (FT-IR) measurements were performed on a Bruker Optics FT-IR Alpha spectrometer equipped with a DTGS detector, KBr beam splitter at 4 $cm^{-1}$ resolution and with a one bounce ATR accessory with diamond windows. All infrared spectra were collected in a range of wavenumber 4000 – 400 $cm^{-1}$. Semi-quantitative elemental analysis and morphological characterization of the sample were performed using a Field Emission Scanning Electron Microscopy-Focused Ion Beam (FESEM-FIB) with Scios2 FEI equipment, coupled with an electron beam and a focused Gallium ion beam. Crystal size was determined using ImageJ software. We analyzed the content of the metals in the non-carbonated samples and also the leached metals in the residual water after the mineralization reaction using Inductively Coupled Plasma Mass Spectrometry (ICP-MS) with an Agilent 7900 instrument equipped with a Micromist concentric nebulizer, Scott spray chamber, platinum interface cones, off-axis double lens system, hyperbolic quadrupole mass filter, and octopolar collision/reaction cell. A 5-10 mg sample was weighed and digested in an acidic solution using a microwave oven at 220ºC. The solution was then diluted to 5 mL with ultrapure water and analyzed. Quantification was achieved using a calibration curve spanning 0–2000 ppb. Particle size distribution (PSD) analyses were performed in a Malvern Mastersizer 2000 equipped with a Hydro 2000SM sample dispersion unit. We use approximately 100–200 mg of the sample with 5 mL of ethanol to prepare the emulsion.



### 5.2.4 $CO_2$ sequestration capacity and carbonation degree.

The $CO_2$ sequestration capacity (SC), quantified as the mass of $CO_2$ sequestered per kilogram of solid waste, was calculated using Eq. 5.2 The $CO_2$(wt%) term represent the weight loss attributed to the volatilization of calcium carbonate polymorphs ($\Delta m_{CaCO3}$) at temperature range between 500 to 900ºC[67,68], based on the dry weight at 105ºC ($m_{105°C}$) and determined by TGA (Eq.5.3). It is pertinent to note that the slags contain an initial $CaCO_3$ content (prior to the carbonation reaction) that varies depending on the type of slag. This value was not subtracted from the overall quantity of calcium carbonate. Moreover, the conversion of MgO to MgCO3 in the waste is expected to be minimal, or absent[69]. The challenging

magnesium aqueous carbonation conditions, requiring $CO_2$ pressures greater than 100 bar, temperature above 144ºC, and hours of reaction time, limit such conversion[39]. Therefore, the degree of carbonation ($\delta CaO$) mainly relies on the transformation of total CaO present in the sample (assuming the calcium-bearing compositions are the main reaction species). This can be calculated using Eq.5.4, where $Mw_{CO_2}$ and $Mw_{CaO}$ are the molar masses of carbon dioxide and calcium oxide, respectively. $CaO_{total}$ represents the weight fraction of calcium oxide in the solid waste sample before the carbonation reaction, expressed as percentage of dry mass and determined by XRF.

$$CO_2 \text{ sequestration } \left(\frac{g_{CO_2}}{kg_{slag}}\right) = \frac{CO_2(\text{wt}\%)}{100 - CO_2(\text{wt}\%)} \times 1000 \tag{5.2}$$

$$CO_2(\text{wt}\%) = \frac{\Delta m_{CaCO_3}}{m_{105°C}} \times 100 \tag{5.3}$$

$$\delta_{CaO} = \frac{\frac{CO_2(\text{wt}\%)}{100-CO_2(\text{wt}\%)} \times \frac{1}{MW_{CO_2}}}{\frac{CaO_{total}}{MW_{CaO}}} \times 100 \tag{5.4}$$



## 5.3 Results and discussion.

### 5.3.1 Characterization of non-carbonated waste.

The initial characterization of the different waste streams before carbonation was conducted, focusing on their CaO content, a key determinant of carbonation extent. White slag (WS): XRF analysis (Table D.5) revealed a total CaO content of 58% in white slag, with trace elements (e.g., $SiO_2$, FeO) not expected to contribute to $CO_2$ sequestration [64]. XRD analysis (Figure D.2a) and Rietveld refinement (Table D.4) identified the primary crystalline mineral phases potentially releasing Ca and Mg ions into water, including $\gamma - Ca_2SiO_4$ (27.6%), $Ca_3Mg[SiO_4]_2$ (8.1%), $\beta - Ca_2SiO_4$ (6.7%), $MgSiO_3$ (5.5%), and $Ca_2Al(AlSi)O_7$ (4.1%). $\gamma - Ca_2SiO_4$ and $\beta - Ca_2SiO_4$, both major phases in ordinary Portland cement (OPC), contribute to the dominance of $Ca_2SiO_4$ as the primary phase. These silicates exhibit varying reactivity[41], influencing water alkalinity and $CO_2$ retention capacity. The sequestration capacity (SC), estimated by TGA (Figure D.1a), is 86.73 $g_{CO_2}kg^{-1}$ slag, corresponding to 17.5% $CaCO_3$ content and 19.14% carbonation degree ($\delta CaO$). This pre-existing

calcium carbonate likely results from the reaction of hot, wet slag with ambient $CO_2$ during initial waste generation. ICP-MS analysis (Table D.7) confirmed calcium (Ca) as the most abundant element (59.9 mg/g) and identified potentially toxic metals, including chromium (Cr) at 189 mg/kg, nickel (Ni) at 130 mg $kg^{-1}$, and lead (Pb) at a lower concentration of 23 mg $kg^{-1}$.

Refractory wastes (RWs): XRF analysis (Table D.6) of RWs revealed a predominant presence of CaO (41.2%) and a significant concentration of MgO (22.2%), along with other metal oxides like $Fe_2O_3$ and $SiO_2$, which are not expected to contribute to the mineralization reaction. XRD analysis (Figure D.4) and Rietveld quantification (Table D.2) identified $\gamma - Ca_2SiO_4$ (18.8%) and $\beta - Ca_2SiO_4$ (8.9%) as the primary crystalline phases promoting $Ca^+$ dissociation, along with minor components such as Portlandite, selenite, $CaOH_2$ (6.1%), $Ca_2Al_2SiO_7$ (2.1%), $Ca_{12}Al_{14}O_{33}$ (6.2%), and Ca2AlFeO5 (3.8%). Notably, MgO (28%) constitutes the principal mineral phase in non-carbonated RWs. The initial sequestration capacity (SC) of RWs was calculated to be 26 $g_{CO_2}kg_{slag}^{-1}$, lower than that of WS, indicating less environmental reactivity and a lower initial $CaCO_3$ concentration (6%) with a carbonation degree ($\delta CaO$) of 8%. Further XRF analysis of individual RWs revealed that ladle RW had the highest CaO content (48.6%), followed by tundish RW (26%) and EAF RW (23%). Mineralogical characteristics varied significantly among individual RWs (Figure D.2b-d). Ladle RW exhibited the lowest SC (22.6 $g_{CO_2}kg_{slag}^{-1}$) and $\delta CaO$ (5.9%), suggesting that despite its high CaO content, a significant portion remained unreacted with the environment. Conversely, tundish RW demonstrated the highest SC (84 $g_{CO_2}kg_{slag}^{-1}$) and $\delta CaO$ (nearly 41%), indicating high environmental reactivity. EAF RW displayed a moderate SC (26 $g_{CO_2}kg_{slag}^{-1}$) and $\delta CaO$ (14.5%).

Comparative analysis of heavy metal concentrations using ICP-MS (Table D.7) revealed slight variations in Cr content among refractory wastes (RWs). Tundish RW exhibited the highest Cr value (1.97 mg $g^{-1}$), followed by EAF RW (1.71 mg $g^{-1}$) and ladle RW (0.473 mg $g^{-1}$). These values were notably higher than those in white slag (0.18 mg $g^{-1}$). Regarding Pb content, tundish RW had the highest concentration (371 mg $kg^{-1}$), while EAF and ladle RWs showed considerably lower values (68 and 51.5 mg $kg^{-1}$, respectively). This discrepancy often leads industries to mix these refractory wastes, aiming to dilute heavy metal concentrations and prevent excessive leaching

into the soil, thereby reducing waste management costs. Analysis of the mixed RWs confirmed a reduction in both Cr (1 mg $g^{-1}$) and Pb (240 mg $g^{-1}$) content compared to the values observed in tundish RW, the primary source of high management costs. Notably, Cr and Pb concentrations in RWs were significantly higher than those in WS. Morphological analysis of both non-carbonated WS and RWs will be discussed in section 5.3.3, comparing their characteristics with those of their carbonated counterparts.

### 5.3.2 Carbon sequestration and Carbonation degree.

The carbonation reaction of white slag (WS) was investigated by examining the influence of key process parameters. Initially, we compared mineralization performance using pure $CO_2$ and a simulated CELSA flue gas (90% $N_2$, 10% $CO_2$) (Figure 5.3a). Under the specified conditions (6 bar, 25ºC, L/S = 20, 500 rpm), both reactions reached completion (carbonation degree plateau) after 60 minutes. With pure $CO_2$, WS achieved a maximum carbonation degree ($\delta CaO$) of 79% and a $CO_2$ sequestration capacity (SC) of 360 $g_{CO_2} kg_{slag}^{-1}$. The gas mixture, despite significantly lower CO2 partial pressure, resulted in a 23% reduction in carbonation capacity ($\delta CaO$ = 61%, SC = 277 $g_{CO_2} kg_{slag}^{-1}$). Notably, the difference in carbonation capacity between the two inlet gases increased with reaction time (28% after 200 minutes vs. 8.3% after 15 minutes), indicating a faster reaction rate with pure $CO_2$. This finding highlights the potential of WS for direct $CO_2$ capture from flue gas, eliminating the need for pre-concentration.

Figure 5.3(b-f) demonstrates the effect of pressure, temperature, stirring rate, and liquid-to-solid (L/S) ratio on WS mineralization using simulated flue gas. At 2 bar, sequestration capacity (SC) is lowest and gradually increases to 259.8 g $kg^{-1}$ over 200 minutes. Conversely, SC at 4 and 6 bar differs only at early reaction times, reaching the same maximum value after 60 minutes ($\delta CaO$ = 59.95%, SC = 273 $g_{CO_2} kg_{slag}^{-1}$ at 4 bar; $\delta CaO$ = 61%, SC = 277 $g_{CO_2} kg_{slag}^{-1}$ at 6 bar). This reveals reaction acceleration with increasing pressure, attributed to enhanced CO2 dissolution in water under higher total gas pressure. Interestingly, despite slower kinetics, reducing pressure from 6 to 2 bar results in similar maximum SC, demonstrating WS's potential for $CO_2$ capture from low-pressure flue gases. Lowering system pressure can also reduce energy consumption in the carbonation process.

Therefore, optimal conditions for subsequent experiments were determined to be 4 bar pressure and 60 minutes reaction time.

Figure 5.3c demonstrates the influence of the liquid-to-solid (L/S) ratio on the mineralization reaction. $CO_2$ sequestration capacity (SC) increases with higher L/S ratios, peaking at 30 ml $g^{-1}$ (SC = 330 $g_{CO_2} kg_{slag}^{-1}$ , $\delta CaO$ = 73%) before declining. This contradicts previous findings where L/S ratio had no significant impact on mineralization[47,62]. Our study reveals a 35% difference in SC (330 vs. 215 $g_{CO_2} kg_{slag}^{-1}$) within the 5-30 ml $g^{-1}$ L/S range. The L/S ratio significantly affects mineralization by influencing slurry alkalinity and ion leaching, thereby impacting carbonation conversion[62,70]. However, an L/S ratio of 20 ml $g^{-1}$ was chosen for further analysis, as it balances liquid and residue amounts, aligning with previous research[25,39,40,44,45,47,61]. It is important to note that while higher solid/liquid ratios can increase carbonation degree, they also necessitate treating larger water volumes, an important consideration[70].

As accelerated mineralization is governed by diffusion-controlled reactions, the influence of rotational speed on carbonation efficiency was investigated. The carbonation degree increased with rotation speed, reaching a maximum at 500 rpm before declining at higher speeds (Figure 5.3d). This aligns with literature findings, where moderate increases in stirring rate enhance gas-phase mass transfer[71]. However, excessively high rotational speeds can decrease gas residence time, subsequently reducing carbonation conversion[40]. The optimal stirring rate of 500 rpm, under our reactor conditions, balances enhanced mass transfer with adequate residence time for optimal carbonation conversion.

The influence of temperature on the mineralization reaction (Figure 5.3e) demonstrates a decrease in sequestration capacity with increasing temperature from 25ºC to 80ºC. While elevated temperatures can accelerate calcium species dissolution kinetics, they may also hinder $CaCO_3$ nucleation and growth due to reduced $CO_2$ solubility, negatively impacting carbonation[46,72]. Additionally, the liquid-to-solid ratio within the reactor could decrease due to water evaporation at high temperatures, further affecting carbonation degree. Therefore, caution is advised when increasing the working temperature for solid-liquid phase carbonation to avoid compromising $CO_2$ sequestration performance. Conversely, solid-gas phase mineralization is typically conducted at significantly higher temperatures (500–650ºC)[25].

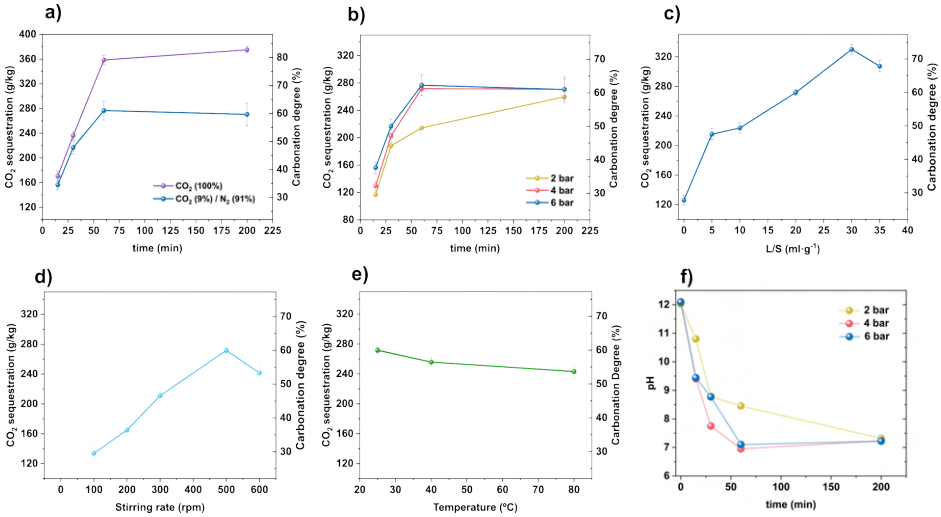


Figure 5.3: a) $\delta CaO$ and SC of WS using pure $CO_2$ and a simulated flue gas mixture; b-e) $\delta CaO$ and CDSC in function of different reaction parameters using a 9%$CO_2$ in $N_2$ gas mixture: b) At different reaction time (15–200 min) and pressure (2–6 bar), c) At different L/S ratios (with t=60min, stirring rate=500 rpm and T=25ºC), d) At different stirring rates (with t=60 min, L/S = 20 ml $g^{-1}$, P = 4 bar and T = 25ºC), and e) At different temperatures (with t= 60 min, L/S = 20 ml $g^{-1}$, P=4bar and Stirring rate=500 rpm); and f) pH value at different reaction times and pressures using gas mixture. reprinted with permission from[54].

Figure 5.3f depicts the pH measured at the end of mineralization for reaction times up to 200 minutes. The initial pH of non-carbonated samples is notably high (11.5–12.1), followed by an exponential decay over time, reaching pH 7.2 after 200 minutes. Increased total gas pressure accelerates reaction kinetics, resulting in a faster pH decline. At 4 and 6 bar, pH drops to 7 after 60 minutes, compared to pH 8.4 at 2 bar. pH monitoring serves as an indicator of carbonation progress, as it influences both gaseous $CO_2$ dissolution and calcium ion leaching from the slag matrix. Carbonate ($CO_3^{2-}$) is the dominant species in the slag slurry above pH 10.3, while bicarbonate ($HCO^{3-}$) dominates within the pH range of 6.3–10.3. Since carbonate is crucial for the carbonation reaction, carbonation efficiency decreases with lower pH values[39,40,55]. Maintaining proper pH control is therefore essential for maximizing carbonation efficiency, despite the associated cost implications for slag mineralization. At

maximum carbonation capacity using pure $CO_2$ (375 $g_{CO_2}kg_{slag}^{-1}$), the corresponding pH was 6.6. Each experiment was replicated thrice to ensure reproducibility, with a 5% deviation observed in pH values. This discrepancy could be attributed to pH measurements taken after carbonation experiments, as reactor cooling and depressurization during the waiting period may have affected measurement precision. Continuous pH monitoring is recommended for optimal accuracy and enhanced carbonation capacity[40].

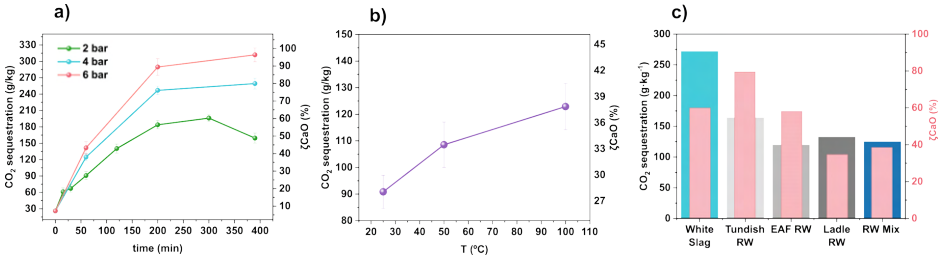


Figure 5.4: Sequestration capacity (SC) and $\delta CaO$: a) RWs at different reaction times (15–390 min) and pressures (2–6 bar), b) RWmix at different temperatures (25ºC–100ºC) at 2 bar and 60 min reaction time, and c) White slag, Tundish RW, EAF RW, Ladle RW, and RWs at the same experimental conditions (4 bar, t = 60 min, and 25ºC). All experiments were performed with an L/S ratio of 20 and a stirring rate of 500 rpm. reprinted with permission from[54].

For refractory wastes (RWs), the carbonation reaction was significantly slower than for white slag (WS). Even after 390 minutes (the longest reaction time analyzed), the $CO_2$ mineralization reaction with RWs mixture at varying pressures (Figure 5.4a) did not reach equilibrium. The maximum sequestration capacity (SC) observed was 311.87 $g_{CO_2}kg_{slag}^{-1}$, with a nearly complete carbonation degree ($\delta CaO$) of 96.45%, achieved at 6 bar and 25ºC. The reaction kinetics intensified with increasing $CO_2$ partial pressure. A rapid pH decline to 7.6 within 60 minutes was observed at 6 bar (Figure D.15). In contrast, at 2 and 4 bar, the pH decreased to a minimum of 7.6 only after 390 minutes. Sequestration capacity decreased with lower pressure, reaching 259.25 $g_{CO_2}kg_{slag}^{-1}$ ($\delta CaO = 80\%$) and 159.39 $g_{CO_2}kg_{slag}^{-1}$ ($\delta CaO = 49\%$) at 4 bar and 2 bar, respectively.

The slower mineralization kinetics in RWs is evident in the gradual pH decrease (Figure D.15), with a pH of 9.5 after 60 minutes at 4 bar and 25°C, while white slag (WS) reaches pH 6.9 under the same

conditions (Figure 5.3f). However, the rapid carbonation in WS, facilitated by its fast pH decline, leads to swift obstruction of $CO_2$ sequestration in the slurry. Consequently, WS reaches equilibrium within 60 minutes even at 6 bar, while RWs do not reach equilibrium even after 390 minutes, demonstrating a superior SC performance at longer reaction times with an 11% higher sequestration capacity. Additionally, RWs exhibit a 36% higher carbonation degree than WS. Carbonate formation is directly proportional to Ca and Mg silicate content (Eq. 5.1), and maintaining optimal pH is crucial for maximizing SC efficiency. Rietveld analysis of non-carbonated species (Table D.2 and D.4) reveals a higher $\gamma - Ca_2SiO_4$ concentration in WS (27.6%) compared to RWs (18.8%). This primary reactive agent in WS accelerates pH reduction through rapid $Ca^+$ ion release, hindering mineralization due to subsequent carbonate ion ($CO_3^{2-}$) depletion[5]. This explains the higher carbonation potential of RWs, evidenced by its near-complete carbonation ($\delta CaO$), despite WS showing considerable initial sequestration potential ($\delta CaO = 61\%$).

The influence of temperature on the RWs mineralization reaction at 2 bar pressure and 60 minutes (Figure 5.4b) shows a 26% increase in both sequestration capacity (SC) (from 90 to 122 $g_{CO_2}kg_{slag}^{-1}$) and carbonation degree ($\delta CaO$) (from 28% to 38%) when the temperature is raised from 25ºC to 100ºC. This parameter requires further optimization for practical applications and confirms the positive effect of temperature on carbonation kinetics in $CO_2$ mineralization using RWs. Figure 5.4c compares the SC and $\delta CaO$ of WS, RWs, and individual RW components under identical conditions (4 bar, 25ºC, 60 minutes). WS exhibits the highest SC (271.7 $g_{CO_2}kg_{slag}^{-1}$, $\delta CaO = 59.9\%$). Tundish RW demonstrates the highest carbonation degree ($\delta CaO = 79.5\%$) with a SC of 163.7 $g_{CO_2}kg_{slag}^{-1}$, surpassing other refractory waste materials. However, the high $\delta CaO$ value of Tundish RW suggests limited potential for further SC improvement with extended reaction times.

### 5.3.3 Characterization of the carbonated solid and aqueous phases.

Figure 5.5 displays SEM-XEDS results, illustrating the structural characteristics and elemental mapping of both non-carbonated and carbonated WS and RWs samples. Morphological comparison (Figure 5.5a-b) reveals irregular-shaped non-carbonated WS and 2–3 $\mu m$

cubic $CaCO_3$ crystals formed upon carbonation. A continuous, compact layer of $CaCO_3$ crystals coats the WS surface, consistent with previous findings[67]. Elemental analysis shows an increase in carbon content, though not quantitatively significant. Elemental mapping (Figure 5.5c) reveals uniform Ca, O, C, and Si distribution throughout the sample, while minor elements like Mg and S are localized in the center. Mn, Al, Fe, and Ti exhibit irregular distribution in the carbonated sample (Figure D.7c). Semi-quantitative XRD analysis (Figure 5.6a) confirms $CaCO_3$ (calcite) as the primary mineral phase (approximately 50%) in carbonated WS. $Ca_2SiO_4$, initially predominant, significantly decreases from 49% to 18%. MgO remains largely unchanged, confirming its inertness. Several phases identified in non-carbonated WS, such as magnesian Gehlenite ($Ca_2Al_2SiO_7$) and Merwinite ($Ca_3Mg(SiO_4)_2$), disappear in the carbonated WS, while new phases like Mayenite ($Ca_{12}Al_{14}O_{33}$), Hibschite ($Al_2Ca_3(SiO_4)_2$), and Wollastonite ($CaSiO_3$) emerge (Figure D.3a). FTIR analysis (Figure D.14a) confirms characteristic C–O bonds in carbonate samples. The intense band at 1409 $cm^{-1}$ corresponds to $\nu 3$ vibrations of $CO_3^{2-}$ (asymmetric C–O stretching), while peaks at 871 $cm^{-1}$ and around 712 $cm^{-1}$ are associated with out-of-plane and in-plane bending ($\nu 2$) vibrations of $CO_3^{2-}$, respectively[73–79]. The peak at 1795 $cm^{-1}$ is also attributed to $CaCO_3$[78,80,81]. The increased intensity of these bands in carbonated WS confirms calcite formation during $CO_2$ mineralization.

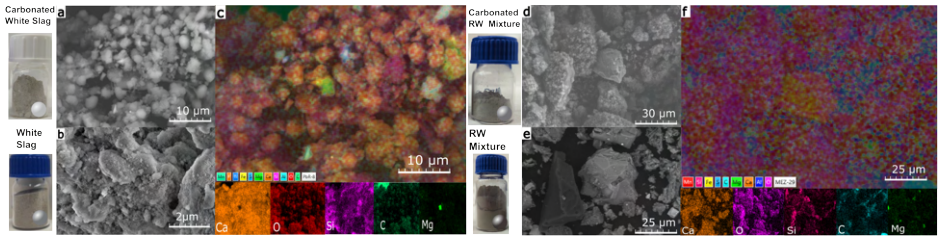


Figure 5.5: Scanning electron micrographs (SEM) and elemental mapping of the carbonated samples of the white slag (a, c), the refractory wastes (d, f), and non-carbonated samples of WS and RWs (b and e, respectively). reprinted with permission from[54].

Morphological comparison of non-carbonated and carbonated RWs mixture (Figure 5.5d-e) reveals tiny calcite crystals adhering to predominantly silicon-based particles after mineralization. Elemental mapping (Figure 5.5f) shows a more uniform distribution of Ca, Si, O,

C, and Mg in carbonated RWs, primarily due to post-mineralization homogenization via ball milling. This step addresses initial inconsistencies in RWs carbonation, which, without homogenization, resulted in varying analytical results across different sampling points due to uneven carbonation (unlike the homogeneous carbonation observed in WS). Figure 5.6b presents the XRD analysis of non-carbonated and carbonated RWs. A clear change in active phase intensity is observed, with calcite ($CaCO_3$) peaks intensifying and $Ca_2SiO_4$ (larnite and olivine forms) either disappearing or partially reducing. Notably, MgO and Srebrodolskite ($Ca_2Fe_2O_5$) remain unchanged. Conversely, new mineral phases such as Bregidite ($Ca_{14}Mg_2(SiO_4)_8$), Enstatite ($MgSiO_3$), and Quartz ($SiO_2$) appear in the carbonated RWs. FTIR spectra (Figure D.14b) reveal a change in the intensity of bands within the 1400-1500 $cm^{-1}$ range, characteristic of asymmetric C–O stretching vibrations in carbonates. Peaks around 872 and 712 $cm^{-1}$, corresponding to out-of-plane and in-plane bending vibrations of carbonate-based compounds, further confirm $CaCO_3$ formation during carbonation. SEM, XRD, and FTIR analyses collectively indicate the absence of $MgCO_3$ formation in RWs, suggesting that mineralization exclusively results in calcite formation. Morphological analysis of individual carbonated RWs (Figure D.11) reveals consistent calcite layer formation enveloping solid particles, particularly pronounced in EAF and ladle RWs. Examination of active mineral phases (Figure 5.6c-e) identifies calcium olivine ($CaSiO_4$) as the primary phase in EAF and ladle RWs.

Analysis of the aqueous phase after mineralization is crucial for understanding process effectiveness. Previous research[39,44,47,57,82] suggests that mineralization significantly reduces heavy metal leaching. Therefore, evaluating the composition of aqueous residues and exploring their potential for recycling within the carbonation process is essential[49]. For WS (Figure D.12), a significant increase in metallic ion concentrations is observed during early carbonation stages, including Ti (up to 56 $\mu gL^{-1}$), Al (up to 1051 $\mu gL^{-1}$), Fe (up to 64.5 $\mu gL^{-1}$), Ni (up to 5.5 $\mu gL^{-1}$), and Pb (up to 612 $\mu gL^{-1}$). These metals leach into the liquid phase but are re-trapped within the solid matrix at longer reaction times, with concentrations decreasing to 10, 0.44, 46.2, and 7.5 $\mu gL^{-1}$ for Ti, Al, Fe, and Pb, respectively. Ca, Mg, and to a lesser extent Cr and Ni, exhibit a monotonic concentration increase throughout mineralization, reaching 373, 274, 2.5, and 17.6 $\mu gL^{-1}$, respectively, after 200 minutes. In RWs carbonation wastew-

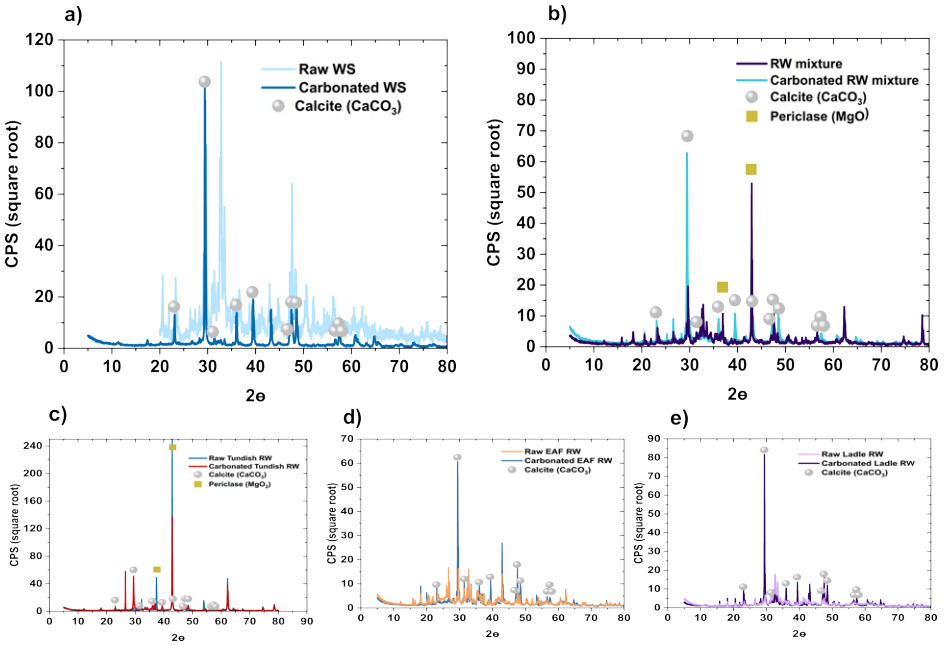


Figure 5.6: XRD patterns of non-carbonated and carbonated samples of a) White Slag, b) RW mixture, c) Tundish RW, d) Electric Arc Furnace RW, and e) Ladle RW. . reprinted with permission from[54].

ater (Figure D.13), Ca concentration peaks at 130 $mgL^{-1}$ after 200 minutes, followed by a gradual decline. Si also increases significantly up to 200 minutes, then grows at a slower rate, reaching 92 $mgL^{-1}$ after 390 minutes. Mg, Al, and Cr concentrations increase steadily, reaching 2458 $mgL^{-1}$, 923 $mgL^{-1}$, and 13.5 $\mu gL^{-1}$ after 390 minutes. Fe, Ti, and V remain stable up to 200 minutes, then increase exponentially to 11.14, 666, and 57.6 $\mu gL^{-1}$, respectively. Pb concentration decreases exponentially after 60 minutes, reaching negligible levels (2 $\mu gL^{-1}$) by the end. Notably, even at short reaction times, Pb concentration remains negligible (<3 $\mu gL^{-1}$) with increasing $CO_2$ partial pressure (Figure D.13i). These findings, confirming minimal leaching, highlight the potential of these mineralization protocols.

## 5.4 Outlook.

The presence of free calcium oxide (free-CaO) and calcium hydroxide ($Ca(OH)_2$) in steel slag often limits its use in concrete, asphalt aggregate, road base, and fill materials due to concerns about water ab-

sorption and expansion[44]. Carbonation treatment effectively removes these reactive calcium-rich components (e.g., free-CaO, $Ca(OH)_2$, $Ca_2SiO_4$) from white slag and refractory wastes, enhancing their safety and sustainability. The sequestration capacities (SC) and carbonation degrees ($\delta CaO$) reported in this study align with the existing literature. Using pure $CO_2$, $\delta CaO$ ranges from 53% to 86%, while 20–30% $CO_2$ gas mixtures yield $\delta CaO$ values between 28% and 57% [22, 25, 32, 40, 54, 57]. This study, however, focuses on flue gases with lower $CO_2$ concentrations, unlike prevalent research on higher $CO_2$ concentrations typical of blast furnace emissions[31]. Importantly, our study introduces refractory wastes (RWs) as carbon capture materials, demonstrating high conversion rates (96%) under extended reaction times, thus opening a new avenue for investigation. Future research should prioritize detailed, source-specific analyses to effectively manage and utilize slag waste in mineralization processes. Thorough validation of the resulting carbonated residues is essential to confirm their efficacy as alternative construction materials, promoting wider adoption. While our study has advanced the understanding of mineralization in steelmaking wastes (white slag and refractory waste), several areas warrant further exploration to develop a comprehensive waste management approach through mineralization: i) *Rigorous Techno-Economic Analysis*: A comprehensive techno-economic analysis, encompassing various scenarios and models for circular economic integration with complementary industries, is crucial. This analysis should quantify costs, energy inputs, and potential savings to assess the economic feasibility and sustainability of waste mineralization. ii) *Leaching Studies for Heavy Metal Stabilization*: Further leaching studies are needed to validate the effectiveness of mineralization in stabilizing heavy metals within the solid carbonate residue. This research is vital for understanding the long-term environmental impact and safety of carbonated waste materials. iii) *Validation of Carbonated Wastes as Construction Material Additives*: Robust validation studies are required to confirm the suitability of carbonated waste materials as additives for construction materials. This could lead to the development of sustainable and environmentally friendly construction practices. By addressing these aspects, future work can contribute to advancing waste mineralization and its integration into a broader sustainable industrial ecosystem.

## 5.5 Conclusions.

Mineralization presents a promising solution for simultaneously addressing $CO_2$ emissions and valorizing high-basicity waste materials, demonstrating the feasibility of a unified $CO_2$ capture and storage approach using industrial byproducts, aligning with circular economy principles. This study focused on the mineralization of both white slag (WS) and refractory wastes (RWs) from the electric arc furnace, ladle furnace, and tundish, highlighting their untapped potential within the secondary steel industry. Carbonated WS achieved a maximum $CO_2$ sequestration capacity (SC) of 276.65 $g_{CO_2}kg_{slag}^{-1}$ (using 10% $CO_2$ gas mixture) and 359.79 $g_{CO_2}kg_{slag}^{-1}$ (using pure $CO_2$), emphasizing the potential for direct mineralization using rolling mill furnace off-gases without energy-intensive $CO_2$ pre-concentration. Optimization studies revealed optimal WS performance at 60 minutes, 4 bar, 25ºC, and a liquid-to-solid ratio of 20 (271.67 $g_{CO_2}kg_{slag}^{-1}$). RWs, despite slower kinetics, reached a higher maximum SC of 311 $g_{CO_2}kg_{slag}^{-1}$ after 390 minutes. Among individual RW fractions, tundish RW exhibited the highest carbonation degree (79%) and SC (165 $g_{CO_2}kg_{slag}^{-1}$). Notably, solution pH critically influences the mineralization reaction, warranting further investigation into pH control strategies during the process. Characterization studies (SEM, XRD, TGA, FTIR, and ICP) confirmed CaO as the primary reactant in mineralization, with MgO remaining largely inert under these conditions. Only structural and mineralogical changes in calcic compounds were observed. Addressing environmental concerns, particularly for tundish RW due to its higher Pb content, our findings suggest that carbonation may stabilize heavy metals like Pb. The reduced Pb concentration in filtrated water as mineralization progresses indicates potential trapping of harmful metals within the carbonated material, warranting further exploration as a waste remediation strategy. In summary, our results demonstrate the potential of mineralization to address both $CO_2$ emissions and various waste streams within the steel industry, contributing to sustainable industrial ecology. The successful use of steel industry off-gas highlights the potential for immediate implementation and emissions reduction. Moreover, the possibility of stabilizing heavy metals in carbonated material presents a promising avenue for future waste management innovation.

# References

1. IEA. Energy Efficiency Indicators Highlights. *International Energy Agency,* 191. ISSN: 1051-1482 (2018).
2. Kurniawan, T. A. *et al.* Decarbonization in waste recycling industry using digitalization to promote net-zero emissions and its implications on sustainability. *Journal of environmental management* **338,** 117765 (2023).
3. DiGiovanni, C., Hisseine, O. A. & Awolayo, A. N. Carbon dioxide sequestration through steel slag carbonation: Review of mechanisms, process parameters, and cleaner upcycling pathways. *Journal of $CO_2$ Utilization* **81,** 102736 (2024).
4. Liu, W. *et al.* $CO_2$ mineral carbonation using industrial solid wastes: A review of recent developments. *Chemical Engineering Journal* **416,** 129093 (2021).
5. Xie, H. *et al.* Scientific and engineering progress in $CO_2$ mineralization using industrial waste and natural minerals. *Engineering* **1,** 150–157 (2015).
6. Yoo, Y. *et al.* Review of contemporary research on inorganic $CO_2$ utilization via $CO_2$ conversion into metal carbonate-based materials. *Journal of Industrial and Engineering Chemistry* **116,** 60–74 (2022).
7. Chen, Z., Cang, Z., Yang, F., Zhang, J. & Zhang, L. Carbonation of steelmaking slag presents an opportunity for carbon neutral: A review. *Journal of $CO_2$ Utilization* **54,** 101738 (2021).
8. Srivastava, S., Snellings, R., Nielsen, P. & Cool, P. Insights into $CO_2$-mineralization using non-ferrous metallurgy slags: $CO_2$ (g)-induced dissolution behavior of copper and lead slags. *Journal of Environmental Chemical Engineering* **10,** 107338 (2022).
9. Ostovari, H., Müller, L., Skocek, J. & Bardow, A. From unavoidable $CO_2$ source to $CO_2$ sink? A cement industry based on $CO_2$ mineralization. *Environmental science & technology* **55,** 5212–5223 (2021).

10. Tanaka, S., Takahashi, K., Abe, M., Noguchi, M. & Yamasaki, A. Preparation of High-Purity Calcium Carbonate by Mineral Carbonation Using Concrete Sludge. *ACS omega* **7,** 19600–19605 (2022).

11. Kusin, F. M., Hasan, S. N. M. S., Molahid, V. L. M., Yusuff, F. M. & Jusop, S. Carbon dioxide sequestration of iron ore mining waste under low-reaction condition of a direct mineral carbonation process. *Environmental Science and Pollution Research* **30,** 22188–22210 (2023).

12. Hanifa, M., Agarwal, R., Sharma, U., Thapliyal, P. & Singh, L. A review on $CO_2$ capture and sequestration in the construction industry: Emerging approaches and commercialised technologies. *Journal of $CO_2$ Utilization* **67,** 102292 (2023).

13. Zhang, T., Chen, M., Wang, Y. & Zhang, M. Roles of carbonated recycled fines and aggregates in hydration, microstructure and mechanical properties of concrete: A critical review. *Cement and Concrete Composites* **138,** 104994 (2023).

14. Li, L., Liu, Q., Huang, T. & Peng, W. Mineralization and utilization of $CO_2$ in construction and demolition wastes recycling for building materials: A systematic review of recycled concrete aggregate and recycled hardened cement powder. *Separation and Purification Technology* **298,** 121512 (2022).

15. Li, Z. *et al.* Towards the Co-benefits of carbon capture, utilization and sequestration: A life cycle assessment study for steel slag disposal. *Journal of Cleaner Production,* 141166 (2024).

16. Bakshi, P. *et al.* Life Cycle Assessment of Calcium-Rich Industrial Waste Reinforced Polypropylene and Low-Density Polyethylene Composites Using the Cradle-to-Gate Approach. *ACS Sustainable Chemistry & Engineering* **10,** 13710–13721 (2022).

17. Li, L., Ling, T.-C. & Pan, S.-Y. Environmental benefit assessment of steel slag utilization and carbonation: A systematic review. *Science of The Total Environment* **806,** 150280 (2022).

18. Li, L., Jiang, Y., Pan, S.-Y. & Ling, T.-C. Comparative life cycle assessment to maximize $CO_2$ sequestration of steel slag products. *Construction and Building Materials* **298,** 123876 (2021).

19. Stefaniuk, D., Hajduczek, M., Weaver, J. C., Ulm, F. J. & Masic, A. Cementing $CO_2$ into CSH: A step toward concrete carbon neutrality. *PNAS nexus* **2,** pgad052 (2023).

20. Ostovari, H., Müller, L., Mayer, F. & Bardow, A. A climate-optimal supply chain for $CO_2$ capture, utilization, and storage by mineralization. *Journal of Cleaner Production* **360,** 131750 (2022).

21. Hu, G. *et al.* $CO_2$ mineral sequestration and faujasite zeolite synthesis by using blast furnace slag: process optimization and $CO_2$ net-emission reduction evaluation. *ACS Sustainable Chemistry & Engineering* **9,** 13963–13971 (2021).

22. Pan, S.-Y. *et al.* $CO_2$ mineralization and utilization by alkaline solid wastes for potential carbon reduction. *Nature Sustainability* **3,** 399–405 (2020).

23. Ragipani, R., Sreenivasan, K., Anex, R. P., Zhai, H. & Wang, B. Direct air capture and sequestration of $CO_2$ by accelerated indirect aqueous mineral carbonation under ambient conditions. *ACS Sustainable Chemistry & Engineering* **10,** 7852–7861 (2022).

24. IRENA. *Global Renewables Outlook: Energy Transformation 2050* tech. rep. (International Renewable Energy Agency, 2020). `https://www.irena.org/publications/2020/Apr/Global-Renewables-Outlook-2020`.

25. Zhang, Y., Yu, L., Cui, K., Wang, H. & Fu, T. Carbon capture and storage technology by steel-making slags: Recent progress and future challenges. *Chemical Engineering Journal* **455,** 140552 (2023).

26. Williams, A. in *Industrial Energy Systems Handbook* 1–24 (River Publishers, 2023).

27. Birol, D. F. *World Energy Outlook 2022* tech. rep. (2022).

28. Xie, J., Xia, Z., Tian, X. & Liu, Y. Nexus and synergy between the low-carbon economy and circular economy: A systematic and critical review. *Environmental impact assessment review* **100,** 107077 (2023).

29. Association, W. S. *et al. Steel-The permanent material in the circular economy* (Worldsteel Association, 2016).

30. Zhao, Q. *et al.* Co-treatment of Waste From Steelmaking Processes: Steel Slag-Based Carbon Capture and Storage by Mineralization. *Frontiers in Chemistry* **8,** 1–7 (2020).

31. Yi, Z., Wang, T. & Guo, R. Sustainable building material from $CO_2$ mineralization slag: Aggregate for concretes and effect of $CO_2$ curing. *Journal of $CO_2$ Utilization* **40,** 101196 (2020).

32. Li, H., Tang, Z., Li, N., Cui, L. & Mao, X.-z. Mechanism and process study on steel slag enhancement for $CO_2$ capture by seawater. *Applied Energy* **276,** 115515 (2020).

33. Yadav, S. & Mehra, A. A review on ex situ mineral carbonation. *Environmental science and pollution research* **28,** 12202–12231 (2021).

34. Pan, S.-Y., Chang, E., Chiang, P.-C., *et al.* $CO_2$ capture by accelerated carbonation of alkaline wastes: a review on its principles and applications. *Aerosol and Air Quality Research* **12,** 770–791 (2012).

35. Tian, S.-c., Jiang, J.-g., Li, K.-m., Yan, F. & Chen, X.-j. Performance of steel slag in carbonation–calcination looping for CO 2 capture from industrial flue gas. *RSC Advances* **4,** 6858–6862 (2014).

36. Vu, M. T. *et al.* Nutrient recovery from digested sludge centrate using alkali metals from steel-making slag. *Chemical Engineering Journal* **450,** 138186 (2022).

37. Yi, H. *et al.* An overview of utilization of steel slag. *Procedia Environmental Sciences* **16,** 791–801 (2012).

38. Zeng, B., Zhang, Z., Yang, S., Mo, L. & Jin, F. Alkanolamines-activated steel slag for stabilization/solidification of heavy metal contaminated soil. *Journal of Environmental Chemical Engineering* **11,** 110301 (2023).

39. Chiang, P.-C. & Pan, S.-Y. *Carbon Dioxide Mineralization and utilization* 1st ed. ISBN: 978-981-10-3268-4. `https://link.springer.com/book/10.1007/978-981-10-3268-4` (Springer Singapore, 2017).

40. Pan, S.-Y. *et al.* $CO_2$ mineralization and utilization using steel slag for establishing a waste-to-resource supply chain. *Scientific reports* **7,** 17227 (2017).

41. Ebrahimi, A. *et al.* Sustainable transformation of fly ash industrial waste into a construction cement blend via $CO_2$ carbonation. *Journal of Cleaner Production* **156,** 660–669 (2017).

42. Di Maria, A., Snellings, R., Alaerts, L., Quaghebeur, M. & Van Acker, K. Environmental assessment of $CO_2$ mineralisation for sustainable construction materials. *International Journal of Greenhouse Gas Control* **93,** 102882 (2020).

43. Du, Y. *et al.* Real-time investigation of the $CO_2$ mineral carbonation reaction rate through direct aqueous route using semi-dry desulfurization slag. *Journal of $CO_2$ Utilization* **51,** 101614 (2021).

44. Pan, S.-Y., Chiang, P.-C., Chen, Y.-H., Tan, C.-S. & Chang, E. Ex Situ $CO_2$ capture by carbonation of steelmaking slag coupled with metalworking wastewater in a rotating packed bed. *Environmental science & technology* **47,** 3308–3315 (2013).

45. Chang, E.-E., Chen, C.-H., Chen, Y.-H., Pan, S.-Y. & Chiang, P.-C. Performance evaluation for carbonation of steel-making slags in a slurry reactor. *Journal of hazardous materials* **186,** 558–564 (2011).

46. Chang, E., Pan, S.-Y., Chen, Y.-H., Tan, C.-S. & Chiang, P.-C. Accelerated carbonation of steelmaking slags in a high-gravity rotating packed bed. *Journal of hazardous materials* **227,** 97–106 (2012).

47. Chang, E.-E. *et al.* $CO_2$ sequestration by carbonation of steelmaking slags in an autoclave reactor. *Journal of Hazardous Materials* **195,** 107–114 (2011).

48. Yan, H. *et al.* A green synthesis strategy for low-cost multiporous solid $CO_2$ adsorbent using blast furnace slag. *Fuel* **329,** 125380 (2022).

49. Lee, J., Ryu, K. H., Ha, H. Y., Jung, K.-D. & Lee, J. H. Techno-economic and environmental evaluation of nano calcium carbonate production utilizing the steel slag. *Journal of $CO_2$ Utilization* **37,** 113–121 (2020).

50. Srivastava, S. *et al.* Carbonated steel slags as supplementary cementitious materials: Reaction kinetics and phase evolution. *Cement and Concrete Composites* **142,** 105213 (2023).

51. Liu, P., Mo, L., Zhong, J. & Tang, M. In-situ investigation on the carbonation behaviors of various mineral phases in steel slag: The role of RO phase. *Cement and Concrete Composites* **149,** 105524 (2024).

52. Sanna, A., Uibu, M., Caramanna, G., Kuusik, R. & Maroto-Valer, M. A review of mineral carbonation technologies to sequester $CO_2$. *Chemical Society Reviews* **43,** 8049–8080 (2014).

53. Reddy, K. R., Gopakumar, A. & Chetri, J. K. Critical review of applications of iron and steel slags for carbon sequestration and environmental remediation. *Reviews in Environmental Science and Bio/Technology* **18,** 127–152 (2019).

54. Capelo-Avilés, S. *et al.* A thorough assessment of mineral carbonation of steel slag and refractory waste. en. *Journal of $CO_2$ Utilization* **82,** 102770. ISSN: 22129820 (Apr. 2024).

55. Azdarpour, A. *et al.* A review on carbon dioxide mineral carbonation through pH-swing process. *Chemical Engineering Journal* **279,** 615–630 (2015).

56. Liu, M., Hohenshil, A. & Gadikota, G. Integrated $CO_2$ capture and removal via carbon mineralization with inherent regeneration of aqueous solvents. *Energy & Fuels* **35,** 8051–8068 (2021).

57. Renforth, P. The negative emission potential of alkaline materials. *Nature communications* **10,** 1401 (2019).

58. Huijgen, W. J., Witkamp, G.-J. & Comans, R. N. Mineral $CO_2$ sequestration by steel slag carbonation. *Environmental science & technology* **39,** 9676–9682 (2005).

59. Lackner, K. S. A guide to $CO_2$ sequestration. *Science* **300,** 1677–1678 (2003).

60. Huijgen, W. J. & Comans, R. N. Carbonation of steel slag for $CO_2$ sequestration: leaching of products and reaction mechanisms. *Environmental science & technology* **40,** 2790–2796 (2006).

61. Gao, J. *et al.* Process simulation and energy integration in the mineral carbonation of blast furnace slag. *Chinese journal of chemical engineering* **27,** 157–167 (2019).

62. Chen, T.-L., Pei, S.-L. & Chiang, P.-C. Integrated leaching–carbonation kinetic model on $CO_2$ mineralization of alkaline solid wastes in a high-gravity rotating packed bed. *Reaction Chemistry & Engineering* **5,** 1929–1938 (2020).

63. Rietveld, H. M. A profile refinement method for nuclear and magnetic structures. *Journal of applied Crystallography* **2,** 65–71 (1969).

64. Cheary, R. W., Coelho, A. A. & Cline, J. P. Fundamental parameters line profile fitting in laboratory diffractometers. *Journal of Research of the National Institute of Standards and Technology* **109,** 1 (2004).

65. Hill, R. & Howard, C. Quantitative phase analysis from neutron powder diffraction data using the Rietveld method. *Journal of Applied Crystallography* **20,** 467–474 (1987).

66. Stokes, A. & Wilson, A. *A method of calculating the integral breadths of Debye-Scherrer lines* in *Mathematical Proceedings of the Cambridge Philosophical Society* **38** (1942), 313–322.

67. Wang, D., Xiong, C., Li, W. & Chang, J. Growth of calcium carbonate induced by accelerated carbonation of tricalcium silicate. *ACS Sustainable Chemistry & Engineering* **8,** 14718–14731 (2020).

68. Chang, J. & Fang, Y. Quantitative analysis of accelerated carbonation products of the synthetic calcium silicate hydrate (C–S–H) by QXRD and TG/MS. *Journal of Thermal Analysis and Calorimetry* **119,** 57–62 (2015).

69. Hong, S., Moon, S., Cho, J., Park, A.-H. A. & Park, Y. Effects of Mg ions on the structural transformation of calcium carbonate and their implication for the tailor-synthesized carbon mineralization process. *Journal of $CO_2$ Utilization* **60,** 101999 (2022).

70. Huijgen, W. J., Ruijg, G. J., Comans, R. N. & Witkamp, G.-J. Energy consumption and net $CO_2$ sequestration of aqueous mineral carbonation. *Industrial & Engineering Chemistry Research* **45,** 9184–9194 (2006).

71. Chen, Y.-H. *et al.* Modeling ozone contacting process in a rotating packed bed. *Industrial & engineering chemistry research* **43,** 228–236 (2004).

72. Pan, S.-Y. *et al.* Systematic approach to determination of maximum achievable capture capacity via leaching and carbonation processes for alkaline steelmaking wastes in a rotating packed bed. *Environmental science & technology* **47,** 13677–13685 (2013).

73. Kuśtrowski, P., Chmielarz, L., Bożek, E., Sawalha, M. & Roessner, F. Acidity and basicity of hydrotalcite derived mixed Mg–Al oxides studied by test reaction of MBOH conversion and temperature programmed desorption of NH3 and $CO_2$. *Materials Research Bulletin* **39,** 263–281 (2004).

74. Fernandez, L., Alonso, C., Hidalgo, A. & Andrade, C. The role of magnesium during the hydration of C3S and CSH formation. Scanning electron microscopy and mid-infrared studies. *Advances in cement research* **17,** 9–21 (2005).

75. Yu, P., Kirkpatrick, R. J., Poe, B., McMillan, P. F. & Cong, X. Structure of calcium silicate hydrate (C-S-H): Near-, Mid-, and Far-infrared spectroscopy. *Journal of the American Ceramic Society* **82,** 742–748 (1999).

76. Kloprogge, J. T. & Frost, R. L. Fourier transform infrared and Raman spectroscopic study of the local structure of Mg-, Ni-, and Co-hydrotalcites. *Journal of Solid State Chemistry* **146,** 506–515 (1999).

77. Aguiar, H., Serra, J., González, P. & León, B. Structural study of sol–gel silicate glasses by IR and Raman spectroscopies. *Journal of Non-Crystalline Solids* **355,** 475–480 (2009).

78. Cadiș, A. I., Rus, F. Ș., Gonçalves, J. N. & Ivanovici, M. Preparing a Ca-Bi-O system by the precipitation method and studying its intermediate structural properties for applications in water treatment. *Inorganics* **11,** 79 (2023).

79. Meiszterics, A. *et al.* Structural characterization of gel-derived calcium silicate systems. *The Journal of Physical Chemistry A* **114,** 10403–10411 (2010).

80. Xyla, A. G. & Koutsoukos, P. G. Quantitative analysis of calcium carbonate polymorphs by infrared spectroscopy. *Journal of the Chemical Society, Faraday Transactions 1: Physical Chemistry in Condensed Phases* **85,** 3165–3172 (1989).

81. Kiefer, J., Stärk, A., Kiefer, A. L. & Glade, H. Infrared spectroscopic analysis of the inorganic deposits from water in domestic and technical heat exchangers. *Energies* **11,** 798 (2018).

82. Ho, H.-J., Iizuka, A. & Kubo, H. Direct aqueous carbonation of dephosphorization slag under mild conditions for $CO_2$ sequestration and utilization: Exploration of new dephosphorization slag utilization. *Environmental Technology & Innovation* **28,** 102905 (2022).

# 6
# Conclusions.

This thesis presents a multi-faceted approach to carbon capture and utilization (CCU) in industrial settings. First, a thorough assessment of current carbon capture (CC) technologies, identifying their strengths, limitations, and potential for improvement in the secondary steel sector. This evaluation provides insights into the technical, economic, and environmental aspects of these technologies. Next, a novel, versatile material is developed with the ability to selectively capture $CO_2$ from both $CO_2/N_2$ and $CO_2/CH_4$ mixtures. This material exhibits promising potential for CO2 capture due to its unique properties and high selectivity. Rigorous thermodynamic and kinetic characterization provides valuable insights for future testing under real industrial conditions. Furthermore, this thesis explored $CO_2$ mineralization as a potential storage solution within industrial waste streams. Comprehensive characterization of steel industry slag contributes valuable knowledge to improve both gaseous ($CO_2$) and solid waste management within a circular economy framework. The main findings can be su summarized as follows:



- In the secondary steel industry, such as CELSA, available benchmark CC technologies like amine scrubbing, adsorption systems, membranes, and calcium looping are not directly suitable or economically viable due to high operating costs (OPEX > 30 €/ton $CO_2$) and energy consumption (>1000 kWh ton$^{-1}$ $CO_2$). In Chapter 2, we present a comprehensive qualitative assessment of these technologies and their potential integration within the secondary steel industry. Based on this assessment, amine scrubbing (with MEA) and VSA with zeolite 13X were identified as the most feasible technologies for CELSA. Thermodynamic models and process modeling tools were employed to critically evaluate the total annualized cost (TAC) and energy consumption associated with these technologies. This analysis provides valuable insights into the economic viability and energy efficiency of $CO_2$ capture in the secondary steel industry.

- TAMOF-1, a stable and robust metal-organic framework, exhibits selective $CO_2$ adsorption from gas streams, reaching capacities up to 3.7 mmol g$^{-1}$ at ambient conditions. In chapter 3 we demonstrate its favorable separation parameters for $CO_2/N_2$ mixtures, with high IAST selectivities (up to 205) across various concentrations, pressures, and temperatures. Its weak $CO_2$ interactions enable facile, low-energy regeneration. Dynamic col-

umn breakthrough experiments confirm concentration-dependent $CO_2$ desorption and high purities (>99.9%) after vacuum regeneration. A 4-step VSA configuration achieves $\sim$ 95% $CO_2$ purity and $\sim$ 77% recovery with minimal vacuum. Notably, vacuum activation significantly enhances TAMOF-1's adsorption capacity compared to $N_2$ purging. Cyclic VSA tests under flue gas conditions demonstrate superior performance compared to zeolite 13X, with 25% higher $CO_2$ recovery at $\sim$ 99.8% purity. Pellet and powder forms exhibit comparable adsorption capacities but differ in desorption behavior. Single-component breakthrough experiments validate kinetic models and reveal fast mass transfer for both forms. Overall, TAMOF-1 pellets show strong potential for post-combustion carbon capture using PVSA technologies, offering a tunable regeneration protocol for flexible operation. Further research will focus on scaling up, process optimization, real-world stability assessment, and techno-economic feasibility analysis.

- TAMOF-1 demonstrates exceptional promise for biogas upgrading, exhibiting high ideal selectivities for $CO_2/CH_4$ ($> 30$) and substantial $CO_2$ adsorption capacities ($> 3 mmol g^{-1}$), surpassing many other adsorbent materials. In Chapter 4, we thoroughly characterize the patented metal-organic framework, TAMOF-1, as a physisorptive adsorbent for $CO_2/CH_4$ separation. Adsorption isotherms confirm preferential $CO_2$ adsorption over $CH_4$ and $N_2$. Dynamic fixed-bed column experiments further validate TAMOF-1 capacity for $CH_4/CO_2$ separation, demonstrating high selectivity (up to 4) and $CO_2$ adsorption capacity (up to 3.87 mmol $g^{-1}$) under ambient conditions. The negligible effect of $CH_4/N_2$ ratio on $CO_2$ elution behavior through TAMOF-1 was also established. Computational evaluations using Monte Carlo and molecular dynamics simulations align with experimental data, underscoring the material's promising performance. Moreover, TAMOF-1 pellets exhibit cyclic stability during adsorption/desorption cycles with biogas-like mixtures (50% $CO_2$: 50% $CH_4$), maintaining good selectivity and a steady-state $CO_2$ adsorption capacity of 1.5 mmol $g^{-1}$.

- Mineralization presents a promising solution for simultaneous $CO_2$ sequestration and valorization of high-basicity industrial

byproducts, aligning with circular economy principles. In chapter 5 our study demonstrates the feasibility of this approach using waste materials from the secondary steel industry. Carbonation of white slag (WS) achieved a maximum $CO_2$ sequestration capacity of up to 359.79 $g_{CO_2} kg_{slag}^{-1}$, highlighting the potential for direct mineralization using industrial off-gases. Optimization studies identified ideal conditions for WS carbonation. Refractory wastes (RWs), while slower, reached a higher maximum sequestration capacity of 311 $g_{CO_2} kg_{slag}^{-1}$. Notably, tundish RW exhibited the highest carbonation degree and sequestration capacity among individual RW fractions. Solution pH was found to be a critical factor influencing mineralization, warranting further investigation into pH control strategies. Characterization studies confirmed CaO as the primary reactant, with minimal MgO involvement. Importantly, carbonation appears to stabilize heavy metals like Pb, suggesting potential for waste remediation. Overall, this study demonstrates the potential of mineralization to address both $CO_2$ emissions and waste streams within the steel industry, contributing to sustainable industrial practices.

# A

# Appendix A: Chapter 2 Support information

Table A.1: List of process equipment and their characteristics for the MEA stripping capture system.

| Tag | Service | Type | Equipment | Fluid | Temperature K | Pressure bar |
|---|---|---|---|---|---|---|
| C-1 | Exhaust gas compressor | Centrifugal | Compressor | Exhaust gas | 313-373 | 1.52 |
| HX-1 | Exhaust gas precooler | Shell & tubes / plates & frame | Heat ex | Exhaust gas /water | 313-513 | 1.05 |
| HX-2 | Exhaust gas aftercooler | Shell & tubes/ plates & frame | Heat ex | Exhaust gas /water | 373-313 | 2 |
| AB-1 | Amine Contactor | Vertical | Column | Acid gas/MDEA | 329 | 1.5 DP=0.1 |
| P-1 | Rich amine pump | Centrifugal | Pump | Rich Amine | 335 | 1.62 |
| HX-3 | Lean/Rich amine heat exchanger | Plates & frame | Heat ex | Lean/rich MDEA | Cold: 341 -365 Hot: 394 -369 | Cold: 1.8 Hot:1.6 |
| STRIP-1 | Amine regenerator | Vertical | Column | Rich Amine | Head: 322 Bottom:397 | 1.6 |
| ST_C-1 | Amine reflux condenser | Total Reflux | Heat ex | CO2 90% | 322 | 1.15 |
| ST_R-1 | Amine Regenerator Reboiler | Kettle | Heat ex | Lean amine | 394 | 1.62 |
| HX-4 | Lean amine cooler | Shell & tubes / plates & frame | Heat ex | Lean amine/water | 364-320 | 1.62 |
| P-2 | MEA makeup pump | Centrifugal | Pump | MEA makeup | 290 | 1.52 |

Table A.2: List of process equipment and their characteristics for the $CO_2$ capture process by adsorption with 13X zeolite.

| TAG | SERVICE | TYPE | CHARACTERISTICS | FLUID | Temp (Op.) K | Pressure (Op.) bar |
|---|---|---|---|---|---|---|
| B1 | Exhaust gas fan | Compressor | Centrifugal | Exhaust gas | 507 | 1.2 |
| DDC1 | Exhaust gas cooler (quench) | Direct contact colum | AISI 316 | Exhaust gas /water | 332 | 1.1 |
| F1 | Gas- liquid separator | Pressure vessel AISI 316 | Heat ex | Exhaust gas /water | 308 | 1.1 |
| Sil_col-i | TSA column - silica Gel | Vertical Pressure vessel | Internal heat exchange. AISI 316. D 400 x 1200 mm | Exhaust gas /water | 308 - 423 | 1.05 |
| C1 | Dry exhaust gas compression | Compressor - intercooling | Two steps of Centrifugal and intercooling | Dry exhaust gas | 298 | 2.7 |
| AC-i | Adsorption columns | Vertical Pressure vessel | AISI 316. D 660 X 3700 mm | Dry exhaust gas | 298 | 0.02 - 2.7 |
| VP-i | $CO_2$ recovery (Evacuation) | vacuum pump | Centrifugal | Dry high CO2-rich gas | 298 | 0.02 |
| BP-i | $CO_2$ concentration (blow-down) | vacuum pump | Centrifugal | $CO_2/N_2$ | 298 | 0.13 |

# B

# Appendix B: Chapter 3 Support information

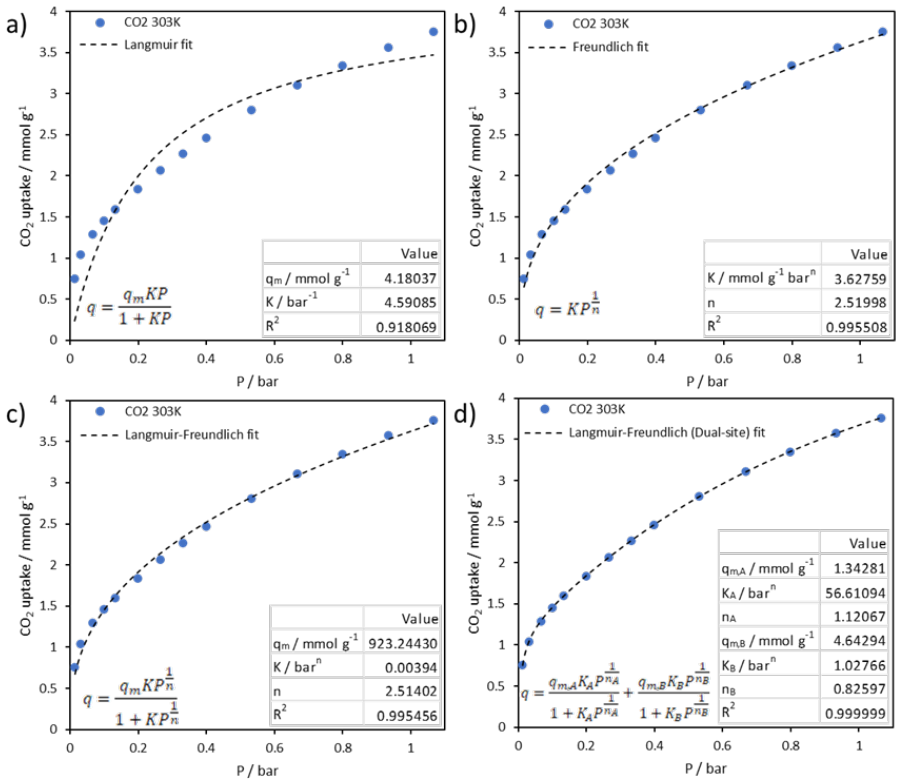


Figure B.1: Langmuir (a), Freundlich (b), Langmuir-Freundlich (c) and Dual-site Langmuir-Freundlich (d) models fitting for the $CO_2$ adsorption isotherm of TAMOF-1 at 303 K.

Table B.1: Crystal data and structure refinement for TAMOF-1 at different temperatures.

| | 100(2) K | 298(2) K | 403(2) K | 100(2) K(rehydrated) |
|---|---|---|---|---|
| Empirical formula | C16H31.33CuN10O11.67 | C16H25.67CuN10O8.83 | C16H16CuN10O4 | C16H31CuN10O11.5 |
| Formula weight | 614.05 | 563 | 475.93 | 611.04 |
| Temperature/K | 100(2) | 298(2) | 404(2) | 100(2) |
| Wavelength/Å | *0.71073* | 0.71073 | 0.71073 | 0.71073 |
| *Crystal system* | Cubic | Cubic | Cubic | Cubic |
| *Space group* | P4332 | *P4332* | *P4332* | *P4332* |
| *a/Å* | 20.120(4) | 20.172(2) | 20.262(2) | 20.1133(7) |
| b/Å | 20.120(4) | 20.172(2) | 20.262(2) | 20.1133(7) |
| c/Å | 20.120(4) | 20.172(2) | 20.262(2) | 20.1133(7) |
| $\alpha$/ º | 90 | 90 | 90 | 90 |
| $\beta$/ º | 90 | 90 | 90 | 90 |
| $\gamma$/º | 90 | 90 | 90 | 90 |
| Volume/Å3 | 8145(4) | 8208(2) | 8319(3) | 8136.7(8) |
| *Z* | 12 | 12 | 12 | 12 |
| $\rho$ *calc/g* $cm^{-3}$ | 1.502 | 1.367 | 1.14 | 1.496 |
| $\mu/mm^{-1}$ | 0.878 | 0.857 | 0.822 | 0.878 |
| *F(000)* | 3836 | 3496 | 2916 | 3816 |
| Crystal size/mm3 | 0.05 × 0.05 × 0.03 | 0.05 × 0.05 × 0.03 | 0.05 × 0.05 × 0.03 | 0.05 × 0.05 × 0.03 |
| $\theta$ range for data collection/° | 1.753 to 35.178 | 1.749 to 32.062 | 1.741 to 27.108 | 1.754 to 33.716 |
| Index ranges | –12 ≤ h ≤ 27<br>–6 ≤ k ≤ 32<br>–27 ≤ l ≤ 8 | –11 ≤ h ≤ 26<br>–7 ≤ k ≤ 26<br>–6 ≤ l ≤ 30 | –6 ≤ h ≤ 21<br>–14 ≤ k ≤ 20<br>–5 ≤ l ≤ 25 | –31 ≤ h ≤ 7<br>–21 ≤ k ≤ 26<br>–31 ≤ l ≤ 17 |
| | 18098 | 14121 | 11230 | 53327 |
| | 5693 | 4677 | 3063 | 5445 |
| *Rint* | 0.031 | 0.0578 | 0.0358 | 0.04 |
| Completeness/% | *98.9* | 97.5 | 99.3 | 99.9 |
| *Absorption correction* | *None* | Multi-scan | Multi-scan | Multi-scan |
| Data/restraints/parameters | 5693/78/263 | 4677/51/222 | 3063/0/141 | 5445/78/263 |
| Goodness-of-fit on F2 | 1.043 | 0.986 | 1.071 | 1.085 |
| Final Ra indexes [I>=2$\sigma$ (I)] | R1 = 0.0341<br>wR2 = 0.0884 | R1 = 0.0439<br>wR2 = 0.1012 | R1 = 0.0331<br>wR2 = 0.0807 | R1 = 0.0290<br>wR2 = 0.0796 |
| Final Ra indexes [all data] | R1 = 0.0406<br>wR2 = 0.0914 | R1 = 0.0625<br>wR2 = 0.1083 | R1 = 0.0442<br>wR2 = 0.0850 | R1 = 0.0333<br>wR2 = 0.0819 |
| Flack parameter | –0.014(4) | 0.004(9) | –0.016(9) | –0.008(3) |
| Largest diff. peak/hole / e Å–3 | 0.458/–0.353 | 0.431/–0.278 | 0.182/–162 | 0.509/–0.271 |

Table B.2: Isotherm parameters for $CO_2$, $CH_4$, and $N_2$ adsorption on the TAMOF-1 at 298K from 0-1 bar.

| | | CO2 | CH4 | N2 |
|---|---|---|---|---|
| Langmuir | *qm,L / mmol g–1* | 4.18037 | 4.06566 | 4.52801 |
| | *KL/bar-1* | 4.59085 | 0.20579 | 0.05677 |
| | *R2* | 0.918069 | 0.99989 | 0.999993 |
| Freundlich | *KF / mmol g–1 bar* | 3.62759 | 0.69853 | 0.24371 |
| | *nF* | 2.51998 | 1.10663 | 1.03064 |
| | *R2* | 0.995508 | 0.99927 | 0.999934 |
| Langmuir-Freundlich (Sips) | *qm,LF/mmol g–1* | 923.2443 | 3.25824 | 3.35045 |
| | *KLF/barn* | 0.00394 | 0.2702 | 0.07825 |
| | *nLF* | 2.51402 | 0.97008 | 0.98785 |
| | *R2* | 0.995456 | 0.99992 | 0.999998 |
| Langmuir-Freundlich (Dual site) | *qm,A/mmol g–1* | 1.34281 | 0.41023 | 0.17408 |
| | *KA/barn* | 56.61094 | 3.73563 | 0.27453 |
| | *nA* | 1.12067 | 0.82172 | 0.40343 |
| | *qm,B/mmol g–1* | 4.64294 | 0.86851 | 0.73201 |
| | *KB/barn* | 1.02766 | 0.74271 | 0.39096 |
| | *nB* | 0.82597 | 0.46732 | 0.96 |
| | *R2* | 0.999999 | 0.99998 | 0.999999 |

Table B.3: Langmuir-Freundlich (Sips) Isotherm parameters for $CO_2$ adsorption on the TAMOF-1 at 298K from 0-1 bar and 1-10 bar.

| Sips models | | CO2 (0-1 bar) | CO2 (1-10bar) |
|---|---|---|---|
| | *qm,LF/mmol g–1* | 4.5752 | 6.86 |
| n=1 , m=1 | *K* | 0.009809 | 0.009809 |
| | *SSE* | 3.16 | 0.75 |
| | *qm,LF/mmol g–1* | 14.1568 | 9.98 |
| n=2, m=1 | *K* | 0.0033 | 0.0033 |
| | *SSE* | 0.3873 | 0.198 |
| | *qm,LF/mmol g–1* | 6.7411 | 6.74 |
| n = 3, m=2 | *K* | 0.00119 | 0.00119 |
| | *SSE* | 1.0966 | 0.194 |

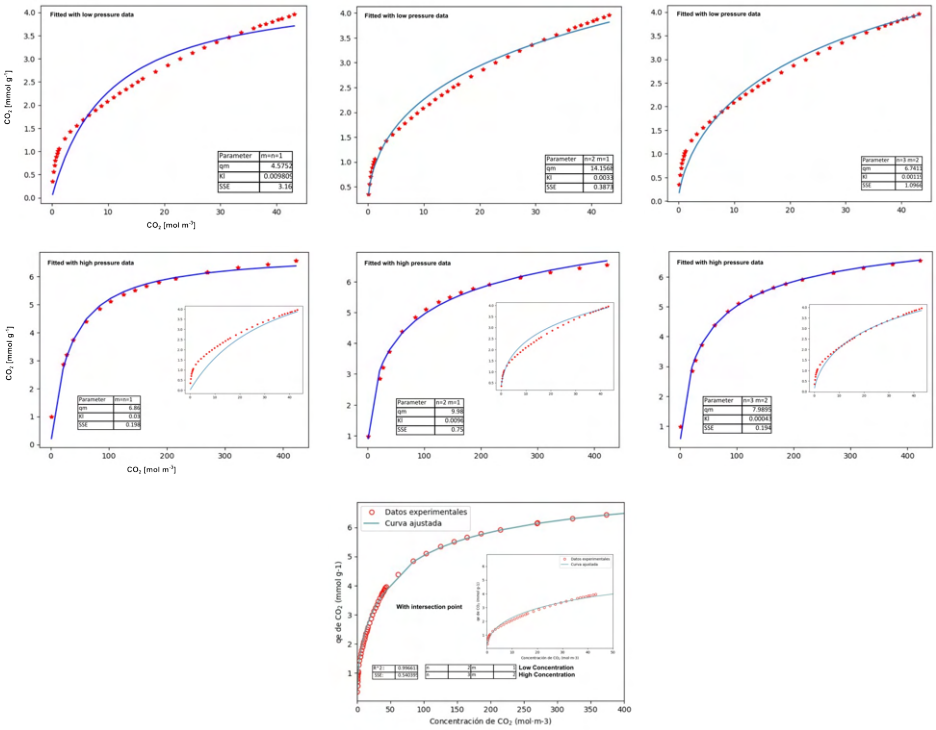


Figure B.2: Sips isotherm model fitting for the $CO_2$ adsorption isotherm of TAMOF-1 at 303 K.

Table B.4: Parameters used for the fitting of the breakthrough curves.

| Parameter | Value |
|---|---|
| Temperature [ºC] | 25 |
| Column lenght [cm] | 5.3-5.8 |
| Column inner diameter [cm] | 1.95 |
| velocity [m/s] | 0.005; 0.010; 0.015 |
| Inlet concentration [mol/m3] | 6% CO2 diluted in He. = 2.10 [mol·m-3] |
| Bulk density [kg/m3] | 680 |
| Column void fraction | 0.58 |

Table B.5: Breakthrough measures performed with Activation 1 ($N_2$ flow) at 298K and 1 bar at different $CO_2/N_2$ ratios (6:94, 15:85, 30:70).

| Inlet $CO_2$ concentration [%] | Breakthrough time [min $g^{-1}$] | $CO_2$ adsorbed $q_b$ [mmol $g^{-1}$] | $CO_2$ adsorbed $q_s$ [mmol $g^{-1}$] | Selectivity (Ss) |
|---|---|---|---|---|
| 6 | 7.3 | 0.57 | 0.79 | 123.7666667 |
| 15 | 3.69 | 0.62 | 0.86 | 48.73333333 |
| 30 | 1.84 | 0.67 | 0.92 | 25.86345382 |

Table B.6: $CO_2$ desorbed and $N_2$ remaining in TAMOF-1 after different vacuum regeneration times, for different gas inlet $CO_2/N_2$ ratios (6:94, 15:85, and 30:70).

| $CO_2/N_2$ Gas concentration ratio | Total vacuum time [min] | Vacuum pressure [mbar] | $CO_2$ Desorbed [mmol g-1] | $N_2$ remaining [mmol g-1] |
|---|---|---|---|---|
| 6:94 | 30 | 2.2 | 0.342 | 0 |
| | 10 | 5.1 | 0.236 | 0 |
| | 2 | 15.2 | 0.161 | 9.22E-04 |
| | 0.5 | 24.3 | 0.136 | 0.0025 |
| | 0.08 | 78.7 | 0.079 | 0.0131 |
| 15:85 | 23 | 4.2 | 0.3478 | 0 |
| | 10 | 6.3 | 0.303 | |
| | 5 | 15.4 | 0.262 | 2.32E-04 |
| | 2 | 20.5 | 0.211 | 9.44E-04 |
| | 0.5 | 34.3 | 0.17 | 0.00195 |
| | 0.08 | 79.1 | 0.131 | 0.00661 |
| 30:70 | 14 | 6.3 | 0.506295 | 0 |
| | 10 | 10 | 0.490525 | 0 |
| | 5 | 16.2 | 0.42563 | 0.000663375 |
| | 2 | 24.5 | 0.35285 | 0.001138455 |
| | 0.5 | 41.8 | 0.30243 | 0.002218974 |
| | 0.08 | 89.6 | 0.22073 | 0.006335372 |

Table B.7: Impact of $O_2$ Presence on $CO_2$ Desorption and $N_2$ remaining in TAMOF-1 Powder under Varying Vacuum Regeneration Times (6% $CO_2$ Inlet Concentration, 298K, 1 bar)

| inlet gas composition [%] | Vacuum Desorption time [min] | $CO_2$ desorbed [mmol g-1] | $N_2$ remaining in the column [mmol g-1] |
|---|---|---|---|
| $6CO_2/94N_2$ | 0.08 | 0.0785 | 0.0131 |
| $6CO_2/84N_2/10O_2$ | 0.08 | 0.1 | 0.0096 |
| $6CO_2/94N_2$ | 0.5 | 0.126 | 0.00202 |
| $6CO_2/84N_2/10O_2$ | 0.5 | 0.136 | 0.00256 |

Table B.8: Breakthrough measures TAMOF-1 powder at different gas velocities, temperatures, and pressures.

| v [m·s-1] | T [ºC] | P [bar] | qs [mmol·g-1] |
|---|---|---|---|
| 0.005 - 0.015 | 25 | 1 | 0.9 |
| | | 3 | 1.37 |
| | | 5 | 1.74 |
| | 50 | 1 | 0.6 |
| | | 3 | 0.93 |
| | | 5 | 1.32 |
| | 80 | 1 | 0.3 |
| | | 3 | 0.53 |
| | | 5 | 0.8 |

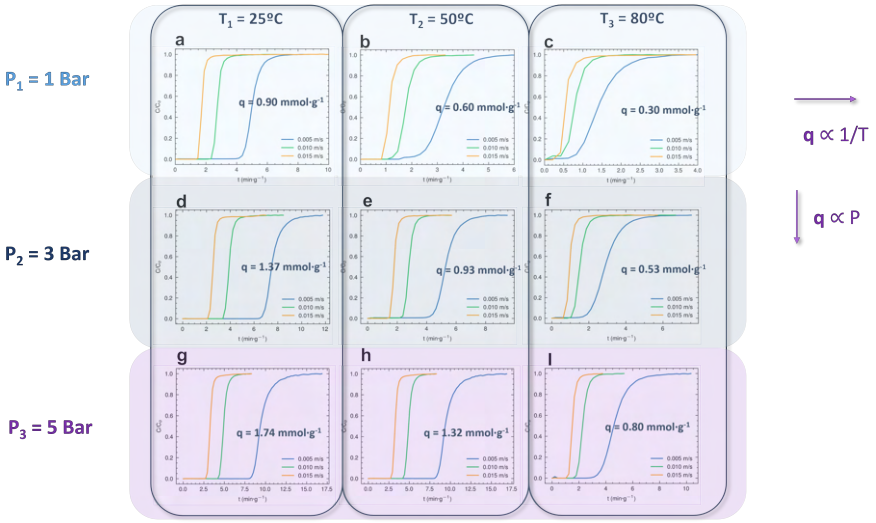


Figure B.3: $CO_2$ Breakthrough curves of TAMOF-1 for different gas velocities (0.005 – 0.15 m/s), in temperature and pressure range of 25–80ºC and 1–5bar, respectively.

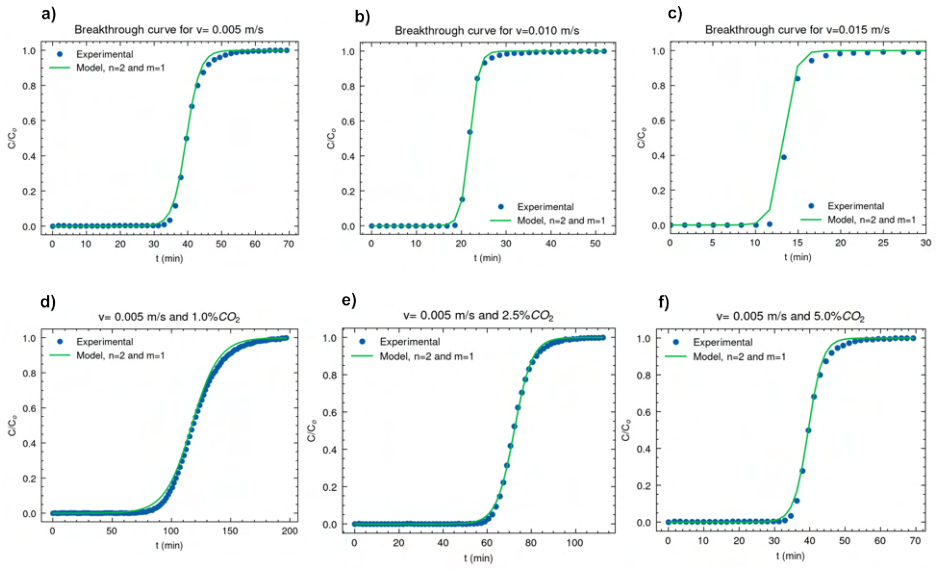


Figure B.4: TAMOF-1 powder $CO_2$ Breakthrough measures (dots) and fitting curves (lines), at 298K and 1 bar, for a) 0.005, b) 0.010, and c) 0.015 m $s^{-1}$ gas velocities. And, d) 1%, 2.5% $CO_2$ gas concentration (He balance) with 0.005 m $s^{-1}$ gas velocity.

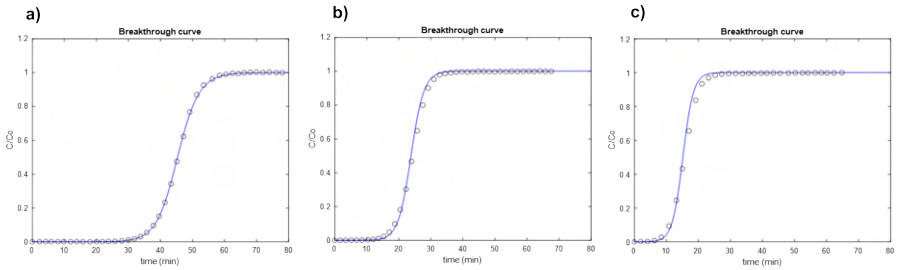


Figure B.5: TAMOF-1 pellet $CO_2$ Breakthrough curves and its fitting curves (lines), at 298K, 1 bar, and 0.005 m $s^{-1}$ for a) , b) 0.010, and c) 0.015 m $s^{-1}$ gas velocities.

# C

# Appendix C: Chapter 4 Support information

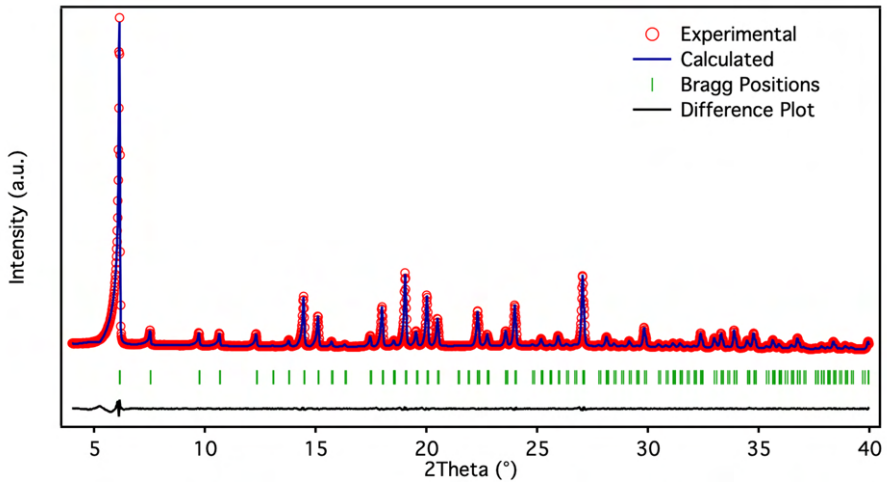


Figure C.1: Powder X-ray diffraction pattern of TAMOF-1 (red dots), compared with the theoretical pattern calculated from the single crystal data (blue line).

Table C.1: Fitting parameters for $CO_2$, $CH_4$, and $N_2$ adsorption isotherms of TAMOF-1 at 298.15 K.

| | | $CO_2$ | $CH_4$ | $N_2$ |
|---|---|---|---|---|
| Langmuir | qm,L / mmol $g^{-1}$ | | 4.06566 | 4.52801 |
| | KL/bar-1 | | 0.20579 | 0.05677 |
| | R2 | | 0.99989 | 0.999993 |
| Langmuir-Freundlich | qm,LF/ mmol $g^{-1}$ | 10.6 | | |
| | KLF/ barn | 0.0033 | | |
| | nLF | 2 | | |
| | R2 | 0.995456 | | |

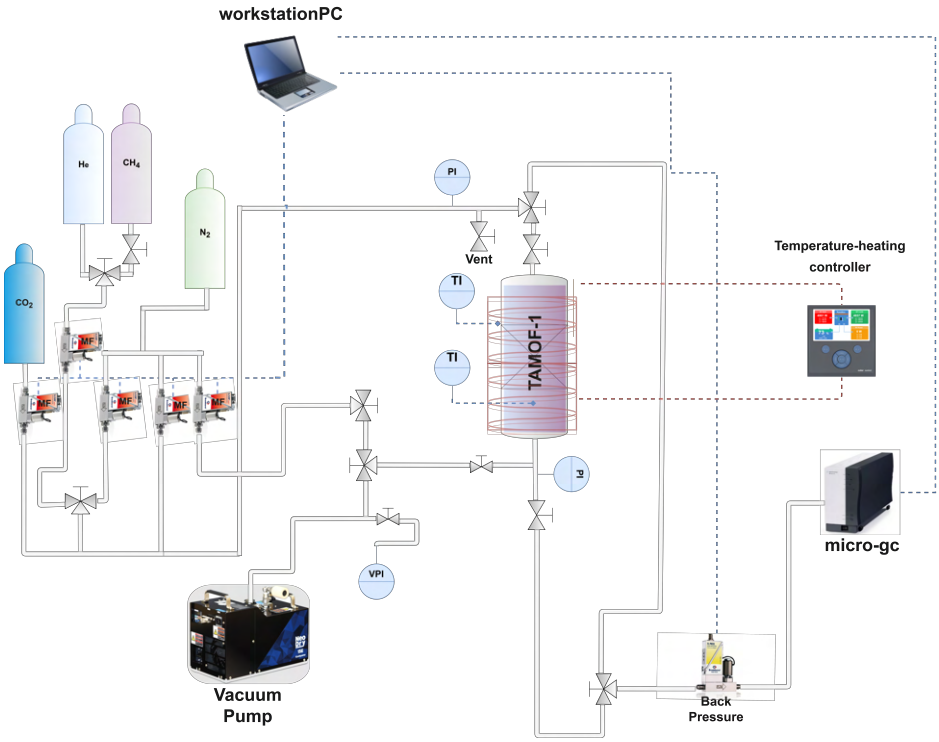


Figure C.2: Schematic diagram of the experimental set-up used for the breakthrough experiments.

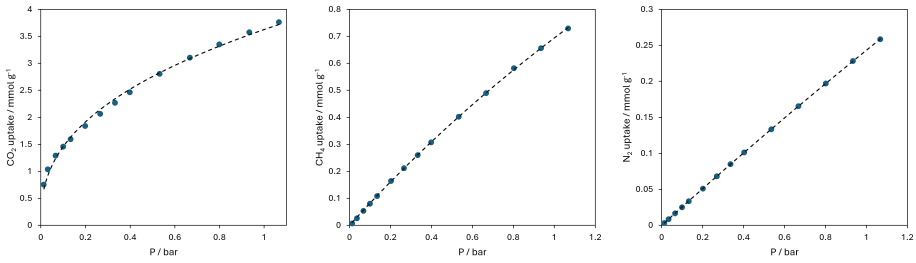


Figure C.3: adsorption isotherms measures (dots) and fittings (lines), for $CO_2$ (left), $CH_4$ (middle), and $N_2$ (right) at 298.15 K. $CO_2$ isotherm fitted with Langmuir-Freundlich single site, and $CH_4$ and $N_2$ with Langmuir single site.

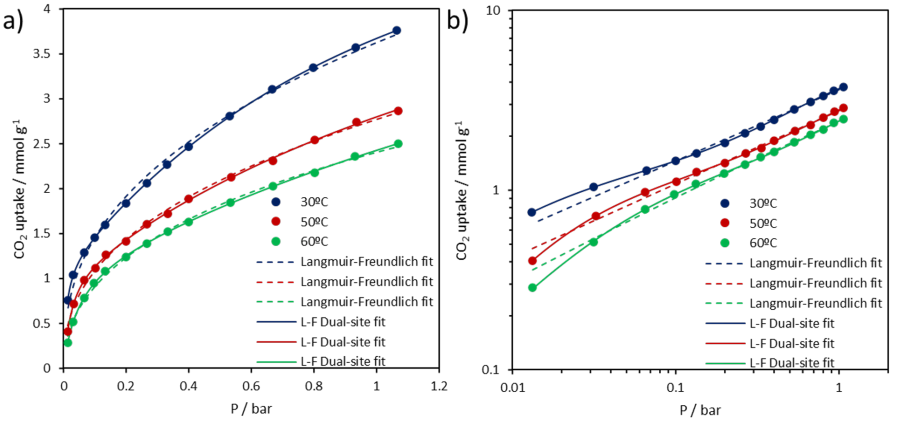


Figure C.4: $CO_2$ adsorption isotherms of TAMOF-1 at 303, 323 and 333 K, fitted to single-site and dual-site Langmuir-Freundlich models plotted as $CO_2$ uptake vs. pressure in linear (a) and logarithmic (b) scales.

Table C.2: IAST Selectivity of TAMOF-1 for $CO_2/CH_4$ mixtures ratios (30:70, 50:50, and 70:30) at 298.15 K and in the pressure range 0.1–10 bar.

| Pressure [bar] | 30:70 CO2/CH4 | 50:50 CO2/CH4 | 70:30 CO2/CH4 |
|---|---|---|---|
| 0.1 | 70.8 | 62 | 56.4 |
| 0.5 | 44 | 38.4 | 35.6 |
| 1 | 35.6 | 32.8 | 31.8 |
| 3 | 31.7 | 32.7 | 34.6 |
| 5 | 32.8 | 36.1 | 39.94 |
| 7 | 34.9 | 40 | 45.3 |
| 10 | 38.2 | 45.9 | 52.6 |

Table C.3: $CO_2$ : $CH_4$ separation performance of TAMOF-1 under different breakthrough operation conditions (overall flow rate and gas composition), in terms of breakthrough time ($B_t$), adsorption capacity at breakthrough ($q_b$) and at saturation ($q_s$) of each gas, $CO_2/CH_4$ breakthrough selectivity ($S_b$) and $CO_2/CH_4$ adsorption selectivity at saturation ($S_s$). Unless otherwise stated, the experiments have been carried out using micro gas chromatograph as effluent analyzer.

| | | | | | | CO2 | | | CH4 | | | |
|---|---|---|---|---|---|---|---|---|---|---|---|---|
| P / bar | T / K | Ft / NmL min-1 | CO2 [%] | CH4 [%] | N2 [%] | BTb / min g-1 | qb / mmol g-1 | qs / mmol g-1 | BTb / min g-1 | qb / mmol g-1 | qs / mmol g-1 | Sb,CO2/CH4 | Ss,CO2/CH4 |
| 1.05 | 298 | 5 | 100b | | | 15.77 | 3.43 | 3.87 | | | | | |
| 1.05 | 298 | 5 | 75b | 25b | | 13.27 | 2.26 | 3.01 | 9.91 | | 0.65 | | 1.54 |
| 1.05 | 298 | 5 | 50b | 50b | | 16.43 | 1.65 | 2.5 | 8.25 | | 1.1 | | 2.55 |
| 1.05 | 298 | 5 | 50b | 0 | 50b | 13.016 | 1.67 | 2.5 | | | | | |
| 1.05 | 298 | 5 | 50b | 25b | 25b | 16.5 | 1.67 | 2.46 | 8.2 | | 0.6 | | 4.10 |
| 1.05 | 298 | 5 | 25b | 75b | | 18.72 | 0.96 | 1.58 | 6.76 | | 1.45 | | 3.27 |
| 1.05 | 298 | 5 | 0 | 100b | | | | | | | 1.41 | | |
| 1.05-1.3 | 298 | 269 | 1.5a,c | 3.5a,c | | 3.62 | 0.52 | 0.59 | | | 0.05 | | |
| 1.05-1.3 | 298 | 269 | 2.5a,c | 2.5a,c | | 2.62 | 0.64 | 0.72 | | | 0.035 | | |
| 1.05-1.3 | 298 | 269 | 3.5a,c | 1.5a,c | | 2.12 | 0.7 | 0.79 | | | 0.02 | | |
| 1.05 | 298 | 30 | 50d (S1a) | 50d (S1a) | | 1.87 | 1.42 | 1.74 | 0.46 | 0.31 | 0.42 | 4.58 | 4.14 |
| 1.05 | 298 | 30 | 50d (S1b-j) | 50d (S1b-J) | | 1.75 | 1.14 | 1.52 | 0.44 | 0.29 | 0.43 | 3.93 | 3.53 |

# D

# Appendix D: Chapter 5 Support information

# TGA analysis

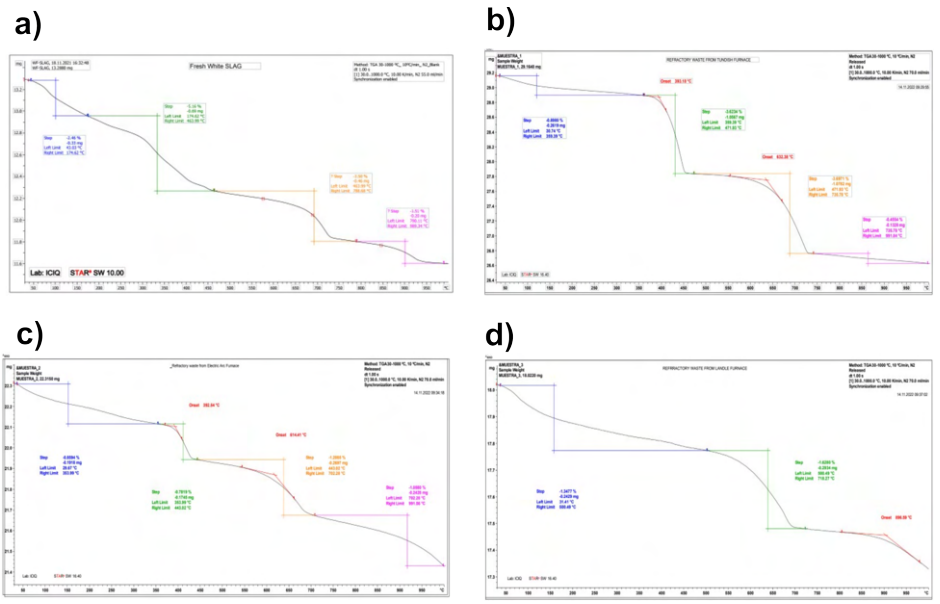


Figure D.1: Thermogravimetric analysis of refractories waste from: a) White Slag, b) Tundish Furnace, c) Electric arc furnace, and d) Ladle Furnace.

# XRD analysis

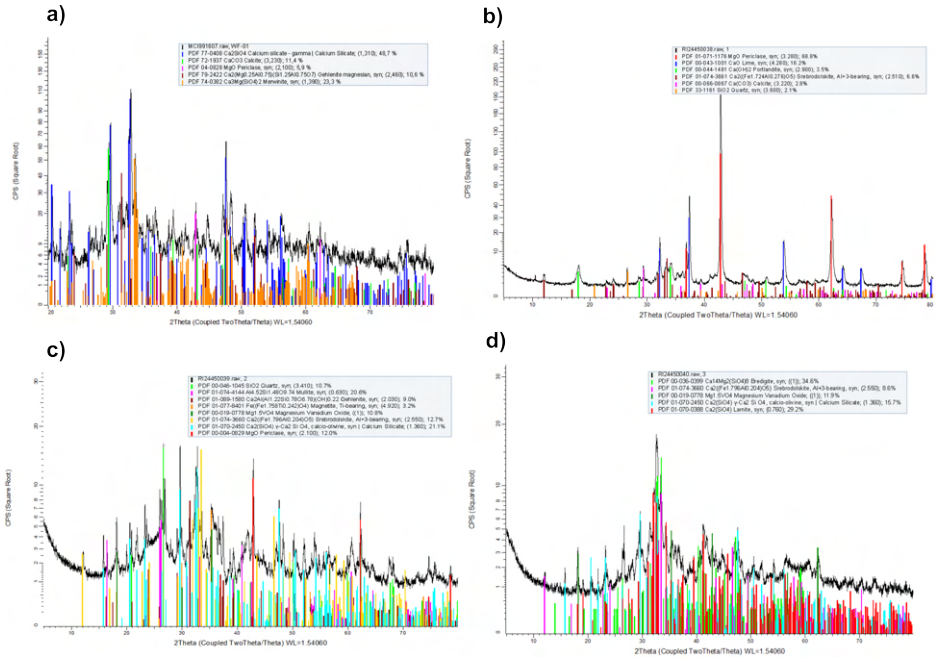


Figure D.2: X-diffraction of non-carbonated: a) White slag, b) Tundish Refractory waste, c) EAF refractory waste and d) Ladle Refractory waste.

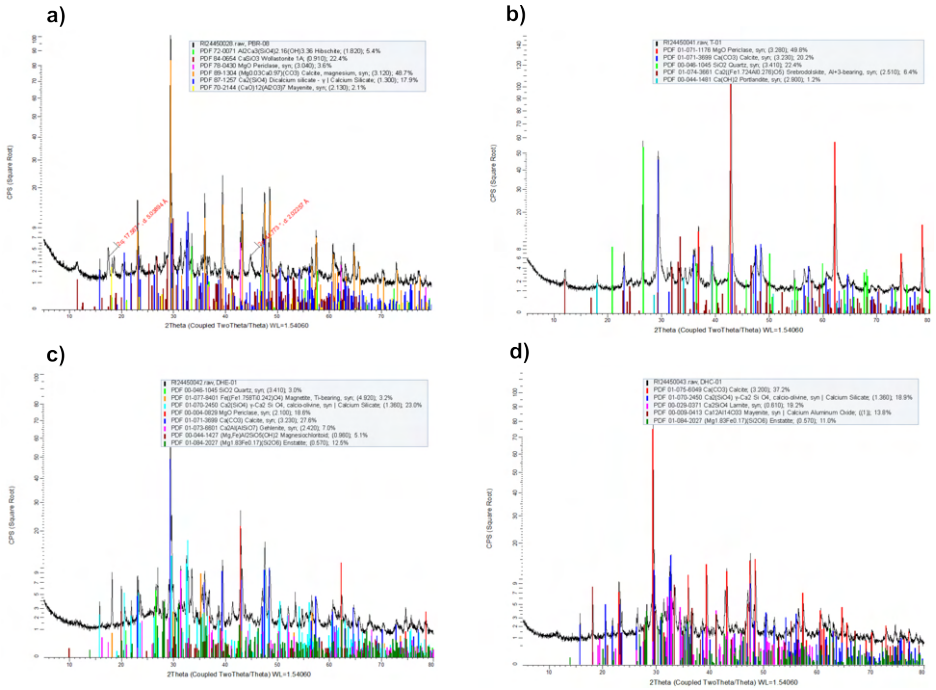


Figure D.3: X-ray diffraction of carbonated a) WS, b) Tundish RW, c) EAF RW, and d) Ladle RW, under same operation condition (4bar, 25$^{o}$C, and 60 min).

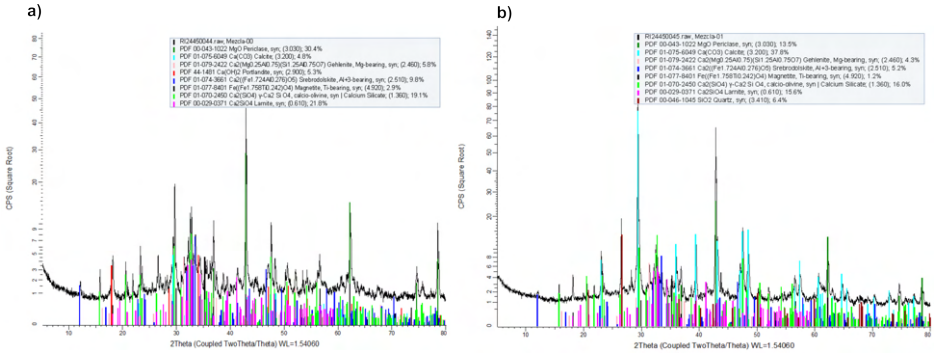


Figure D.4: X-ray diffraction of a) non-carbonated RWs, and b) Carbonated RWs.

# Rietveld mineral phase quantification.

## D.0.1 Description of the method.

The Rietveld refinement[1] was performed with the TOPAS v6 software[2,3]. The background was modelized with a 2nd order Chebyshev polynomial . The instrumental contribution to the diffraction profile was calculated with the Fundamental Parameters Approach[4]. The relative quantitative phase analysis was obtained by refining the Rietveld scale factor for each phase and applying the corresponding well-known equations[5]. The peak width of each phase was modelled with the Double-Voigt Approach[6] by considering only the Lorentzian contribution of the crystallite size effect and discarting any contribution of the microstrain to the peak width. The averaged integral breadth was obtained from the resulting fitted Voigt function to the whole diffractogram. The Scherrer equation[7] was then applied to obtain the apparent crystallite size.

### XRD measurements with D8-Advance.

X-ray diffraction measurements (XRD) were made using a Bruker-AXS D8- Advance diffractometer with vertical theta-theta goniometer, incident- and diffracted-beam Soller slits of $2.5^{o}$, a fixed $0.5^{o}$ receiving slit and an automatic Airscattering knife on the sample surface. The angular $2\theta$ range was between 5 and $90^{o}$. The data were collected with an angular step of $0.02^{o}$ at a step/time of 2s. $Cuk\alpha$ radiation was obtained from a copper X-ray tube operated at 40 kV and 40 mA. Diffracted X-rays were detected with a PSD detector LynxEye-XE-T with an opening angle of $2.94^{o}$.

The RW mixture sample presents several low intensity peaks that have not been possible to assign to any crystal phase. We have assumed that no amorphous phase is present in the sample. We could have added some standard to the sample in order to calculate an absolute wt% of the phases but we discarded this option because of to the high number of phases detected in the sample and some of them with low concentrations. The presence on Zincite was stablished from its reflections (100) and (-210) that are not overlapped by other peaks. The presence of Quartz was stablished from its main peak (101). The presence of Grossite was stablished from its main peak (020). The presence of Boehmite was stablished from its main peak (020). The

presence of Anhydrite cannot be assured because its main peak (021) is partially overlapped by other phases. The presence of $Ca_3Al_2O_6$ cannot be assured because its main peak (440) is totally overlapped by other phases. The presence of Wuestite cannot be assured because its main peak (200) is totally overlapped by other phases. The presence of Franklinite cannot be assured because its main peak (311) is partially overlapped by other phases. The composition of Franklinite (spinel crystal structure) was fixed as $ZnFe_2O_4$ but the real ratio Zn:Fe is unknown. The presence and exact chemical composition (K substituted by Ca or Na) of Microcline cannot be asured because its main peaks is totally overlapped by other phases. The presence of $Na_2Si_2O_5$ cannot be asured because its main peaks are completely overlapped by other phases. The exact chemical composition (Fe substituted by Al) of $Ca_2AlFeO_5$ cannot be determined because of its low concentration. We have calculated the Mass Absorption Coefficient (MAC)[8] for each crystal phase and for the sample taking the wt% of each phase. The microabsorption effect[9] is an important drawback in quantitative phase analysis with the Rietveld method. This effect is especially important when highly absorption phases are mixed with low absorption ones. In the present case, phases as Quartz and Periclase have a low MAC compared with Wuestite, Franklinite and Ca2AlFeO5. This gives an overestimation of the low absorption phases and an underestimation of the high absorption ones. In order to minimize this effect, the literature suggests to minimize the sample grain size ($< 15\mu m$) or apply theoretical corrections[9] not always successfully[10,11] because it is necessary to know the grain size of each crystal phase in the sample. A better approximation to the true wt% of the phases could be by using a shorter wavelength and transmission geometry, i.e. synchrotron radiation and a capillary sample holder. In order to check the validity of the calculations, we have compared the chemical composition of the sample obtained by X-ray fluorescence (XRD) and the calculated chemical composition from the quantitative analysis by X-ray diffraction (QA-XRD). The following table shows the results of these calculations together with the difference between the two techniques. The lost-on ignition (LOI) has not been included in the QA-XRD.

### D.0.2 Rietveld method to non-carbonated RWs.

Table D.1: Elemental quantification of non-carbonated RWs by Rietveld method.

| **Sample** | **RWs** | | |
|---|---|---|---|
| | XRF* | **QA-XRD*** | **DIF** |
| **Al** | **3.128** | 3.664 (0.168) | **0.536 (0.170)** |
| **Fe** | **13.702** | 2.809 (0.224) | **-10.893 (0.226)** |
| **Si** | **6.334** | 8.396 (0.172) | **2.062 (0.173)** |
| **S** | **0.292** | 0.118 (0.138) | **-0.174 (0.140)** |
| **Ti** | **0.348** | 0.000 (0.000) | **-0.348 (0.030)** |
| **Zn** | **0.53** | 1.408 (0.084) | **0.877 (0.093)** |
| **Na** | **0.193** | 0.909 (0.097) | **0.716 (0.104)** |
| **Mg** | **13.381** | 17.327 (0.315) | **3.946 (0.316)** |
| **Mn** | **2.804** | 0.291 (0.017) | **-2.513 (0.042)** |
| **Ca** | **29.212** | 24.921 (0.263) | **4.213 (0.266)** |
| **LOI** | **5.41** | | |

The main differences arise from Fe that by QA-XRD is underestimated whereas with Si happens the contrary. These differences can be attributed to the microabsorption effect. With Mn happens the same as with Fe but here the problem is that the only detected phase that can contain Mn is Franklinite. This spinel structure was introduced in the calculation as $Zn(Fe_{0.75}Mn_{0.25})_2O_4$ as it has been reported the Fe–Mn substitution in spinels ($MnFe_2O_4$, ICSD 40702). However, there is an uncertainty where the rest of Mn is in the sample. There is a good coincidence with Ca as most of the crystal structures contain this element. The results of the quantitative phase analysis for sample RWmixture are shown in the following table. Between parentheses is indicated the error of the last significant digit. This error corresponds to the uncertainty of the fitting process, it does not correspond to the experimental error.

Table D.2: Results of the Quantitative Rieltveld mineral phases analysis of non-carbonated RWs.

| Composition Phase name | Wt % |
|---|---|
| **ZnO Zincite** | 0.9 (1) |
| $SiO_2$ **Quartz** | 2.7 (1) |
| **MgO Perciclase** | 28.1 (5) |
| $CaCO_3$ **Calcite** | 4.7 (3) |
| $Ca(OH)_2$ **Portlandite** | 6.1 (3) |
| $CaSO_4$ **Anhydrite** | 0.5 (4) |
| $\beta - Ca_2SiO_4$ **Larnite** | 8.9 (4) |
| $Ca_2Al_2SiO_7$ **Gehlenite** | 2.1 (3) |
| $\gamma - Ca_2SiO_4$ | 18.8 (4) |
| $CaAl_4O_7$ **Grossite** | 1.0 (2) |
| $Ca_{12}A_{14}O_{33}$ **Mayenite** | 6.2 (3) |
| $Ca_3Al_2O_6$ | 1.6 (5) |
| $Ca_3Mg(SiO_4)_2$ **Merwinite** | 4.8 (3) |
| **AlOOH Boehmite** | 0.8 (2) |
| **FeO Wuestite** | 1.1 (1) |
| $ZnFe_2O_4$ **Franklinite** | 2.5 (1) |
| $KAlSi_3O_8$ **Microcline** | 1.5 (3) |
| $Na_2Si_2O_5$ | 3.6 (4) |
| $Ca_2AlFeO_5$ | 3.8 (7) |

### D.0.3 Rietveld method applied to non-carbonated white Slag.

Table D.3: Elemental quantification of non-carbonated White Slag by Rietveld method.

| Atom | Wt% | Error |
|---|---|---|
| **Al** | 4.2805 | 0.1285 |
| **C** | 2.2507 | 0.0744 |
| **Ca** | 33.683 | 0.2382 |
| **F** | 0.0358 | 0.0107 |
| **Fe** | 2.1149 | 0.1451 |
| **H** | 0.1695 | 0.0095 |
| **Mg** | 3.8607 | 0.2464 |
| **O** | 42.4767 | 0.1512 |
| **S** | 0.1139 | 0.0202 |
| **Si** | 9.9333 | 0.143 |
| **Ti** | 1.081 | 0.0915 |

Table D.4: Results of the Quantitative mineral phases by Rietveld analysis of non-carbonated WS.

| Composition Phase name | Wt % |
|---|---|
| **CaCO3 Calcite** | 13.4 (4) |
| **Ca2Al2SiO7 Gehlenite** | 4.1 (2) |
| **MgO Perciclase** | 2.8 (2) |
| **Ca12A14O33 Mayenite** | 2.2 (2) |
| **$\gamma$-Ca2SiO4** | 27.6 (4) |
| **Ca2.93Al1.97(Si.64O2.56)(OH)9.44 Katoite** | 2.1 (2) |
| **Ca3Al2O6(OH)6** | 6.4 (3) |
| **Ca3Al2(SiO4)1.25(OH)7 Hibschite** | 2.5 (3) |
| **Al(OH)3 Nordstrandite** | 2.5 (3) |
| **(CaxMg1-x)CO3 Mg-Calcite** | 1.8 (5) |
| **$\beta$-Ca2SiO4 Larnite** | 6.7 (4) |
| **Ca(OH)2 Portlandite** | 0.86 (5) |
| **Ca2AlFeO5** | 3.3 (3) |
| **SiO2 Quartz** | 0.22 (4) |
| **Fe3O4 Magnetite** | 1.05 (9) |
| **FeO Wustite** | 0.78 (15) |
| **Ca6(Al(OH)6)2(SO4)3(H2O)25.7 Ettringite** | 1.4 (3) |
| **Ca3Mg(SiO4)2 Merwinite** | 8.1 (4) |
| **CaCO3(H2O) Monohydrocalcite** | 1.8 (2) |
| **CaTiO3 Perovskite** | 1.69 (18) |
| **MgSiO3 Enstatite** | 5.5 (4) |
| **CaMg(CO3)2 Dolomite** | 2.0 (2) |
| **TiO2 Rutile** | 0.66 (10) |
| **Ca(Ti0.818Al0.182)(O0.818F0.182)(SiO4)** | 0.46 (14) |

# XRF analysis.

Table D.5: XRF analysis of the non-carbonated White Slag.

| Component (metal oxide) | Value (%) |
|---|---|
| **SiO2** | 26.59 |
| **Al2O3** | 7.01 |
| **Fe2O3** | 4.03 |
| **MnO** | 1.59 |
| **CaO** | 57.78 |
| **MgO** | 5.52 |
| **P2O5** | 0.06 |
| **TiO2** | 0.43 |
| **Cr2O3** | 0.13 |
| **Na2O** | 0.13 |
| **K2O** | 0.02 |
| **SO3** | 1.098 |

Table D.6: XRF analysis of Ladle, EAF, and Tundish refractory wastes and its mixture (RWs).

| Metal Oxides | Ladle refractory waste | Electric arc furnace refractory waste | Tundish Refractory waste | RWs |
|---|---|---|---|---|
| **Na2O** (%) | 0.14 | 0.45 | 0.19 | 0.26 |
| **MgO** (%) | 4.01 | 9.85 | 52.16 | 22.19 |
| **Al2O3** (%) | 4.71 | 8.65 | 4.23 | 5.91 |
| **SiO2** (%) | 18.92 | 17.99 | 3.39 | 13.55 |
| **SO3** (%) | 0.74 | 0.54 | 0.9 | 0.73 |
| **CaO** (%) | 48.64 | 23.08 | 26.16 | 41.2 |
| **TiO2** (%) | 0.51 | 1.03 | 0.18 | 0.58 |
| **MnO** (%) | 3.72 | 6.04 | 1.02 | 3.62 |
| **Fe2O3** (%) | 18.6 | 28.44 | 11.24 | 11.29 |
| **ZnO** (%) | 0.1 | 1.34 | 0.51 | 0.66 |

# SEM–XEDS.

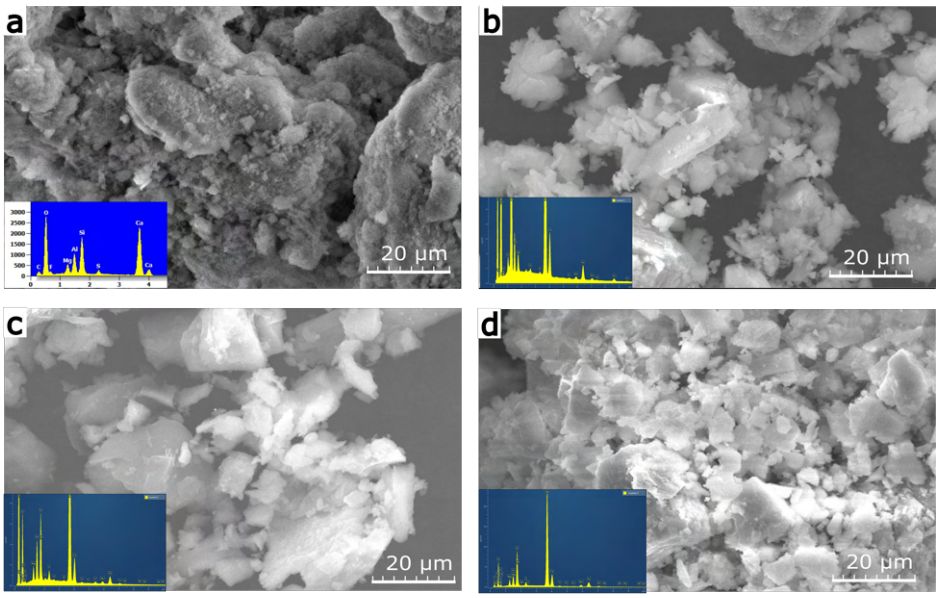


Figure D.5: SEM-XEDS spectra of non-carbonated samples: a) white slag, b) tundish refractory waste, c) EAF refractory waste and d) Ladle refractory waste.

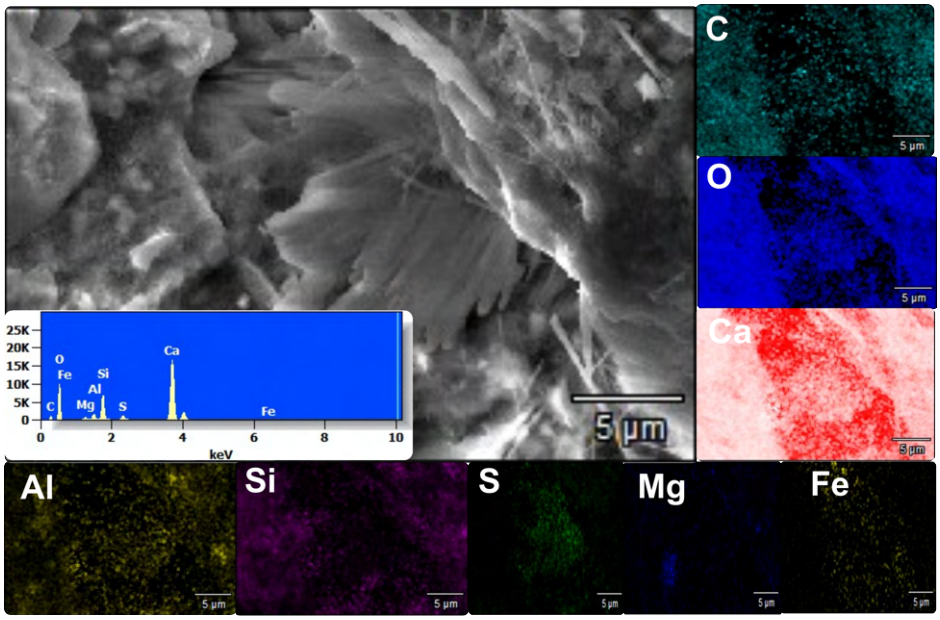


Figure D.6: SEM-XED of the non-carbonated white slag.

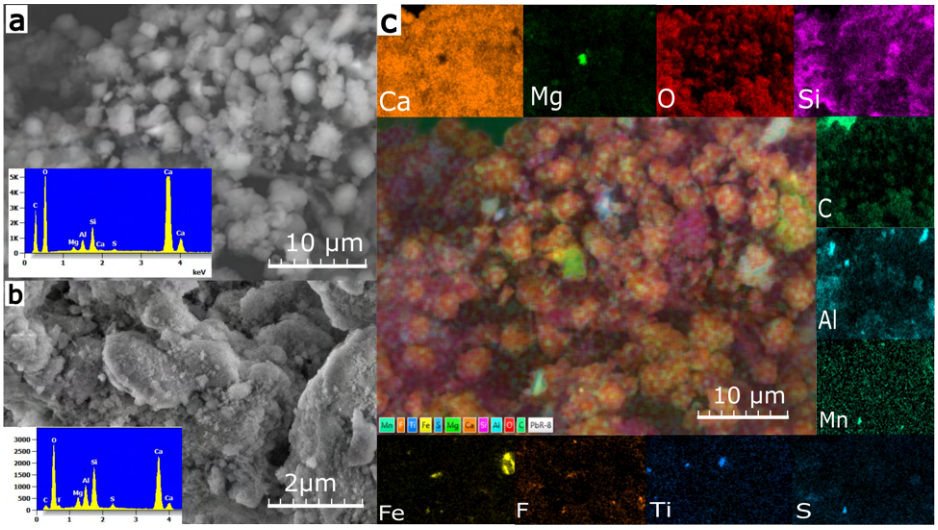


Figure D.7: SEM–XEDS for the a) carbonated and b) non-carbonated white slag. c)Elemental mapping composition analysis for the carbonated white slag.

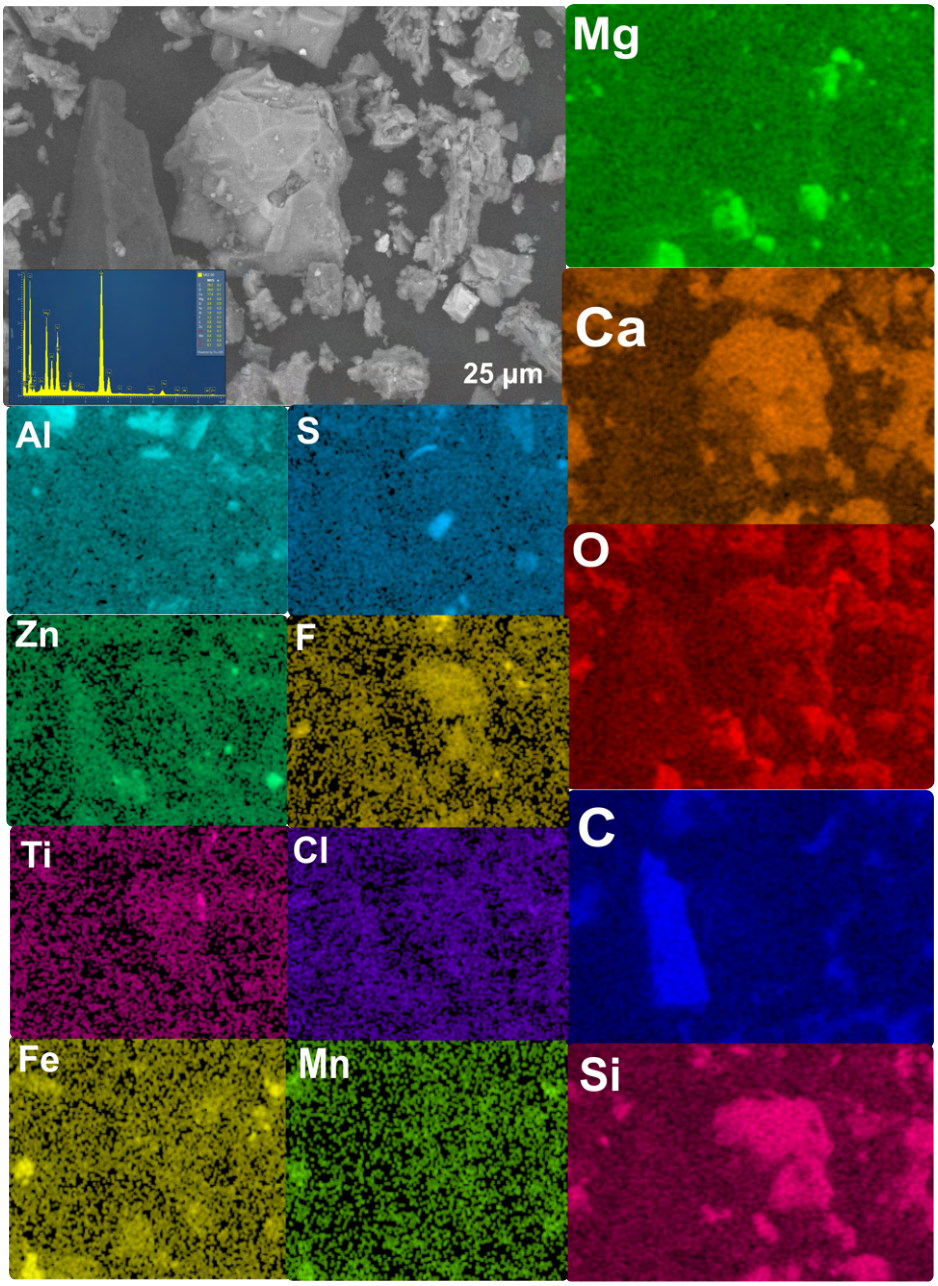


Figure D.8: SEM-XEDS for the non-carbonated Refractory waste mixture.

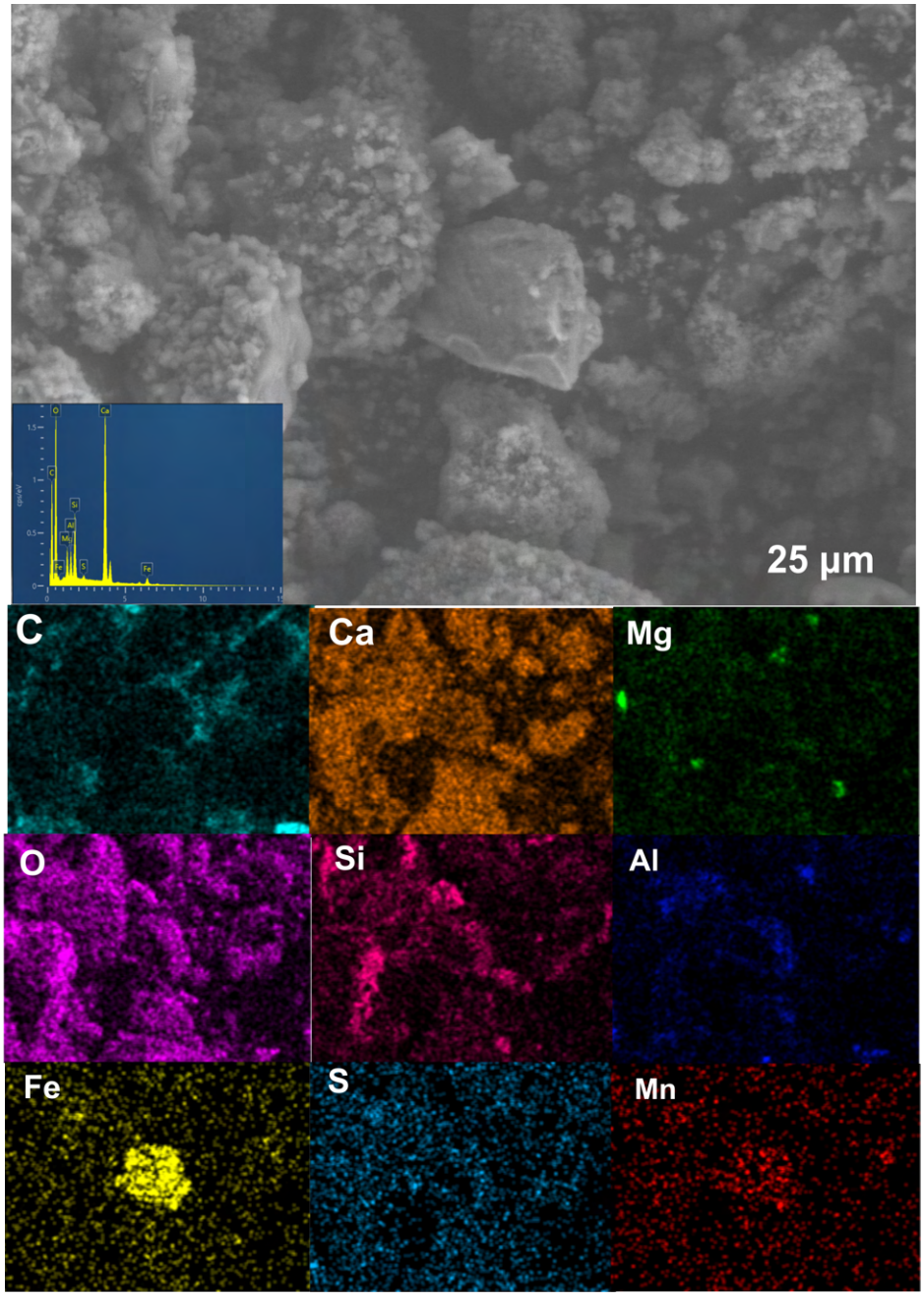


Figure D.9: SEM–XEDS of carbonated RWs.

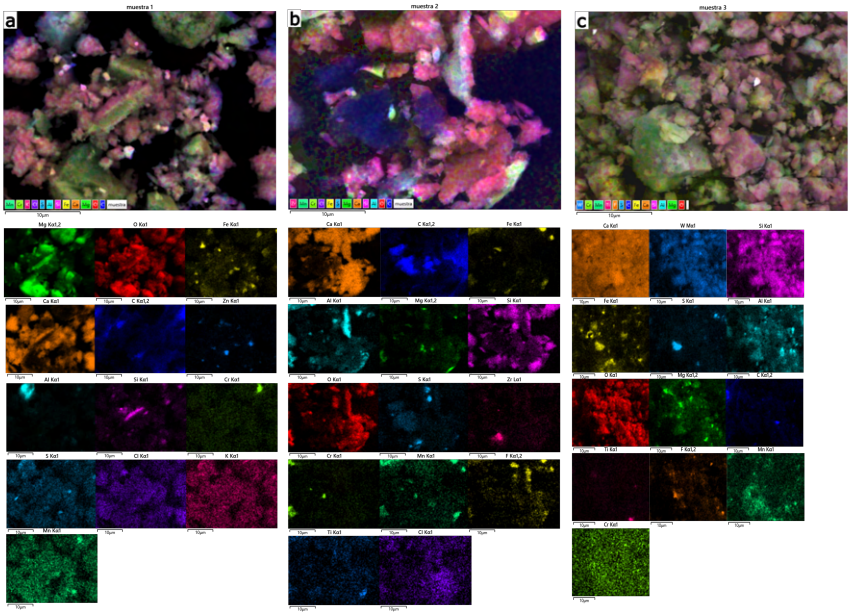


Figure D.10: SEM-XEDS of the non-carbonated refractory wastes. a) Tundish RW, b) EAF RW, and c) Ladle RW

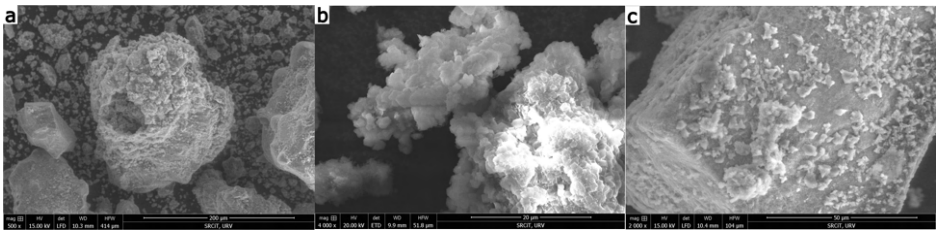


Figure D.11: SEM of individual carbonated RW: a) Tundish RW, b) EAF RW, and c) Ladle RW

# ICP–MS.

## D.0.4 Non-carbonated samples.

Table D.7: Metals presents in the non-carbonated residues (white slag and refractory wastes) determined by ICP-MS.

| Component | White Slag | Tundish RW | EAF RW | Ladle RW | RWmix |
|---|---|---|---|---|---|
| **Mg (mg/g)** | 18.3 ± 0,3 | 254 ± 7 | 89 ± 2 | 31 ± 0.5 | 114 ± 4 |
| **Al (mg/g)** | 13.83 ± 0,10 | 8.4 ± 0.4 | 47.7 ± 1.7 | 45.5 ± 0.7 | 5.29 ± 0.06 |
| **Si (mg/g)** | 3.42 ± 0,05 | 8.09 ± 0.08 | 14.37 ± 0.17 | 10.28 ± 0.09 | 5.42 ± 0.04 |
| **Ca (mg/g)** | 59.2 ± 1,7 | 150 ± 2 | 365 ± 12 | 396 ± 7 | 272 ± 6 |
| **Ti (mg/g)** | 2.151 ± 0,017 | 0.99 ± 0.02 | 2.49 ± 0.03 | 2.458 ± 0.017 | 1.744 ± 0.013 |
| **V (mg/kg)** | 17.9 ± 1,7 | 69 ± 4 | 72 ± 6 | 29.2 ± 1.6 | 58 ± 3 |
| **Cr (mg/g)** | 0.189 ± 0,003 | 1.97 ± 0.04 | 1.71 ± 0.03 | 0.473 ± 0.018 | 1.009 ± 0.017 |
| **Fe (mg/g)** | 13.09 ± 0,16 | 78.8 ± 1.6 | 47.3 ± 0.7 | 46.1 ± 0.9 | 43.2 ± 0.9 |
| **Pb (mg/kg)** | 23 ± 0.3 | 3709 ± 50 | 68 ± 3 | 51.5 ± 1.5 | 247 ± 3 |
| **Ni (mg/kg)** | 130 ± 2 | - | - | - | - |

## D.0.5 Carbonated samples.

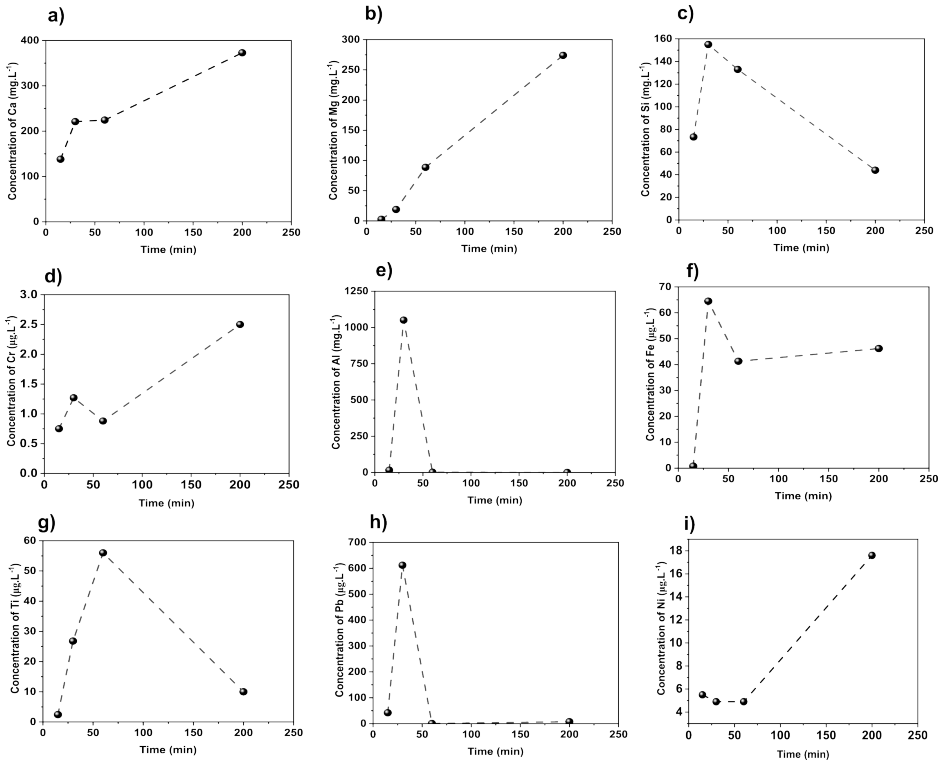


Figure D.12: Element concentration of Ca, Mg, Si, Cr, Al, Fe, Ti and Pb leaching as a function of mineralization reaction time in the carbonated white Slag (WS) at 4 bar and 25ºC.

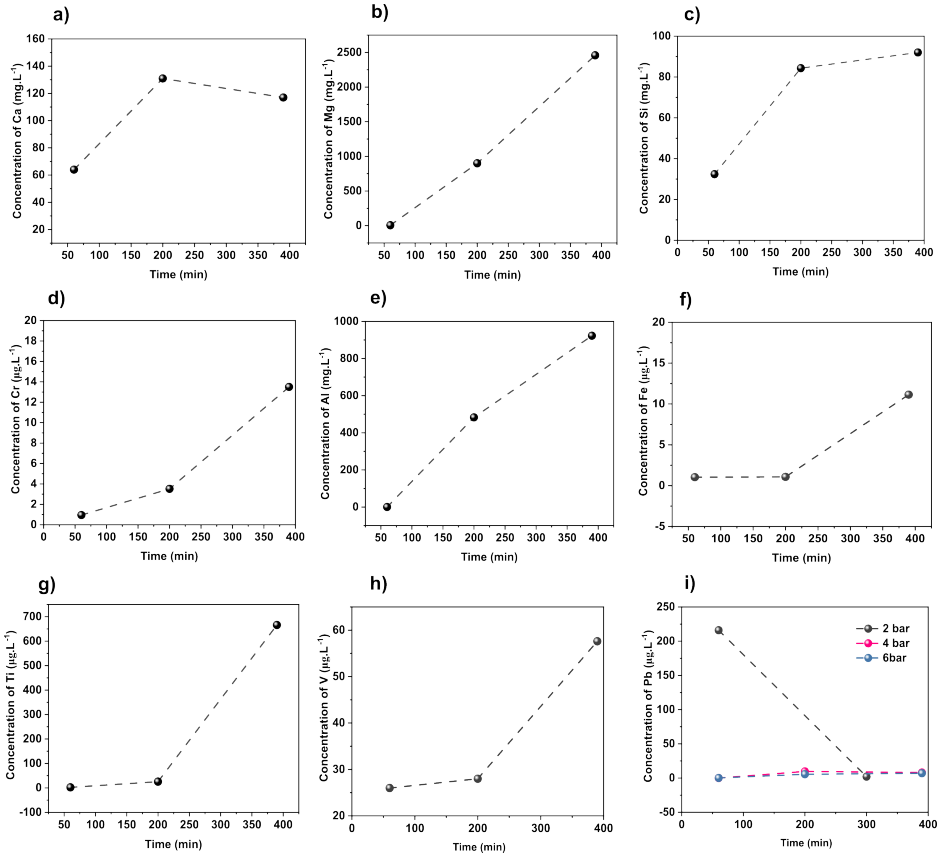


Figure D.13: Element concentration of Ca, Mg, Si, Cr, Al, Fe, Ti, and Pb of RWs residual water after mineralization process as function of reaction time at 4 bar and 25ºC.

# FTIR analysis.

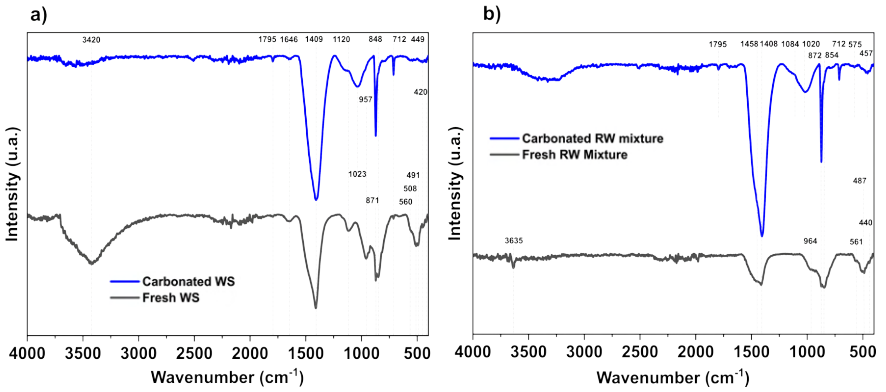


Figure D.14: FTIR spectra of a) Fresh and Carbonated WS at 25ºC, 4bar and 60 min reaction time and b) Fresh and Carbonated RW mixture at 25ºC, 2 bar and 5h of reaction time.

Figure D.14a presents the FTIR spectra of the non-carbonated and carbonated white slag samples under optimal conditions recorded in the range between 4000 $cm^{-1}$ and 400 $cm^{-1}$ in order to gather information about the presence of functional groups. In the IR spectrum of the non-carbonated white slag, a broad and intense band at about 3420 $cm^{-1}$ could be assigned to the stretching vibration of hydroxyl groups attached to Ca, Fe, and Al, compounds that were previously identified using the Rietveld method, and interlaminar water molecules[12–15]. The minor peak at 1646 $cm^{-1}$ was attributed to O-H bending vibration also indicating the presence of H2O molecules in the interlayer space or absorbed physically water molecules[12–16]. The significant decrease in the intensity of the band in the 3700–3300 $cm^{-1}$ region for the carbonated WS sample, can be related to the loss of water molecules after the drying process of the sample at 80 ºC, and also the formation of carbonates from Ca-Al silicates containing hydroxyl groups. The presence of carbonates was also observed by analyses of the IR spectra of both non-carbonated and carbonated samples. The intense band centered at about 1409 $cm^{-1}$ corresponds to the $\nu 3$ vibrations of $CO_3^{-2}$ (asymmetric $C-O$ stretching), while the peaks at 871 $cm^{-1}$ and around 712 $cm^{-1}$ are associated with out-plane and in-plane bending ($\nu 2$) vibrations of $CO_3^{-2}$, respectively[12,16–21]. The peak at 1795 $cm^{-1}$ can also be ascribed to $CaCO_3$ [20,22,23]. The in-

crease in intensity of these bands for WS carbonated sample suggests that carbonation of the sample took place during the $CO_2$ mineralization process, as confirmed by the growth of the carbonate crystalline phrases in the X-ray diffractograms (XRD). The FTIR spectra of both fresh and carbonated samples also reveal the presence of bands of the silicate groups in the region between 400 and 1250 $cm^{-1}$ [16,17,19]. The bands located at approximately 1120 y 957 $cm^{-1}$ in the spectrum of the white slag are due to asymmetric stretching mode $Si-O-Si$ and $Si-O$ with one non-bridging oxygen (Si-O-NBO) per $SiO_4$ tetrahedron (Q3 groups), respectively[19–24]. For the spectrum of the carbonated sample, both bands appear as shoulders located in the band in the 900-1250 $cm^{-1}$ range centered at 1023 $cm^{-1}$, which can also be associated with $Si-O-Si$ asymmetric stretching vibrations [21,24,25]. The bands at 848 $cm^{-1}$ can be attributed to Si-O with two non-bridging oxygens (Si-O-2NBO) per SiO4 tetrahedron (Q2 groups) or to stretching vibrations derived from Mg-O bonds [26,27]. Finally, the group of bands in the range of 400–500 $cm^{-1}$ may be correlated with the internal deformation of the $SiO_4$ tetrahedra form[16,17]. In both samples, the small peak appearing at 420 $cm^{-1}$ may be associated with the bending mode of $Mg-O$ [26,28–30]. The shoulder at 560 $cm^{-1}$ observed in the spectrum of the fresh white residue can be attributed to stretching vibrations derived from $Mg-O$ bonds [27,29]. The results are consistent with the XRD measurements that identified MgO crystalline phases.

Figure D.14b The FTIR spectra of the RW mixture sample after carbonation exhibited bands in the range of 1400-1500 $cm^{-1}$ that are attributed to the asymmetric C-O stretching from carbonates, as well as peaks around 872 and 712 $cm^{-1}$, which correspond to the out-of-plane and in-plane bending vibrations from the traces of carbonate-based compounds, respectively[16–21]. A minor peak also appears at about 1795 $cm^{-1}$, which is relative to $CaCO_3$ [20,22,23]. In the infrared spectrum of the non-carbonated RW mixture sample, carbonate-specific bands also appeared as the asymmetric $C-O$ stretching bands located in the region between 1400 and 1500 $cm^{-1}$, and the weak shoulder of out-of-plane bending vibration around 872 $cm^{-1}$ [16,17]. It is clearly noticeable the increase in intensity of these bands for the carbonated sample and also the appearance of new peaks typical of carbonate-based compounds. These results confirm the existence of carbonation during $CO_2$ mineralization, and are in accordance with the XRD measurements, which detected the pres-

ence of calcite in the fresh sample, and a growth of calcite crystalline phases and the appearance of aragonite (another form of calcium carbonate) in the carbonated sample. Other peaks are also seen in the IR spectra of the fresh and carbonated samples. In both samples, the narrow band located between 3000 and 3700 $cm^{-1}$ may be due to the stretching vibrations of O-H groups in $H_2O$ or hydroxyls[16,17,19]. A narrow band is observed around 3635 $cm^{-1}$ in the IR spectra of the fresh RW mixture sample, while an intense band is seen between 3000 and 3700 $cm^{-1}$ in the spectra of the carbonated sample. Since no compounds containing hydroxyl groups were identified by XRD analysis of the carbonated RW mixture sample, it is assumed that water molecules may have been absorbed physically during storage of this sample. Silicate groups are also evident in the FTIR spectra of the fresh and carbonated RW mixture samples with the corresponding bands at 964 $cm^{-1}$ ($Si-O$ with one non-bridging oxygen per $SiO_4$ tetrahedron), the range of 900-1200 $cm^{-1}$ centered at 1020 $cm^{-1}$ ($Si-O-Si$ asymmetric stretching vibrations) [21,24,25], and the region 400-500 $cm^{-1}$ (internal deformation of the $SiO_4$ tetrahedra form). The peak at 854 $cm^{-1}$ can be assigned to $Si-O$ with two non-bridging oxygens per $SiO_4$ tetrahedron or the $\nu 1$ stretching of $Mg-O$ [26,27]. The stretching and bending mode vibration bands derived from the $Mg-O$ bonds are also shown at 574 $cm^{-1}$ and in the range of $410-450 cm^{-1}$, respectively[26–30]. All the results found in the FTIR spectra are in accordance with the XRD measurements.

# pH measurement in the RWs carbonation.

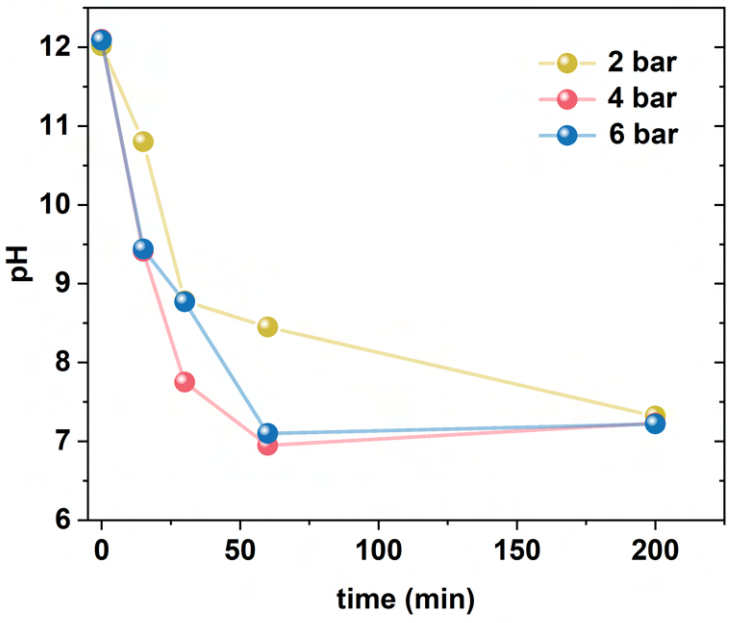


Figure D.15: pH value at different reaction times and pressures using gas mixture in the RWs carbonation.

# Mineralization reactor geometrical characteristics.

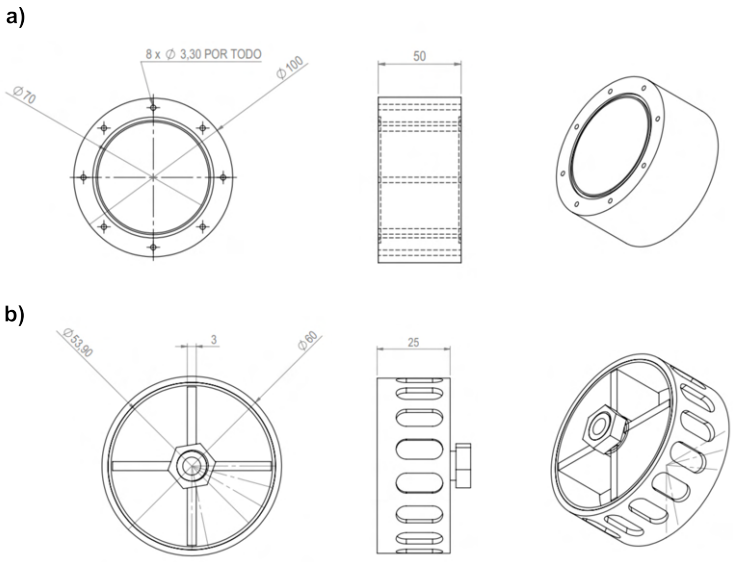


Figure D.16: Geometric characteristics of a) External part of the mineralization reactor and b) External part of the mineralization reactor.

# Experimental design.

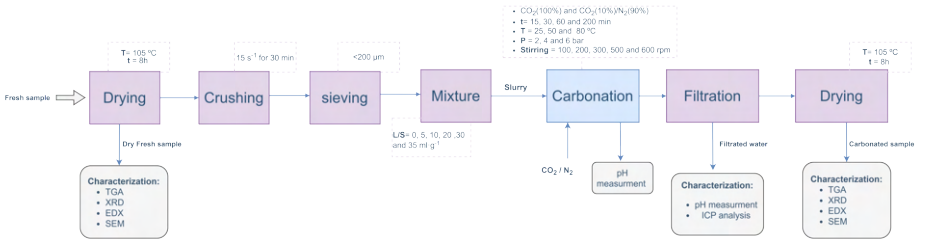


Figure D.17: Diagram Flow for the experimental design in the mineralization experiment for WS and RW samples.

# References.

[1] H.M. Rietveld, A profile refinement method for nuclear and magnetic structures, Journal of Applied Crystallography. 2 (1969) 65–71.

[2] TOPAS 6 Technical Reference, Bruker AXS GmbH, 2017.

[3] A.A. Coelho, TOPAS and TOPAS-Academic: an optimization program integrating computer algebra and crystallographic objects written in C++, J. Appl. Crystallogr. 51 (2018) 210–218.

[4] R.W. Cheary, A.A. Coelho, J.P. Cline, Fundamental Parameters Line Profile Fitting in Laboratory Diffractometers Volume 109 Number 1 January-February 2004, (n.d.). https://nvlpubs.nist.gov/nistpubs/jres/109/

[5] R.J. Hill, C.J. Howard, Quantitative phase analysis from neutron powder diffraction data using the Rietveld method, J. Appl. Crystallogr. 20 (1987) 467–474.

[6] D. Balzar, Voigt-function model in diffraction line-broadening analysis, (n.d.).

[7] A.R. Stokes, A.J.C. Wilson, A method of calculating the integral breadths of Debye-Scherrer lines, Math. Proc. Camb. Philos. Soc. 38 (1942) 313–322.

[8] H.P. Klug, L.E. Alexander, X-ray diffraction procedures: For polycrystalline and amorphous materials, 2nd ed., John Wiley & Sons, Nashville, TN, 1974.

[9] G.W. Brindley, XLV. The effect of grain or particle Size on x-ray reflections from mixed powders and alloys, considered in relation to the quantitative determination of crystalline substances by x-ray methods, Lond. Edinb. Dublin Philos. Mag. J. Sci. 36 (1945) 347–369.

[10] N.V.Y. Scarlett, I.C. Madsen, L.M.D. Cranswick, T. Lwin, E. Groleau, G. Stephenson, M. Aylmore, N. Agron-Olshina, Outcomes of the International Union of Crystallography Commission on Powder Diffraction Round Robin on Quantitative Phase Analysis: samples 2, 3, 4, synthetic bauxite, natural granodiorite and pharmaceuticals, J. Appl. Crystallogr. 35 (2002) 383–400.

[11] I.C. Madsen, N.V.Y. Scarlett, L.M.D. Cranswick, T. Lwin, Outcomes of the International Union of Crystallography Commission on Powder Diffraction round robin on quantitative phase analysis: Samples 1ato 1h, J. Appl. Crystallogr. 34 (2001) 409–426.

[12] P. Kuśtrowski, L. Chmielarz, E. Bożek, M. Sawalha, F. Roessner, Acidity and basicity of hydrotalcite derived mixed Mg–Al oxides studied by test reaction of MBOH conversion and temperature pro-

grammed desorption of NH3 and CO2, Mater. Res. Bull. 39 (2/2004) 263–281.

[13] W. Xie, H. Peng, L. Chen, Calcined Mg–Al hydrotalcites as solid base catalysts for methanolysis of soybean oil, J. Mol. Catal. A Chem. 246 (03/2006) 24–32.

[14] C. Li, Y. Wang, Y. Zhang, M. Wang, X. Sun, H. Cui, Y. Xie, Isomerization Kinetics of Glucose to Fructose in Aqueous Solution with Magnesium-Aluminum Hydrotalcites, ChemistrySelect. 5 (2020) 270–279.

[15] H. Yan, G. Zhang, Y. Wang, J. Liu, G. Li, Y. Zhao, Y. Xu, Y. Lv, A green synthesis strategy for low-cost multi-porous solid CO2 adsorbent using blast furnace slag, Fuel. 329 (12/2022) 125380.

[16] L. Fernandez, C. Alonso, A. Hidalgo, C. Andrade, The role of magnesium during the hydration of C3S and C-S-H formation. Scanning electron microscopy and mid-infrared studies, Adv. Cem. Res. (2015). https://doi.org/10.1680/adcr.2005.17.1.9.

[17] P. Yu, R.J. Kirkpatrick, B. Poe, P.F. McMillan, X. Cong, Structure of Calcium Silicate Hydrate (C-S-H): Near-, Mid-, and Far-Infrared Spectroscopy, J. Am. Ceram. Soc. 82 (1999) 742–748.

[18] J.T. Kloprogge, R.L. Frost, Fourier Transform Infrared and Raman Spectroscopic Study of the Local Structure of Mg-, Ni-, and Co-Hydrotalcites, J. Solid State Chem. 146 (1999) 506–515.

[19] H. Aguiar, J. Serra, P. González, B. León, Structural study of sol–gel silicate glasses by IR and Raman spectroscopies, J. Non-Cryst. Solids. 355 (2009) 475–480.

[20] A.I. Cadiș, F. Ștefania Rus, J.N. Gonçalves, M. Ivanovici, Preparing a Ca-Bi-O System by the Precipitation Method and Studying Its Intermediate Structural Properties for Applications in Water Treatment, Inorganics. 11 (2023/2) 79.

[21] A. Meiszterics, L. Rosta, H. Peterlik, J. Rohonczy, S. Kubuki, P. Henits, K. Sinkó, Structural Characterization of Gel-Derived Calcium Silicate Systems, J. Phys. Chem. A. 114 (2010) 10403–10411.

[22] A.G. Xyla, P.G. Koutsoukos, Quantitative analysis of calcium carbonate polymorphs by infrared spectroscopy, J. Chem. Soc. Lond. Faraday Trans. 1. 85 (1989) 3165.

[23] J. Kiefer, A. Stärk, A.L. Kiefer, H. Glade, Infrared Spectroscopic Analysis of the Inorganic Deposits from Water in Domestic and Technical Heat Exchangers, Energies. 11 (2018/4) 798.

[24] J. Serra, P. González, S. Liste, C. Serra, S. Chiussi, B. León, M. Pérez-Amor, H.O. Ylänen, M. Hupa, FTIR and XPS studies of

bioactive silica based glasses, J. Non-Cryst. Solids. 332 (2003) 20–27.

[25] I. Izquierdo-Barba, A.J. Salinas, M. Vallet-Regí, Bioactive Glasses: From Macro to Nano, International Journal of Applied Glass Science. 4 (2013) 149–161.

[26] H. Dhaouadi, H. Chaabane, F. Touati, Mg(OH)2 Nanorods Synthesized by A Facile Hydrothermal Method in the Presence of CTAB, Nano-Micro Lett. 3 (09/2011) 153–159.

[27] S.V.G. Kumari, K. Pakshirajan, G. Pugazhenthi, Synthesis and characterization of MgO nanostructures: A comparative study on the effect of preparation route, Mater. Chem. Phys. 294 (2023) 127036.

[28] I.W. Sutapa, A.W. Wahab, P. Taba, N.L. Nafie, Synthesis and Structural Profile Analysis of the MgO Nanoparticles Produced Through the Sol-Gel Method Followed by Annealing Process, Oriental J. Chem. 34 (2018) 1016–1025.

[29] N.M.A. Hadia, H.A.-H. Mohamed, Characteristics and optical properties of MgO nanowires synthesized by solvothermal method, Mater. Sci. Semicond. Process. 29 (2015) 238–244.

[30] R. Mahadevaiah, H.S. Lalithamba, S. Shekarappa, R. Hanumanaika, Synthesis of N$\alpha$-protected formamides from amino acids using MgO nano catalyst: Study of molecular docking and antibacterial activity, Scientia Iranica. 24 (2017) 3002–3013.

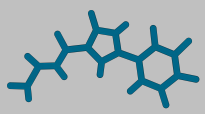

ICIQ

Institut
Català
d'Investigació
Química

UNIVERSITAT
ROVIRA i VIRGILI